

From Nuclei to Compact Stars

Contents

1	Topics	1055
2	Participants	1057
2.1	ICRANet	1057
2.2	External on going collaborations	1057
2.3	Postdocs	1058
2.4	Graduate Students	1059
2.5	Undergraduate Students	1059
3	Publications 2016	1061
3.1	Refereed Journals	1061
3.1.1	Printed	1061
3.1.2	Accepted for publication or in press	1062
3.1.3	Submitted	1064
3.1.4	To be submitted	1066
3.2	Conference Proceedings	1067

1 Topics

The study of compact objects such as white dwarfs, neutron stars and black holes requires the interplay between nuclear and atomic physics together with relativistic field theories, e.g., general relativity, quantum electrodynamics, quantum chromodynamics, as well as particle physics. In addition to the theoretical physics aspects, the study of astrophysical scenarios characterized by the presence of a compact object has also started to be focus of extensive research within our group. The research which has been done and is currently being developed within our group can be divided into the following topics:

- **Nuclear and Atomic Astrophysics.** Within this subject of research we study the properties and processes occurring in compact stars in which nuclear and atomic physics have to be necessarily applied. We focus on the properties of nuclear matter under extreme conditions of density and pressure found in these objects. The equation of state of the matter in compact star interiors is studied in detail taking into account all the interactions between the constituents within a full relativistic framework.
- **White Dwarfs Physics and Structure.** The aim of this part of our research is to construct the structure of white dwarfs within a self-consistent description of the equation of state of the interior together with the solution of the hydrostatic equilibrium equations in general relativity. Both non-magnetized and magnetized white dwarfs are studied.
- **White Dwarfs Astrophysics.** We are within this topic interested in the astrophysics of white dwarfs both isolated and in binaries systems. Magnetized white dwarfs, soft gamma repeaters, anomalous X-ray pulsars, white dwarf pulsars, cataclysmic variables, binary white dwarf mergers, and type Ia supernovae are studied. The role of a realistic white dwarf interior structure is particularly emphasized.
- **Neutron Stars Physics and Structure.** We calculate the properties of the interior structure of neutron stars using realistic models of the nuclear matter equation of state within the general relativistic equations of equilibrium. Strong, weak, electromagnetic and gravitational interactions

have to be jointly taken into due account within a self-consistent fully relativistic framework. Both non-magnetized and magnetized neutron stars are studied.

- **Neutron Stars Astrophysics.** We study astrophysical systems harboring neutron stars such as isolated and binary pulsars, low and intermediate X-ray binaries, inspiraling and merging double neutron stars. Most extreme cataclysmic events involving neutron stars and their role in the explanation of extraordinarily energetic astrophysical events such as gamma-ray bursts are analyzed in detail.
- **Radiation Mechanisms of White Dwarfs and Neutron Stars.** We here study the possible emission mechanisms of white dwarfs and neutron stars. We are thus interested in both electromagnetic and gravitational radiation at work in astrophysical systems such as compact star magnetospheres, inspiraling and merging relativistic double neutron stars, neutron star-white dwarfs, and neutron star-black hole binaries represent some examples.
- **Exact Solutions of the Einstein and Einstein-Maxwell Equations in Astrophysics.** We analyze the ability of analytic exact solutions of the Einstein and Einstein-Maxwell equations to describe the exterior spacetime of compact stars such as white dwarfs and neutron stars. The problem of matching between interior and exterior spacetimes is addressed in detail. The effect of the quadrupole moment on the properties of the spacetime is also investigated. Particular attention is given to the application of exact solutions in astrophysics, e.g. the dynamics of particles around compact stars and its relevance in astrophysical systems such as X-ray binaries.
- **Critical Fields and Non-linear Electrodynamics Effects in Astrophysics.** We study the conditions under which ultrastrong electromagnetic fields can develop in astrophysical systems such as neutron stars and in the process of gravitational collapse to a black hole. The effects of non-linear electrodynamics minimally coupled to gravity are investigated. New analytic and numeric solutions to the Einstein-Maxwell equations representing black holes or the exterior field of a compact star are obtained and analyzed. The consequences on extreme astrophysical systems, for instance gamma-ray bursts, is studied.

2 Participants

2.1 ICRANet

- D. Arnett (Steward Observatory, University of Arizona, USA)
- C. L. Bianco (ICRANet; University of Rome, Italy)
- D. Bini (Istituto Nazionale per l'Applicazione del Calcolo, Italy)
- L. Izzo (ICRANet; University of Rome, Italy)
- H. Kleinert (Free University of Berlin , Germany)
- V. Popov (ITEP, Moscow, Russia)
- J. A. Rueda (ICRANet; Sapienza University of Rome, Italy)
- R. Ruffini (ICRANet; University of Rome, Italy)
- G. Vereschagin (ICRANet; Sapienza University of Rome, Italy)
- S.-S. Xue (ICRANet; Sapienza University of Rome, Italy)

2.2 External on going collaborations

- C. G. Bernal (Universidade Federal do Rio Grande, Brazil)
- K. Boshkayev (Al-Farabi Kazakh National University, Kazakhstan)
- R. Camargo (Universidade do Estado de Santa Catarina, Florianópolis, Brazil)
- C. Cherubini (Università Campus Biomedico, Rome, Italy)
- S. Chiapparini (Universidade do Estado do Rio de Janeiro, Brazil)
- S. B. Duarte (Centro Brasileiro de Pesquisas Físicas, Brazil)
- S. Filippi (Università Campus Biomedico, Rome, Italy)

- C. L. Fryer (University of Arizona; Los Alamos National Laboratory, USA)
- E. Gacía-Berro (Universitat Politècnica de Catalunya, Spain)
- P. Lorén Aguilar (University of Exeter, United Kingdom)
- S. O. Kepler (Universidade Federal do Rio Grande do Sul, Brazil)
- B. Külebi (Institut de Ciències de l'Espai, Spain)
- M. Malheiro (Instituto Tecnológico de Aeronáutica, Brazil)
- R. M. Jr. Marinho (Instituto Tecnológico de Aeronáutica, Brazil)
- S. M. de Carvalho (Universidade Federal do Tocantins, Brazil)
- M. M. Guzzo (Universidade Estadual de Campinas, Brazil)
- G. Mathews (University of Notre Dame, USA)
- D. P. Menezes (Universidade Federal de Santa Catarina, Brazil)
- R. Negreiros (Universidade Federal de Fluminense, Brazil)
- L. Pachón (Universidad de Antioquia, Colombia)
- H. Quevedo (Universidad Nacional Autónoma de México, Mexico)
- F. Torres (Universidade Estadual de Campinas, Brazil)
- C. Valenzuela (Universidad del Valle, Colombia)
- C. A. Z. Vasconcellos (Universidade Federal do Rio Grande do Sul, Brazil)
- B. Wiggins (Los Alamos National Laboratory, USA)

2.3 Postdocs

- B. S. Arsioli (Agenzia Spaziale Italiana; ASI Space Data Center, Italy)
- R. Belvedere (Centro Brasileiro de Pesquisas Físicas; ICRANet-Rio, Brazil)
- J. G. Coelho (Instituto Nacional de Pesquisas Espaciais, Brazil)
- M. Muccino (ICRANet; University of Rome, Italy)
- J. P. Pereira (Universidade Federal do ABC, Brazil)
- Y. Wu (Max Planck Institute for Nuclear Physics, Germany)

2.4 Graduate Students

- L. Becerra (ICRANet; Sapienza University of Rome, Italy)
- D. L. Cáceres (ICRANet; Sapienza University of Rome, Italy)
- F. Cipolletta (ICRANet; Sapienza University of Rome, Italy)
- R. V. Lobato (Instituto Tecnológico de Aeronáutica, Brazil)
- F. G. Oliveira (ICRANet; University of Rome, Italy and Université de Nice Sophia-Antipolis, France)
- R. Riahi (Isfahan University of Technology, Iran)
- J. F. Rodriguez (ICRANet; Sapienza University of Rome, Italy)
- S. Shakeri (Isfahan University of Technology, Iran)
- M. L. Warren (University of Notre Dame, USA)

2.5 Undergraduate Students

- D. Gizzi (Sapienza University of Rome, Italy)
- S. Petroni (Sapienza University of Rome, Italy)

3 Publications 2016

3.1 Refereed Journals

3.1.1 Printed

1. R. Ruffini, M. Muccino, Y. Aimuratov, C. L. Bianco, C. Cherubini, M. Enderli, M. Kovacevic, R. Moradi, A. V. Penacchioni, G. B. Pisani, J. A. Rueda, and Y. Wang, *GRB 090510: a genuine short-GRB from a binary neutron star coalescing into a Kerr-Newman black hole*, ApJ 831, 178 2016.

In a new classification of merging binary neutron stars (NSs) we separate short gamma-ray bursts (GRBs) into two subclasses. The ones with $E_{\text{iso}} \lesssim 10^{52}$ erg coalesce to form a massive NS and are indicated as short gamma-ray flashes (S-GRFs). The hardest, with $E_{\text{iso}} \gtrsim 10^{52}$ erg, coalesce to form a black hole (BH) and are indicated as genuine short GRBs (S-GRBs). Within the fireshell model, S-GRBs exhibit three different components: the proper GRB (P-GRB) emission, observed at the transparency of a self-accelerating baryon-e+e- plasma; the prompt emission, originating from the interaction of the accelerated baryons with the circumburst medium; and the high energy (GeV) emission, observed after the P-GRB and indicating the formation of a BH. GRB 090510 gives the first evidence for the formation of a Kerr BH or, possibly, a KerrNewman BH. Its P-GRB spectrum can be fitted by a convolution of thermal spectra whose origin can be traced back to an axially symmetric dyadotorus. A large value of the angular momentum of the newborn BH is consistent with the large energetics of this S-GRB, which reach in the 1-10,000 keV range $E_{\text{iso}} = (3.95 \pm 0.21) \times 10^{52}$ erg and in the 0.1-100 GeV range $E_{\text{LAT}} = (5.78 \pm 0.60) \times 10^{52}$ erg, the most energetic GeV emission ever observed in S-GRBs. The theoretical redshift $z_{\text{th}} = 0.75 \pm 0.17$ that we derive from the fireshell theory is consistent with the spectroscopic measurement $z = 0.903 \pm 0.003$, showing the self-consistency of the theoretical approach. All S-GRBs exhibit GeV emission, when inside the Fermi-LAT field of view, unlike S-GRFs, which never evidence it. The GeV emission appears to be the discriminant for the formation of a BH in GRBs, confirmed by their observed overall energetics.

3.1.2 Accepted for publication or in press

1. J. G. Coelho, D. L. Cáceres, R. C. R. de Lima, M. Malheiro, J. A. Rueda, and R. Ruffini, *On the nature of some SGRs and AXPs as rotation-powered neutron stars*, to appear in A&A.

Soft gamma repeaters (SGRs) and anomalous X-ray pulsars (AXPs) are slow rotating isolated pulsars whose energy reservoir is still matter of debate. Adopting neutron star (NS) fiducial parameters; mass $M = 1.4M_{\odot}$, radius $R = 10$ km, and moment of inertia, $I = 10^{45}$ g cm², the rotational energy loss, \dot{E}_{rot} , is lower than the observed luminosity (dominated by the X-rays) L_X for many of the sources. We investigate the possibility that some members of this family could be canonical rotation-powered pulsars using realistic NS structure parameters instead of fiducial values. We compute the NS mass, radius, moment of inertia and angular momentum from numerical integration of the axisymmetric general relativistic equations of equilibrium. We then compute the entire range of allowed values of the rotational energy loss, \dot{E}_{rot} , for the observed values of rotation period P and spin-down rate \dot{P} . We also estimate the surface magnetic field using a general relativistic model of a rotating magnetic dipole. We show that realistic NS parameters lowers the estimated value of the magnetic field and radiation efficiency, L_X/\dot{E}_{rot} , with respect to estimates based on fiducial NS parameters. We show that nine SGRs/AXPs can be described as canonical pulsars driven by the NS rotational energy, for L_X computed in the soft (2–10 keV) X-ray band. We compute the range of NS masses for which $L_X/\dot{E}_{\text{rot}} < 1$. We discuss the observed hard X-ray emission in three sources of the group of nine potentially rotation-powered NSs. This additional hard X-ray component dominates over the soft one leading to $L_X/\dot{E}_{\text{rot}} > 1$ in two of them. We show that 9 SGRs/AXPs can be rotation-powered NSs if we analyze their X-ray luminosity in the soft 2–10 keV band. Interestingly, four of them show radio emission and six have been associated with supernova remnants (including Swift J1834.9-0846 the first SGR observed with a surrounding wind nebula). These observations give additional support to our results of a natural explanation of these sources in terms of ordinary pulsars. Including the hard X-ray emission observed in three sources of the group of potential rotation-powered NSs, this number of sources with $L_X/\dot{E}_{\text{rot}} < 1$ becomes seven. It remains open to verification 1) the accuracy of the estimated distances and 2) the possible contribution of the associated supernova remnants to the hard X-ray emission.

2. D. L. Cáceres, S. M. de Carvalho, J. G. Coelho, R. C. R. de Lima, and J.

A. Rueda, *Thermal X-ray emission from massive, fast rotating, highly magnetized white dwarfs*, to appear in MNRAS.

There is solid observational evidence on the existence of massive, $M \sim 1 M_{\odot}$, highly magnetized white dwarfs (WDs) with surface magnetic fields up to $B \sim 10^9$ G. We show that, if in addition to these features, the star is fast rotating, it can become a rotation-powered pulsar-like WD and emit detectable high-energy radiation. We infer the values of the structure parameters (mass, radius, moment of inertia), magnetic field, rotation period and spin-down rates of a WD pulsar death-line. We show that WDs above the death-line emit blackbody radiation in the soft X-ray band via the magnetic polar cap heating by back flowing pair-created particle bombardment and discuss as an example the X-ray emission of soft gamma-repeaters and anomalous X-ray pulsars within the WD model.

3. L. Becerra, C. L. Bianco, C. L. Fryer, J. A. Rueda, and R. Ruffini, *On the induced gravitational collapse scenario of gamma-ray bursts associated with supernovae*, to appear in ApJ; arXiv:1606.02523.

Following the induced gravitational collapse (IGC) paradigm of gamma-ray bursts (GRBs) associated with type Ib/c supernovae, we present numerical simulations of the explosion of a carbon-oxygen (CO) core in a binary system with a neutron-star (NS) companion. The supernova ejecta trigger a *hypercritical* accretion process onto the NS thanks to a copious neutrino emission and the trapping of photons within the accretion flow. We show that temperatures 1–10 MeV develop near the NS surface, hence electron-positron annihilation into neutrinos becomes the main cooling channel leading to accretion rates 10^{-9} – $10^{-1} M_{\odot} \text{ s}^{-1}$ and neutrino luminosities 10^{43} – $10^{52} \text{ erg s}^{-1}$ (the shorter the orbital period the higher the accretion rate). We estimate the maximum orbital period, P_{max} , as a function of the NS initial mass, up to which the NS companion can reach by hypercritical accretion the critical mass for gravitational collapse leading to black-hole (BH) formation. We then estimate the effects of the accreting and orbiting NS companion onto a novel geometry of the supernova ejecta density profile. We present the results of a 1.4×10^7 particle simulation which show that the NS induces accentuated asymmetries in the ejecta density around the orbital plane. We elaborate on the observables associated with the above features of the IGC process. We apply this framework to specific GRBs: we find that X-ray flashes (XRFs) and binary-driven hypernovae (BdHNe) are produced in binaries with $P > P_{\text{max}}$ and $P < P_{\text{max}}$, respectively. We analyze in detail the case of XRF 060218.

4. R. Ruffini, J. A. Rueda, M. Muccino, Y. Aimuratov, L. M. Becerra, C. L. Bianco, M. Kovacevic, R. Moradi, F. G. Oliveira, G. B. Pisani, and Y. Wang, *On the classification of GRBs and their occurrence rates*, to appear in ApJ; arXiv: 1602.02732.

There is mounting evidence for the binary nature of the progenitors of gamma-ray bursts (GRBs). For a long GRB, the induced gravitational collapse (IGC) paradigm proposes as progenitor, or "in-state", a tight binary system composed of a carbon-oxygen core (CO_{core}) undergoing a supernova (SN) explosion which triggers hypercritical accretion onto a neutron star (NS) companion. For a short GRB, a NS-NS merger is traditionally adopted as the progenitor. We divide long and short GRBs into two sub-classes, depending on whether or not a black hole (BH) is formed in the merger or in the hypercritical accretion process exceeding the NS critical mass. For long bursts, when no BH is formed we have the sub-class of X-ray flashes (XRFs), with isotropic energy $E_{\text{iso}} \lesssim 10^{52}$ erg and rest-frame spectral peak energy $E_{p,i} \lesssim 200$ keV. When a BH is formed we have the sub-class of binary-driven hypernovae (BdHNe), with $E_{\text{iso}} \gtrsim 10^{52}$ erg and $E_{p,i} \gtrsim 200$ keV. In analogy, short bursts are similarly divided into two sub-classes. When no BH is formed, short gamma-ray flashes (S-GRFs) occur, with $E_{\text{iso}} \lesssim 10^{52}$ erg and $E_{p,i} \lesssim 2$ MeV. When a BH is formed, the authentic short GRBs (S-GRBs) occur, with $E_{\text{iso}} \gtrsim 10^{52}$ erg and $E_{p,i} \gtrsim 2$ MeV. We give examples and observational signatures of these four sub-classes and their rate of occurrence. From their respective rates it is possible that "in-states" of S-GRFs and S-GRBs originate from the "out-states" of XRFs. We indicate two additional progenitor systems: white dwarf-NS and BH-NS. These systems have hybrid features between long and short bursts. In the case of S-GRBs and BdHNe evidence is given of the coincidence of the onset of the high energy GeV emission with the birth of a Kerr BH.

3.1.3 Submitted

1. R. Ruffini, J. F. Rodriguez, M. Muccino, J. A. Rueda, Y. Aimuratov, U. Barres de Almeida, L. Becerra, C. L. Bianco, C. Cherubini, S. Filippi, D. Gizzi, M. Kovacevic, R. Moradi, F. G. Oliveira, G. B. Pisani, and Y. Wang, *On the rate and on the gravitational wave emission of short and long GRBs*, submitted to ApJ; arXiv:1602.03545.

GRBs, traditionally classified as "long" and "short", have been often assumed, till recently, to originate from a single black hole (BH) with an ultrarelativistic jetted emission. There is evidence that both long and short bursts have as progenitors merging and/or accreting bina-

ries, each composed by a different combination of carbon-oxygen cores (CO_{core}), neutron stars (NSs), BHs and white dwarfs (WDs). Consequently, the traditional long bursts have been sub-classified as (I) X-ray flashes (XRFs), (II) binary-driven hypernovae (BdHNe), and (III) BH-supernovae (BH-SNe). They are framed within the induced gravitational collapse (IGC) paradigm which envisages as progenitor a tight binary composed of a CO_{core} and a NS or BH companion. The SN explosion of the CO_{core} , originating a new NS (νNS), triggers a hypercritical accretion process onto the companion NS or BH. If the accretion is not sufficient for the NS to reach its critical mass, an XRF occurs, leading to a νNS -NS system. Instead, when the BH is already present or formed by the hypercritical accretion, a BdHN occurs, leading to a νNS -BH system. Similarly, the traditional short bursts, originating in NS-NS mergers, are sub-classified as (IV) short gamma-ray flashes (S-GRFs) and (V) short GRBs (S-GRBs), respectively when the merging process does not lead or leads to BH formation. Two additional families are (VI) ultra-short GRBs (U-GRBs) and (VII) gamma-ray flashes (GRFs), respectively formed in νNS -BH and NS-WD mergers. We use the estimated occurrence rate of the above sub-classes to assess the gravitational wave emission in the merging process and its detectability by Advanced LIGO, Advanced Virgo, eLISA, and resonant bars.

2. L. Becerra, J. A. Rueda, P. Lorén-Aguilar, E. García-Berro, *The Spin Evolution of Fast-Rotating, Magnetized Super-Chandrasekhar White Dwarfs in the Aftermath of White Dwarf Mergers*, submitted to ApJ.

The evolution of the remnant of the merger of two white dwarfs is still an open problem. Furthermore, few studies have studied the case in which the remnant is a magnetic white dwarf with a mass larger than the Chandrasekhar limiting mass. Angular momentum losses might bring the remnant of the merger to the physical conditions suitable for developing a thermonuclear explosion. Alternatively, the remnant may be prone to gravitational and/or rotational instabilities, depending on the initial conditions reached after the coalescence. Dipole magnetic braking is one of the mechanisms that can drive such losses of angular momentum. However, the timescale on which these losses occur depend on several parameters, like the strength of the magnetic field, the inclination angle with respect to the rotation axis of the remnant, and the properties of the white dwarf. In addition, the coalescence leaves a surrounding Keplerian disk that can be accreted by the newly formed white dwarf. Here we compute the post-merger evolution of a super-Chandrasekhar magnetized white dwarf taking into account all the relevant physical processes. These include magnetic torques acting on the

star, accretion from the Keplerian disk, the threading of the magnetic field lines through the disk, as well as the thermal evolution of the white dwarf core. We find that the central remnant can reach the conditions suitable to develop a thermonuclear explosion before other instabilities, such as the inverse beta-decay instability or the secular axisymmetric instability, are reached which would instead lead to gravitational collapse of the magnetized remnant.

3.1.4 To be submitted

1. F. Cipolletta, C. Cherubini, S. Filippi, J. A. Rueda, R. Ruffini, *On the last stable circular orbit around rapidly rotating neutron stars*, to be submitted to Phys. Rev. D.

We compute the binding energy and angular momentum of a test-particle at the last stable circular orbit on the equatorial plane around a general relativistic fast rotating neutron star. We present simple fitting formulas of these quantities which can be used in several astrophysical applications. We compare and contrast the properties of this orbit with the corresponding around a Kerr black-hole of the same mass and angular momentum.

2. J. F. Rodriguez, J. A. Rueda, and R. Ruffini, *What can we really infer from GW 150914? (II)*, arXiv:1605.07609.

Abstract In a recent letter we have outlined some issues on GW 150914, we hereby give additional details. We analyze the event GW 150914 announced by the Advanced Laser Interferometer Gravitational-Wave Observatory (LIGO) as the gravitational-wave emission of a black-hole binary merger. We show that the parameters of the coalescing system and of the newly formed Kerr black-hole can be extracted from basic results of the gravitational-wave emission during the inspiraling and merger phases without sophisticated numerical simulations. Our strikingly accurate estimates are based on textbook formulas describing two different regimes: 1) the binary inspiraling analysis treated in Landau and Lifshitz textbook, 2) the plunge of a particle into a black-hole, treated in the Rees-Ruffini-Wheeler textbook as well as 3) the transition between these two regimes following Detweiler's treatment of a particle infalling with non-zero angular momentum onto a black-hole. It is stressed that in order to infer any astrophysical information on the masses of the system both regimes have to be independently and observationally constrained by LIGO, which does not appear to be the case.

3. J. F. Rodriguez, J. A. Rueda, and R. Ruffini, *What can we really infer from GW 150914?*, arXiv:1605.04767.

We analyze the event GW 150914 announced by the Advanced Laser Interferometer Gravitational-Wave Observatory (LIGO) as the gravitational-wave emission of a black-hole binary merger. We show that the parameters of the coalescing system and of the newly formed Kerr black-hole can be extracted from basic results of the gravitational-wave emission during the inspiraling and merger phases without sophisticated numerical simulations. Our strikingly accurate estimates are based on textbook formulas describing two different regimes: 1) the binary inspiraling analysis treated in Landau and Lifshitz textbook, and 2) the plunge of a particle into a black-hole, treated in the Rees-Ruffini-Wheeler textbook. It is stressed that in order to infer any astrophysical information on the masses of the system both regimes have to be independently and observationally constrained by LIGO, which does not appear to be the case.

3.2 Conference Proceedings

1. K. A. Boshkayev, J. A. Rueda, B. A. Zhami, Z. A. Kalymova, and G. S. Balgymbekov, *Equilibrium structure of white dwarfs at finite temperatures*, IJMPCS, vol. 41, p. 1660129, Mar. 2016.

Recently, it has been shown by S. M. de Carvalho et al. (2014) that the deviations between the degenerate case and observations were already evident for $0.7\text{--}0.8 M_{\odot}$ white dwarfs. Such deviations were related to the neglected effects of finite temperatures on the structure of a white dwarf. Therefore, in this work by employing the Chandrasekhar equation of state taking into account the effects of temperature we show how the total pressure of the white dwarf matter depends on the mass density at different temperatures. Afterward we construct equilibrium configurations of white dwarfs at finite temperatures. We obtain the mass-radius relations of white dwarfs for different temperatures by solving the Tolman-Oppenheimer-Volkoff equation, and compare them with the estimated masses and radii inferred from the Sloan Digital Sky Survey Data Release 4.

2. K. A. Boshkayev, J. A. Rueda, and B. A. Zhami, *Rotating hot white dwarfs in Gravitation, Astrophysics, and Cosmology* (J.-P. Hsu and et al., eds.), pp. 189–190, 2016.

We consider the effects of rotation and temperature on the structure of

white dwarfs in order to compare them with the estimated data from observations.



GRB 090510: A GENUINE SHORT GRB FROM A BINARY NEUTRON STAR COALESCING INTO A KERR–NEWMAN BLACK HOLE

R. RUFFINI^{1,2,3,4}, M. MUCCINO^{1,2}, Y. AIMURATOV^{1,3}, C. L. BIANCO^{1,2}, C. CHERUBINI⁵, M. ENDERLI^{1,3}, M. KOVACEVIC^{1,3},
R. MORADI^{1,2}, A. V. PENACCHIONI^{6,7}, G. B. PISANI^{1,2}, J. A. RUEDA^{1,2,4}, AND Y. WANG^{1,2}

¹ Dipartimento di Fisica, Sapienza Università di Roma and ICRA, Piazzale Aldo Moro 5, I-00185 Roma, Italy

² ICRA/Net, Piazza della Repubblica 10, I-65122 Pescara, Italy

³ Université de Nice Sophia-Antipolis, Grand Château Parc Valrose, Nice, CEDEX 2, France

⁴ ICRA/Net-Rio, Centro Brasileiro de Pesquisas Fisicas, Rua Dr. Xavier Sigaud 150, Rio de Janeiro, RJ, 22290-180, Brazil

⁵ ICRA and Unit of Nonlinear Physics and Mathematical Modeling, Department of Engineering, Università Campus Bio-Medico di Roma, Via Alvaro del Portillo 21, I-00128, Rome, Italy

⁶ University of Siena, Department of Physical Sciences, Earth and Environment, Via Roma 56, I-53100 Siena, Italy

⁷ ASI Science Data Center, via del Politecnico s.n.c., I-00133 Rome Italy

Received 2015 October 9; revised 2016 September 1; accepted 2016 September 3; published 2016 November 7

ABSTRACT

In a new classification of merging binary neutron stars (NSs) we separate short gamma-ray bursts (GRBs) into two subclasses. The ones with $E_{\text{iso}} \lesssim 10^{52}$ erg coalesce to form a massive NS and are indicated as short gamma-ray flashes (S-GRFs). The hardest, with $E_{\text{iso}} \gtrsim 10^{52}$ erg, coalesce to form a black hole (BH) and are indicated as genuine short GRBs (S-GRBs). Within the fireshell model, S-GRBs exhibit three different components: the proper GRB (P-GRB) emission, observed at the transparency of a self-accelerating baryon- e^+e^- plasma; the prompt emission, originating from the interaction of the accelerated baryons with the circumburst medium; and the high-energy (GeV) emission, observed after the P-GRB and indicating the formation of a BH. GRB 090510 gives the first evidence for the formation of a Kerr BH or, possibly, a Kerr–Newman BH. Its P-GRB spectrum can be fitted by a convolution of thermal spectra whose origin can be traced back to an axially symmetric dyadotorus. A large value of the angular momentum of the newborn BH is consistent with the large energetics of this S-GRB, which reach in the 1–10,000 keV range $E_{\text{iso}} = (3.95 \pm 0.21) \times 10^{52}$ erg and in the 0.1–100 GeV range $E_{\text{LAT}} = (5.78 \pm 0.60) \times 10^{52}$ erg, the most energetic GeV emission ever observed in S-GRBs. The theoretical redshift $z_{\text{th}} = 0.75 \pm 0.17$ that we derive from the fireshell theory is consistent with the spectroscopic measurement $z = 0.903 \pm 0.003$, showing the self-consistency of the theoretical approach. All S-GRBs exhibit GeV emission, when inside the *Fermi*-LAT field of view, unlike S-GRFs, which never evidence it. The GeV emission appears to be the discriminant for the formation of a BH in GRBs, confirmed by their observed overall energetics.

Key words: gamma-ray burst: general – gamma-ray burst: individual (GRB 090510)

1. INTRODUCTION

Thanks to a fortunate coincidence of observations by *AGILE*, *Fermi*, and *Swift* satellites, together with the optical observations by the Very Large Telescope (VLT)/FORIS2 and the Nordic Optical Telescope, it has been possible to obtain an unprecedented set of data, extending from the optical–UV, through the X-rays, all the way up to the high-energy (GeV) emission, which allowed detailed temporal/spectral analyses of GRB 090510 (De Pasquale et al. 2010).

In contrast with this outstanding campaign of observations, a theoretical analysis of the broadband emission of GRB 090510 has been advanced within the synchrotron/self-synchrotron Compton and traditional afterglow models (see, e.g., Sections 5.2.1 and 5.2.2 in Ackermann et al. 2010). Paradoxically, this same methodology has been applied in the description of markedly different types of sources: e.g., Soderberg et al. (2006b) for the low energetic long gamma-ray burst (GRB) 060218, Perley et al. (2014) for the high energetic long GRB 130427A, and Soderberg et al. (2006a) for the short gamma-ray flash (S-GRF) 051221A (see also Curran et al. 2008, and references therein).

In the meantime, it has become evident that GRBs can be subdivided into a variety of classes and subclasses (Ruffini et al. 2015b, 2015c, 2016), each of them characterized by specific different progenitors, which deserve specific theoretical

treatments and understanding. In addition, every subclass shows different episodes corresponding to specifically different astrophysical processes, which can be identified thanks to specific theoretical treatments and data analysis. In this article, we take GRB 090510 as a prototype for S-GRBs and perform a new time-resolved spectral analysis, in excellent agreement with the above temporal and spectral analysis performed by, e.g., the *Fermi* team. Now this analysis, guided by a theoretical approach successfully tested in this new family of short GRBs (S-GRBs; Muccino et al. 2013a; Ruffini et al. 2015b), is directed to identify a precise sequence of different events made possible by the exceptional quality of the data of GRB 090510. This includes a new structure in the thermal emission of the proper GRB (P-GRB) emission, followed by the onset of the GeV emission linked to the black hole (BH) formation, allowing us, as well, to derive the structure of the circumburst medium (CBM) from the spiky structure of the prompt emission. This sequence, for the first time, illustrates the formation process of a BH.

Already in 1974 February, soon after the public announcement of the GRB discovery (Strong et al. 1975), Damour & Ruffini (1975) presented the possible relation of GRBs to the vacuum polarization process around a Kerr–Newman BH. There, evidence was given for (a) the formation of a vast amount of e^+e^- -baryon plasma; (b) the energetics of GRBs to be of the order of $E_{\text{max}} \approx 10^{54} M_{\text{BH}}/M_{\odot}$ erg, where M_{BH} is the

BH mass; and (c) additional ultra-high-energy cosmic rays with energy up to $\sim 10^{20}$ eV originating from such extreme processes. A few years later, the role of an e^+e^- plasma of comparable energetics for the origin of GRBs was considered by Cavallo & Rees (1978), and it took almost 30 yr to clarify some of the analogies and differences between these two processes, leading, respectively, to the alternative concepts of “fireball” and “fireshell” (Aksenov et al. 2007, 2009). In this article we give the first evidence for the formation of a Kerr–Newman BH, in GRB 090510, from the merger of two massive neutron stars (NSs) in a binary system.

GRBs are usually separated into two categories, based on their duration properties (e.g., Mazets et al. 1981; Dezalay et al. 1992; Klebesadel 1992, pp. 161–68; Kouveliotou et al. 1993; Tavani 1998). S-GRBs have a duration $T_{90} \lesssim 2$ s, while the remaining ones with $T_{90} \gtrsim 2$ s are traditionally classified as long GRBs.

S-GRBs are often associated with NS–NS mergers (see, e.g., Goodman 1986; Paczynski 1986; Eichler et al. 1989; Narayan et al. 1991; Meszaros & Rees 1997, Rosswog et al. 2003; Lee et al. 2004; Nakar 2007; Endrizzi et al. 2016; Ruiz et al. 2016; see also Berger 2014 for a recent review): their host galaxies are of both early and late type, their localization with respect to the host galaxy often indicates a large offset (Sahu et al. 1997; van Paradijs et al. 1997; Bloom et al. 2006; Troja et al. 2008; Fong et al. 2010; Berger 2011; Kopač et al. 2012) or a location of minimal star-forming activity with typical CBM densities of $\sim 10^{-5}$ – 10^{-4} cm $^{-3}$, and no supernovae (SNe) have ever been associated with them.

The progenitors of long GRBs, on the other hand, have been related to massive stars (Woosley & Bloom 2006). However, in spite of the fact that most massive stars are found in binary systems (Smith 2014), that most Type Ib/c SNe occur in binary systems (Smith et al. 2011), and that SNe associated with long GRBs are indeed of Type Ib/c (Della Valle 2011), the effects of binarity on long GRBs have been for a long time largely ignored in the literature. Indeed, until recently, long GRBs have been interpreted as single events in the jetted *collapsar* fireball model (see, e.g., Rees & Meszaros 1992; Woosley 1993; Kobayashi et al. 1997; Piran 2005; Gehrels et al. 2009; Kumar & Zhang 2015 and references therein).

Multiple components evidencing the presence of a precise sequence of different astrophysical processes have been found in several long GRBs (e.g., Izzo et al. 2012; Penacchioni et al. 2012). Following this discovery, further results led to the introduction of a new paradigm explicating the role of binary sources as progenitors of the long GRB–SN connection. New developments have led to the formulation of the induced gravitational collapse (IGC) paradigm (Ruffini et al. 2001a, 2007, 2015c; Rueda & Ruffini 2012). The IGC paradigm explains the GRB–SN connection in terms of the interactions between an evolved carbon–oxygen core (CO_{core}) undergoing an SN explosion and its hypercritical accretion on a binary NS companion (Ruffini 2015). A large majority of long bursts are related to SNe and are spatially correlated with bright star-forming regions in their host galaxies (Fruchter et al. 2006; Svensson et al. 2010), with a typical CBM density of ~ 1 cm $^{-3}$ (Izzo et al. 2012; Penacchioni et al. 2012).

A new situation has occurred with the observation of the high-energy GeV emission by the *Fermi*-LAT instrument and its correlation with both long and short bursts with isotropic energy $E_{\text{iso}} \gtrsim 10^{52}$ erg, which has been evidenced in Ruffini

et al. (2015b, 2015c), respectively. On the basis of this correlation, the occurrence of such prolonged GeV emission has been identified with the onset of the formation of a BH (Ruffini et al. 2015b, 2015c).

As recalled above, the long GRBs associated with SNe have been linked to the hypercritical accretion process occurring in a tight binary system when the ejecta of an exploding CO_{core} accrete onto an NS binary companion (see, e.g., Rueda & Ruffini 2012; Fryer et al. 2014; Becerra et al. 2015). When the hypercritical accretion occurs in a widely separated system with an orbital separation $> 10^{11}$ cm (Becerra et al. 2015), the accretion is not sufficient to form a BH. For these softer systems with rest-frame spectral peak energy $E_{\text{peak}} < 200$ keV the upper limit of their observed energy is $E_{\text{iso}} \approx 10^{52}$ erg, which corresponds to the maximum energy attainable in the accretion onto an NS (Ruffini et al. 2015c). Such a long burst corresponds to an X-ray flash (XRF). The associated X-ray afterglow is also explainable in terms of the interaction of the prompt emission with the SN ejecta (C. L. Fryer et al. 2016, in preparation). In these systems no GeV emission is expected in our theory and, indeed, is not observed. Interestingly, pioneering evidence for such an XRF had already been given in a different context by Heise (2003), Amati et al. (2004), and Soderberg et al. (2006b). For tighter binaries ($< 10^{11}$ cm; Becerra et al. 2015), the hypercritical accretion onto the companion NS leads to the formation of a BH. For these harder systems with $E_{\text{peak}} > 200$ keV the lower limit of their observed energy is $E_{\text{iso}} \approx 10^{52}$ erg, which necessarily needs the accretion process into a BH. An associated prolonged GeV emission occurs after the P-GRB emission and at the beginning of the prompt emission and originates at the onset of the BH formation (Ruffini et al. 2015c). These more energetic events are referred to as binary-driven hypernovae (BdHNe). Specific constant power-law behaviors are observed in their high-energy GeV, X-rays, and optical luminosity light curves (Pisani et al. 2013; Ruffini et al. 2014, 2015c).

In total analogy, the formation of a BH can occur in short bursts, depending on the mass of the merged core of the binary system. When the two NS masses are large enough, the merged core can exceed the NS critical mass and BH formation is possible. In the opposite case, a massive NS (MNS) is created, possibly, with some additional orbiting material to guarantee the angular momentum conservation. We then naturally expect the existence of two short-burst subclasses: authentic S-GRBs, characterized by the formation of a BH (Ruffini et al. 2015b), with $E_{\text{iso}} \gtrsim 10^{52}$ erg, a harder spectrum (see Section 5.2), and associated with a prolonged GeV emission (see Section 6.5); and S-GRBs, producing an MNS (Ruffini et al. 2015b), with $E_{\text{iso}} \lesssim 10^{52}$ erg. In this second subclass, of course, the GeV emission should not occur and, indeed, is never observed.

Following the discovery of the first prototype of this S-GRB class, namely, GRB 090227B (Muccino et al. 2013a), the first detailed analysis of such a genuine S-GRB originating from a binary NS merger leading to a BH was done for GRB 140619B by Ruffini et al. (2015b), determining as well the estimated emission of gravitational waves. The latter has been estimated following the method applied by Oliveira et al. (2014) for GRB 090227B. From the spectral analysis of the early ~ 0.2 s, they inferred an observed temperature $kT = (324 \pm 33)$ keV of the e^+e^- plasma at transparency (P-GRB), a theoretically derived redshift $z = 2.67 \pm 0.37$, a total burst energy $E_{e^+e^-}^{\text{tot}} = (6.03 \pm 0.79) \times 10^{52}$ erg, a rest-frame peak energy

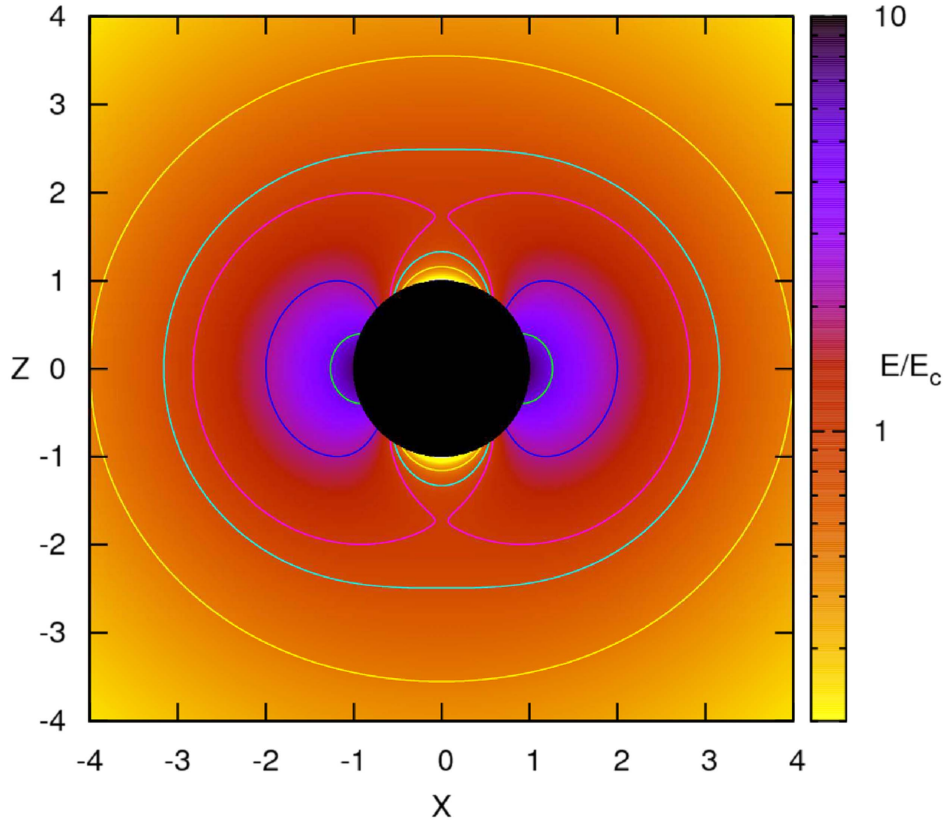


Figure 1. Projection of the dyadotorus of a Kerr–Newman BH corresponding to selected values of the ratio E/E_c , where E_c is the critical value for vacuum polarization and E is the electric field strength. The plot assumes a black hole mass energy $\mu = M_{\text{BH}}/M_{\odot} = 10$. This figure is reproduced from Cherubini et al. (2009), with their kind permission.

$E_{p,i} = 4.7$ MeV, a baryon load $B = (5.52 \pm 0.73) \times 10^{-5}$, and an average CBM density $n_{\text{CBM}} = (4.7 \pm 1.2) \times 10^{-5} \text{ cm}^{-3}$.

We turn in this article to the most interesting case of GRB 090510, which has, in addition to very similar properties of the members of this new class of S-GRB sources, a spectroscopically determined value of redshift and represents one of the most energetic sources of this family both in the γ -ray and in the GeV ranges. Actually, a first attempt to analyze GRB 090510 was made by interpreting this source as a long GRB (Muccino et al. 2013b). An unusually large value of the CBM density was needed in order to fit the data: this interpretation was soon abandoned when it was noticed that GRB 090510 did not fulfill the nesting conditions of the late X-ray emission typical of long GRBs (Ruffini et al. 2014); see also Section 5.1 and Figure 5.

In light of the recent progress in the understanding of the fireshell theory, we address the interpretation of GRB 090510 as the merging of a binary NS. We give clear evidence for the validity of this interpretation. In view of the good quality of the data both in γ -rays and in the GeV range, we have performed a more accurate description of the P-GRB, best fitted by a convolution of thermal spectra. This novel feature gives the first indication for the existence of an axially symmetric configuration of the dyadotorus emitting the e^+e^- plasma, which had been previously theoretically considered and attentively searched for. This gives the first indication that indeed the angular momentum plays a role and a dyadotorus is formed, as theoretically predicted in a series of papers (see Cherubini et al. 2009; Ruffini 2009; see also Figure 1). This naturally leads to the evidence for the formation of a rotating

BH as the outcome of the gravitational collapse. We turn then to the main new feature of GRB 090510, which is the high-energy 0.1–100 GeV emission (see Figure 10). The direct comparison of the GeV emission in this source and in the BdHN 130427A shows the remarkable similarities of these two GeV components (see Figure 10). The fact that the S-GRB 090510 originates from a binary NS merger and the BdHN 130427A originates from the IGC of an SN hypercritical accretion process onto a companion NS clearly points to the BH as originating this GeV emission, the reason being that these two astrophysical systems are different in their progenitors and physical processes and have in the formation of a BH their unique commonality.

This paper is structured as follows: in Section 2 we summarize the relevant aspects of the fireshell theory and compare and contrast it with alternative approaches. In Section 3 we discuss the recent progress on the NS equilibrium configuration relevant for S-GRBs and BdHNe. In Section 4 we move on to describe the observations of GRB 090510 and their analysis. The S-GRB nature of GRB 090510 is justified in Section 5, and we offer an interpretation of our results in Section 6. Section 7 concludes this work.

A standard flat Λ CDM cosmological model with $\Omega_m = 0.27$ and $H_0 = 71 \text{ km s}^{-1} \text{ Mpc}^{-1}$ is adopted throughout the paper.

2. SUMMARY OF THE FIRESHELL MODEL

The fireshell scenario (Ruffini et al. 2001a, 2001b, 2001c) has been initially introduced to describe a GRB originating in a gravitational collapse leading to the formation of a

Kerr–Newman BH. A distinct sequence of physical and astrophysical events are taken into account:

- (1) An optically thick pair plasma—the fireshell of total energy $E_{e^+e^-}^{\text{tot}}$ —is considered. As a result, it starts to expand and accelerate under its own internal pressure (Ruffini et al. 1999). The baryonic remnant of the collapsed object is engulfed by the fireshell—the baryonic contamination is quantified by the baryon load $B = M_B c^2 / E_{e^+e^-}^{\text{tot}}$, where M_B is the mass of the baryonic remnant (Ruffini et al. 2000; Aksenov et al. 2007, 2009).
- (2) After the engulfment, the fireshell is still optically thick and continues to self-accelerate until it becomes transparent. When the fireshell reaches transparency, a flash of thermal radiation termed proper-GRB (P-GRB) is emitted (Ruffini et al. 1999, 2000).
- (3) In GRBs, the e^+e^- -baryon plasma expands with ultra-relativistic velocities from the ultrarelativistic region near the BH to large distances. To describe such a dynamics that deals with unprecedentedly large Lorentz factors and also regimes sharply varying with time, Ruffini et al. (2001c) introduced the appropriate relative spacetime transformation paradigm. This paradigm gives particular attention to the constitutive equations relating four time variables: the comoving time, the laboratory time, the arrival time, and the arrival time at the detector corrected by the cosmological effects. This paradigm is essential for the interpretation of the GRB data: the absence of adopting such a relativistic paradigm in some current works has led to a serious misinterpretation of the GRB phenomenon.
- (4) In compliance with the previous paradigm, the interactions between the ultrarelativistic shell of accelerated baryons left over after transparency and the CBM have been considered. They lead to a modified blackbody spectrum in the comoving frame (Patricelli et al. 2012). The observed spectrum is, however, nonthermal in general; this is due to the fact that, once the constant arrival time effect is taken into account in the equitemporal surfaces (EQTSs; see Bianco & Ruffini 2005a, 2005b), the observed spectral shape results from the convolution of a large number of modified thermal spectra with different Lorentz factors and temperatures.
- (5) All the above relativistic effects, after the P-GRB emission, are necessary for the description of the prompt emission of GRBs, as outlined in Ruffini et al. (2001b). The prompt emission originates in the collisions of the accelerated baryons, moving at Lorentz factor $\gamma \approx 100$ –1000, with interstellar clouds of CBM with masses of $\sim 10^{22}$ – 10^{24} g, densities of ~ 0.1 – 1 cm^{-3} , and size of $\sim 10^{15}$ – 10^{16} cm, at typical distances from the BH of $\sim 10^{16}$ – 10^{17} cm (see, e.g., Izzo et al. 2012 for long bursts). Our approach differs from alternative treatments purporting late activities from the central engine (see, e.g., the collapsar model in Woosley 1993; Popham et al. 1999; Woosley & Bloom 2006, and references therein; and the magnetar model in Zhang & Mészáros 2001; Dai et al. 2006; Metzger et al. 2011; Bucciantini et al. 2012; Lü & Zhang 2014, and references therein).
- (6) $E_{e^+e^-}^{\text{tot}}$ and B are the only two parameters that are needed in a spherically symmetric fireshell model to determine the physics of the fireshell evolution until the

transparency condition is fulfilled. Three additional parameters, all related to the properties of the CBM, are needed to reproduce a GRB light curve and its spectrum: the CBM density profile n_{CBM} , the filling factor \mathcal{R} that accounts for the size of the effective emitting area, and an index α that accounts for the modification of the low-energy part of the thermal spectrum (Patricelli et al. 2012). They are obtained by running a trial-and-error simulation of the observed light curves and spectra that starts at the fireshell transparency.

- (7) A more detailed analysis of the pair creation process around a Kerr–Newman BH has led to the concept of dyadotorus (Cherubini et al. 2009). There, the axially symmetric configuration with a specific distribution of the e^+e^- , as well as its electromagnetic field, has been presented as a function of the polar angle. The total spectrum at the transparency of the e^+e^- plasma is a convolution of thermal spectra at different angles.

This formalism describing the evolution of a baryon-loaded pair plasma is describable in terms of only three intrinsic parameters: the e^+e^- plasma energy $E_{e^+e^-}^{\text{tot}}$, the baryon load B , and the specific angular momentum a of the incipient newly formed BH. It is, therefore, independent of the way the pair plasma is created.

In addition to the specific case, developed for the sake of example, of the dyadotorus created by a vacuum polarization process in an already-formed Kerr–Newman BH, more possibilities have been envisaged in the meantime:

- (a) The concept of dyadotorus can be applied as well in the case of a pair plasma created via the $\bar{\nu} \leftrightarrow e^+e^-$ mechanism in an NS merger as described in Narayan et al. (1992), Salmonson & Wilson (2002), Rosswog et al. (2003), and Zalamea & Beloborodov (2011), assuming that the created pair plasma is optically thick. The relative role of neutrino and weak interactions vs. the electromagnetic interactions in building the dyadotorus is currently topic of intense research.
- (b) Equally important is the relativistic magnetohydrodynamical process leading to a dyadotorus, indicated in the general treatment of Ruffini & Wilson (1975), and leading to the birth of a Kerr–Newman BH, surrounded by an opposite-charged magnetosphere in a system endowed with global charge neutrality. Active research is ongoing.
- (c) Progress in understanding the NS equilibrium configuration imposing the global charge neutrality condition, as opposed to the local charge neutrality usually assumed (Rotondo et al. 2011a, 2011b; Rueda et al. 2011, 2014; Rueda & Ruffini 2013). A critical mass for a nonrotating NS of $M_{\text{crit}}^{\text{NS}} \approx 2.67M_{\odot}$ has been found for the NL3 nuclear equation of state (Belvedere et al. 2012). The effects of rotation and of the nuclear equation of state on the critical mass are presented in Belvedere et al. (2014, 2015) and Cipolletta et al. (2015). The existence of electromagnetic fields close to the critical value has been evidenced in the interface between the core and the crust in the above global neutrality model, as well as very different density distributions in the crust and in the core, which could play an important role during the NS–NS mergers (see Figure 2 and Oliveira et al. 2014).

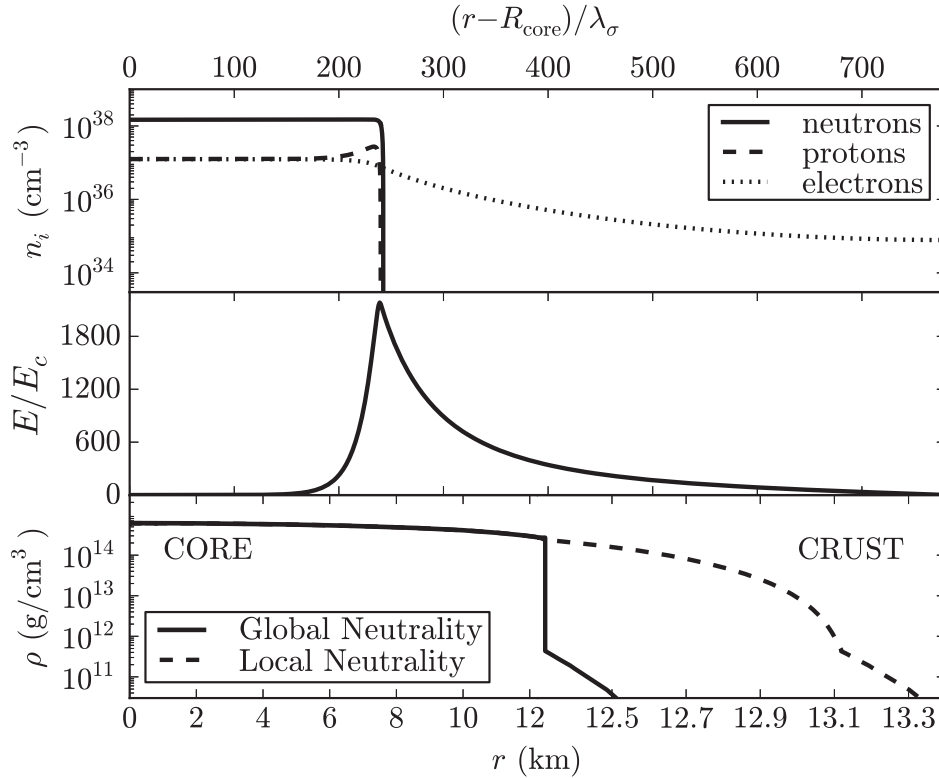


Figure 2. Particle density profiles (top panel) and the electric field in units of E_c (middle panel) in the core-crust transition layer normalized to the σ -meson Compton wavelength $\lambda_\sigma = \hbar/(m_\sigma c) \sim 0.4$ fm. Bottom panel: density profile inside an NS star with central density $\rho \sim 5\rho_{\text{nuc}}$, where ρ_{nuc} is the nuclear density, from the solution of the Tolman–Oppenheimer–Volkoff (TOV) equations (locally neutral case) and the globally neutral solution presented in Belvedere et al. (2012). The density at the edge of the crust is the neutron drip density $\rho_{\text{drip}} = 4.3 \times 10^{11} \text{ g cm}^{-3}$. This figure is reproduced from Belvedere et al. (2012), with their kind permission.

The above three possibilities have been developed in recent years, but they do not have to be considered exhaustive for the formation of a dyadotorus endowed by the above three parameters.

In conclusion, the evolution in the understanding of the GRB phenomenon, occurring under very different initial conditions, has evidenced the possibility of using the dyadotorus concept for describing sources of an optically thick baryon-loaded e^+e^- plasma within the fireshell treatment in total generality.

3. ON THE ROLE OF THE $\approx 10^{52}$ ERG LIMIT FOR S-GRBs AND BdHNe

The key role of neutrino emission in the hypercritical accretion process onto an NS has been already examined in the literature (see, e.g., Zel’dovich et al. 1972; Ruffini & Wilson 1973). The problem of hypercritical accretion in a binary system composed of a CO_{core} and a companion NS has been studied in Becerra et al. (2015, 2016) (see also references therein). The energy released during the process, in the form of neutrinos and photons, is given by the gain of gravitational potential energy of the matter being accreted by the NS and depends also on the change of binding energy of the NS while accreting matter and on the angular momentum carried by the accreting material (see, e.g., Becerra et al. 2016 and Ruffini et al. 2016). For a typical NS mass of $\approx 1.4 M_\odot$, a value observed in galactic NS binaries (Zhang et al. 2011; Antoniadis 2015), and an NS critical mass $M_{\text{crit}}^{\text{NS}}$ in the range from $2.2 M_\odot$ up to $3.4 M_\odot$ depending on the equations of state and angular momentum (see Becerra et al. 2015, 2016; Cipolletta et al. 2015, for details), the accretion luminosity can be as high as $L_{\text{acc}} \sim 0.1 \dot{M}_b c^2 \sim 10^{47} - 10^{51} \text{ erg s}^{-1}$ for accretion rates $\dot{M}_b \sim 10^{-6} - 10^{-2} M_\odot \text{ s}^{-1}$ (see Becerra et al. 2015, 2016, for

details). For binary systems with a separation of $\sim 10^{10}$ cm ($P \sim 5$ minutes), our numerical simulations indicate that (a) the accretion process duration lasts $\Delta t_{\text{acc}} \sim 10^2$ s (see, e.g., Becerra et al. 2015, 2016), (b) the NS collapses to a BH, and (c) a total energy larger than $\approx 10^{52}$ erg is released during the hypercritical accretion process. These systems correspond to the BdHNe (Becerra et al. 2016). For systems with larger separations the hypercritical accretion is not sufficient to induce the collapse of the NS into a BH and the value of $\approx 10^{52}$ erg represents a theoretical estimate of the upper limit to the energy emitted by the norm in the hypercritical accretion process. This subclass of sources corresponds to the XRFs (Becerra et al. 2016).

The same energetic considerations do apply in the analysis of the hypercritical accretion occurring in a close binary NS system undergoing merging (Ruffini 2015). Therefore, in total generality, we can conclude that the energy emitted during an NS–NS merger leading to the formation of a BH should be larger than $\approx 10^{52}$ erg (see Figure 3).

The limit of $\approx 10^{52}$ erg clearly depends on the initial NS mass undergoing accretion, by norm assumed to be $\approx 1.4 M_\odot$, and on the yet-unknown value of $M_{\text{crit}}^{\text{NS}}$, for which only an absolute upper limit of $3.2 M_\odot$ has been established for the nonrotating case (Rhoades & Ruffini 1974). As already pointed out in Ruffini (2015), for NS–NS mergers, the direct determination of the energy threshold of $\approx 10^{52}$ erg dividing S-GRFs and S-GRBs, as well as XRFs and BdHNe, provides fundamental information for the determination of the actual value of $M_{\text{crit}}^{\text{NS}}$, for the minimum mass of the newly born BH, and for the mass of the accreting NS.

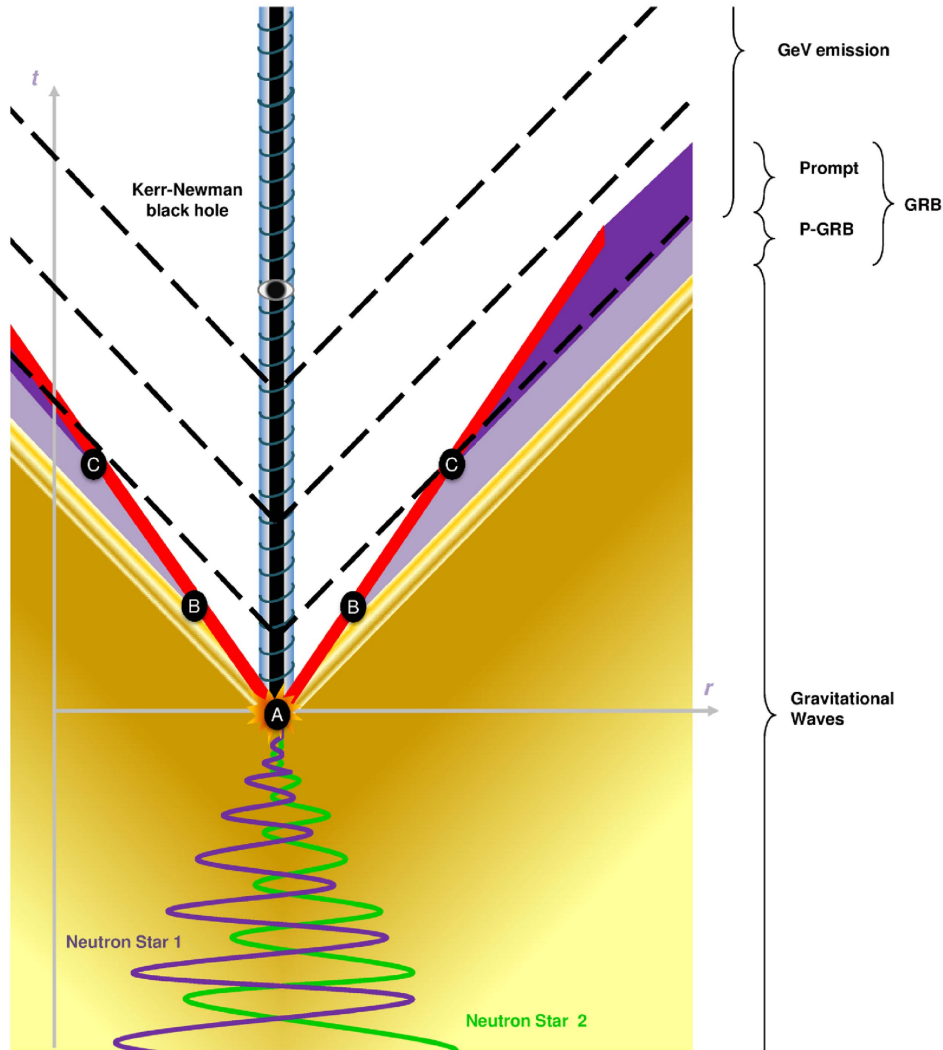


Figure 3. Spacetime diagram of an S-GRB, a binary NS merger leading to BH formation (taken from Enderli et al. 2015, with their kind permission). The binary orbit gradually shrinks due to energy loss through gravitational-wave emission (yellow–brown). At point A, the merger occurs: the fireshell (in red) is created and starts its expansion. It reaches transparency at point B, emitting the P-GRB (light purple). The prompt emission (deep purple) then follows at point C. The dashed lines represent the GeV emission (delayed relative to the start of the GRB) originating in the newly born BH. This spacetime diagram well illustrates how the GeV emission originates in the newly born BH and follows a different spacetime path from the prompt emission, contrary to what is stated in Ackermann et al. (2010). The prompt emission originates from the interactions of the baryons, accelerated to ultrarelativistic Lorentz factors during the pair-baryon electromagnetic pulse, with the clumpy CBM (see Section 2). The analysis of the spiky structure of the prompt emission allows us to infer the structure of the CBM (see Figure 9). There is the distinct possibility that the GeV emission prior to 0.6 s in the arrival time may interact with the prompt emission. In this sense the work by Zou et al. (2011) may become of interest.

4. ANALYSIS OF GRB 090510

In this section, we summarize the observations of GRB 090510, as well as the data analysis. We used *Fermi* (GBM and LAT) and *Swift*/XRT data for the purposes of this work.

4.1. Observations

The *Fermi*/GBM instrument (Meegan et al. 2009) was triggered at $T_0 = 00:22:59.97$ UT on 2009 May 10 by the short and bright burst GRB 090510 (Guiriec et al. 2009, trigger 263607781/090510016). The trigger was set off by a precursor emission of duration 30 ms, followed ~ 0.4 s later by a hard episode lasting ~ 1 s. This GRB was also detected by *Swift* (Hoversten et al. 2009), *Fermi*/LAT (Ohno & Pelassa 2009), *AGILE* (Longo et al. 2009), *Konus-Wind* (Golenetskii et al. 2009), and *Suzaku*-WAM (Ohmori et al. 2009). The

position given by the GBM is consistent with that deduced from *Swift* and LAT observations.

During the first second after LAT trigger at 00:23:01.22 UT, *Fermi*/LAT detected over 50 (over 10) events with an energy above 100 MeV (1 GeV) up to the GeV range, and more than 150 (20) within the first minute (Omodei et al. 2009). This makes GRB 090510 the first bright S-GRB with an emission detected from the keV to the GeV range.

Observations of the host galaxy of GRB 090510, located by VLT/FORS2, provided a measurement of spectral emission lines. This led to the determination of a redshift $z = 0.903 \pm 0.003$ (Rau et al. 2009). The refined position of GRB 090510 obtained from the Nordic Optical Telescope (Olofsson et al. 2009) is offset by $0''.7$ relative to the center of the host galaxy in the VLT/FORS2 image. At $z = 0.903$, this corresponds to a projected distance of 5.5 kpc. The identified host galaxy is a late-type galaxy

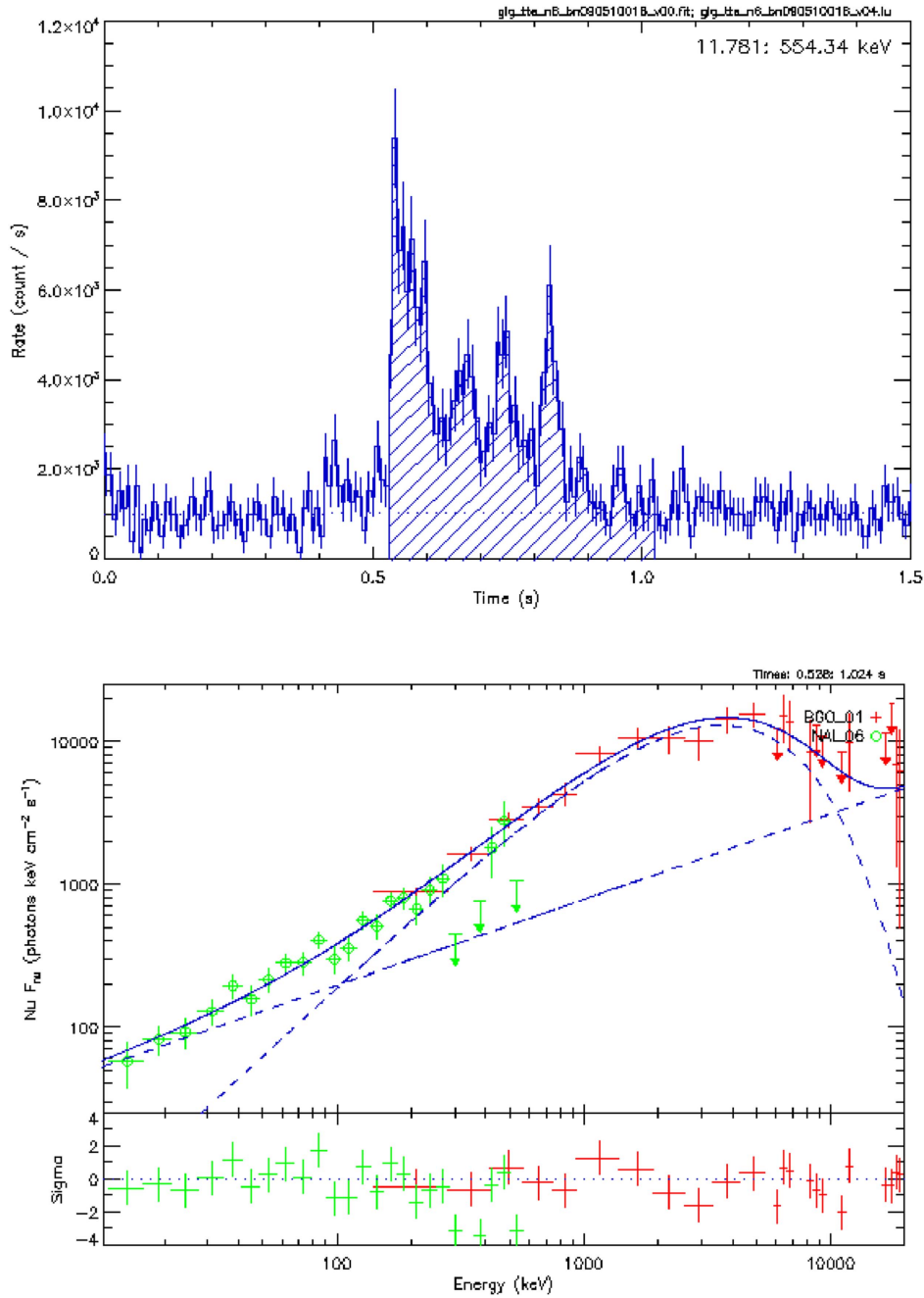


Figure 4. Top panel: GBM NaI-n6 light curve of GRB 090510 and interval considered to compute E_{iso} . Bottom panel: Comptonized+power-law best fit of the corresponding spectrum (from $T_0 + 0.528$ to $T_0 + 1.024$ s).

of stellar mass $5 \times 10^9 M_{\odot}$, with a rather low star formation rate $\text{SFR} = 0.3 M_{\odot} \text{ yr}^{-1}$ (Berger 2014, and references therein).

4.2. Data Analysis

Our analysis focused on *Fermi* (GBM and LAT) and *Swift*/XRT data. The *Fermi*/GBM signal is the most luminous in the NaI-n6 (8–900 keV, dropping the overflow high-energy channels and cutting out the K edge between ~ 30 and ~ 40 keV) and BGO-b1 (260 keV–40 MeV, again dropping the overflow high-energy channels) detectors. We additionally considered *Fermi*/LAT data in the 100 MeV–100 GeV energy range. We made use of standard software in our analysis: GBM time-tagged data—suitable in particular for S-GRBs—were

analyzed with the *rmfit* package⁸; LAT data were analyzed with the *Fermi* Science tools.⁹ The data were retrieved from the *Fermi* science support center.¹⁰ *Swift*/XRT data were retrieved from the UK *Swift* Data Centre at the University of Leicester,¹¹ and they have been reduced and analyzed using XSPEC.

Using GBM time-tagged event data binned in 16 ms intervals, the best fit in the interval $T_0 + 0.528$ s to $T_0 + 1.024$ s is a Comptonized+power-law model (see

⁸ http://fermi.gsfc.nasa.gov/ssc/data/analysis//rmfit/vc_rmfit_tutorial.pdf

⁹ <http://fermi.gsfc.nasa.gov/ssc/data/analysis//documentation/Cicerone/>

¹⁰ <http://fermi.gsfc.nasa.gov/ssc/data/access/>

¹¹ <http://www.swift.ac.uk/archive/index.php>

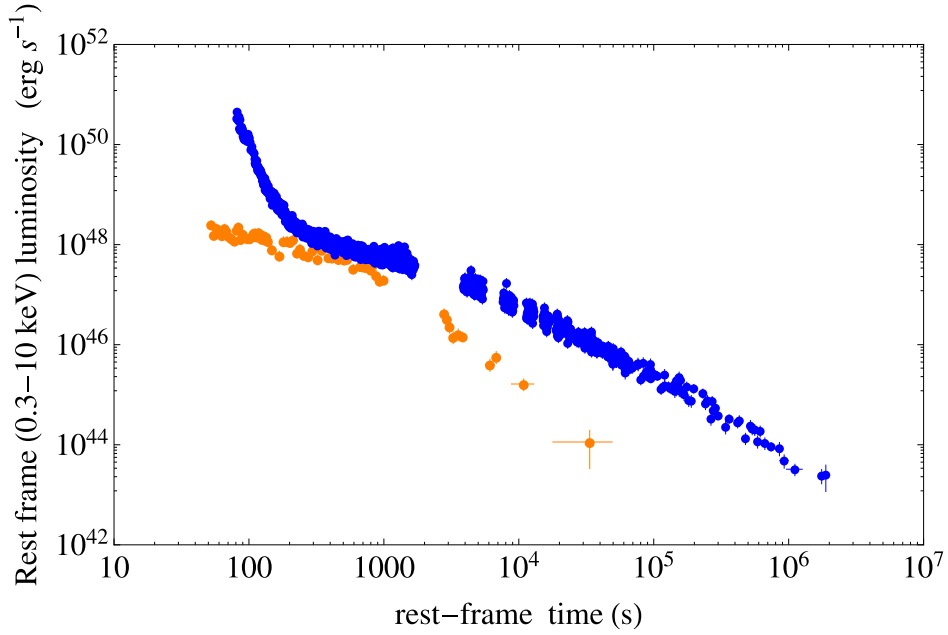


Figure 5. Rest-frame 0.3–10 keV luminosity light curves of GRB 090510 (in orange) and GRB 090618 (in blue), the prototypical IGC source. An overlapping pattern has been observed in IGC sources (Pisani et al. 2013), as well as a nesting behavior (Ruffini et al. 2014); it is clear from the deviation between the two light curves that GRB 090510 does not follow this characteristic pattern, thereby confirming its non-IGC nature.

Table 1
Spectral Analysis of the P-GRB of GRB 090510 in the Time Interval $T_0 + 0.528$ s to $T_0 + 0.640$ s.

Model	$C - \text{STAT}/\text{dof}$	E_{peak} (keV)	α	β	γ	kT (keV)
Band	221.46/237	2987 ± 343	-0.64 ± 0.05	-3.13 ± 0.42
Comp	392.65/238	3020 ± 246	-0.64 ± 0.05
Comp+PL	209.26/236	2552 ± 233	-0.26 ± 0.14	...	-1.45 ± 0.07	...
PL	492.83/239	-1.20 ± 0.02	...
BB+PL	250.09/237	-1.38 ± 0.04	477.5 ± 24.9

Note. The Columns List the Model, its C-STAT Over the Number of Degrees of Freedom (dof), the Peak Energy E_{peak} is the Peak Energy of the Comp or Band Component, the Low-energy Index α of the Comp or Band Component, the High-energy Index β of the Band Component, the Power-law Index γ , and the Temperature kT of the Blackbody Component.

Figure 4). Using this spectral model, we find an isotropic energy $E_{\text{iso}} = (3.95 \pm 0.21) \times 10^{52}$ erg. The observed peak energy of the best-fit Band model of the time-integrated GBM data is 4.1 ± 0.4 MeV, which corresponds to a rest-frame value of 7.89 ± 0.76 MeV.

The best-fit model during the first pulse (from $T_0 + 0.528$ s to $T_0 + 0.640$ s) in the 8 keV–40 MeV range is also a Comptonized+power-law model, preferred over a power law (PL, $\Delta C - \text{STAT} = 100$), a blackbody plus PL (BB + PL, $\Delta C - \text{STAT} = 41$), or a Band model ($\Delta C - \text{STAT} = 12$). The fitting statistics are summarized in Table 1. The peak energy E_{peak} of the Comptonized component is 2.6 MeV. The total isotropic energy contained in this time interval is $\sim 1.77 \times 10^{52}$ erg, while the isotropic energy contained in the Comptonized part reaches $\sim 1.66 \times 10^{52}$ erg.

5. GRB 090510 AS AN S-GRB

We here justify the interpretation of GRB 090510 as an S-GRB event. In addition to the duration and hardness properties that are similar to other GRBs interpreted as binary NS mergers, the

pattern of the late X-ray emission and the position of GRB 090510 in the $E_{\text{peak}} - E_{\text{iso}}$ plane favor this interpretation.

5.1. Late X-Ray Emission (Episode 3)

An important feature of BdHNe is the existence of a pattern in the behavior of their 0.3–10 keV late X-ray luminosity light curves, which we refer to as Episode 3 (see, e.g., Ruffini et al. 2015c). This emission is observationally characterized by the overlapping of the common late power-law behavior (Pisani et al. 2013), as well as by the nesting, namely, an inverse (direct) proportionality relation between the duration (the luminosity) of the plateau phase and the energy of the GRB emission: the more energetic the source, the smaller (higher) the duration (the luminosity) of the plateau (Ruffini et al. 2014).

If GRB 090510 were to be an IGC event exploding in a high-density environment, this characteristic Episode 3 would be expected and should be seen. Thanks to adequate coverage by the *Swift*/XRT instrument, the late X-ray (0.3–10 keV) emission of GRB 090510 has been well sampled. We computed its rest-frame 0.3–10 keV luminosity light curve, using a simple power-law

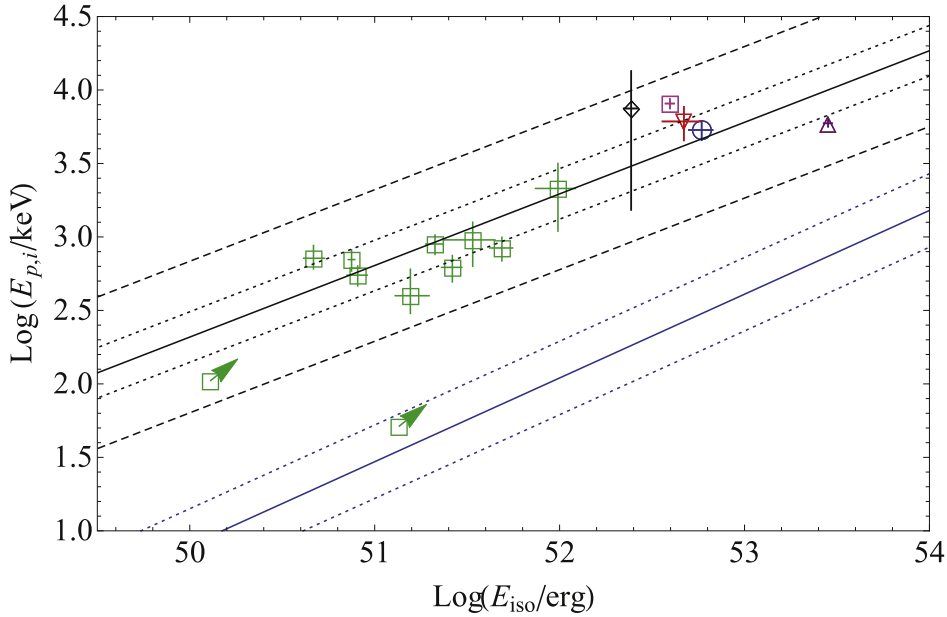


Figure 6. $E_{\text{peak}}-E_{\text{iso}}$ plot of all short bursts with redshift. The black line marks the relation for S-GRBs (which includes the theoretical redshifts we obtained for four GRBs). This relation takes the form $\log E_{\text{peak}} = A + \gamma(\log E_{\text{iso}})$, where $A = -22.0 \pm 3.2$, $\gamma = 0.49 \pm 0.06$, and E_{peak} and E_{iso} are respectively given in keV and erg. The dotted and dashed lines represent the 1σ and 3σ scatter of the relation, respectively ($\sigma_{\text{sc}} = 0.17 \pm 0.04$ dex). Green boxes indicate S-GRFs with a measured redshift; only lower limits are available for the two S-GRFs singled out by an arrow. GRB 090510 is marked by the pink square. The other four symbols indicate S-GRBs with a redshift derived from the fireshell analysis. The black diamond indicates GRB 081024B, the red inverted triangle GRB 140402A, the blue square GRB 140619B, and the purple triangle GRB 090227B. For comparison, the blue line marks the relation for long GRBs given in Calderone et al. (2015), $\log E_{\text{peak}} = A + \gamma(\log E_{\text{iso}} - B)$, where $A = 2.73$, $B = 53.21$, and $\gamma = 0.57 \pm 0.06$. The dotted lines represent the 1σ scatter of the relation ($\sigma_{\text{sc}} = 0.25$ dex).

spectral fit and taking care of the K -correction as follows:

$$L_{\text{rf}} = 4\pi d_l^2(z) f_{\text{obs}} \frac{\int_{0.3/(1+z)}^{10/(1+z)} \text{keV} E^{-\gamma} dE}{\int_{0.3}^{10} \text{keV} E^{-\gamma} dE}, \quad (1)$$

where f_{obs} is the XRT flux (in $\text{erg s}^{-1} \text{cm}^{-2}$) in the observed 0.3–10 keV range, d_l is the luminosity distance, γ is the photon index of the XRT spectrum, and $E^{-\gamma}$ is the spectral model (here, a simple power law) fitting the observed XRT flux.

The rest-frame 0.3–10 keV luminosity light curve is plotted in Figure 5: the comparison with the prototypical IGC source GRB 090618 shows a clear deviation from the overlapping and nesting patterns. Indeed, the late X-ray emission of GRB 090510 is much weaker than that of typical IGC sources and does not follow the typical power-law behavior as a function of time, which has a slope $-1.7 \leq \alpha_X \leq -1.3$. As a consequence, this result is inconsistent with the hypothesis of GRB 090510 being a BdHN disguised as a short burst. Instead, the interpretation as an S-GRB is in full agreement with the theory and the data (see below).

5.2. $E_{\text{peak}}-E_{\text{iso}}$ Relation

Although the sample of short bursts with a measured redshift and an estimate of E_{peak} is of modest size in comparison to that of long GRBs, it has been noted that a relation similar to the Amati one (Amati et al. 2002; Amati & Della Valle 2013) exists for short bursts (see, e.g., Zhang et al. 2012; Calderone et al. 2015). Plotted in Figure 6, this $E_{\text{peak}}-E_{\text{iso}}$ relation has almost the same slope as the Amati relation, but they drastically differ in their amplitudes.

While Zhang et al. (2012) extended this analysis to the above-defined S-GRFs, we have recently added four S-GRBs in this $E_{\text{peak}}-E_{\text{iso}}$ relation, which we have called the MuRuWaZha relation (Ruffini et al. 2015a).

With the parameters $E_{\text{peak}} = (7.89 \pm 0.76)$ MeV and $E_{\text{iso}} = (3.95 \pm 0.21) \times 10^{52}$ erg obtained in the previous sections, GRB 090510 falls right on the relation fulfilled by S-GRBs, and far from that of long GRBs (see Figure 6). This point further strengthens the identification of GRB 090510 as an S-GRB.

5.3. The Offset from the Host Galaxy

Long bursts are known to trace star formation (e.g., Bloom et al. 2002). They explode mainly in low-mass galaxies with high specific star formation rates. On the other hand, short bursts occur in a wider range of host galaxies, including old, elliptical galaxies with little star formation and young galaxies. Their median projected offset from the center of their host, about 5 kpc, is also known to be four times larger than that of long bursts (Bloom et al. 2002). With a projected offset of 5.5 kpc, as detailed previously, GRB 090510 falls in the typical short-burst range. Its host galaxy is a late-type one.

The results of the fireshell analysis summarized in the next section also support this conclusion. The average CBM density of GRB 090510 is indeed evaluated at $\langle n_{\text{CBM}} \rangle = 8.7 \times 10^{-6} \text{ cm}^{-3}$ (see next section), a low value that is typical of galactic halos.

6. INTERPRETATION

GRB 090510 exhibits several peculiar features: the spectrum of the P-GRB is not purely thermal, a weak precursor emission is clearly seen, and a GeV emission is observed—which never occurs in S-GRFs but appears to be a general property of the S-GRBs. This section is devoted to the analysis and interpretation of these features.

Ruffini et al. (2015b) establish theoretical predictions concerning S-GRBs that originate in a binary NS merger, with and without BH formation. We find that these predictions are fulfilled and that

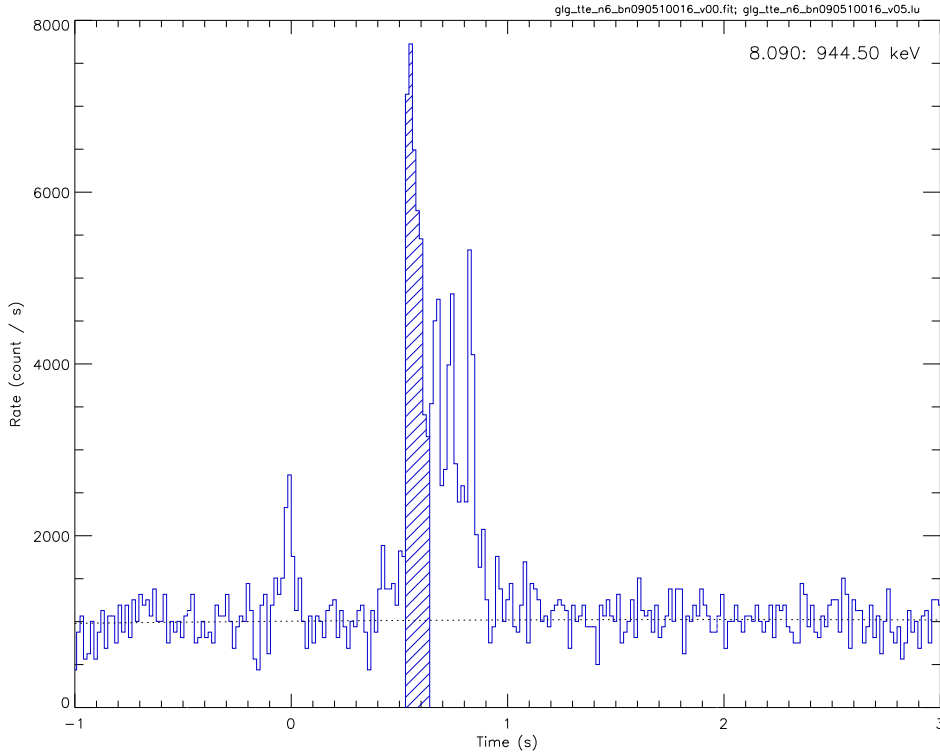


Figure 7. Counts light curve of GRB 090510 as seen by the NaI-n6 detector of *Fermi*/GBM with a 16 ms binning. The dashed area represents the interval in which the P-GRB is identified.

all features are consistent with GRB 090510 resulting from an NS merger, leading to the formation of a Kerr–Newman BH.

6.1. P-GRB

The identification of the P-GRB is especially relevant to the fireshell analysis, since it marks the reaching of the transparency of the fireshell. The P-GRB is followed by the prompt emission (Ruffini et al. 2001a). It is suggested in Ruffini et al. (2015b) that the GeV emission is produced by the newborn BH and starts only after the P-GRB is emitted, at the beginning of the prompt emission. Here, the bulk of the GeV emission is detected after the first main spike is over. Therefore, we identify the first main spike (from $T_0 + 0.528$ to $T_0 + 0.644$ s; see Figure 7) with the P-GRB. The results of the analysis within the fireshell theory (presented hereafter) also offer an a posteriori confirmation of this identification of the P-GRB.

The best-fit model of the P-GRB spectrum consists of a Comptonized+power-law model. We note that a Comptonized component may be viewed as a convolution of blackbodies (see Figure 8 and Table 2, for details).

The geometry of the fireshell is dictated by the geometry of the pair-creation region. It is in general assumed to be a spherically symmetric dyadosphere, which leads to a P-GRB spectrum generally described by a single thermal component in good agreement with the spectral data. Cherubini et al. (2009) found that the region of pair creation in a Kerr–Newman geometry becomes axially symmetric, thus effectively becoming a dyadotorus. Qualitatively, one expects a pure thermal spectrum resulting from the dyadosphere, while a convolution of thermal spectra of different temperatures is expected for a dyadotorus (see Figure 1).

In the present case of GRB 090510, also in view of the good quality of the γ -ray data, the P-GRB is best fitted by a

convolution of thermal spectra. The theoretically expected temperatures of the thermal components in the dyadotorus are a function of the polar angle. Knowing that the final spectrum at the transparency condition is a convolution of such thermal spectra at different angles, we adopted for simplicity a discrete number of thermal components (see Table 2). The number of such thermal components, leading in principle to a continuum, is a function of the quality of the data. This provides the first indication that indeed the angular momentum plays a role in the merging of the two NSs and that the dyadotorus is formed as theoretically predicted in a series of papers (Cherubini et al. 2009; Ruffini 2009). This opens a new area of research that is not going to be addressed in the present article. Previous identifications of pure thermal components in the P-GRB of other GRBs (e.g., Izzo et al. 2012; Ruffini et al. 2015b) nevertheless evidence that the angular momentum of the BH formed by GRB 090510 must be substantially large in order to affect the P-GRB spectrum.

Finally, the extra power-law component observed in the P-GRB spectrum is very likely related to a mildly jetted component necessary to fulfill the conservation of the energy and angular momentum of the system.

6.2. Prompt Emission

In order to simulate the light curve and spectrum of the prompt emission of GRB 090510, we assume that the initial fireshell energy $E_{e^+e^-}^{\text{tot}}$ is equal to E_{iso} . Since the P-GRB spectrum is not purely thermal, we derive an effective blackbody temperature from the peak energy of the Comptonized component. We obtain a temperature $kT_{\text{bs}} = (633 \pm 62)$ keV.

The fireshell theory allows the determination of all essential quantities of the model from the total pair plasma energy $E_{e^+e^-}^{\text{tot}}$

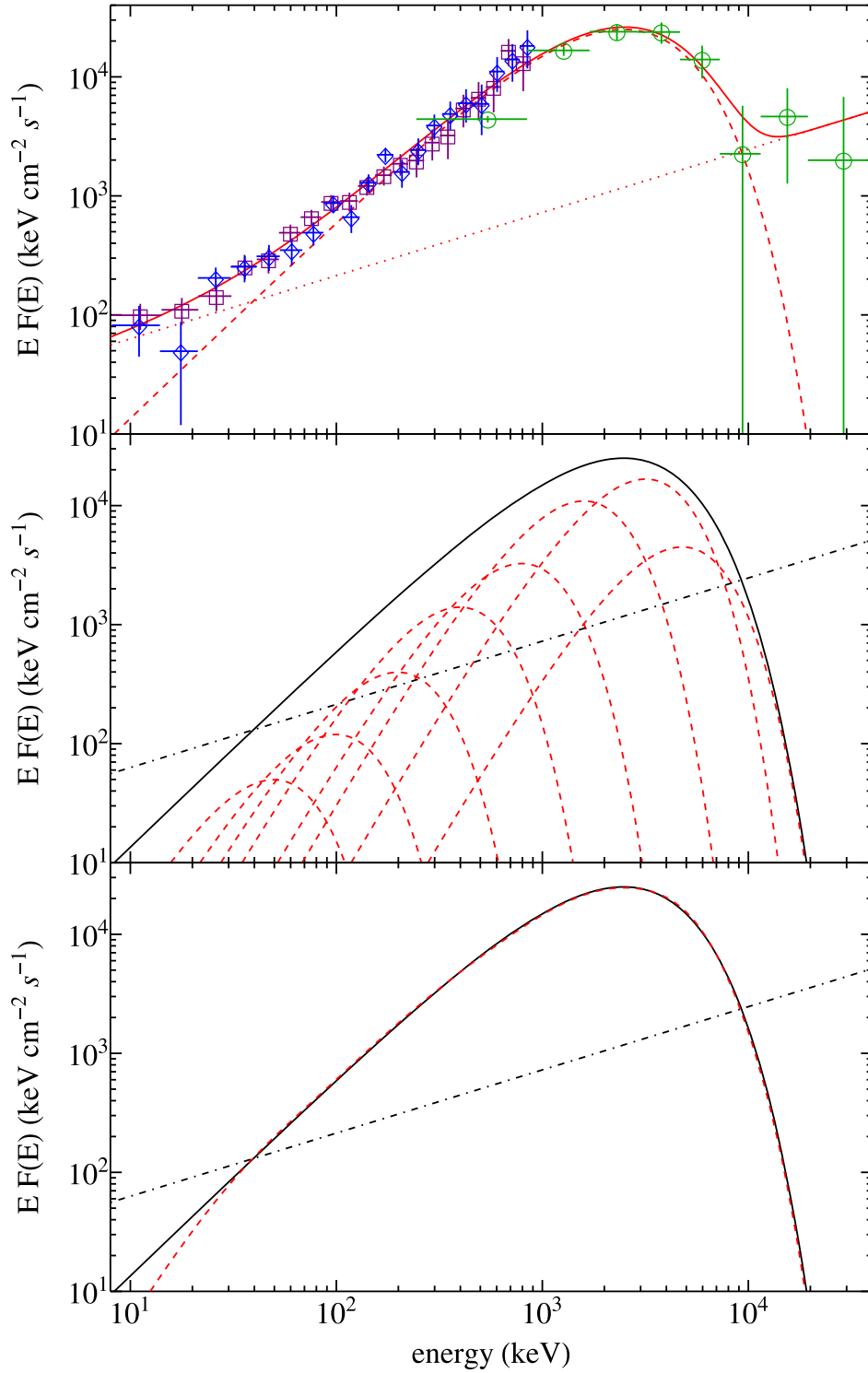


Figure 8. Top panel: P-GRB spectrum of GRB 090510 from the *Fermi*-GBM NaI-n6 (purple squares) and n7 (blue diamonds) and the BGO-b1 (green circles) detectors, in the time interval from $T_0 + 0.528$ to $T_0 + 0.644$ s. The best fit (solid red line) is composed of a power-law model (dotted red line) and a Comptonized model (dashed red curve). Middle panel: above Comptonized model (here the solid black line), viewed as a convolution of thermal components (dashed red curves). The convolution of blackbodies produces the result plotted in the bottom panel, namely, a dashed red curve reproducing the Comptonized model. The power-law component (dot-dashed black line in the middle and bottom panels) is very likely related to a mildly jetted component necessary to fulfill the conservation of the energy and angular momentum of the system.

and from the ratio of the energy contained in the P-GRB to $E_{e^+e^-}^{\text{tot}}$. This ratio directly leads to the baryon load B , which, in conjunction with $E_{e^+e^-}^{\text{tot}}$ and the relation between the predicted and observed temperatures, gives the Lorentz factor at

transparency, the temperature of the fireshell at transparency, and the radius at transparency.

Given $E_{\text{iso}} = 3.95 \times 10^{52}$ erg and $E_{\text{P-GRB}} = (42.1 \pm 3.8)\% E_{e^+e^-}^{\text{tot}}$, we deduce a baryon load $B = 5.54 \times 10^{-5}$, a Lorentz

Table 2

The Parameters of the Blackbody (BB) Spectra Used in the Convolution Shown in Figure 8

BB	kT (keV)	$E_{\text{BB}}/E_{\text{P-GRB}}$ (%)
1	1216	8.8
2	811	43.6
3	405	31.8
4	203	9.6
5	101	4.4
6	51	1.2
7	25	0.4
8	13	0.2

Note. The columns list the number of BBs, their temperatures, and their energy content with respect to the P-GRB energy computed from the Comptonized model.

Table 3

Parameters Derived from the Fireshell Analysis of GRB 090510

Parameter	Value
B	$(5.54 \pm 0.70) \times 10^{-5}$
γ_{tr}	$(1.04 \pm 0.07) \times 10^4$
r_{tr}	$(7.60 \pm 0.50) \times 10^{12}$ cm
$E_{e^+e^-}^{\text{tot}}$	$(3.95 \pm 0.21) \times 10^{52}$ erg
kT_{blue}	$(1.20 \pm 0.11) \times 10^3$ keV
$\langle n \rangle$	$(8.7 \pm 2.1) \times 10^{-6}$ cm $^{-3}$

Note. Shown in the table are the baryon load B , the Lorentz factor at transparency γ_{tr} , the fireshell radius at transparency r_{tr} , the total energy of the electron-pair plasma $E_{e^+e^-}^{\text{tot}}$, the blueshifted temperature of the fireshell at transparency kT_{blue} , and the CBM average density $\langle n \rangle$

factor $\gamma = 1.04 \times 10^4$, a temperature at transparency $kT = 1.2$ MeV, and a radius at transparency $r_{\text{tr}} = 7.60 \times 10^{12}$ cm (see Table 3).

In order to determine the profile of the CBM, a simulation of the prompt emission following the P-GRB has been performed. The simulation starts at the transparency of the fireshell with the parameters that we determined above. A trial-and-error procedure is undertaken, guided by the necessity to fit the light curve of GRB 090510. The results of this simulation (reproduction of the light curve and spectrum, in the time interval from $T_0 + 0.644$ to $T_0 + 0.864$ s, and CBM profile) are shown in Figure 9. The average CBM density is found to be $\langle n_{\text{CBM}} \rangle = 8.7 \times 10^{-6}$ cm $^{-3}$. This low value, typical of galactic halo environments, is consistent with the large offset from the center of the host and further justifies the interpretation of GRB 090510 as an S-GRB originating in a binary NS merger.

Our theoretical fit of the prompt emission (see red line in the middle panel of Figure 9) predicts a cutoff at ~ 10 MeV. The spectrum at energy $\gtrsim 10$ MeV could be affected by the onset of the high-energy power-law component manifested both in the data of the Mini-Calorimeter on board *AGILE* (see top panel of Figure 4 in Giuliani et al. 2010) and in the data points from the *Fermi*-GBM BGO-b1 detector.

6.3. Precursor Emission

There is a weak precursor emission about 0.4 s before the P-GRB (or ~ 0.21 s in the cosmological rest frame). Two GeV

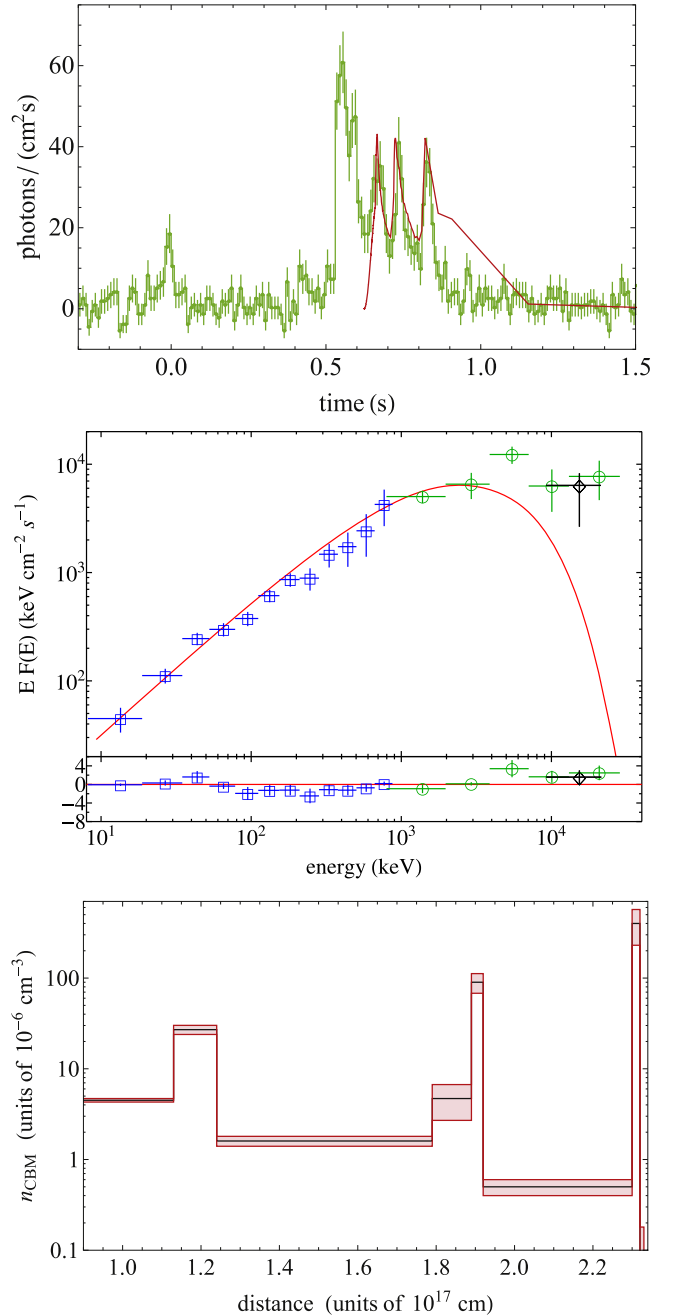


Figure 9. Results of the fireshell simulation of GRB 090510. Top panel: fit of the prompt emission *Fermi*-GBM Nal-n6 light curve. Middle panel: fit of the corresponding spectrum including the *Fermi*-Nal-6 (blue squares) and BGO-b1 (green circles) data in the time interval from $T_0 + 0.644$ to $T_0 + 0.864$ s. A single data point obtained from the Mini-Calorimeter on board *AGILE*, in the range 10–20 MeV and in the first 0.2 s of the *AGILE* light curve (from $T_0 + 0.5$ to $T_0 + 0.7$ s in the *Fermi* light curve), is shown for comparison (reproduced from Figure 4 in Giuliani et al. 2010). Bottom panel: density profile of the CBM inferred from the simulation of CBM clouds of $\sim 10^{22}$ g.

photons have been detected during the precursor emission. Precursors are commonly seen in long bursts: Lazzati (2005) found that $\sim 20\%$ of them show evidence of an emission preceding the main emission by tens of seconds. Short bursts are less frequently associated with precursors.

No significant emission from the GRB itself is expected prior to the P-GRB—since it marks the transparency of the fireshell

—but the precursor may be explainable in the context of a binary NS merger by invoking the effects of the interaction between the two NSs just prior to merger. Indeed, it has been suggested that precursor emission in short bursts may be caused by resonant fragmentation of the crusts (Tsang et al. 2012) or by the interaction of the NS magnetospheres (Hansen & Lyutikov 2001).

The timescale (~ 0.21 s between the precursor and the P-GRB) is consistent with a pre-merger origin of the precursor emission. From its formation to its transparency, the fireshell undergoes a swift evolution. The thermalization of the pair plasma is achieved almost instantaneously ($\sim 10^{-13}$ s; Aksenov et al. 2007), and the e^+e^- plasma of GRB 090510 reaches the ultrarelativistic regime (i.e., a Lorentz factor $\gamma > 10$) in a matter of 4.2×10^{-2} s, according to the numerical simulation. The radius of the fireshell at transparency, $r_{tr} = 7.60 \times 10^{12}$ cm, corresponds to more than 100 lt-s; however, relativistic motion in the direction of the observer squeezes the light curve by a factor of $\sim 2\gamma^2$, which makes the fireshell capable of traveling that distance under the observed timescale.

The spectral analysis of this precursor is limited by the low number of counts. Muccino et al. (2013b) interpreted the spectrum with a blackbody plus power-law model. This leads to a blackbody temperature of 34.2 ± 7.5 keV. The isotropic energy contained in the precursor amounts to $(2.28 \pm 0.39) \times 10^{51}$ erg.

6.4. Redshift Estimate

An interesting feature of the fireshell model is the possibility to infer a theoretical redshift from the observations of the P-GRB and the prompt emission. In the case of GRB 090510, a comparison is therefore possible between the measured redshift $z = 0.903 \pm 0.003$ and its theoretical derivation. An agreement between the two values would in particular strengthen the validity of our P-GRB choice, which would in turn strengthen our results obtained with this P-GRB.

The feature of the redshift estimate stems from the relations, engraved in the fireshell theory, between different quantities computed at the transparency point: the radius in the laboratory frame, the comoving frame and blueshifted temperatures of the plasma, the Lorentz factor, and the fraction of energy radiated in the P-GRB and in the prompt emission as functions of B (see Figure 4 in Ruffini et al. 2015b). Thus, the ratio $E_{P-GRB}/E_{e^+e^-}^{\text{tot}}$ implies a finite range for the coupled parameters $E_{e^+e^-}^{\text{tot}}$ and B (last panel of Figure 4 in Ruffini et al. 2015b). Assuming $E_{e^+e^-}^{\text{tot}} = E_{\text{iso}}$, this ratio is known since it is equal to the ratio between the observed fluences of the respective quantities:

$$\frac{E_{P-GRB}}{E_{e^+e^-}^{\text{tot}}} \approx \frac{4\pi S_{P-GRB} d_l^2(z)/(1+z)}{4\pi S_{e^+e^-}^{\text{tot}} d_l^2(z)/(1+z)} = \frac{S_{P-GRB}}{S_{e^+e^-}^{\text{tot}}}. \quad (2)$$

With the measured values $S_{P-GRB} = (9.31 \pm 0.76) \times 10^{-6}$ erg cm $^{-2}$ and $S_{e^+e^-}^{\text{tot}} = (2.19 \pm 0.18) \times 10^{-5}$ erg cm $^{-2}$, we find $E_{P-GRB}/E_{e^+e^-}^{\text{tot}} = (42.1 \pm 3.8)\%$.

In addition, knowing the couple $[E_{e^+e^-}^{\text{tot}}, B]$ gives the (blueshifted toward the observer) temperature of the fireshell at transparency kT_{blue} (Figure 4 in Ruffini et al. 2015b, second panel). But we also have the following relation between kT_{blue} and the observed temperature at transparency kT_{obs} , linking

their ratio to the redshift:

$$\frac{kT_{\text{blue}}}{kT_{\text{obs}}} = 1 + z. \quad (3)$$

Finally, since we assume that $E_{e^+e^-}^{\text{tot}} = E_{\text{iso}}$, we also have an expression of $E_{e^+e^-}^{\text{tot}}$ as a function of z using the formula of the K -corrected isotropic energy:

$$E_{\text{iso}} = 4\pi d_l^2(z) \frac{S_{\text{tot}}}{1+z} \frac{\int_{1/(1+z) \text{ keV}}^{10000/(1+z) \text{ keV}} EN(E) dE}{\int_8^{40000 \text{ keV}} EN(E) dE} \quad (4)$$

where $N(E)$ is the photon spectrum of the GRB and the fluence S_{tot} is obtained in the full GBM energy range 8–40,000 keV.

The use of all these relations allows a redshift to be determined by an iterative procedure, testing at every step the value of the parameters $E_{e^+e^-}^{\text{tot}}(z)$ and kT_{blue} . The procedure successfully ends when both values are consistent according to the relations described above. In the case of GRB 090510, we find $z = 0.75 \pm 0.17$, which provides a satisfactory agreement with the measured value $z = 0.903 \pm 0.003$.

6.5. GeV Emission

GRB 090510 is associated with a high-energy emission, consistently with all other observed S-GRBs, i.e., energetic events with $E_{\text{iso}} \gtrsim 10^{52}$ erg. The only case of an S-GRB without GeV emission, namely, GRB 090227B, has been explained by the absence of alignment between the LAT and the source at the time of the GRB emission. Nevertheless, evidence of some GeV emission in this source has been recently obtained (R. Ruffini et al. 2016, in preparation).

The GeV light curve of GRB 090510 is plotted in Figure 10, together with other S-GRB light curves and showing a common power-law behavior, which goes as $t^{-1.32}$, similar to the clustering of the GeV light curves found by Nava et al. (2014). These S-GRBs are compared with that of the BdHN 130427A, which shares a similar behavior. Ruffini et al. (2015b) suggest and argue that the GeV emission is related to the presence of a BH and its activity. This view is supported by the fact that the GeV emission is delayed with respect to the γ -ray emission: it starts only after the P-GRB is over.

The GeV emission of GRB 090510 is particularly intense, reaching $E_{\text{LAT}} = (5.78 \pm 0.60) \times 10^{52}$ erg. Such a large value, one of the largest observed among S-GRBs, is consistent with the large angular momentum of the newborn BH. This energetic cannot be explained in terms of NSs in view of the lower value of the gravitational binding energy.

The absence of GeV emission in S-GRFs is also confirmed from the strong upper limit to the GeV emission for S-GRBs imposed by the *Fermi*-LAT sensitivity. We assume for a moment that the GeV emission of an S-GRF is similar to that of S-GRBs. We then compute the observed GeV flux light curve of S-GRB 090510 at different redshifts, e.g., $z = 2.67$ and 5.52 , which correspond to the redshifts of the S-GRB 081024B and of the S-GRB 140402A, respectively (Y. Aimuratsov et al. 2016, in preparation). The result is that if we compare these computed flux light curves with the *Fermi*-LAT sensitivity of the Pass 8 Release 2 Version 6 Instrument Response Functions,¹² which is approximately 10^{-11} erg cm $^{-2}$ s $^{-1}$, all

¹² http://www.slac.stanford.edu/exp/glast/groups/canda/lat_Performance_files/broadband_flux_sensitivity_p8r2_source_v6_all_10yr_zmax100_n03.0_e1.50_ts25.png

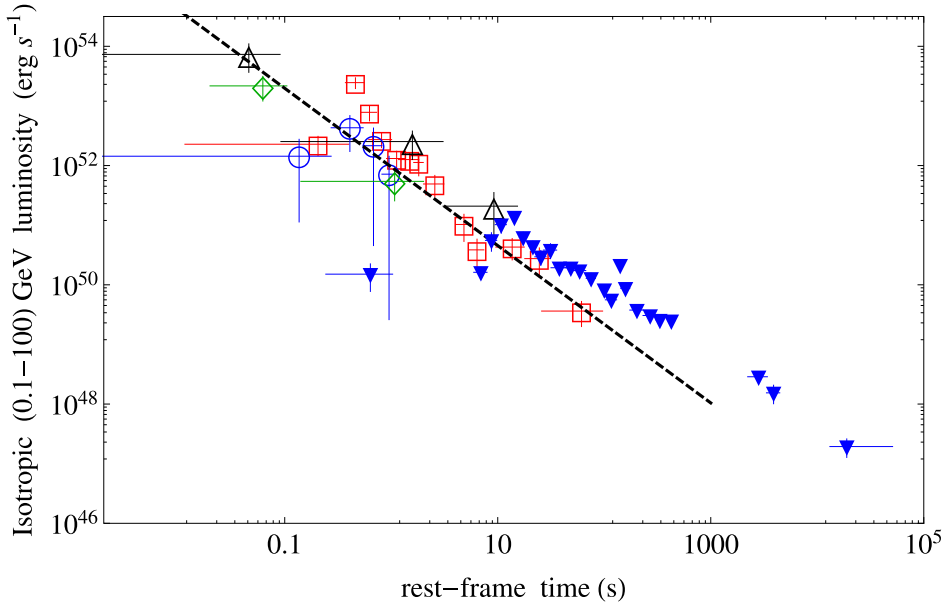


Figure 10. Isotropic rest-frame 0.1–100 GeV luminosity light curves of the S-GRBs 090510 (red squares), 081024B (green diamonds), 140402A (black triangles), and 140619B (blue circles) compared to that of the BdHN 130427A (blue downward-pointing triangles). The dashed black line marks the common behavior of all the S-GRB light curves, which goes as $t^{-1.32}$. In our approach this communality follows straightforwardly from the equality of the masses of the emerging extreme BH.

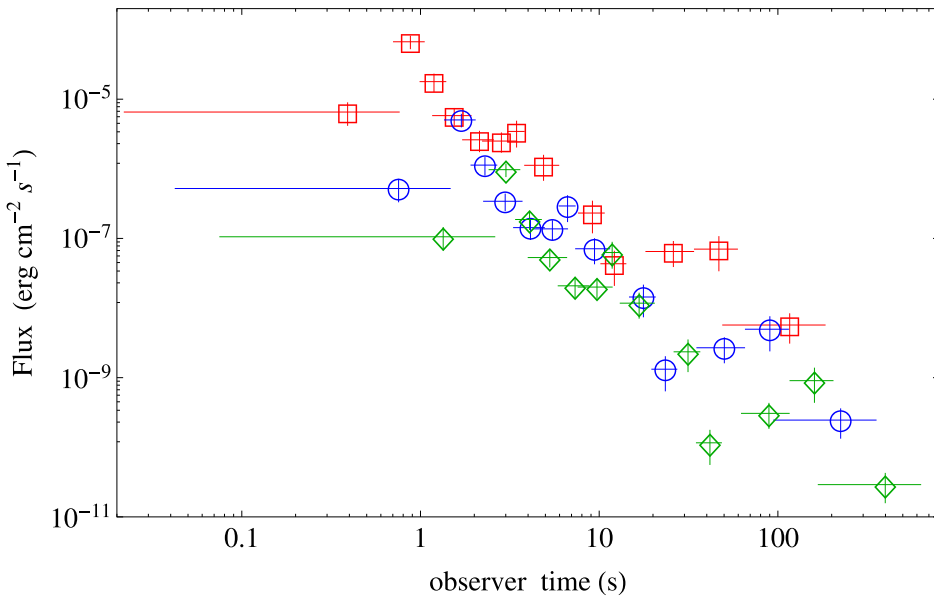


Figure 11. Observed 0.1–100 GeV flux light curve of the S-GRB 090510 (red squares) and the corresponding ones obtained by translating this S-GRB at $z = 2.67$ (blue circles) and at $z = 5.52$ (green diamonds).

of them are always well above the LAT broadband sensitivity by a factor of $\sim 10^5$ (see Figure 11). This result does not depend on the choice of the source. In their rest frame all the S-GRB GeV light curves follow a similar behavior. Therefore, the GeV emission of S-GRB 090510 is always above $\sim 10^5$ times the LAT sensitivity, even at higher redshifts. If we now assume that S-GRFs do conform to the same behavior of S-GRBs, the absence of detection of GeV emission implies that the S-GRFs necessarily have fluxes at least 10^5 – 10^6 times smaller than those of S-GRBs.

6.6. On the Energy Requirement of the GeV Emission

In order to estimate the energy requirement of the 0.1–100 GeV emission of Figure 10, we consider the accretion of mass M_{acc} onto a Kerr–Newman BH, dominated by its angular momentum and endowed with electromagnetic fields not influencing the geometry, which remains approximately that of a Kerr BH. We recall that if the infalling accreted material is in an orbit co-rotating with the BH spin, up to $\eta_+ = 42.3\%$ of the initial mass is converted into radiation, for a maximally rotating Kerr BH, while this efficiency drops to

$\eta_- = 3.8\%$ when the infalling material is on a counter-rotating orbit (see Ruffini & Wheeler 1969, in problem 2 of Section 104 in Landau & Lifshitz 2003). Therefore, the GeV emission can be expressed as

$$E_{\text{LAT}} = f_b^{-1} \eta_{\pm} M_{\text{acc}} c^2, \quad (5)$$

and depends not only on the efficiency η_{\pm} in the accretion process of matter M_{acc} but also on the geometry of the emission described by the beaming factor $f_b \equiv 1 - \cos \theta$ (here θ is the half-opening angle of jet-like emission).

Depending on the assumptions we introduce in Equation (5), we can give constraints on the amount of accreted matter or on the geometry of the system.

For an isotropic emission, $f_b \equiv 1$, the accretion of $M_{\text{acc}} \gtrsim 0.08 M_{\odot}$, for the co-rotating case, and of $M_{\text{acc}} \gtrsim 0.86 M_{\odot}$, for the counter-rotating case, is required.

Alternatively, we can assume that the accreted matter comes from the crustal material from a $1.6 + 1.6 M_{\odot}$ NS–NS binary progenitor. The crustal mass from the NL3 nuclear model for each of these NSs is $M_c = 4.30 \times 10^{-5} M_{\odot}$ (see, e.g., Belvedere et al. 2012, and Figure 2). Assuming that crustal material accounts also for the baryon load mass, e.g., $M_B \equiv E_{e^+e^-}^{\text{tot}} B/c^2 = 1.22 \times 10^{-6} M_{\odot}$, the total available mass for accretion is $M_{\text{acc}} \equiv 2M_c - M_B = 8.48 \times 10^{-5} M_{\odot}$. Then, the presence of a beaming is necessary: from Equation (5), a half-opening beaming angle $\theta \gtrsim 2^{\circ}70$, for the co-rotating case, and $\theta \gtrsim 0^{\circ}81$, for the counter-rotating case, would be required.

The above considerations are clearly independent from the relativistic beaming angle $\theta_r = \gamma_{\text{LAT}}^{-1} \approx 0^{\circ}1$, where the lower limit on the Lorentz factor $\gamma_{\text{LAT}} \approx 550$ has been derived, in a different context, by Lithwick & Sari (2001) to the GeV luminosity light curve (see Figure 10).

Further consequences on these results for the estimate of the rate of these S-GRBs will be presented elsewhere (R. Ruffini et al. 2016, in preparation).

7. CONCLUSIONS

It is interesting to recall some of the main novelties introduced in this paper with respect to previous works on GRB 090510. Particularly noteworthy are the differences from the previous review of short bursts by Nakar (2007), made possible by the discovery of the high-energy emission by the *Fermi* team in this specific source (Ackermann et al. 2010). A new family of short bursts characterized by the presence of a BH and associated high-energy emission with LAT data now available comprises GRBs 081024B, 090227B, 090510, 140402A, and 140619B (see, e.g., Figure 10). The excellent data obtained by the *Fermi* team and interpreted within the fireshell model have allowed us to relate in this paper the starting point of the high-energy emission to the birth of a BH.

Our fireshell analysis assumes that the γ -ray and the GeV components originate from different physical processes. First, the interpretation of the prompt emission differs from the standard synchrotron model: we model the collisions of the baryon accelerated by the GRB outflow with the ambient medium following a fully relativistic approach (see Section 2). Second, we assume that the GeV emission originates from the matter accretion onto the newly born BH, and we show that indeed the energy requirement is fulfilled. This approach explains also the delayed onset of the GeV emission, i.e., it is

observable only after the transparency condition, namely, after the P-GRB emission.

The joint utilization of the excellent data from the *Fermi*-GBM NaI-n6 and n7 and the BGO-b1 detectors and from the Mini-Calorimeter on board *AGILE* (Giuliani et al. 2010) has given strong observational support to our theoretical work. GRB 090510 has been analyzed in light of the recent progress achieved in the fireshell theory and the resulting new classification of GRBs. We show that GRB 090510 is an S-GRB, originating in a binary NS merger (see Figure 3). Such systems, by the absence of the associated SN events, are by far the simplest GRBs to be analyzed. Our analysis indicates the presence of three distinct episodes in S-GRBs: the P-GRB, the prompt emission, and the GeV emission. By following the precise identification of successive events predicted by the fireshell theory, we show evidence for the first indication of a Kerr BH or, possibly, a Kerr–Newman BH formation:

1. The P-GRB spectrum of GRB 090510, in the time interval from $T_0 + 0.528$ to $T_0 + 0.644$ s, is best fitted by a Comptonized component (see Figures 7 and 8 and Table 1), which is interpreted as a convolution of thermal spectra originating in a dyadotorus (see Cherubini et al. 2009; Ruffini 2009; see also Figure 1 and Section 2).
2. The prompt emission follows at the end of the P-GRB (see Figure 4). The analysis of the prompt emission within the fireshell model allows us to determine the inhomogeneities in the CBM giving rise to the spiky structure of the prompt emission and to estimate as well an averaged CBM density of $\langle n_{\text{CBM}} \rangle = 8.7 \times 10^{-6} \text{ cm}^{-3}$ obtained from a few CBM clouds of mass $\sim 10^{22}$ g and typical dimensions of $\sim 10^{16}$ cm (see Figure 9). Such a density is typical of galactic halos where binary NSs are expected to migrate due to large natal kicks.
3. The late X-ray emission of GRB 090510 does not follow the characteristic patterns expected in BdHN events (see Figure 5 and Pisani et al. 2013).
4. The GeV emission occurs at the end of the P-GRB emission and is initially concurrent with the prompt emission. This sequence occurs in both S-GRBs (Ruffini et al. 2015b) and BdHNe (Ruffini et al. 2015c). This delayed long-lasting (≈ 200 s) GeV emission in GRB 090510 is one of the most intense ever observed in any GRB (see Figure 10; see also Ackermann et al. 2013; Ruffini et al. 2016).
5. We then consider accretion on co-rotating and counter-rotating orbits (see Ruffini & Wheeler 1969, in problem 2 of Section 104 in Landau & Lifshitz 2003) around an extreme Kerr BH. Assuming the accretion of the crustal mass $2M_c = 8.60 \times 10^{-5} M_{\odot}$ from a $1.6 + 1.6 M_{\odot}$ NS–NS binary, fulfilling global charge neutrality (see Figure 2), geometrical beaming angles of $\theta \gtrsim 0^{\circ}81$, for the co-rotating case, and $\theta \gtrsim 2^{\circ}70$, for the counter-rotating case, are inferred. In order to fulfill the transparency condition, the initial Lorentz factor of the jetted material has to be $\gamma \gtrsim 550$ (see Section 6.6).
6. While there is evidence that the GeV emission must be jetted, no beaming appears to be present in the P-GRB and in the prompt emission, with important consequences for the estimate of the rate of such events (Ruffini et al. 2016).

7. The energetic and the possible beaming of the GeV emission requires the presence of a Kerr BH, or a Kerr–Newman BH dominated by its angular momentum and with electromagnetic fields not influencing the geometry (see also Section 6.5).
8. The self-consistency of the entire procedure has been verified by estimating, on the ground of the fireshell theory, the cosmological redshift of the source. The theoretical redshift is $z = 0.75 \pm 0.17$ (see Section 6.4), close to and consistent with the spectroscopically measured value $z = 0.903 \pm 0.003$ (Rau et al. 2009).
9. The values of E_{peak} and E_{iso} of GRB 090510 fulfill with excellent agreement the MuRuWaZha relation (see Section 5.2 and Figure 6; see also Ruffini et al. 2015a).

The main result of this article is that the dyadoturus manifests itself by the P-GRB emission and clearly precedes the prompt emission phase, as well as the GeV emission originating from the newly formed BH. This contrasts with the usual assumption made in almost the totality of works relating BHs and GRBs in which the BH precedes the GRB emission. In conclusion, in this article, we take GRB 090510 as the prototype of S-GRBs and perform a new time-resolved spectral analysis, in excellent agreement with that performed by the *AGILE* and the *Fermi* teams. Now this analysis, guided by a theoretical approach successfully tested in this new family of S-GRBs, is directed to identify a precise sequence of different events made possible by the exceptional quality of the data of GRB 090510. This includes a new structure in the thermal emission of the P-GRB emission, followed by the onset of the GeV emission linked to the BH formation, allowing us, as well, to derive the structure of the CBM from the spiky structure of the prompt emission. This sequence, for the first time, illustrates the formation process of a BH.

It is expected that this very unique condition of generating a jetted GeV emission in such a well-defined scenario of a newly born BH will possibly lead to a deeper understanding of the equally jetted GeV emission observed, but not yet explained, in a variety of systems harboring a Kerr BH. Among these systems we recall binary X-ray sources (see, e.g., Giacconi & Ruffini 1978, and references therein), microquasars (see, e.g., Chaty et al. 2015, and references therein), and, at larger scale, active galactic nuclei (see, e.g., Arsioli et al. 2015, and references therein).

We thank the editor and the referee for their comments, which helped to improve the presentation and the contextualization of our results. We are indebted to Marco Tavani for very interesting comments, as well as for giving us observational supporting evidence. This work made use of data supplied by the UK *Swift* Data Center at the University of Leicester. M.E., M.K., and Y.A. are supported by the Erasmus Mundus Joint Doctorate Program by Grant Numbers 2012-1710, 2013-1471, and 2014-0707, respectively, from the EACEA of the European Commission. C.C. acknowledges INdAM-GNFM for support. M.M. acknowledges the partial support of the project N 3101/GF4 IPC-11 and the target program F.0679 of the Ministry of Education and Science of the Republic of Kazakhstan.

REFERENCES

- Ackermann, M., Ajello, M., Asano, K., et al. 2013, *ApJS*, 209, 11
 Ackermann, M., Asano, K., Atwood, W. B., et al. 2010, *ApJ*, 716, 1178
 Aksenov, A. G., Ruffini, R., & Vereshchagin, G. V. 2007, *PhRvL*, 99, 125003

- Aksenov, A. G., Ruffini, R., & Vereshchagin, G. V. 2009, *PhRvD*, 79, 043008
 Amati, L., & Della Valle, M. 2013, *IJMPD*, 22, 30028
 Amati, L., Frontera, F., in't Zand, J. J. M., et al. 2004, *A&A*, 426, 415
 Amati, L., Frontera, F., Tavani, M., et al. 2002, *A&A*, 390, 81
 Antoniadis, J. 2015, *ASSP*, 40, 1
 Arsioli, B., Fraga, B., Giommi, P., Padovani, P., & Marrese, P. M. 2015, *A&A*, 579, A34
 Becerra, L., Bianco, C. L., Fryer, C. L., Rueda, J. A., & Ruffini, R. 2016, arXiv:1606.02523
 Becerra, L., Cipolletta, F., Fryer, C. L., Rueda, J. A., & Ruffini, R. 2015, *ApJ*, 812, 100
 Belvedere, R., Pugliese, D., Rueda, J. A., Ruffini, R., & Xue, S.-S. 2012, *NuPhA*, 883, 1
 Belvedere, R., Rueda, J. A., & Ruffini, R. 2014, *JKPS*, 65, 897
 Belvedere, R., Rueda, J. A., & Ruffini, R. 2015, *ApJ*, 799, 23
 Berger, E. 2011, *NewAR*, 55, 1
 Berger, E. 2014, *ARA&A*, 52, 43
 Bianco, C. L., & Ruffini, R. 2005a, *ApJL*, 620, L23
 Bianco, C. L., & Ruffini, R. 2005b, *ApJL*, 633, L13
 Bloom, J. S., Kulkarni, S. R., & Djorgovski, S. G. 2002, *AJ*, 123, 1111
 Bloom, J. S., Prochaska, J. X., Pooley, D., et al. 2006, *ApJ*, 638, 354
 Bucciantini, N., Metzger, B. D., Thompson, T. A., & Quataert, E. 2012, *MNRAS*, 419, 1537
 Calderone, G., Ghirlanda, G., Ghisellini, G., et al. 2015, *MNRAS*, 448, 403
 Cavallo, G., & Rees, M. J. 1978, *MNRAS*, 183, 359
 Cherubini, C., Giralico, A. J. A., Rueda, H., & Ruffini, R. 2009, *PhRvD*, 79, 124002
 Cipolletta, F., Cherubini, C., Filippi, S., Rueda, J. A., & Ruffini, R. 2015, *PhRvD*, 92, 023007
 Curran, P. A., Starling, R. L. C., O'Brien, P. T., et al. 2008, *A&A*, 487, 533
 Dai, Z. G., Wang, X. Y., Wu, X. F., & Zhang, B. 2006, *Sci*, 311, 1127
 Damour, T., & Ruffini, R. 1975, *PhRvL*, 35, 463
 Della Valle, M. 2011, *IJMPD*, 20, 1745
 De Pasquale, M., Schady, P., Kuin, N. P. M., et al. 2010, *ApJL*, 709, L146
 Dezalay, J.-P., Barat, C., Talon, R., et al. 1992, in *Gamma-ray bursts*, Proc. of the Workshop, AIP Conf. Ser. 265, ed. W. S. Paciesas & G. J. Fishman (Melville, NY: AIP), 304
 Eichler, D., Livio, M., Piran, T., & Schramm, D. N. 1989, *Natur*, 340, 126
 Enderli, M., Bianco, C. L., Izzo, L., et al. 2014, in *Proceedings of Swift: 10 Years of Discovery (SWIFT 10)* (Trieste: SISSA) (pos.sissa.it/archive/conferences/233/073/SWIFT%2010_073.pdf)
 Endrizzi, A., Ciolfi, R., Giacomazzo, B., Kastaun, W., & Kawamura, T. 2016, arXiv:1604.03445
 Fong, W., Berger, E., & Fox, D. B. 2010, *ApJ*, 708, 9
 Fruchter, A. S., Levan, A. J., Strolger, L., et al. 2006, *Natur*, 441, 463
 Fryer, C. L., Rueda, J. A., & Ruffini, R. 2014, *ApJL*, 793, L36
 Gehrels, N., Ramirez-Ruiz, E., & Fox, D. B. 2009, *ARA&A*, 47, 567
 Giacconi, R., & Ruffini, R. (ed.) 1978, *Physics and Astrophysics of Neutron Stars and Black Holes* (Amsterdam: North Holland Publishing Company), 907
 Giuliani, A., Fuschino, F., Vianello, G., et al. 2010, *ApJL*, 708, L84
 Golenetskii, S., Aptekar, R., Mazets, E., et al. 2009, *GCN*, 9344, 1
 Goodman, J. 1986, *ApJL*, 308, L47
 Guirrec, S., Connaughton, V., & Briggs, M. 2009, *GCN*, 9336, 1
 Hansen, B. M. S., & Lyutikov, M. 2001, *MNRAS*, 322, 695
 Heise, J. 2003, in *AIP Conf. Ser. 662, Gamma-Ray Burst and Afterglow Astronomy 2001: A Workshop Celebrating the First Year of the HETE Mission*, ed. G. R. Ricker & R. K. Vanderspek (Melville, NY: AIP), 229
 Hoversten, E. A., Barthelmy, S. D., Burrows, D. N., et al. 2009, *GCN*, 9331, 1
 Izzo, L., Ruffini, R., Penacchioni, A. V., et al. 2012, *A&A*, 543, A10
 Klebesadel, R. W. 1992, in *Gamma-Ray Bursts—Observations, Analyses and Theories*, ed. C. Ho, R. I. Epstein, & E. E. Fenimore (Cambridge: Cambridge Univ. Press)
 Kobayashi, S., Piran, T., & Sari, R. 1997, *ApJ*, 490, 92
 Kopač, D., D'Avanzo, P., Melandri, A., et al. 2012, *MNRAS*, 424, 2392
 Kouveliotou, C., Meegan, C. A., Fishman, G. J., et al. 1993, *ApJL*, 413, L101
 Kumar, P., & Zhang, B. 2015, *PhR*, 561, 1
 Landau, L. D., & Lifshitz, E. M. 2003, *The Classical Theory of Fields* (Oxford: Butterworth-Heinemann) IV rev. Engl. ed.
 Lazzati, D. 2005, *MNRAS*, 357, 722
 Lee, W. H., Ramirez-Ruiz, E., & Page, D. 2004, *ApJL*, 608, L5
 Lithwick, Y., & Sari, R. 2001, *ApJ*, 555, 540
 Longo, F., Moretti, E., Barbiellini, G., et al. 2009, *GCN*, 9343, 1
 Lü, H.-J., & Zhang, B. 2014, *ApJ*, 785, 74
 Mazets, E. P., Golenetskii, S. V., Ilinskii, V. N., et al. 1981, *Ap&SS*, 80, 3

- Meegan, C., Lichti, G., Bhat, P. N., et al. 2009, *ApJ*, **702**, 791
- Meszáros, P., & Rees, M. J. 1997, *ApJL*, **482**, L29
- Metzger, B. D., Giannios, D., Thompson, T. A., Bucciantini, N., & Quataert, E. 2011, *MNRAS*, **413**, 2031
- Mirabel, I. F., Chaty, S., Rodríguez, L. F., & Sauvage, M. M. 2015, in IAU Symp. 313, Extragalactic Jets from Every Angle (Paris: IAU), 370
- Muccino, M., Ruffini, R., Bianco, C. L., Izzo, L., & Penacchioni, A. V. 2013a, *ApJ*, **763**, 125
- Muccino, M., Ruffini, R., Bianco, C. L., et al. 2013b, *ApJ*, **772**, 62
- Nakar, E. 2007, *PhR*, **442**, 166
- Narayan, R., Paczynski, B., & Piran, T. 1992, *ApJL*, **395**, L83
- Narayan, R., Piran, T., & Shemi, A. 1991, *ApJL*, **379**, L17
- Nava, L., Vianello, G., Omodei, N., et al. 2014, *MNRAS*, **443**, 3578
- Ohmori, N., Noda, K., Sonoda, E., et al. 2009, GCN, **9355**, 1
- Ohno, M., & Pelassa, V. 2009, GCN, **9334**, 1
- Oliveira, F. G., Rueda, J. A., & Ruffini, R. 2014, *ApJ*, **787**, 150
- Olofsson, G., Ergon, M., Malesani, D., et al. 2009, GCN, **9338**, 1
- Omodei, N., Granot, J., Meszaros, P., et al. 2009, GCN, **9350**, 1
- Paczynski, B. 1986, *ApJL*, **308**, L43
- Patricelli, B., Bernardini, M. G., Bianco, C. L., et al. 2012, *ApJ*, **756**, 16
- Penacchioni, A. V., Ruffini, R., Izzo, L., et al. 2012, *A&A*, **538**, A58
- Perley, D. A., Cenko, S. B., Corsi, A., et al. 2014, *ApJ*, **781**, 37
- Piran, T. 2005, *RvMP*, **76**, 1143
- Pisani, G. B., Izzo, L., Ruffini, R., et al. 2013, *A&A*, **552**, L5
- Popham, R., Woosley, S. E., & Fryer, C. 1999, *ApJ*, **518**, 356
- Rau, A., McBreen, S., & Kruehler, T. 2009, GCN, **9353**, 1
- Rees, M. J., & Meszaros, P. 1992, *MNRAS*, **258**, 41
- Rhoades, C. E., & Ruffini, R. 1974, *PhRvL*, **32**, 324
- Rosswog, S., Ramirez-Ruiz, E., & Davies, M. B. 2003, *MNRAS*, **345**, 1077
- Rotondo, M., Rueda, J. A., Ruffini, R., & Xue, S.-S. 2011a, *PhLB*, **701**, 667
- Rotondo, M., Rueda, J. A., Ruffini, R., & Xue, S.-S. 2011b, *PhRvC*, **83**, 045805
- Rueda, J. A., & Ruffini, R. 2012, *ApJ*, **758**, L7
- Rueda, J. A., & Ruffini, R. 2013, *IJMPD*, **22**, 1360007
- Rueda, J. A., Ruffini, R., Wu, Y.-B., & Xue, S.-S. 2014, *PhRvC*, **89**, 035804
- Rueda, J. A., Ruffini, R., & Xue, S.-S. 2011, *NuPhA*, **872**, 286
- Ruffini, R. 2009, in *The Ergosphere and Dyadosphere of Black Holes*, ed. D. L. Wiltshire, M. Visser, & S. Scott (Cambridge: Cambridge Univ. Press), 161
- Ruffini, R. 2015, in *Thirteenth Marcel Grossmann Meeting: On Recent Developments in Theoretical and Experimental General Relativity, Astrophysics and Relativistic Field Theories*, Proc. of the MG13 Meeting on General Relativity, ed. K. Rosquist (Singapore: World Scientific Publishing), 242
- Ruffini, R., Bernardini, M. G., Bianco, C. L., et al. 2007, in *The Obscured Universe*, Proc. of the VI INTEGRAL Workshop, ESA SP-622, ed. S. Grebenev, R. Sunyaev, & C. Winkler (Noordwijk: ESA Publication Division), 561
- Ruffini, R., Bianco, C. L., Enderli, M., et al. 2015a, GCN, **18296**, 1
- Ruffini, R., Bianco, C. L., Frascchetti, F., Xue, S.-S., & Chardonnet, P. 2001a, *ApJL*, **555**, L107
- Ruffini, R., Bianco, C. L., Frascchetti, F., Xue, S.-S., & Chardonnet, P. 2001b, *ApJL*, **555**, L113
- Ruffini, R., Bianco, C. L., Frascchetti, F., Xue, S.-S., & Chardonnet, P. 2001c, *ApJL*, **555**, L117
- Ruffini, R., Muccino, M., Bianco, C. L., et al. 2014, *A&A*, **565**, L10
- Ruffini, R., Muccino, M., Kovacevic, M., et al. 2015b, *ApJ*, **808**, 190
- Ruffini, R., Rueda, J. A., Muccino, M., et al. 2016, arXiv:1602.02732
- Ruffini, R., Salmonson, J. D., Wilson, J. R., & Xue, S. 2000, *A&A*, **359**, 855
- Ruffini, R., Salmonson, J. D., Wilson, J. R., & Xue, S.-S. 1999, *A&A*, **350**, 334
- Ruffini, R., Wang, Y., Enderli, M., et al. 2015c, *ApJ*, **798**, 10
- Ruffini, R., & Wilson, J. 1973, *PhRvL*, **31**, 1362
- Ruffini, R., & Wilson, J. R. 1975, *PhRvD*, **12**, 2959
- Ruffini, R., & Wheeler, J. A. 1969, in *Significance of Space Research for Fundamental Physics*, Proc. of the ESRO Collaboration, ed. A. F. Moore & V. Hardy (Paris: European Space Research Organization), 45
- Ruiz, M., Lang, R. N., Paschalidis, V., & Shapiro, S. L. 2016, *ApJL*, **824**, L6
- Sahu, K. C., Livio, M., Petro, L., et al. 1997, *Natur*, **387**, 476
- Salmonson, J. D., & Wilson, J. R. 2002, *ApJ*, **578**, 310
- Smith, N. 2014, *ARA&A*, **52**, 487
- Smith, N., Li, W., Filippenko, A. V., & Chornock, R. 2011, *MNRAS*, **412**, 1522
- Soderberg, A. M., Berger, E., Kasliwal, M., et al. 2006a, *ApJ*, **650**, 261
- Soderberg, A. M., Kulkarni, S. R., Nakar, E., et al. 2006b, *Natur*, **442**, 1014
- Strong, I. B., Klebesadel, R. W., & Evans, W. D. 1975, in *Annals of the New York Academy of Sciences 262, Seventh Texas Symp. on Relativistic Astrophysics*, ed. P. G. Bergman, E. J. Fenyves, & L. Motz (New York: New York Academy of Sciences), 145
- Svensson, K. M., Levan, A. J., Tanvir, N. R., Fruchter, A. S., & Strolger, L.-G. 2010, *MNRAS*, **405**, 57
- Tavani, M. 1998, *ApJL*, **497**, L21
- Troja, E., King, A. R., O'Brien, P. T., Lyons, N., & Cusumano, G. 2008, *MNRAS*, **385**, L10
- Tsang, D., Read, J. S., Hinderer, T., Piro, A. L., & Bondarescu, R. 2012, *PhRvL*, **108**, 011102
- van Paradijs, J., Groot, P. J., Galama, T., et al. 1997, *Natur*, **386**, 686
- Woosley, S. E. 1993, *ApJ*, **405**, 273
- Woosley, S. E., & Bloom, J. S. 2006, *ARA&A*, **44**, 507
- Zalamea, I., & Beloborodov, A. M. 2011, *MNRAS*, **410**, 2302
- Zel'dovich, Y. B., Ivanova, L. N., & Nadezhin, D. K. 1972, *SvA*, **16**, 209
- Zhang, B., & Mészáros, P. 2001, *ApJL*, **552**, L35
- Zhang, C. M., Wang, J., Zhao, Y. H., et al. 2011, *A&A*, **527**, A83
- Zhang, F.-W., Shao, L., Yan, J.-Z., & Wei, D.-M. 2012, *ApJ*, **750**, 88
- Zou, Y.-C., Fan, Y.-Z., & Piran, T. 2011, *ApJL*, **726**, L2

On the nature of some SGRs and AXPs as rotation-powered neutron stars

Jaziel G. Coelho^{1,2} *, D. L. Cáceres², R. C. R. de Lima^{3,4}, M. Malheiro⁵, J. A. Rueda^{2,3,6} **, and R. Ruffini^{2,3,6} ***

¹ Div. Astrofísica, Instituto Nacional de Pesquisas Espaciais, Av. dos Astronautas 1758, 12227–010 São José dos Campos, Brazil

² Dipartimento di Fisica and ICRA, Sapienza Università di Roma, P.le Aldo Moro 5, I–00185 Rome, Italy

³ ICRA Net, P.zza della Repubblica 10, I–65122 Pescara, Italy

⁴ Universidade do Estado de Santa Catarina, Av. Madre Benvenuta, 2007 Itacorubi, 88.035–901, Florianópolis, Brazil

⁵ Instituto Tecnológico de Aeronáutica, Praça Marechal Eduardo Gomes, 50 Vila das Acácias, 12228–900 São José dos Campos, Brazil

⁶ ICRA Net-Rio, Centro Brasileiro de Pesquisas Físicas, Rua Dr. Xavier Sigaud 150, 2290–180 Rio de Janeiro, Brazil

Accepted XXX. Received YYY; in original form ZZZ

ABSTRACT

Context. Soft gamma repeaters (SGRs) and anomalous X-ray pulsars (AXPs) are slow rotating isolated pulsars whose energy reservoir is still matter of debate. Adopting neutron star (NS) fiducial parameters; mass $M = 1.4M_{\odot}$, radius $R = 10$ km, and moment of inertia, $I = 10^{45}$ g cm², the rotational energy loss, \dot{E}_{rot} , is lower than the observed luminosity (dominated by the X-rays) L_X for many of the sources.

Aims. We investigate the possibility that some members of this family could be canonical rotation-powered pulsars using realistic NS structure parameters instead of fiducial values.

Methods. We compute the NS mass, radius, moment of inertia and angular momentum from numerical integration of the axisymmetric general relativistic equations of equilibrium. We then compute the entire range of allowed values of the rotational energy loss, \dot{E}_{rot} , for the observed values of rotation period P and spin-down rate \dot{P} . We also estimate the surface magnetic field using a general relativistic model of a rotating magnetic dipole.

Results. We show that realistic NS parameters lowers the estimated value of the magnetic field and radiation efficiency, L_X/\dot{E}_{rot} , with respect to estimates based on fiducial NS parameters. We show that nine SGRs/AXPs can be described as canonical pulsars driven by the NS rotational energy, for L_X computed in the soft (2–10 keV) X-ray band. We compute the range of NS masses for which $L_X/\dot{E}_{\text{rot}} < 1$. We discuss the observed hard X-ray emission in three sources of the group of nine potentially rotation-powered NSs. This additional hard X-ray component dominates over the soft one leading to $L_X/\dot{E}_{\text{rot}} > 1$ in two of them.

Conclusions. We show that 9 SGRs/AXPs can be rotation-powered NSs if we analyze their X-ray luminosity in the soft 2–10 keV band. Interestingly, four of them show radio emission and six have been associated with supernova remnants (including Swift J1834.9–0846 the first SGR observed with a surrounding wind nebula). These observations give additional support to our results of a natural explanation of these sources in terms of ordinary pulsars. Including the hard X-ray emission observed in three sources of the group of potential rotation-powered NSs, this number of sources with $L_X/\dot{E}_{\text{rot}} < 1$ becomes seven. It remains open to verification 1) the accuracy of the estimated distances and 2) the possible contribution of the associated supernova remnants to the hard X-ray emission.

Key words. pulsars: general – stars: neutron – stars: rotation – stars: magnetic field

1. Introduction

SGRs and AXPs constitute a class of pulsars with the following main properties (Mereghetti 2008): rotation periods $P \sim (2-12)$ s, slowing down rates $\dot{P} \sim (10^{-15} - 10^{-10})$ s/s, persistent X-ray luminosity as large as 10^{35} erg s⁻¹ and transient activity in the form of outbursts of energies around $(10^{41}-10^{43})$ erg. Giant flares of even larger energies, $(10^{44}-10^{47})$ erg, up to now only observed in SGRs.

A spinning down NS loses rotational energy at a rate given by

$$\dot{E}_{\text{rot}} = -4\pi^2 I \frac{\dot{P}}{P^3} \quad (1)$$

which, adopting fiducial moment of inertia $I = 10^{45}$ g cm², becomes

$$\dot{E}_{\text{rot}}^{\text{fid}} = -3.95 \times 10^{46} \frac{\dot{P}}{P^3} \text{ erg s}^{-1}. \quad (2)$$

Correspondingly to the fiducial moment of inertia, usual fiducial values for the mass and radius of a NS adopted in the literature are, respectively, $M = 1.4M_{\odot}$ and radius $R = 10$ km. For the observed values of P and \dot{P} , Eq. (2) leads to values lower than the observed X-ray luminosity from SGR/AXPs (i.e. $\dot{E}_{\text{rot}}^{\text{fid}} < L_X$). This is in contrast with traditional rotation-powered pulsars which show $\dot{E}_{\text{rot}} > L_X^{\text{obs}}$.

The apparent failure of the traditional energy reservoir of pulsars in SGR/AXPs has led to different scenarios for the explanation of SGRs and AXPs, e.g.: magnetars (Duncan & Thompson 1992; Thompson & Duncan 1995); drift waves near the light-cylinder of NSs (see Malov 2010, and references therein); fallback accretion onto NSs (Trümper et al. 2013); accretion

* jaziel.coelho@inpe.br

** jorge.rueda@icra.it

*** ruffini@icra.it

onto exotic compact stars such as quark stars (Xu et al. 2006); the quark-nova remnant model (Ouyed et al. 2011); and massive, fast rotating, highly magnetized WDs (Malheiro et al. 2012; Boshkayev et al. 2013; Rueda et al. 2013; Coelho & Malheiro 2014)

None of the above scenarios appears to be ruled out by the current observational data, thus further scrutiny of the nature and the possible energy reservoir of SGRs and AXPs deserves still attention.

Following the above reasoning, we aim to revisit in this work the possibility that some SGR/AXPs could be rotation-powered NSs, but now exploring the entire range of NS parameters allowed by the conditions of stability of the star, and not only on the use of fiducial parameters. We have already examined this possibility in Malheiro et al. (2012); Coelho & Malheiro (2013, 2014, 2015); Lobato et al. (2016) and have found at the time four sources (1E 1547.0–5408, SGR 1627–41, PSR J1622–4950, and XTE J1810–197) of the SGR/AXPs catalog explainable as rotation-powered NSs (see, also, Rea et al. 2012). We show in this article that this conclusion can be indeed extended to other seven sources. For the total eleven objects we report the range of masses where the rotation-power condition $\dot{E}_{\text{rot}} > L_X$ is satisfied.

Once identified as rotation-powered NSs, one is led to the theoretical prediction that some of the phenomena observed in ordinary pulsars could also be observed in SGRs and AXPs. Indeed, we found that for the above 11 SGRs/AXPs describable as rotation-powered NSs:

- The energetics of their observed outbursts can be explained from the gain of rotational energy during an accompanied glitch. Such a glitch-outburst connection is not expected in a source not driven by rotational energy.
- The radio emission, a property common in pulsars but generally absent in SGRs and AXPs, is observed in four of these objects (see, e.g., Halpern et al. 2005; Camilo et al. 2006; Helfand et al. 2006; Camilo et al. 2007a,b; Levin et al. 2010, 2012; Eatough et al. 2013).
- Six sources have possible associations with supernova remnants (SNRs), including Swift J1834.9-0846 the first SGR for which a pulsar wind nebula has been observed (Younes et al. 2016).

We also analyze the observed hard X-ray emission in the 20–150 keV band in 5 of the above 11 sources. As we shall discuss, this emission dominates over the soft X-rays leading to $L_X/\dot{E}_{\text{rot}} > 1$ in 4 of them. With this, the number of potential rotation-powered sources becomes seven. However, this conclusion remains open for further verification since it critically depends 1) on the accuracy of the estimated distances to the sources and 2) on the possible contribution of the supernova remnants present in the hard X-ray component.

This article is organized as follows. We first compute in section 2 the structure properties of NSs, and then in section 3 we estimate the surface magnetic field using both realistic structure parameters and a general relativistic model of a rotating magnetic dipole. We compute in section 4 the ratio L_X/\dot{E}_{rot} for all the SGRs/AXPs for the entire range of possible NS masses. We also show in section 5 an analysis of the glitch/outburst connection in the nine aforementioned sources. Finally, in Section 6, we summarize the main conclusions and remarks.

2. Neutron star structure

In order to compute the rotational energy loss of a NS as a function of its structure parameters, e.g. mass and radius, we need

Table 1. Meson masses and coupling constants in the parameterizations NL3, TM1, and GM1

	NL3	TM1	GM1
$M(\text{MeV})$	939.00	938.00	938.93
$m_\sigma(\text{MeV})$	508.194	511.198	512.000
$m_\omega(\text{MeV})$	782.501	783.000	783.000
$m_\rho(\text{MeV})$	763.000	770.000	770.000
g_σ	10.2170	10.0289	8.9073
g_ω	12.8680	12.6139	10.6089
g_ρ	4.4740	7.2325	4.0972

to construct the equilibrium configurations of a uniformly rotating NS in the range of the observed periods. We have shown in Rotondo et al. (2011); Rueda et al. (2011); Belvedere et al. (2012, 2014) that, in the case of both static and rotating NSs, the Tolman-Oppenheimer-Volkoff (TOV) system of equations (Oppenheimer & Volkoff 1939; Tolman 1939) is superseded by the Einstein-Maxwell system of equations coupled to the general relativistic Thomas-Fermi equations of equilibrium, giving rise to what we have called the Einstein-Maxwell-Thomas-Fermi (EMTF) equations. In the TOV-like approach, the condition of local charge neutrality is applied to each point of the configuration, while in the EMTF equations the condition of global charge neutrality is imposed. The EMTF equations account for the weak, strong, gravitational and electromagnetic interactions within the framework of general relativity and relativistic nuclear mean field theory. In this work we shall use both global (EMTF) and local (TOV) charge neutrality to compare and contrast their results.

2.1. Nuclear EOS

The NS interior is made up of a core and a crust. The core of the star has densities higher than the nuclear one, $\rho_{\text{nuc}} \approx 3 \times 10^{14} \text{ g cm}^{-3}$, and it is composed of a degenerate gas of baryons (e.g. neutrons, protons, hyperons) and leptons (e.g. electrons and muons). The crust, in its outer region ($\rho \leq \rho_{\text{drip}} \approx 4.3 \times 10^{11} \text{ g cm}^{-3}$), is composed of ions and electrons, and in the inner crust ($\rho_{\text{drip}} < \rho < \rho_{\text{nuc}}$), there are also free neutrons that drip out from the nuclei. For the crust, we adopt the Baym-Pethick-Sutherland (BPS) EOS (Baym et al. 1971b), which is based on the Baym et al. (1971a) work. For the core, we adopt relativistic mean-field (RMF) theory models. We use an extension of the Boguta & Bodmer (1977) formulation with a massive scalar meson (σ) and two vector mesons (ω and ρ) mediators, and possible interactions amongst them. We adopt in this work three sets of parameterizations of these models (see table 1 and figure 1): the NL3 (Lalazissis et al. 1997), TM1 (Sugahara & Toki 1994), and GM1 (Glendenning & Moszkowski 1991) EOS.

2.2. Mass-Radius Relation and Moment of Inertia

For the rotational periods as the ones observed in SGR/AXPs ($P \sim 2\text{--}12 \text{ s}$), the structure of the rotating NS can be accurately described by small rotation perturbations from the spherically symmetric configuration (see, e.g., Belvedere et al. 2014, 2015), using the Hartle’s formalism (Hartle 1967). Following this method we compute rotating configurations, accurate up to second-order in Ω , with the same central density as the seed static non-rotating configurations. The mass-radius relation for non-rotating configurations in the cases of global and local

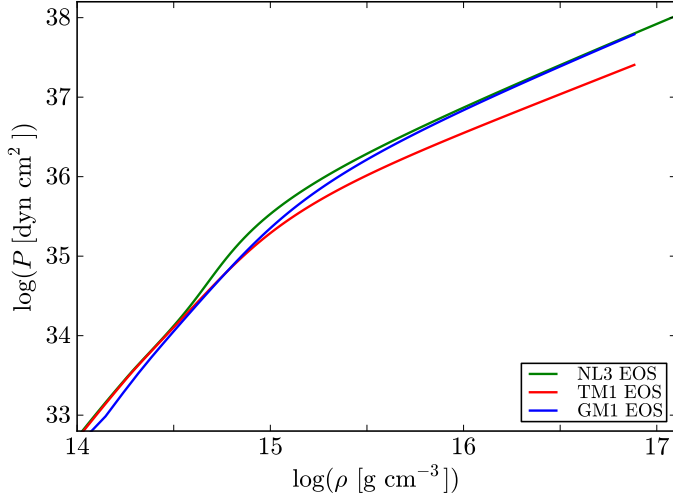


Fig. 1. NL3, TM1, and GM1 EOS behavior at sub and supranuclear densities.

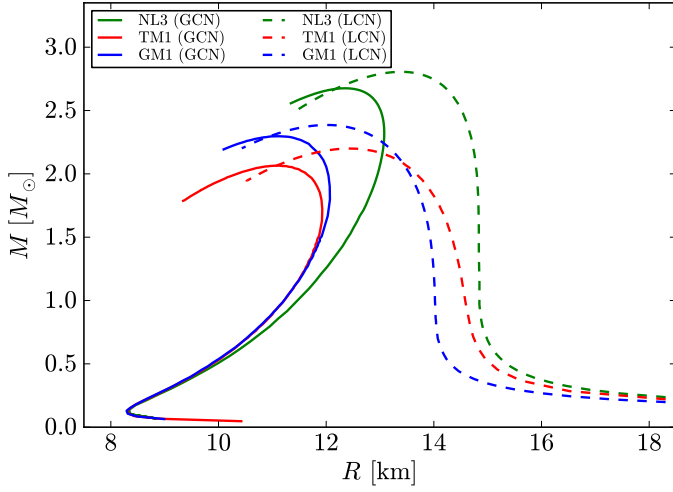


Fig. 2. Mass-Radius relation for the NL3, TM1, and GM1 EOS in the cases of global (solid curves) and local (dashed curves) charge neutrality.

charge neutrality are shown in Fig. 2. For the rotation periods of interest here, the mass-equatorial radius relation of the uniformly rotating NSs practically overlaps the one given by the static sequence (see Fig. 1 in Belvedere et al. 2015). Thus, we take here advantage of this result and consider hereafter, as masses and corresponding radii, the values of the non-rotating NSs.

The moment of inertia is given by

$$I = \frac{J}{\Omega}, \quad (3)$$

where Ω is the angular velocity and J is the angular momentum given by

$$J = \frac{1}{6} R^4 \left(\frac{d\bar{\omega}}{dr} \right)_{r=R}. \quad (4)$$

Here R is the radius of the non-rotating star with the same central density as the rotating one, $\bar{\omega} = \Omega - \omega(r)$ is the angular velocity of the fluid relative to the local inertial frame, and ω is the angular velocity of the local frame. The angular velocity Ω is related to the angular momentum J by

$$\Omega = \bar{\omega}(R) + \frac{2J}{R^3}. \quad (5)$$

Fig. 3 shows the behavior of the moment of inertia as a function of the mass of the NS for the three EOS NL3, TM1 and GM1 and both in the case of global and local charge neutrality. Although in general there is a dependence of all the structure parameters on the nuclear EOS, we use below, without loss of generality and for the sake of exemplification, only the GM1 EOS. Similar qualitatively and quantitatively results are obtained for the other EOSs. It is worth mentioning that the chosen EOS lead to a maximum stable mass larger than $2 M_{\odot}$, the heaviest NS mass measured (Demorest et al. 2010; Antoniadis et al. 2013).

3. Surface Magnetic Field

Since the range of P for SGRs and AXPs is similar to the one concerning the high-magnetic field pulsar class, we can directly apply the results of Belvedere et al. (2015), applying only the most relevant correction for this range of periods to estimate the surface magnetic field, namely the finite-size correction. The exact solution of the radiation power of a (slowly) rotating, magnetic dipole, which duly generalizes the classic solution by Deutsch (1955), is given by (see Rezzolla & Ahmedov 2004, and references therein)

$$P_{\text{dip}}^{\text{GR}} = -\frac{2}{3} \frac{\mu_{\perp}^2 \Omega^4}{c^3} \left(\frac{f}{N^2} \right)^2, \quad (6)$$

where $\mu_{\perp} = \mu \sin \chi$, is the component of the magnetic dipole moment perpendicular to the rotation axis, $\mu = BR^3$ with B the surface magnetic field at the star's equator, χ is the inclination angle between the magnetic dipole and rotation axis, and f and N are the general relativistic corrections

$$f = -\frac{3}{8} \left(\frac{R}{M} \right)^3 \left[\ln(N^2) + \frac{2M}{R} \left(1 + \frac{M}{R} \right) \right], \quad (7)$$

$$N = \sqrt{1 - \frac{2M}{R}}, \quad (8)$$

with M the mass of the non-rotating configuration. Now, equating the rotational energy loss, Eq. (1) to the above electromagnetic radiation power, Eq. (6), one obtains the formula to infer the surface magnetic field, given the rotation period and the spin-down rate:

$$B_{\text{GR}} = \frac{N^2}{f} \left(\frac{3c^3}{8\pi^2} \frac{I}{R^6} P\dot{P} \right)^{1/2}, \quad (9)$$

where we have introduced the subscript 'GR' to indicate explicitly the magnetic field inferred from the above general relativistic expression, and we have adopted for simplicity an inclination angle $\chi = \pi/2$.

Figs. 4 and 5 show our theoretical prediction for the surface magnetic fields of the SGR/AXPs as a function of the NS mass, using Eq. (9), for the GM1 EOS and for the global and local charge neutrality cases, respectively. We find that in both cases some of the sources have inferred magnetic fields lower than the critical value, B_c , for some range of NS masses. Clearly this set of sources includes SGR 0418+5729, Swift J1822.3-1606 and 3XMM J185246.6+003317, which are already known to show this feature even using fiducial NS parameters and the classic magnetic dipole model (see e.g., Olausen & Kaspi 2014). It is worth to note that Eq. (9) is derived for a rotating magnetic dipole in electrovacuum, thus neglecting the extra torque from the presence of magnetospheric plasma. The addition of this torque certainly leads to values of the magnetic field still lower

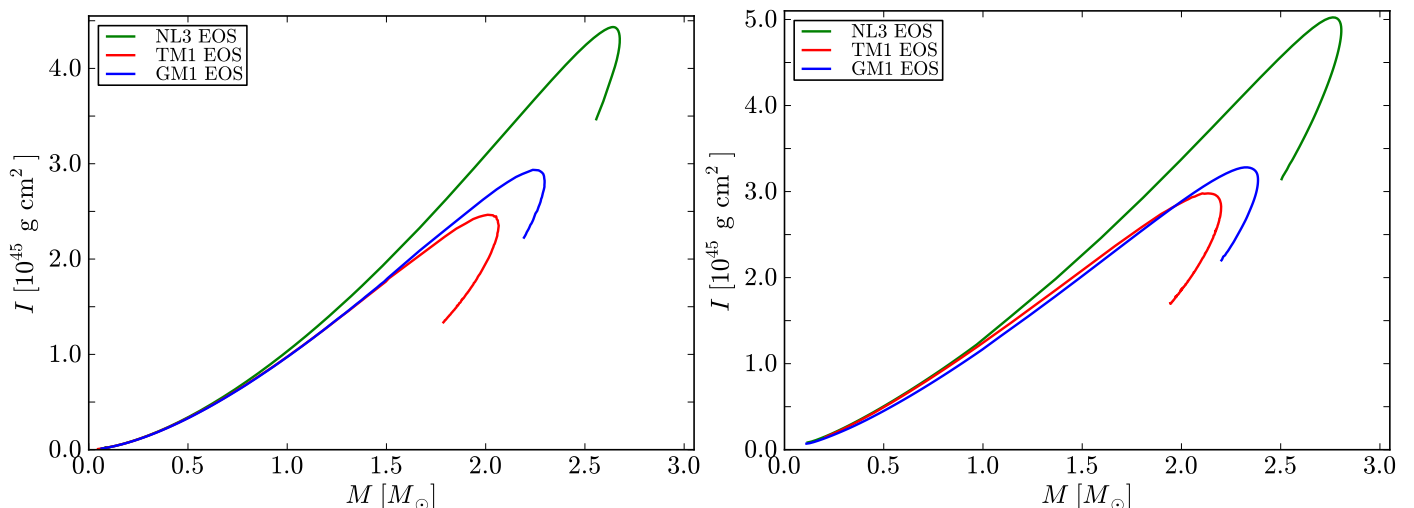


Fig. 3. Moment of inertia as a function of the NS mass for the NL3, TM1, and GM1 EOS in the cases of global (left panel) and local (right panel) charge neutrality.

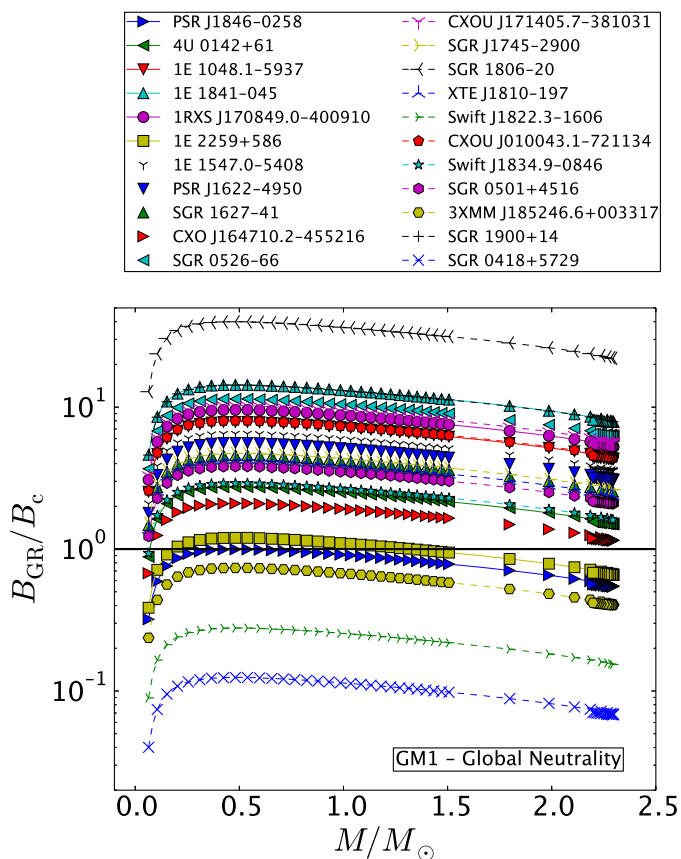


Fig. 4. (Color online) Magnetic field B_{GR} given by equation (9), in units of $B_c = m_c^2 c^3 / (e \hbar) = 4.4 \times 10^{13} \text{ G}$, as function of the mass (in solar masses) in the global charge neutrality case.

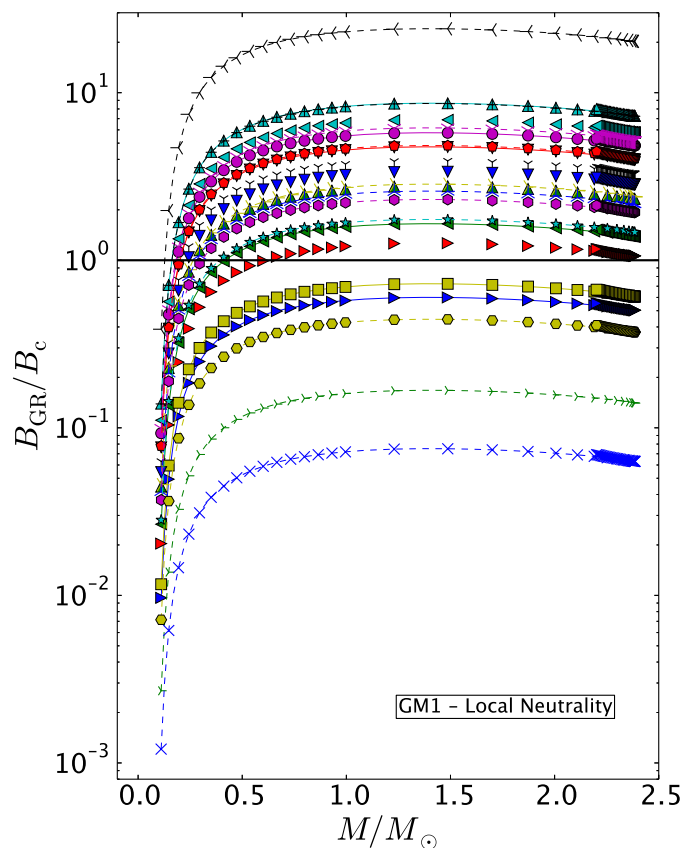


Fig. 5. (Color online) Magnetic field B_{GR} given by equation (9), in units of $B_c = m_c^2 c^3 / (e \hbar) = 4.4 \times 10^{13} \text{ G}$, as function of the mass (in solar masses) in the local charge neutrality case.

than the ones shown here. However, the inclusion of the torques from the magnetosphere is beyond the scope of this work and will be taken into account in future works.

4. SGRs and AXPs Efficiency

Another important quantity for the identification of the nature of the sources is the radiation efficiency, namely the ratio between

the observed luminosity and the rotational energy loss (1). It is clear from figure 3 that such a ratio is a function of the NS mass, via the moment of inertia. For SGR/AXPs the dominant emission is in X-rays, thus we analyze all the possible values of the ratio L_X/\dot{E}_{rot} in the entire parameter space of NSs. As we show below, some SGRs and AXPs allow a wide range of masses for which $L_X/\dot{E}_{\text{rot}} \lesssim 1$, implying a possible rotation-powered nature for those sources.

Figure 6 shows the X-ray luminosity to rotational energy loss ratio as a function of the NS mass, for both global and local charge neutrality configurations. We can see from these figures that nine out of the twenty three SGR/AXPs could have masses in which $L_X < \dot{E}_{\text{rot}}$, and therefore they could be explained as ordinary rotation-powered NSs. Such sources are: Swift J1834.9–0846, PSR J1846–0258, 1E 1547.0–5408, SGR J1745–2900, XTE J1810–197, PSR J1622–4950, SGR 1627–41, SGR 0501+4516, CXOU J171405.7381031 (see Table 2). In view of the proximity of some of the sources to the line $L_X/\dot{E}_{\text{rot}} = 1$ (e.g., SGR 1900+14, SGR 0418+5729, and Swift J1822.3–1606), and the currently poorly constrained determination of the distance to the sources, there is still the possibility of having additional sources as rotation powered NSs.

In this line, two sources are particularly interesting, namely SGR 1900+14 and SGR 1806–20, which appear very close (but above) to the limit of becoming rotation-powered NSs. The soft X-rays spectra of SGRs and AXPs are usually well fitted by a blackbody + power-law spectral model (see e.g., Mereghetti 2008). The blackbody temperature is usually of the order $k_B T \sim 0.5$ keV and surface radii of the emitting region are ~ 1 km. In the case of a NS, one could interpret such a thermal component as due to the surface temperature of the NS, namely associated with the thermal reservoir of the star. The power-law component has instead a non-thermal nature and must be due to magnetospheric processes which are connected with the rotational energy reservoir in a rotation-powered star. Within this interpretation, the request that the rotational energy loss pays also for the contribution of the thermal component of the luminosity is unnecessarily rigorous. Thus, the above ratio L_X/\dot{E}_{rot} becomes an upper limit to the actual efficiency for the conversion of rotational into electromagnetic energy. We can now apply this interpretation, for the sake of example, to the above two sources.

SGR 1900+14: the blackbody component of the spectrum is characterized by $k_B T_{\text{BB}} = 0.47$ keV, and a surface radius of $R_{\text{BB}} = 4.0$ km, assuming a distance of 15 kpc (Mereghetti et al. 2006). The total (blackbody + power-law) flux in the 2–10 keV energy band is $F_X = 4.8 \times 10^{-12}$ erg cm $^{-2}$ s $^{-1}$. With the above data, we infer that the blackbody and the power-law components contribute respectively 28% and 72% to the total flux. Namely, we have $F_X^{\text{BB}} = 0.28F_X$ and $F_X^{\text{PL}} = 0.72F_X$. This leads to $L_X^{\text{PL}} = 9.3 \times 10^{34}$ erg s $^{-1}$.

SGR 1806–20: in this case we have $k_B T_{\text{BB}} = 0.55$ keV and $R_{\text{BB}} = 3.7$ km, assuming a distance of 15 kpc (Esposito et al. 2007). For this source $F_X = 1.8 \times 10^{-11}$ erg cm $^{-2}$ s $^{-1}$, and we infer $F_X^{\text{BB}} = 0.16F_X$ and $F_X^{\text{PL}} = 0.84F_X$. This leads to $L_X^{\text{PL}} = 4.1 \times 10^{35}$ erg s $^{-1}$. If we use instead the revised distance of 8.7 kpc (Bibby et al. 2008), we have $L_X^{\text{PL}} = 1.4 \times 10^{35}$ erg s $^{-1}$.

Figure 7 shows the ratio $L_X^{\text{PL}}/\dot{E}_{\text{rot}}$ as a function of the NS mass in the case of SGR 1900+14 and SGR 1806–20, adopting the GM1 EOS and assuming a distance of 15 kpc for both sources. It is clear from this analysis the importance of identifying the different contributions to the emission of the object. There is no doubt that the subtraction of the contribution from the thermal reservoir to the total flux in soft X-rays can be important for the correct identification of the nature of these sources: now there is a range of masses for which the luminosity to rotational energy loss ratio becomes lower than unity. Again, it is worth to recall that there are still additional effects which could improve the above analysis: (i) the distance to the sources are not known accurately; (ii) the spectrum could be equally well-fitted by a different spectral model such as a double blackbody which would have a different interpretation; (iii) the NS EOS is still un-

known and so the moment of inertia and radius for a given mass might be different. These effects might lead to a different value of the luminosity, and of the contributions of thermal and rotational energy reservoirs to it. Clearly, the above analysis can be extended to all the other SGRs and AXPs, and in the case of the nine sources already identified with $L_X/\dot{E}_{\text{rot}} < 1$, it will further diminish their radiation efficiency.

It is now appropriate to discuss the non-thermal hard X-ray emission (above 10 keV) in SGRs/AXPs which has been observed by some missions like *RXTE*, *INTEGRAL*, *Suzaku* and *NuSTAR*. First we discuss the observations of the above two sources which could in principle join the rotation-powered group. Adopting a distance of 15 kpc, SGR 1900+14 has an observed 20–100 keV band luminosity of $L_X^{\text{hard}} = 4 \times 10^{35}$ erg s $^{-1}$ (Götz et al. 2006). This implies $L_X^{\text{hard}} \approx 4.3L_X^{\text{PL}}$, so a total X-ray luminosity (hard + soft) $L_x = 5.3L_X^{\text{PL}} \approx 4.9 \times 10^{35}$ erg s $^{-1}$. SGR 1806–20 has a 20–100 keV band flux three times higher than the one of SGR 1900+14 (Götz et al. 2006), thus assuming also a distance of 15 kpc for this source we obtain $L_X^{\text{hard}} \approx 2.9L_X^{\text{PL}}$, so a total X-ray luminosity (hard + soft) $L_x = 3.9L_X^{\text{PL}} \approx 1.6 \times 10^{36}$ erg s $^{-1}$. This means that the points in Figure 7 would shift 5 and 4 times up respectively and therefore there will be no solution for these sources as rotation-powered, unless their distances are poorly constrained. In this line it is worth mentioning that the distance to these sources has been established via their possible association with star clusters (see Vrba et al. 2000; Corbel & Eikenberry 2004, for details).

From the set of nine potential rotation-powered sources, only three ones have persistent hard X-ray emission (see Table 2): SGR 0501+4516, 1E 1547.0–5408 and SGR J1745–2900. For these sources we can see the hard X-ray luminosity in the 20–150 keV band overcomes the soft X-ray contribution to the luminosity respectively by a factor 50, 149 and 527. Figure 8 shows the ratio $L_X^{\text{hard}}/\dot{E}_{\text{rot}}$ as a function of the NS mass in the case of SGR 0501+4516, 1E 1547.0–5408 and SGR J1745–2900. We can see that, after including the hard X-ray component in these three sources, 1E 1547.0–5408 stands still below the line $L_X/\dot{E}_{\text{rot}} = 1$, while the other two sources appear above it.

The existence of persistent hard X-ray emission provides new constraints on the emission models for SGRs/AXPs since, as in ordinary pulsars, the higher the energy band the higher the luminosity, namely their luminosities can be dominated by hard X-rays and/or gamma-rays. At the present, the mechanisms responsible for the hard energy emission is still poorly understood, what causes the hard X-ray tails is still an open issue. In this respect it is worth mentioning that, since these sources are also associated with supernova remnants (see Table 2 and Sec. 6), the emission in hard X and/or gamma-rays could be contaminated by the remnant emission. The disentanglement of the contributions of the remnant and the central pulsar to the total emission is an interesting issue to be explored, in addition to the confirmation of the estimated distances. If the above numbers will be confirmed, then the number of rotation-powered SGRs/AXPs becomes seven.

5. Glitches and bursts in SGRs/AXPs

We have shown in the last section that nine (and up to eleven) of the twenty three SGR/AXPs are potential rotation-powered NSs. Once the possible rotation-power nature of the source is established, one expects that also the transient phenomena observed in these sources could be powered by rotation. Based on that idea, we here discuss a possible glitch-outburst connection. Thus, it is

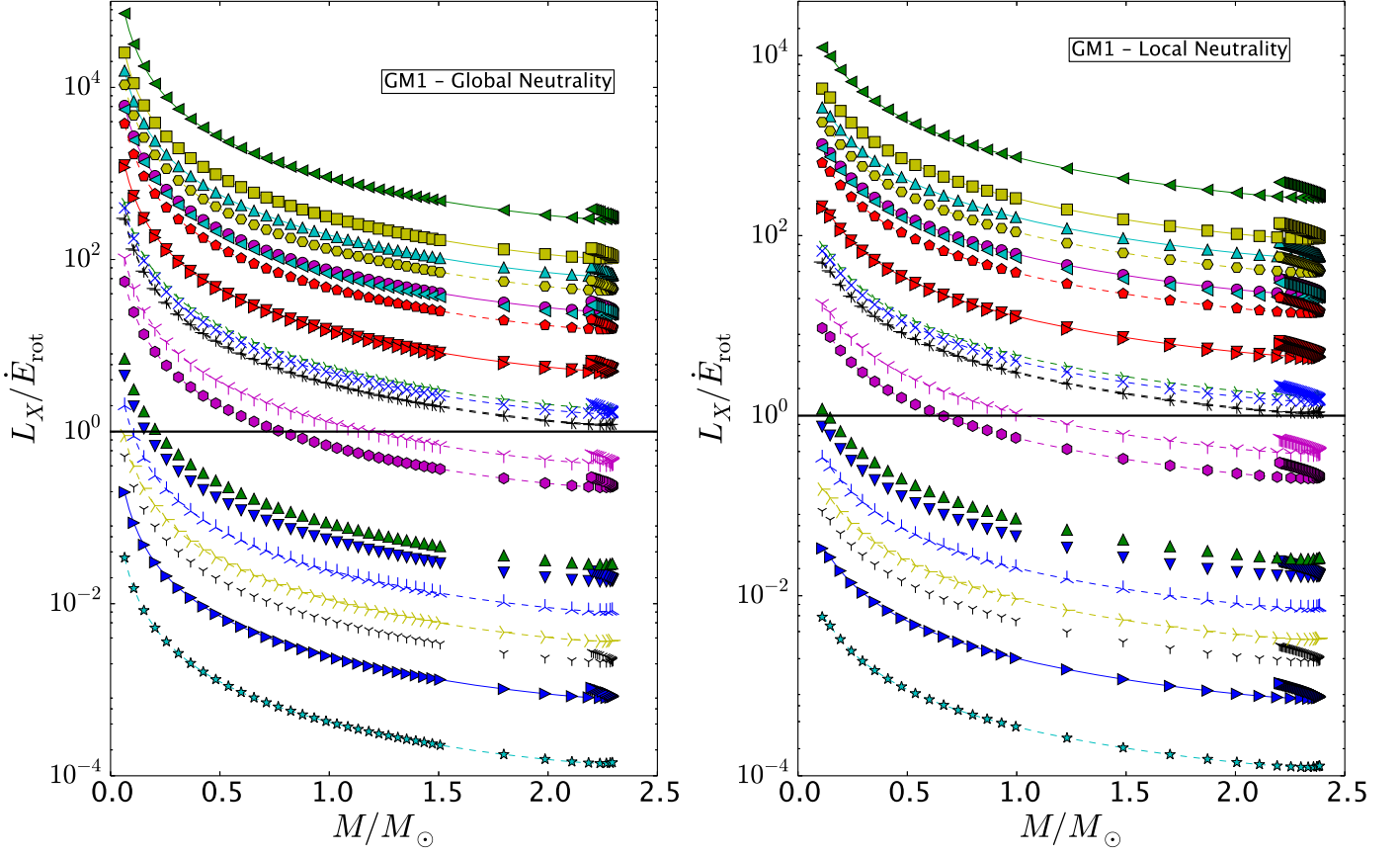


Fig. 6. (Color online) Radiation efficiency L_X/\dot{E}_{rot} as a function of the NS mass (in solar masses), for the global (left panel) and local (right panel) neutrality cases.

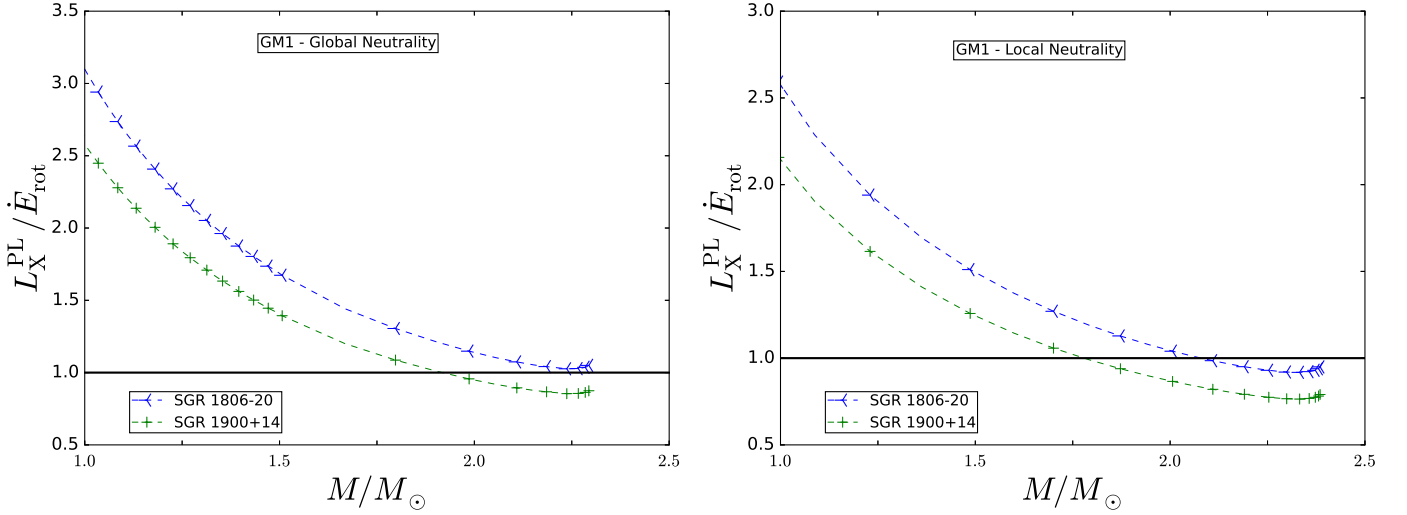


Fig. 7. (Color online) Radiation efficiency L_X/\dot{E}_{rot} as a function of the NS mass (in solar masses), for the global (left panel) and local (right panel) neutrality cases.

interesting to scrutinize the outburst data of SGR/AXPs, to seek for associated glitches, and check if the energetics of its bursting activity could be explained by the gain of rotational energy during an associated (observed or unobserved) glitch.

In a glitch, the release of the accumulated stress leads to a sudden decrease of the moment of inertia and, via angular momentum conservation,

$$J = I\Omega = (I + \Delta I)(\Omega + \Delta\Omega) = \text{constant}, \quad (10)$$

to a decrease of both the rotational period (spin-up) and the radius, i.e.

$$\frac{\Delta I}{I} = 2 \frac{\Delta R}{R} = \frac{\Delta P}{P} = -\frac{\Delta\Omega}{\Omega}. \quad (11)$$

The sudden spin-up leads to a gain of rotational energy

$$\Delta E_{\text{rot}} = -\frac{2\pi^2 I \Delta P}{P^2 P}, \quad (12)$$

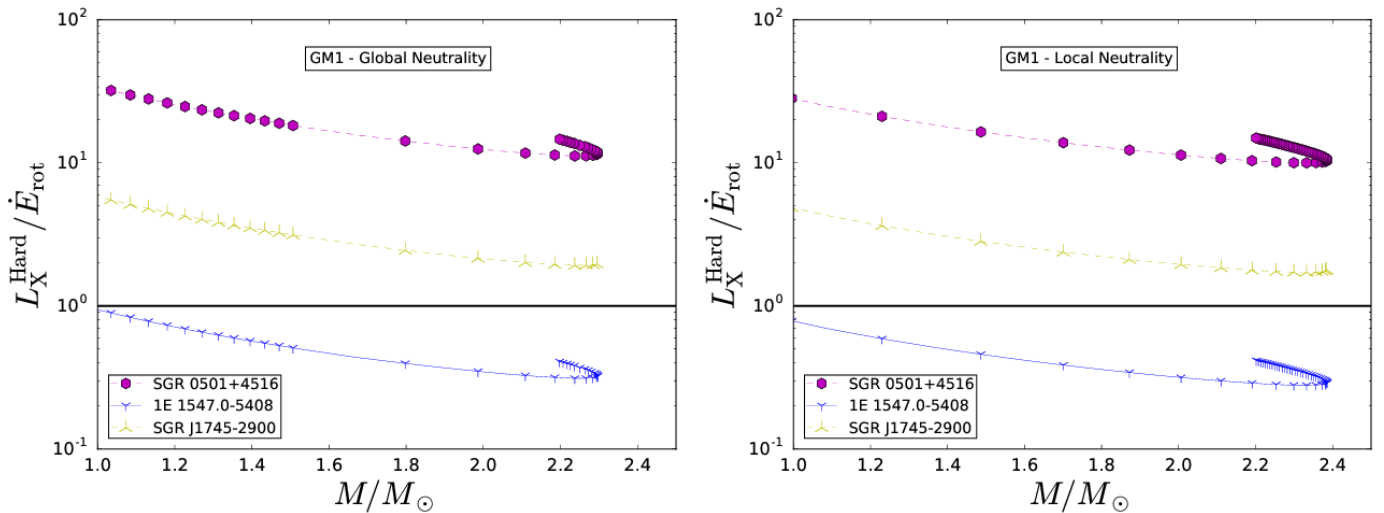


Fig. 8. (Color online) Radiation efficiency $L_X^{\text{Hard}}/\dot{E}_{\text{rot}}$ as a function of the NS mass (in solar masses), for the global (left panel) and local (right panel) neutrality cases.

Table 2. Some properties of nine SGRs/AXPs potential rotation-powered NSs. Column 1: source name. Column 2: rotation period P in units of seconds. Column 3: spin-down rate \dot{P} in units of 10^{-11} . Column 4: source distance in units of kpc. Column 5: X-ray luminosity in the 2–10 keV band in units of 10^{33} erg s $^{-1}$. Column 6: hard X-ray luminosity in the 20–150 keV band in units of 10^{33} erg s $^{-1}$. Column 7: radio luminosity per solid angle at the frequency $f_0 = 1.4$ GHz, i.e. $L_{\text{radio}} = S_{1.4}d^2$ in units of 10^{28} sr $^{-1}$ erg s $^{-1}$ where $S_{1.4}$ is the measured flux density at f_0 . In the case of SGR J1745-2900 we report the luminosity per beam at the frequency 41 GHz according to Yusef-Zadeh et al. (2015). In the columns 8–11 we report respectively if the source has reported association with SNR, observed glitches, outbursts, and if it is considered as a transient X-ray luminosity (in the sense explained in Sec. 6). Data have been taken from the McGill catalog (Olausen & Kaspi 2014; see <http://www.physics.mcgill.ca/pulsar/magnetar/main.html>).

Source	P (s)	\dot{P}	d (kpc)	L_X (10^{33} erg s $^{-1}$)	L_X^{hard} (10^{33} erg s $^{-1}$)	L_{radio} (10^{28} sr $^{-1}$ erg s $^{-1}$)	SNR Assoc.	Obs. Glitches	Burst	Transient
SGR 0501+4516	5.8	0.59	2	0.81	40.2	–	HB 9 (?)	No	Yes	Yes
1E 1547.0–5408	2.07	4.77	4.5	1.3	193.9	1.19	G327.24-0.13	Yes	Yes	Yes
PSR J1622-4950	4.33	1.7	9	0.44	–	5.18	G333.9+0.0	No	No	Yes
SGR 1627-41	2.59	1.9	11	3.6	–	–	G337.0-0.1	No	Yes	Yes
CXOU J171405.7-381031	3.8	6.4	13.2	56	–	–	CTB 37B	No	No	No
SGR J1745-2900	3.76	1.38	8.5	0.11	57.9	84.6	–	No	Yes	Yes
XTE J1810-197	5.54	0.77	3.5	0.043	–	0.98	–	No	Yes	Yes
Swift J1834.9-0846	2.48	0.79	4.2	0.0084	–	–	W41	No	Yes	Yes
PSR J1846-0258	0.33	0.71	6	19	–	–	Kes 75	Yes	Yes	No

which is paid by the gravitational energy gain by the star’s contraction (Malheiro et al. 2012).

It is important to start our analysis by recalling the case of PSR J1846–0258, which has $L_X < \dot{E}_{\text{rot}}$ even when fiducial NS parameters are adopted. The importance of this source relies on the fact that, although it is recognized as rotation-powered NS, it has been classified as SGR/AXP (Olausen & Kaspi 2014) owing to its outburst event in June 2006 (Gavriil et al. 2008). In view of the possible NS rotation-power nature of PSR, Malheiro et al. (2012) explored the possibility that the outburst energetics $(3.8\text{--}4.8) \times 10^{41}$ erg (Kumar & Safi-Harb 2008) can be explained by the rotational energy gained by a NS glitch. It was there found that a glitch with fractional change of period $|\Delta P|/P \sim (1.73\text{--}2.2) \times 10^{-6}$ could explain the outburst of 2006. This theoretical result is in full agreement with the observational analysis by Kuiper & Hermsen (2009), who showed that indeed a major glitch with $|\Delta P|/P \sim (2\text{--}4.4) \times 10^{-6}$ is associated with the outburst. Very recently, Archibald et al. (2016) reported another example of an X-ray outburst from a radio pulsar, PSR J1119–6127, which also has $L_X < \dot{E}_{\text{rot}}$. This source is similar to the rotation-powered pulsar PSR J1846–0258. The pulsar’s spin period $P = 0.407$ s and spin-down rate $\dot{P} = 4.0 \times 10^{-12}$ imply a dipolar surface magnetic field $B = 4.1 \times 10^{13}$ G adopting fiducial values. It is clear from Figs. 4 and 5 that also in this case

the magnetic field would become undercritical for realistic NS parameters.

We follow this reasoning and proceed to theoretically infer the fractional change of rotation period, $|\Delta P|/P$, which explains the energetics of the bursts of the family of SGR/AXPs with $L_X < \dot{E}_{\text{rot}}$ presented in this work. We do this by assuming that $|\Delta E_{\text{rot}}|$, given by Eq. (12), equals the observed energy of the burst event, E_{burst} , namely

$$\frac{|\Delta P|}{P} = \frac{E_{\text{burst}} P^2}{2\pi^2 I}. \quad (13)$$

From the set of nine potential rotation-powered sources, only two ones have glitches detected: PSR J1846–0258 which has been discussed above and 1E 1547.0–5408 with $|\Delta P|/P \approx 1.9 \times 10^{-6}$ (Kuiper et al. 2012). In particular, figure 9 shows the value of $|\Delta P|/P$ obtained from equation (13) as a function of the NS mass for PSR J1846–0258 (a similar analysis can be applied to the radio pulsar PSR J1119–6127, whose timing analysis presented in Archibald et al. 2016 suggests the pulsar had a similar-sized spin-up glitch with $|\Delta P|/P \sim 5.8 \times 10^{-6}$). Indeed a minimum mass for the NS can be established for the sources by requesting that: 1) the entire moment of inertia is involved in the glitch and 2) the theoretical value of $|\Delta P|/P$ coincides with the observed value. We obtain a minimum mass for PSR J1846–0258, $M_{\text{min}} = 0.72 M_{\odot}$ and $M_{\text{min}} = 0.61 M_{\odot}$,

for the global and local charge neutrality cases, respectively. On the other hand, if we substitute the moment of inertia I in equation (13) by $I_{\text{glitch}} = \eta I$ where $\eta \leq 1$, being I_{glitch} the moment of inertia powering the glitch, then we can obtain a lower limit for the parameter η : we obtain $\eta = 0.20$ and $\eta = 0.18$ for the global and local charge neutrality cases, respectively. Tables 3 and 4 show the theoretically predicted value of $|\Delta P|/P$ for the seven sources with known bursts energy, assuming the mass of the NS is larger than $1 M_{\odot}$ and $\eta = 1$, in the cases of global and local charge neutrality, respectively.

Table 4 shows that from the nine potentially rotation-powered sources, two have a firmly established glitch-outburst connection. For the other sources there are two possibilities. 1) The glitch could be missed because absence of timing monitoring of the source prior to the burst, as it is certainly the case of the SGRs/AXPs discovered from an outburst. 2) The source timing was monitored and indeed there is no glitch associated with the outburst. In this case, it remains open the possibility that the outburst could be of magnetospheric origin. 3) There are also observed glitches without associated outburst activity. It is worth mentioning that a recent systematic analysis of the glitch-outburst connection in five AXPs by Dib & Kaspi (2014) concluded (amongst other important results): 1) glitches associated and not associated with outbursts or radiative changes show similar timing properties, namely outburst activity is not necessarily associated with large glitches; and 2) all glitches observed point to have their origin in the stellar interior. The second conclusion gives observational support to our theoretical interpretation of glitches as a phenomenon associated to cracking occurring in the NS interior. Whether a glitch can or not lead to observable radiative changes depends on specific properties of the phenomenon such as the energy budget and the localization of the event in the star's interior (Dib & Kaspi 2014), as well as on the efficiency in converting mechanical energy into radiation. The first two features have been here analyzed through ΔE_{rot} and the parameter η , the latter which defines I_{glitch} , the amount of moment of inertia involved in the glitch.

Thus, the glitch-outburst connection remains one of the most interesting problems of SGR/AXP physics and astrophysics. There are still several issues which need to be addressed both from systematic observational analyses and from theoretical point of view of NS physics.

6. Possible additional evidence

We have shown above for the nine potential rotation-powered SGRs/AXPs that, when timing observations allowed for the glitch/outburst connection identification, the rotational energy gain in the glitch can explain the outburst energetics. This characteristic is expected from a rotation-powered object.

We discuss now three additional pieces of astrophysical evidence pointing to a rotation-power nature of these sources. First, we note that four of the above nine sources, namely 1E 1547.0–5408, SGR J1745–2900, XTE J1810–197, and PSR J1622–4950, are the only SGR/AXPs with detected radio emission (see, e.g., Halpern et al. 2005; Camilo et al. 2006; Helfand et al. 2006; Kramer et al. 2007; Camilo et al. 2007a,b, 2008; Levin et al. 2010, 2012; Eatough et al. 2013; Olausen & Kaspi 2014; Lobato et al. 2015; Yusef-Zadeh et al. 2015). This property, expected in ordinary rotation-powered pulsars, is generally absent in SGR/AXPs. As discussed in Kramer et al. (2007), the radio emission of SGRs/AXPs and normal radio pulsars shows differences but also similarities, e.g. the case of XTE J1810–197. We show in Table 2 the observed radio luminosity per solid angle

at the 1.4 GHz frequency. For all of them we have $L_{\text{radio}} \ll L_X$, a feature also observed in ordinary pulsars. The continuous observation, as well as theoretical analysis and comparison of the radio emission of rotating radio transients (RRATS), high-B pulsars, SGRs/AXPs, and ordinary radio pulsars will allow us to understand the NS properties leading to the differences and similarities of the radio emission of these sources. New observational capabilities such as the ones of the Square Kilometer Array (SKA) expect to give also important contributions in this direction (Tauris et al. 2015).

In order to understand better the nature of these nine SGRs/AXPs it is worth to seek for additional emission features which could distinguish them from the rest of the sources. In this line we would like to point out that, at present, eleven SGRs/AXPs have been identified as *transient* sources, i.e. sources which show flux variations by a factor $\sim(10-1000)$ over the quiescent level (see, e.g., Turolla et al. 2015), in timescales from days to months. Such a variations are usually accompanied by an enhancement of the bursting activity. Seven of the nine potentially rotation-powered sources shown in Table 2 are transient sources. Therefore it is possible to identify common features in these sources, although more observational and theoretical investigation is needed. For instance, the above shows that all radio SGR/AXPs are rotation-powered sources and have a transient nature in the X-ray flux. The theoretical analysis of the evolution of the X-ray flux can constrain the properties of the NS and the emission geometry, for instance the angles between the rotation axis, the line of sight and the magnetic field (see, e.g., Albano et al. 2010). Such constraints can help in constraining, at the same time, the properties of the radio emission. Such an analysis is however out of the scope of the present work and opens a window of new research which we plan to present elsewhere.

There is an additional observational property which support to a NS nature for the nine sources of Table 2, namely six of them have possible associations with supernova remnants (SNRs). As it is summarized in Table 2, Swift J1834.9–0846 has been associated with SNR W41 (see, Younes et al. 2016, for the detection of a wind nebula around this source); PSR J1846–0258 with SNR Kes75; 1E 1547.0–5408 with SNR G327.24–0.13; PSR J1622–4950 with SNR G333.9+0.0; SGR 1627–41 with NR G337.0-0; and CXOU J171405.7–381031 with SNR CTB37B (Olausen & Kaspi 2014). If these associations will be fully confirmed, then it is clear that the NS was born from the core-collapse of a massive star which triggered the SN explosion. Further analysis of the supernova remnant and/or pulsar wind nebulae energetics and emission properties is needed to check their consistency with the rotation-powered nature of the object at the center.

7. Conclusions

We considered in this work the possibility that some SGRs and AXPs can be rotation-powered NSs exploring the allowed range of realistic NS structure parameters for the observed rotation periods of SGRs/AXPs, instead of using only fiducial parameters $M = 1.4 M_{\odot}$, $R = 10$ km, and $I = 10^{45}$ g cm². We obtained the NS properties from the numerical integration of the general relativistic axisymmetric equations of equilibrium for EOS based on relativistic nuclear mean-field models both in the case of local and global charge neutrality. We thus calculated the rotational energy loss, \dot{E}_{rot} , (hence to a radiation efficiency L_X/\dot{E}_{rot}) as a function of the NS mass. In addition, we estimate the surface magnetic field from a general relativistic model of a rotating magnetic dipole in vacuum.

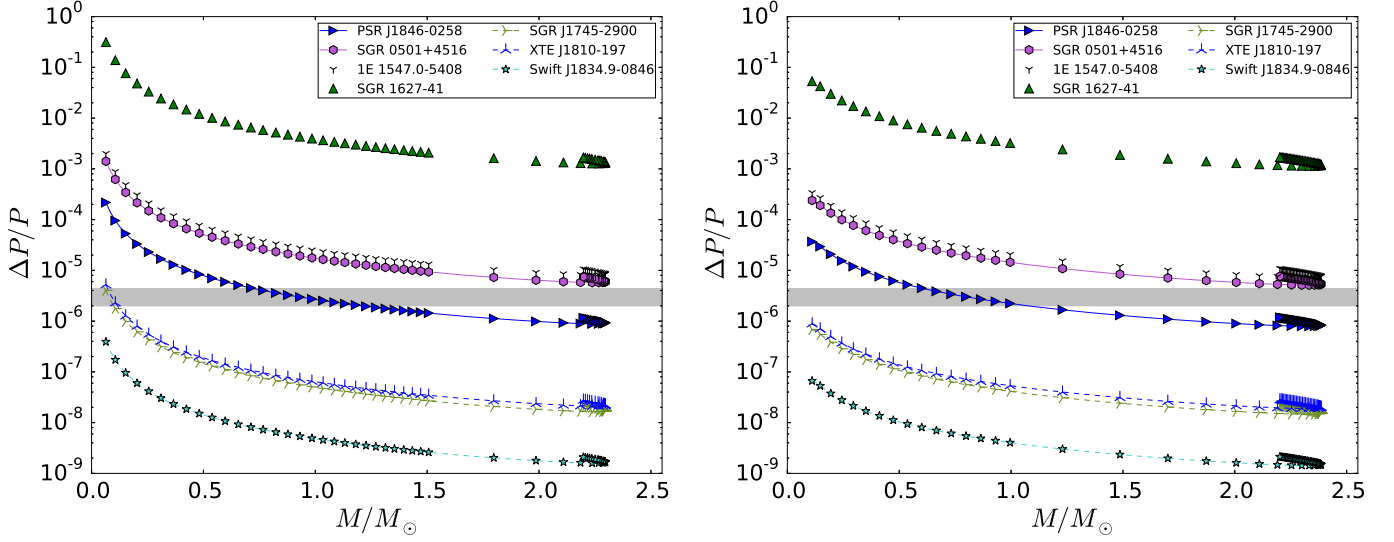


Fig. 9. (Color online) Inferred fractional change of rotation period during the glitch, $\Delta P/P$, obtained by equating the rotational energy gained during the glitch, ΔE_{rot} , to the energy of the burst, for globally neutral (left panel) and locally neutral (right panel) NSs. In this example the NS obeys the GM1 EOS. The gray-shaded area corresponds to the value of $|\Delta P|/P$ in the observed glitch of PSR J1846–0258 in June 2006 (Kuiper & Hermsen 2009).

Table 3. Predicted values of $|\Delta P|/P$ assuming rotation-powered NSs - Global charge neutrality case

Source name	Year of burst	Total isotropic burst energy (erg)	Predicted $ \Delta P /P$ for $M > 1 M_{\odot}$
PSR J1846–0258	2006	4.8×10^{41}	$8.8 \times 10^{-7} - 2.6 \times 10^{-6}$
1E 1547.0–5408	2009	1.1×10^{41}	$8.1 \times 10^{-6} - 2.4 \times 10^{-5}$
XTE J1810–197	2004	4.0×10^{37}	$2.1 \times 10^{-8} - 6.3 \times 10^{-8}$
SGR 1627–41	1998	1.0×10^{41}	$1.0 \times 10^{-5} - 3.8 \times 10^{-5}$
SGR 0501+4516	2008	1.0×10^{40}	$5.7 \times 10^{-6} - 1.7 \times 10^{-5}$
Swift J1834.9–0846	2011	1.5×10^{37}	$1.6 \times 10^{-9} - 4.8 \times 10^{-9}$
SGR 1745–2900	2013	6.7×10^{37}	$1.61 \times 10^{-8} - 4.9 \times 10^{-8}$

Table 4. Predicted values of $|\Delta P|/P$ assuming rotation-powered NSs - Local charge neutrality case

Source name	Year of burst	Total isotropic burst energy (erg)	Predicted $ \Delta P /P$ for $M > 1 M_{\odot}$
PSR J1846–0258	2006	4.8×10^{41}	$7.9 \times 10^{-7} - 2.2 \times 10^{-6}$
1E 1547.0–5408	2009	1.1×10^{41}	$7.2 \times 10^{-6} - 2.0 \times 10^{-5}$
XTE J1810–197	2004	4.0×10^{37}	$1.9 \times 10^{-8} - 5.3 \times 10^{-8}$
SGR 1627–41	1998	1.0×10^{41}	$1.1 \times 10^{-5} - 3.2 \times 10^{-5}$
SGR 0501+4516	2008	1.0×10^{40}	$5.0 \times 10^{-6} - 1.4 \times 10^{-5}$
Swift J1834.9–0846	2011	1.5×10^{37}	$1.4 \times 10^{-9} - 3.9 \times 10^{-9}$
SGR 1745–2900	2013	6.7×10^{37}	$1.4 \times 10^{-8} - 4.1 \times 10^{-8}$

Based on the above, the following conclusions can be drawn:

- Fiducial parameters overestimate both the radiation efficiency and the surface magnetic field of pulsars.
- The X-ray luminosity of nine sources shown in Table 2, i.e. Swift J1834.9–0846, PSR J1846–0258, 1E 1547.0–5408, SGR J1745–2900, XTE J1810–197, PSR J1622–4950, SGR 1627–41, SGR 0501+4516, CXOU J171405.7381031, can be explained via the loss of rotational energy of NSs (see Fig. 6). Thus, they fit into the family of ordinary rotation-powered pulsars.
- For the above nine sources, we obtained lower mass limits from the request $\dot{E}_{\text{rot}} \geq L_X$.
- We show that, if the thermal reservoir of the NS is the responsible of the blackbody component observed in soft X-rays, both SGR 1900+14 and SGR 1806-20 join the above family of rotation-powered NSs since the rotational energy loss

is enough to cover their non-thermal X-ray luminosity. This implies that up to 11 SGR/AXPs could be rotation-powered pulsars. This argument could be in principle also applied to the other sources, lowering further their radiation efficiency L_X/\dot{E}_{rot} .

- Thus we argue that the observational uncertainties in the determination of the distances and/or luminosities, as well as the uncertainties in the NS nuclear EOS, as well as the different interpretations of the observed spectrum leave still room for a possible explanation in terms of spin-down power for additional sources.
- We then proceeded to discuss the observed emission in hard X-rays (in the 20–150 keV band) first in both SGR 1900+14 and SGR 1806-20. Including this contribution the luminosity increases up to a factor 5 and 4 respectively for each source, leaving no room for them as rotation-powered sources un-

less their estimated distances are poorly constrained. Then we examine the three sources part of the group of nine potential rotation-powered sources for which hard X-ray emission has been observed: SGR J1745–2900, 1E 1547.0–5408 and SGR 0501+4516. Fig. 8 shows that 1E 1547.0–5408 remains still within the rotation-powered group while the other two sources do not. Thus, it becomes critical for these sources to verify the accuracy of the estimated distances and to explore the possible contribution of their associated supernova remnants to the hard X-ray emission.

- If these sources are powered by rotation, then other phenomena observed in known rotation-powered NSs could also be observed in these objects. Thus, we explored for the nine sources with $L_X < \dot{E}_{\text{rot}}$ the possibility that the energetics of their bursting activity, E_{burst} , can be explained from the rotational energy gained in an associated glitch, ΔE_{rot} . We thus computed lower limits to the fractional change of rotation period of NSs caused by glitches, $|\Delta P|/P$, by requesting $\Delta E_{\text{rot}} = E_{\text{burst}}$. The fact that there exist physically plausible solutions for $|\Delta P|/P$ reinforces the possible rotation-powered nature for these sources (e.g., the cases of PSR J1846–0258 and PSR J1119–6127).
- We discuss in Sec. 6 possible additional evidences pointing to the rotation-power nature of these nine sources. 1) Radio emission is observed in four SGRs/AXPs and all of them are part of these nine sources. Radio emission characterizes ordinary pulsars but it is generally absent/unobserved in SGRs/AXPs. 2) We call also the attention to a peculiar emission property of the majority of these nine sources: seven of them belong to the group of the so-called transient sources (which are eleven in total). Within these seven transient rotation-powered objects we find the four showing radio emission. We argue that the analysis of the varying X-ray flux can give information on the NS properties and magnetospheric geometry, shedding light into the understanding of the properties of the radio emission. 3) Six of the nine sources have potential associations with supernova remnants, supporting a NS nature. See Table 2 for details.

Although we have shown the possibility that some SGRs and AXPs be rotation-powered pulsars, we are far from getting a final answer to the question of the nature of SGRs/AXPs. It is not yet clear whether all the current members of the SGR/AXP family actually form a separate class of objects, e.g. with respect to traditional pulsars, or if their current classification have led to misleading theoretical interpretations. Therefore we encourage further theoretical predictions and observations in additional bands of the electromagnetic spectrum such as the optical, high and ultra-high gamma-rays and cosmic-rays to discriminate amongst the different models and being able to elucidate the nature of SGRs and AXPs.

Acknowledgements

JGC, RCR de Lima, and JAR, acknowledges the support by the International Cooperation Program CAPES-ICRANet financed by CAPES - Brazilian Federal Agency for Support and Evaluation of Graduate Education within the Ministry of Education of Brazil. MM and JGC acknowledge the support of FAPESP through the projects 2013/15088–0 and 2013/26258–4. JAR acknowledges partial support of the project No. 3101/GF4 IPC-11, and the target program F.0679 of the Ministry of Education and Science of the Republic of Kazakhstan.

References

- Albano, A., Turolla, R., Israel, G. L., et al. 2010, *ApJ*, 722, 788
 Antoniadis, J., Freire, P. C. C., Wex, N., et al. 2013, *Science*, 340, 448
 Archibald, R. F., Kaspi, V. M., Tendulkar, S. P., & Scholz, P. 2016, *ArXiv e-prints* [arXiv:1608.01007]
 Baym, G., Bethe, H. A., & Pethick, C. J. 1971a, *Nucl. Phys. A*, 175, 225
 Baym, G., Pethick, C., & Sutherland, P. 1971b, *ApJ*, 170, 299
 Belvedere, R., Boshkayev, K., Rueda, J. A., & Ruffini, R. 2014, *Nuclear Physics A*, 921, 33
 Belvedere, R., Pugliese, D., Rueda, J. A., Ruffini, R., & Xue, S.-S. 2012, *Nuclear Physics A*, 883, 1
 Belvedere, R., Rueda, J. A., & Ruffini, R. 2015, *ApJ*, 799, 23
 Bibby, J. L., Crowther, P. A., Furness, J. P., & Clark, J. S. 2008, *MNRAS*, 386, L23
 Boguta, J. & Bodmer, A. R. 1977, *Nuclear Physics A*, 292, 413
 Boshkayev, K., Izzo, L., Rueda Hernandez, J. A., & Ruffini, R. 2013, *A&A*, 555, A151
 Camilo, F., Cognard, I., Ransom, S. M., et al. 2007a, *ApJ*, 663, 497
 Camilo, F., Ransom, S. M., Halpern, J. P., & Reynolds, J. 2007b, *ApJ*, 666, L93
 Camilo, F., Ransom, S. M., Halpern, J. P., et al. 2006, *Nature*, 442, 892
 Camilo, F., Reynolds, J., Johnston, S., Halpern, J. P., & Ransom, S. M. 2008, *ApJ*, 679, 681
 Coelho, J. G. & Malheiro, M. 2013, Contribution for the Conference Proceedings of the Compact Stars in the QCD Phase Diagram III [arXiv:1307.8158]
 Coelho, J. G. & Malheiro, M. 2014, *PASJ*, 66, 14
 Coelho, J. G. & Malheiro, M. 2015, in Thirteenth Marcel Grossmann Meeting: On Recent Developments in Theoretical and Experimental General Relativity, Astrophysics and Relativistic Field Theories, ed. K. Rosquist, 2465–2467
 Corbel, S. & Eikenberry, S. S. 2004, *A&A*, 419, 191
 Demorest, P. B., Pennucci, T., Ransom, S. M., Roberts, M. S. E., & Hessels, J. W. T. 2010, *Nature*, 467, 1081
 Deutsch, A. J. 1955, *Annales d’Astrophysique*, 18, 1
 Dib, R. & Kaspi, V. M. 2014, *ApJ*, 784, 37
 Duncan, R. C. & Thompson, C. 1992, *ApJ*, 392, L9
 Eatough, R. P., Falcke, H., Karuppusamy, R., et al. 2013, *Nature*, 501, 391
 Esposito, P., Mereghetti, S., Tiengo, A., et al. 2007, *A&A*, 476, 321
 Gavriil, F. P., Gonzalez, M. E., Gotthelf, E. V., et al. 2008, *Science*, 319, 1802
 Glendenning, N. K. & Moszkowski, S. A. 1991, *Physical Review Letters*, 67, 2414
 Götz, D., Mereghetti, S., Tiengo, A., & Esposito, P. 2006, *A&A*, 449, L31
 Halpern, J. P., Gotthelf, E. V., Becker, R. H., Helfand, D. J., & White, R. L. 2005, *ApJ*, 632, L29
 Hartle, J. B. 1967, *ApJ*, 150, 1005
 Helfand, D. J., Camilo, F., Ransom, S. M., et al. 2006, in *Bulletin of the American Astronomical Society*, Vol. 38, AAS/High Energy Astrophysics Division #9, 349
 Kramer, M., Stappers, B. W., Jessner, A., Lyne, A. G., & Jordan, C. A. 2007, *MNRAS*, 377, 107
 Kuiper, L. & Hermsen, W. 2009, *A&A*, 501, 1031
 Kuiper, L., Hermsen, W., den Hartog, P. R., & Urama, J. O. 2012, *ApJ*, 748, 133
 Kumar, H. S. & Safi-Harb, S. 2008, *ApJ*, 678, L43
 Lalazissis, G. A., König, J., & Ring, P. 1997, *Phys. Rev. C*, 55, 540
 Levin, L., Bailes, M., Bates, S., et al. 2010, *ApJ*, 721, L33
 Levin, L., Bailes, M., Bates, S. D., et al. 2012, *MNRAS*, 422, 2489
 Lobato, R. V., Coelho, J., & Malheiro, M. 2015, *Journal of Physics Conference Series*, 630, 012015
 Lobato, R. V., Malheiro, M., & Coelho, J. G. 2016, *International Journal of Modern Physics D*, 25, 1641025
 Malheiro, M., Rueda, J. A., & Ruffini, R. 2012, *PASJ*, 64, 56
 Malov, I. F. 2010, *Astronomy Reports*, 54, 925
 Mereghetti, S. 2008, *A&A Rev.*, 15, 225
 Mereghetti, S., Esposito, P., Tiengo, A., et al. 2006, *ApJ*, 653, 1423
 Olausen, S. A. & Kaspi, V. M. 2014, *ApJS*, 212, 6
 Oppenheimer, J. R. & Volkoff, G. M. 1939, *Phys. Rev.*, 55, 374
 Ouyed, R., Leahy, D., & Niebergal, B. 2011, *MNRAS*, 415, 1590
 Rea, N., Pons, J. A., Torres, D. F., & Turolla, R. 2012, *ApJ*, 748, L12
 Rezzolla, L. & Ahmedov, B. J. 2004, *MNRAS*, 352, 1161
 Rotondo, M., Rueda, J. A., Ruffini, R., & Xue, S.-S. 2011, *Physics Letters B*, 701, 667
 Rueda, J. A., Boshkayev, K., Izzo, L., et al. 2013, *ApJ*, 772, L24
 Rueda, J. A., Ruffini, R., & Xue, S.-S. 2011, *Nuclear Physics A*, 872, 286
 Sugahara, Y. & Toki, H. 1994, *Nuclear Physics A*, 579, 557
 Tauris, T. M., Kaspi, V. M., Breton, R. P., et al. 2015, *Advancing Astrophysics with the Square Kilometre Array (AASKA14)*, 39
 Thompson, C. & Duncan, R. C. 1995, *MNRAS*, 275, 255
 Tolman, R. C. 1939, *Physical Review*, 55, 364
 Trümper, J. E., Dennerl, K., Kylafis, N. D., Ertan, Ü., & Zezas, A. 2013, *ApJ*, 764, 49
 Turolla, R., Zane, S., & Watts, A. L. 2015, *Reports on Progress in Physics*, 78, 116901
 Vrba, F. J., Henden, A. A., Luginbuhl, C. B., et al. 2000, *ApJ*, 533, L17
 Xu, R. X., Tao, D. J., & Yang, Y. 2006, *MNRAS*, 373, L85
 Younes, G., Kouveliotou, C., Kargaltsev, O., et al. 2016, *ArXiv e-prints* [arXiv:1604.06472]
 Yusef-Zadeh, F., Dising, R., Wardle, M., et al. 2015, *ApJ*, 811, L35

Thermal X-ray emission from massive, fast rotating, highly magnetized white dwarfs

D. L. Cáceres,^{1,2*} S. M. de Carvalho,^{3†} J. G. Coelho,^{4‡} R. C. R. de Lima,^{2,5§}
 Jorge A. Rueda,^{1,2,6¶}

¹*Dipartimento di Fisica and ICRA, Sapienza Università di Roma, P.le Aldo Moro 5, I-00185 Rome, Italy*

²*ICRANet, P.zza della Repubblica 10, I-65122 Pescara, Italy*

³*Universidade Federal do Tocantins, Campus Araguaína, Av. Paraguai 77814-970 Araguaína, TO, Brazil*

⁴*Div. Astrofísica, Instituto Nacional de Pesquisas Espaciais, Av. dos Astronautas 1758, 12227-010 São José dos Campos, SP, Brazil*

⁵*Universidade do Estado de Santa Catarina, Av. Madre Benvenuta, 2007 Itacorubi, 88.035-901, Florianópolis, Brazil*

⁶*ICRANet-Rio, Centro Brasileiro de Pesquisas Físicas, Rua Dr. Xavier Sigaud 150, 2290-180 Rio de Janeiro, Brazil*

Accepted XXX. Received YYY; in original form ZZZ

ABSTRACT

There is solid observational evidence on the existence of massive, $M \sim 1 M_{\odot}$, highly magnetized white dwarfs (WDs) with surface magnetic fields up to $B \sim 10^9$ G. We show that, if in addition to these features, the star is fast rotating, it can become a rotation-powered pulsar-like WD and emit detectable high-energy radiation. We infer the values of the structure parameters (mass, radius, moment of inertia), magnetic field, rotation period and spin-down rates of a WD pulsar death-line. We show that WDs above the death-line emit blackbody radiation in the soft X-ray band via the magnetic polar cap heating by back flowing pair-created particle bombardment and discuss as an example the X-ray emission of soft gamma-repeaters and anomalous X-ray pulsars within the WD model.

Key words: white dwarfs — stars: magnetic field — starspots — radiation mechanisms: thermal — acceleration of particles

1 INTRODUCTION

The increasing data from observational campaigns leave no room for doubts on the existence of massive ($M \sim 1 M_{\odot}$) white dwarfs (WDs) with magnetic fields comprised in the range $B = 10^6$ – 10^9 G (Külebi et al. 2009; Kepler et al. 2013, 2015). It has been recently shown that massive, highly magnetized WDs, could be formed by mergers of double WDs (García-Berro et al. 2012). The fact that WDs produced in mergers, besides being massive and highly magnetized, can be also fast rotators with periods $P \sim 10$ s, was used in Rueda et al. (2013) to show that they could be the WDs postulated in Malheiro et al. (2012) to describe the observational properties of soft gamma repeaters (SGRs) and anomalous X-Ray pulsars (AXPs), in alternative to the “magnetar” model (Duncan & Thompson 1992; Thompson & Duncan 1995). The gravitational stability of the WD imposes a lower bound to the rotation period $P \approx 0.5$ s, in

agreement with the minimum measured rotation period of SGRs/AXPs, $P \sim 2$ s (Boshkayev et al. 2013b). On the other hand, the surface area and temperature of the emitting region inferred from the available infrared, optical, and ultraviolet data of SGR/AXPs (i.e. for SGR 0418+5729, J1822.3–1606, 1E 2259+586 and 4U 0142+61), were shown to be consistent with the values expected from WDs (Boshkayev et al. 2013a; Rueda et al. 2013). The similarities of these WDs with ordinary, rotation-powered pulsars, imply that similar radiation mechanisms are expected to be at work in their magnetosphere. Indeed, the loss of rotational energy of the WD, owing to magnetic braking, is sufficient to explain the X-ray luminosity observed in SGRs/AXPs, and the inferred magnetic field from the observed spindown rates, $B \sim 10^9$ G, agree with the aforementioned observed values in galactic WDs (Malheiro et al. 2012; Coelho & Malheiro 2014).

Following this line, it was advanced in Rueda et al. (2013) that the blackbody observed in the soft X-rays of SGRs/AXPs, with observationally inferred radii $R_{\text{bb}} \sim 1$ km and temperatures $T_{\text{bb}} \sim 10^6$ K, could be due to a known phenomenon expected to occur in pulsars, namely the magnetospheric currents flowing back towards the WD, heating up the magnetic polar caps creating surface hot spots (see,

* diegoleonardocu@gmail.com

† sheyse.martins@icra.it

‡ jaziell.coelho@inpe.br

§ rafael.camargo@icranet.org

¶ jorge.rueda@icra.it

e.g., Usov 1988, 1993). The aim of this work is to estimate this magnetospheric process for massive, highly magnetized, fast rotating WDs, exploiting the full analogy with pulsars. This calculation is interesting by its own and becomes of observational relevance in view of the latest results by Marsch et al. (2016) which points to the observational evidence of pulsar behavior in magnetized WDs. We calculate the observable emission from isolated magnetized WDs in the X-rays. In order to exemplify the mechanism with appealing numbers, we apply it to the case of the WD model of SGRs and AXPs. Specifically, we evaluate the decay rate of curvature radiation photons in e^-e^+ pairs, and the subsequent backward flow of pair-produced particles that bombards and heats-up the magnetosphere polar caps, producing the observable thermal radiation. We compute in section 2 the condition for e^-e^+ pair creation within the inner gap model. In section 3 we calculate the expected thermal luminosity and infer the values of mass, radius, magnetic field, potential drop that ensure that the polar cap thermal emission explains the observed blackbody in the soft X-ray spectrum of SGRs/AXPs. The cases of 1E 2259+586 and 4U 0142+61 are analyzed as specific examples. In section 4 we simulate the observed X-ray flux from this spotty emission and compute the expected pulsed fraction which we compare with the observed values in SGRs and AXPs. We outline the conclusions in section 5.

2 WD MAGNETOSPHERE

Rotating, highly magnetized WDs can develop a magnetosphere analog to the one of pulsars. A corotating magnetosphere (Davis 1947; Ferraro & Unthank 1949; Gold 1962; Ferraro & Bhatia 1967) is enforced up to a maximum distance given by the so-called light cylinder, $R_{lc} = c/\Omega = cP/(2\pi)$, where c is the speed of light and Ω is the angular velocity of the star, since corotation at larger distances would imply superluminal velocities for the magnetospheric particles. For an axisymmetric star with aligned magnetic moment and rotation axes, the local density of charged plasma within the corotating magnetosphere is (Goldreich & Julian 1969)

$$\rho_{GJ} = -\frac{\mathbf{\Omega} \cdot \mathbf{B}}{2\pi c} \frac{1}{1 - (\Omega r_{\perp}/c)^2}, \quad (1)$$

where $r_{\perp} = r \sin \theta$ with θ the polar angle.

The last B -field line closing within the corotating magnetosphere can be easily located from the B -field lines equation for a magnetic dipole $r/\sin^2 \theta = \text{constant} = R_{lc}$, and is located at an angle $\theta_{pc} = \arcsin(\sqrt{R/R_{lc}}) \approx \sqrt{R/R_{lc}} = \sqrt{R\Omega/c} = \sqrt{2\pi R/(cP)}$ from the star's pole, with R the radius of the star. The B -field lines that originate in the region between $\theta = 0$ and $\theta = \theta_{pc}$ (referred to as *magnetic polar caps*) cross the light cylinder, and are called "open" field lines. The size of the cap is given by the polar cap radius $R_{pc} = R\theta_{pc} \approx R\sqrt{2\pi R/(cP)}$. Clearly, by symmetry, there are two (antipodal) polar caps on the stellar surface from which the charged particles leave the star moving along the open field lines and escaping from the magnetosphere passing through the light cylinder.

Particle acceleration is possible in regions called *vacuum gaps* where corotation cannot be enforced, i.e. where

the density of charged particles is lower than the Goldreich-Julian value ρ_{GJ} given by Eq. (1). For aligned(anti-aligned) rotation and magnetic axes we have $\rho_{GJ} < 0$ ($\rho_{GJ} > 0$), hence magnetosphere has to be supplied by electrons(ions) from the WD surface. This work is done by the existence of an electric field parallel to the magnetic field. Independently on whether $\mathbf{\Omega} \cdot \mathbf{B}$ is positive or negative, we assume that the condition of a particle injection density lower than ρ_{GJ} is fulfilled. In this *inner gap* model the gaps are located just above the polar caps (Ruderman & Sutherland 1975) and the potential drop generated by the unipolar effect and that accelerates the electrons along the open B -field lines above the surface is

$$\Delta V = \frac{B_s \Omega h^2}{c}, \quad (2)$$

where h is the height of the vacuum gap and B_s is the surface magnetic field, which does not necessarily coincides with the dipole field B_p .

The electrons (or positrons) accelerated through this potential and following the B -field lines will emit curvature photons whose energy depends on the γ -factor, $\gamma = e\Delta V/(mc^2)$, where e and m are the electron charge and mass, and on the B -field line curvature radius r_c , i.e. $\omega_c = \gamma^3 c/r_c$. Following Chen & Ruderman (1993), we adopt the constraint on the potential ΔV for pair production via $\gamma + B \rightarrow e^- + e^+$,

$$\frac{1}{2} \left(\frac{e\Delta V}{mc^2} \right)^3 \frac{\lambda}{r_c} \frac{h}{r_c} \frac{B_s}{B_q} \approx \frac{1}{15}, \quad (3)$$

or in terms of a condition on the value of the potential,

$$\Delta V \approx \left(\frac{2}{15} \right)^{2/7} \left(\frac{r_c}{\lambda} \right)^{4/7} \left(\frac{\lambda \Omega}{c} \right)^{1/7} \left(\frac{B_s}{B_q} \right)^{-1/7} \frac{mc^2}{e}, \quad (4)$$

where we have used Eq. (2), $\lambda = \hbar/(mc)$, $B_q \equiv m^2 c^3/(e\hbar) = 4.4 \times 10^{13}$ G, is the quantum electrodynamic field, with \hbar the reduced Planck's constant.

For a magnetic dipole geometry, i.e. $B_s = B_d$ and $r_c = \sqrt{Rc/\Omega}$, the potential drop ΔV cannot exceed the maximum potential (i.e., for $h = h_{\max} = R_{pc}/\sqrt{2}$),

$$\Delta V_{\max} = \frac{B_d \Omega^2 R^3}{2c^2}. \quad (5)$$

We are here interested in the possible magnetospheric mechanism of X-ray emission from magnetized WDs, thus we will consider the heating of the polar caps by the inward flux of pair-produced particles in the magnetosphere. These particles of opposite sign to the parallel electric field moves inward and deposit most of their kinetic energy on an area

$$A_{\text{spot}} = f A_{pc}, \quad (6)$$

i.e. a fraction $f \leq 1$ of the polar cap area, $A_{pc} = \pi R_{pc}^2$. The temperature T_{spot} of this surface hot spot can be estimated from the condition that it re-radiates efficiently the deposit kinetic energy, as follows. The rate of particles flowing to the polar cap is $\dot{N} = JA_{pc}/e$, where $J = \eta \rho_{GJ} c$ is the current density in the gap, and $\eta < 1$ a parameter that accounts for the reduction of the particle density in the gap with respect to the Goldreich-Julian value (Cheng & Ruderman 1977 used $\eta = 1$ for order-of-magnitude estimates). In this model the filling factor f is not theoretically constrained and it has been estimated from pulsar's observations in X-rays

that it can be much smaller than unity (Cheng & Ruderman 1977). The condition that the hot spot luminosity equals the deposited kinetic energy rate reads

$$A_{\text{spot}}\sigma T_{\text{spot}}^4 = e\Delta V\dot{N} = JA_{\text{pc}}\Delta V = \eta\rho_{\text{GJ}}(R)cA_{\text{pc}}\Delta V, \quad (7)$$

where σ is the Stefan-Boltzmann constant. From Eqs. (1), (6) and (7) we obtain the spot temperature

$$T_{\text{spot}} = \left(\eta \frac{B_d \Delta V}{\sigma f P} \right)^{1/4}. \quad (8)$$

It is worth to mention that in the above estimate we have assumed a full efficiency in the conversion from the deposited kinetic energy to the hot spot emission. This assumption is accurate if the heating source namely the energy deposition occurs not too deep under the star's surface and it is not conducted away to larger regions being mainly re-radiated from the surface area filled by the penetrating particles (Cheng & Ruderman 1980). In Appendix A we estimate the cooling and heating characteristic times and the heating and re-radiation efficiency. For the densities and temperatures of interest here we show that the polar cap surface re-radiates efficiently most of the kinetic energy deposited by the particle influx validating our assumption.

3 SPECIFIC EXAMPLES

As in our previous analyzes (Malheiro et al. 2012; Boshkayev et al. 2013a; Rueda et al. 2013; Coelho & Malheiro 2014), we use the traditional dipole formula to get an estimate for the WD dipole magnetic field, i.e.:

$$B_d = \left(\frac{3c^3}{8\pi^2} \frac{I}{R^6} P\dot{P} \right)^{1/2}, \quad (9)$$

where I is the moment of inertia of the star, $\dot{P} \equiv dP/dt$ is the first time derivative of the rotation period (spindown rate), and an inclination of $\pi/2$ between the magnetic dipole and the rotation axis, has been adopted. It is worth to recall that the estimate of the B -field by (9) is not necessarily in contrast, from the quantitative point of view, with an estimate using an aligned field but introducing a breaking from the particles escaping from the magnetosphere, since also in this case a quantitatively and qualitatively similar energy loss is obtained.

For a given rotation period P , the WD structure parameters such as mass M , radius R , and moment of inertia I are bounded from below and above if the stability of the WD is requested (Boshkayev et al. 2013a). From those bounds, we established there lower and upper bounds for the field B_d of the WD.

3.1 1E 2259+586

We apply the above theoretical framework to a specific source, AXP 1E 2259+586. This source, with a rotation period $P = 6.98$ s (Fahlman & Gregory 1981) and a spindown rate $\dot{P} = 4.8 \times 10^{-13}$ (Davies et al. 1990), has a historical importance since Paczynski (1990) first pointed out the possibility of this object being a WD. This object produced a major outburst in 2002 (Kaspi et al. 2003; Woods et al. 2004), in which the pulsed and persistent fluxes rose suddenly by

a factor of ≥ 20 and decayed on a timescale of months. Coincident with the X-ray brightening, the pulsar suffered a large glitch of rotation frequency fractional change 4×10^{-6} (Kaspi et al. 2003; Woods et al. 2004). It is worth to recall that the observed temporal coincidence of glitch/bursting activity, as first pointed out by Usov (1994) in the case of 1E 2259+586, and then extended in Malheiro et al. (2012); Boshkayev et al. (2013a), can be explained as due to the release of the rotational energy, gained in a starquake occurring in a total or partially crystallized WD. Since we are interested in the quiescent behavior, we will not consider this interesting topic here. Therefore, only X-ray data prior to this outburst event will be used in this work (Zhu et al. 2008).

The soft X-ray spectrum of 1E 2259+586 is well fitted by a blackbody plus a power law model. The blackbody is characterized by a temperature $kT_{\text{bb}} \approx 0.37$ keV ($T_{\text{bb}} \approx 4.3 \times 10^6$ K) and emitting surface are $A_{\text{bb}} \approx 1.3 \times 10^{12}$ cm² (Zhu et al. 2008). These values of temperature and radius are inconsistent (too high and too small, respectively) with an explanation based on the cooling of a hot WD, and therefore such a soft X-ray emission must be explained from a spotty surface due to magnetospheric processes, as the one explored in this work.

The stability of the WD for such a rotation period constrains the WD radius to the range $R \approx (1.04\text{--}4.76) \times 10^8$ cm. For example, in the case of a WD with radius $R \approx 10^8$ cm, the polar cap area is $A_{\text{pc}} = 6.6 \times 10^{14}$ cm, hence using Eq. (6) we have $f \approx 0.002$ and from Eq. (8). The spot temperature $kT_{\text{spot}} \approx 0.37$ keV can be obtained using $B_d \approx 6 \times 10^9$ G from the dipole formula (9), a potential drop $\Delta V \approx 3.5 \times 10^{11}$ Volts (lower than $\Delta V_{\text{max}} \approx 5.4 \times 10^{12}$ Volts), and using the typical value $\eta = 1/2$ of the reduced particle density in the gap adopted in the literature. These parameters suggests a height of the gap, obtained with Eq. (2), $h \approx 0.11R_{\text{pc}}$.

The smallness of the filling factor, which appears to be not attributable to the value of h , could be explained by a multipolar magnetic field near the surface. It is interesting that the existence of complex multipolar magnetic field close to the WD surface is observationally supported (see, e.g., Ferrario et al. 2015). We would like to emphasize that this filling factor has only a physical meaning when besides a strong non-dipolar surface field, the physical parameters of the star (magnetic field and rotational velocity) fulfill the requirement for the creation of electron-positron pairs and the subsequent avalanche of particles heat the surface. Such a local, strong non-dipolar field in the surface, diminishes the area bombarded by the incoming particles and, via magnetic flux conservation, the filling factor establishes the intensity of the multipolar magnetic field component as (see, e.g., Cheng & Zhang 1999; Gil & Sendyk 2000; Gil & Melikidze 2002, and references therein)

$$B_s = \frac{B_d}{f}, \quad (10)$$

which implies that, close to the surface, there could be small magnetic domains with magnetic field intensity as large as $10^{11} - 10^{12}$ G (see Fig. 1).

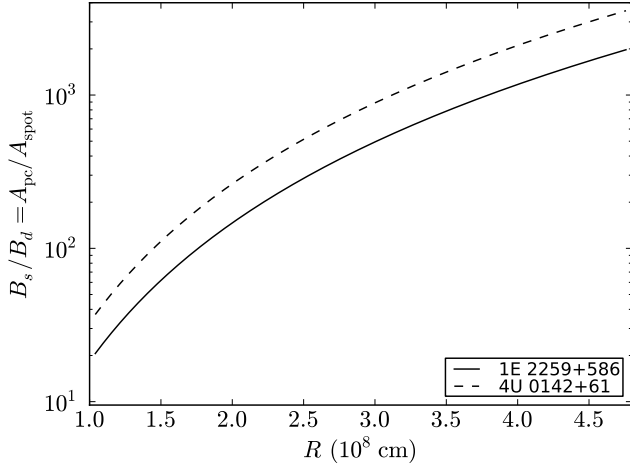


Figure 1. Surface to dipole magnetic field ratio given by magnetic flux conservation (10) for the AXPs 1E 2259+586 and 4U 0142+61.

3.2 4U 0142+61

We can repeat the above analysis for the case of 4U 0142+61. This source, with a rotation period $P \approx 8.69$ s, was first detected by *Uhuru* (Forman et al. 1978). The measured period derivative of this source is $\dot{P} = 2.03 \times 10^{-12}$ (Hulleman et al. 2000). The time-integrated X-ray spectrum of 4U 0142+61 is also described by a blackbody plus a power-law model. The blackbody component shows a temperature $kT_{\text{bb}} = 0.39$ keV ($T_{\text{bb}} \approx 4.6 \times 10^6$ K) and a surface area $A_{\text{bb}} \approx 5.75 \times 10^{11}$ cm² (Göhler et al. 2005). As for the above case of 1E 2259+5726, such a blackbody cannot be explained from the cooling of a WD but instead from a magnetospheric hot spot created by the heating of the polar cap.

For a WD radius $R = 10^8$ cm and a magnetic field $B_d \approx 10^{10}$ G for a rotating dipole (9), we have a filling factor $f \approx 0.001$, a potential drop $\Delta V \approx 1.4 \times 10^{11}$ Volts (smaller than $\Delta V_{\text{max}} \approx 5.8 \times 10^{12}$ Volts) and a gap height $h \approx 0.06R_{\text{pc}}$. Again the filling factor suggests the presence of a strong multipolar component as shown in Fig. 1.

We show in Fig. 2 the potential drop inferred from Eq. (8) using the X-rays blackbody data for the above two sources. We check that for all the possible stable WD configurations the potential drop satisfies the self-consistence condition $\Delta V < \Delta V_{\text{max}}$, where the latter is given by Eq. (5).

4 FLUX PROFILES AND PULSED FRACTION

We turn now to examine the properties of the flux emitted by such hot spots. Even if the gravitational field of a WD is not strong enough to cause appreciable general relativistic effects, for the sake of generality we compute the flux from the star taken into account the bending of light. We shall follow here the treatment in Turolla & Nobili (2013) to calculate the observed flux, which allows to treat circular spots of arbitrary finite size and arbitrarily located in the star surface. The mass and radius of the star are denoted by M and R , and the outer spacetime is described by the Schwarzschild metric, i.e. we shall neglect at first approximation the effects of rotation. Let be (r, θ, ϕ) the spherical

coordinate system centered on the star and the line of sight (LOS) the polar axis.

We consider an observer at $r \rightarrow \infty$ and a photon that arises from the star surface at $dS = R^2 \sin \theta d\theta d\phi$ making an angle α with the local surface normal, where $0 \leq \alpha \leq \pi/2$. The photon path is then bended by an additional angle β owing to the spacetime curvature, reaching the observer with an angle $\psi = \alpha + \beta$. Since we have chosen the polar axis aligned with the LOS, it is easy to see that $\psi = \theta$ (see Fig. 3). Beloborodov (2002) showed that a simple approximate formula can be used to relate the emission angle α to the final angle θ :

$$1 - \cos \alpha = (1 - \cos \theta) \left(1 - \frac{R_s}{R}\right), \quad (11)$$

where $R_s = 2GM/c^2$ is the Schwarzschild radius and, as usual, G denotes the gravitational constant.

For an emission with a local Planck spectrum, the intensity is given by a blackbody of temperature T , $B_\nu(T)$, where ν is the photon frequency. The flux is proportional to the visible area of the emitting region (S_V) plus a relativistic correction proportional to the surface, given by the equation

$$\begin{aligned} F_\nu &= \left(1 - \frac{R_s}{R}\right) B_\nu(T) \int_{S_V} \cos \alpha \frac{d\cos \alpha}{d(\cos \theta)} ds \\ &= \left(1 - \frac{R_s}{R}\right)^2 B_\nu(T) (I_p + I_s), \end{aligned} \quad (12)$$

where

$$I_p = \int_{S_V} \cos \theta \sin \theta d\theta d\phi, \quad I_s = \int_{S_V} \sin \theta d\theta d\phi. \quad (13)$$

In polar coordinates, the circular spot has its center at θ_0 and a semi-aperture θ_c . The spot is bounded by the function $\phi_b(\theta)$, where $0 \leq \phi_b \leq \pi$, and since we must consider just the star visible part, the spot must be also limited by a constant θ_F . For a given bending angle β , the maximum θ_F is given by the maximum emission α , i.e. $\alpha = \pi/2$. One can see that in a Newtonian gravity, where $\beta = 0$, the maximum visible angle is $\theta_F = \pi/2$ which means half of the star is visible, while in a relativistic star, values $\theta_F > \pi/2$ are possible, as expected. Then

$$\begin{aligned} I_p &= 2 \int_{\theta_{\min}}^{\theta_{\max}} \cos \theta \sin \theta \phi_b(\theta) d\theta, \\ I_s &= 2 \int_{\theta_{\min}}^{\theta_{\max}} \sin \theta \phi_b(\theta) d\theta, \end{aligned} \quad (14)$$

where $\theta_{\min}, \theta_{\max}$ are the limiting values to be determined for the spot considered. Turolla & Nobili (2013) showed how to solve these integrals and how to treat carefully the limiting angles. The I_p and I_s integrals can be then written as $I_{p,s} = I_{1,2}(\theta_{\max}) - I_{1,2}(\theta_{\min})$ and we refer the reader to that work for the precise expressions. Finally, the flux (12) is written as

$$F_\nu = \left(1 - \frac{R_s}{R}\right)^2 B_\nu(T) A_{\text{eff}}(\theta_c, \theta_0), \quad (15)$$

where A_{eff} is the effective area, given by

$$A_{\text{eff}}(\theta_c, \theta_0) = R^2 \left[\frac{R_s}{R} I_s + \left(1 - \frac{R_s}{R}\right) I_p \right]. \quad (16)$$

The total flux produced by two antipodal spots, with

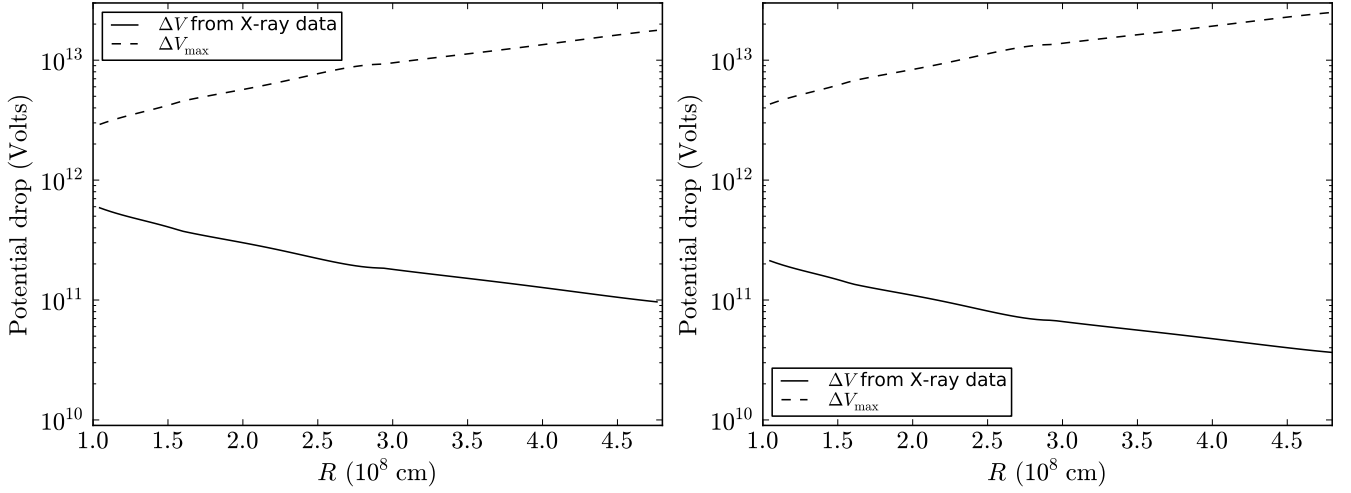


Figure 2. WD polar gap potential drop ΔV inferred via Eq. (8) using the blackbody observed in soft X-rays in 1E 2259+586 (left panel) and 4U 0142+61 (right panel). In this plot we check the potential drop developed in the WD polar gap does not exceed the maximum potential reachable ΔV_{\max} given by Eq. (5).

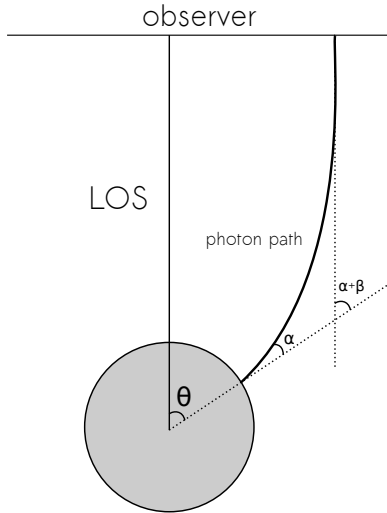


Figure 3. View of the photon trajectory and angles θ , α , and β .

semi-apertures $\theta_{c,i}$ and temperatures T_i ($i=1,2$), can be calculated by adding each contribution, so we have

$$F_{\nu}^{TOT} = \left(1 - \frac{R_s}{R}\right)^2 [B_{\nu}(T_1)A_{\text{eff}}(\theta_{c,1}, \theta_0) + B_{\nu}(T_2)A_{\text{eff}}(\theta_{c,2}, \theta_0 + \pi/2)]. \quad (17)$$

Besides, the pulse profile in a given energy band $[\nu_1, \nu_2]$ for one spot is given by

$$F(\nu_1, \nu_2) = \left(1 - \frac{R_s}{R}\right)^2 A_{\text{eff}}(\theta_c, \theta_0) \int_{\nu_1}^{\nu_2} B_{\nu}(T) d\nu. \quad (18)$$

The star rotates with a period P (angular velocity $\Omega = 2\pi/P$), so we consider $\hat{\mathbf{r}}$ the unit vector parallel to the rotating axis. It is useful to introduce the angles ξ , the angle between the LOS (unit vector $\hat{\mathbf{l}}$) and the rotation axis, and the angle χ between the spot axis (unit vector $\hat{\mathbf{c}}$) and the rotation axis, i.e., $\cos \xi = \hat{\mathbf{r}} \cdot \hat{\mathbf{l}}$ and $\cos \chi = \hat{\mathbf{r}} \cdot \hat{\mathbf{c}}$. As the star rotates the spot's center, θ_0 , changes. Let $\gamma(t) = \Omega t$ be

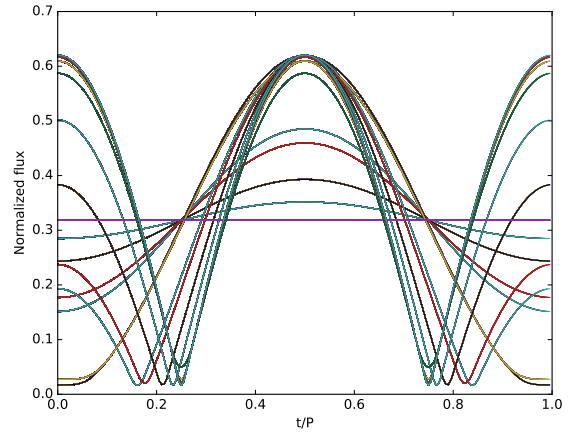


Figure 4. Flux profiles for different configurations of antipodal spots as a function of the phase. The semi-aperture for all the lines is $\theta_c = 3^\circ$. The WD parameters correspond to the ones of the WD of minimum radius adopted for AXP 1E 2259+586.

the rotational phase, thus by geometrical reasoning we have

$$\cos \theta_0(t) = \cos \xi \cos \chi - \sin \xi \sin \chi \cos \gamma(t), \quad (19)$$

where it is indicated that ξ and χ do not change in time. When the total flux (17) is calculated for a given configuration (ξ, χ) in the whole period of time, the typical result is a pulsed flux with a maximum (F_{\max}) and a minimum flux (F_{\min}). As an example, we show in Fig. 4 flux profiles for different configurations of antipodal spots as a function of the phase for the WD of minimum radius in the case of AXP 1E 2259+586 used in Sec. 3.1.

We can measure the amount of pulsed emission by defining the *pulsed fraction*

$$\text{PF} = \frac{F_{\max} - F_{\min}}{F_{\max} + F_{\min}}, \quad (20)$$

which we show in Fig. 5, as a function of the angles ξ and χ , for AXP 1E 2259+586. In the left panel of this figure we consider only the flux given by the blackbody produced by the two antipodal hot spots on the WD. We can see that indeed pulsed fractions as small as the above values can be obtained from magnetized WDs, for appropriate values of the geometric angles ξ and χ . However, the soft X-ray spectrum shows a non-thermal power-law component, additional to the blackbody one. As we have shown, the blackbody itself can contribute to the PF if produced by surface hot spots and thus the observed total PF of a source in those cases includes both contributions, mixed. It is thus of interest to explore this problem from the theoretical point of view. To do this we first recall that total intrinsic flux of this source in the 2–10 keV band is $F_{\text{tot}} \approx 1.4 \times 10^{-11} \text{ erg cm}^{-2} \text{ s}^{-1}$, and the power-law flux is $F_{\text{PL}} \approx 1.8F_{\text{bb}} \approx 8.5 \times 10^{-12} \text{ erg cm}^{-2} \text{ s}^{-1}$ (Zhu et al. 2008). The right panel of Fig. 5 shows the PF map for this source taking into account both the blackbody and the power-law components. By comparing this PF map with the one in the left panel which considers only the pulsed blackbody we can see that they are very similar each other. This means that in these cases where both pulsed components are in phase and have comparable fluxes it is difficult (although still possible if good data are available), to disentangle the single contributions.

5 CONCLUSIONS

We exploited the analogy with pulsars to investigate whether or not massive, highly magnetized, fast rotating WDs, can behave as neutron star pulsars and emit observable high-energy radiation. We conclude:

(i) We showed that WDs can produce e^-e^+ pairs in their magnetosphere from the decay of curvature radiation photons, i.e. we infer the structure parameters for which they are located above the WD pulsar death-line. We evaluated the rate of such a process. Then, we calculated the thermal emission produced by the polar cap heating by the pair-created particles that flow back to the WD surface due to the action of the induction electric field.

(ii) In order to give a precise example of the process, we applied the theoretical results to the case of the WD model of SGRs and AXPs. We have shown that the inferred values of the WD parameters obtained from fitting with this magnetospheric emission the blackbody spectrum observed in the soft X-rays of SGRs and AXPs, are in agreement with our previous estimates using the IR, optical, and UV data, and fall within the constraints imposed by the gravitational stability of the WD.

(iii) We have related the size of the spot with the size of the surface under the polar cap filled by the inward particle bombardment. We have shown that the spot area is much smaller than the polar cap area pointing to the existence of strong non-dipolar magnetic fields close to the WD surface.

(iv) We have used the heat transport and energy balance equations to show that, for the actual conditions of density and temperature under the polar cap, the hot spot re-radiates efficiently the heat proportioned by the inward particle bombardment.

(v) The spot, which is aligned with the magnetic dipole moment of the WD, produces a pulsed emission in phase

with the rotation period of the object. We showed that the theoretically inferred pulsed fraction of the WD span from very low values all the way to unity depending on the viewing angles. Therefore it can also account for the observed pulsed fraction in SGRs and AXPs for appropriate choices of the viewing angles. In addition, the low-energy tail of the blackbody spectrum of the hot spot could produce a non-null pulsed fraction of the flux in the optical bands as well. However, this depends on the flux produced by the surface temperature of the WD which certainly dominates the light curve at low energies. From the quantitative point of view, the size of the surface area of the spots is crucial for the explanation of the observed pulsed fraction in soft X-rays.

(vi) We have also shown that the addition of a pulsed power-law component as the one observed in SGRs/AXPs does not modify appreciable the above result. The reason for this is that the non-thermal power-law component and the blackbody due to the surface hot spot have comparable fluxes and are in phase each other. In those cases it is difficult to disentangle the single contributions to the pulsed fraction.

We have shown that, as advanced in Rueda et al. (2013), indeed the blackbody observed in the optical wavelengths of SGRs and AXPs can be due to the surface temperature of the WD, while the one observed in the X-rays can be of magnetospheric origin. For the power-law component, also observed in the soft X-rays, a deeper analysis of processes such as curvature radiation, inverse Compton scattering, as well as other emission mechanisms, is currently under study.

There is also room for application and extension of the results presented in this work to other astrophysical phenomena. WD mergers can lead to a system formed by a central massive, highly magnetized, fast rotating WD, surrounded by a Keplerian disk (see Rueda et al. 2013, and references therein). At the early stages, the WD and the disk are hot and there is ongoing accretion of the disk material onto the WD. In such a case, the WD surface shows hot regions that deviate from the spotty case, e.g. hot surface rings. That case is also of interest and will be presented elsewhere.

ACKNOWLEDGMENTS

It is a great pleasure to thank M. Malheiro for thoughtful discussions and for the comments and suggestions on the presentation of our results. Likewise, we would like to thank N. Rea. We are grateful to L. Becerra for providing us tables of the heat capacity and thermal conductivity in the range of densities and temperatures of interest for this work. D.L.C. acknowledges the financial support by the International Relativistic Astrophysics (IRAP) Ph. D. Program. J.G.C., R.C.R.L., S. M. C. and J.A.R. acknowledge the support by the International Cooperation Program CAPES-ICRANet financed by CAPES - Brazilian Federal Agency for Support and Evaluation of Graduate Education within the Ministry of Education of Brazil. JGC acknowledges the support of FAPESP through the project 2013/15088-0 and 2013/26258-4.

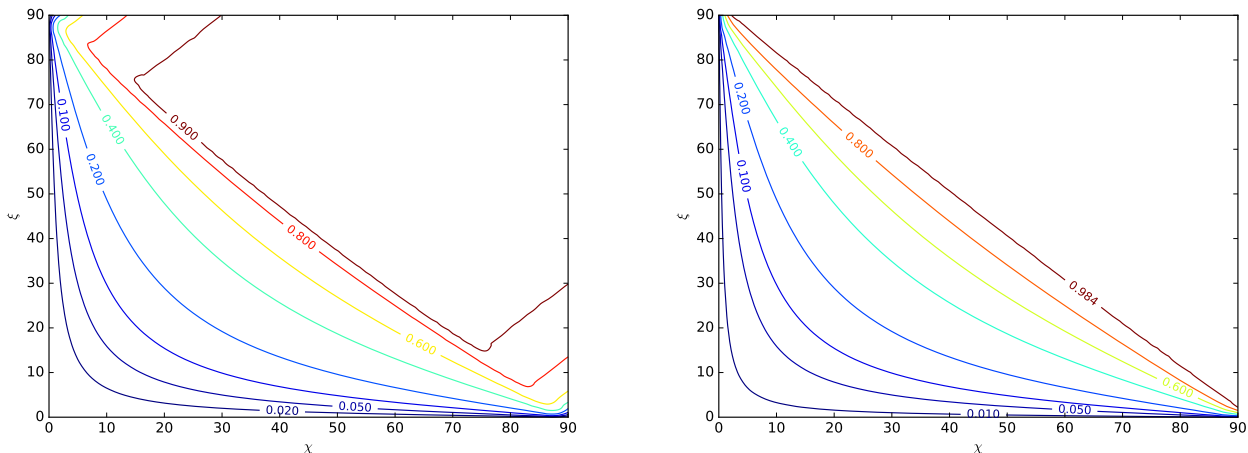


Figure 5. Theoretical PF as a function of the angles ξ and χ , computed in this work for the source 1E 2259+586 modeled as a WD of radius $R_{\min} \approx 1.04 \times 10^8$ cm. The left panel shows the results of the PF produced by the blackbody given by the two antipodal hot spots. The right panel shows the results for the total flux given by the blackbody plus the non-thermal power-law component, both pulsed. The observed total PF of this source in the 2–10 keV is about 20% (Zhu et al. 2008).

REFERENCES

- Beloborodov A. M., 2002, *ApJ*, **566**, L85
 Boshkayev K., Izzo L., Rueda Hernandez J. A., Ruffini R., 2013a, *A&A*, **555**, A151
 Boshkayev K., Rueda J. A., Ruffini R., Siutsou I., 2013b, *ApJ*, **762**, 117
 Chabrier G., Potekhin A. Y., 1998, *Phys. Rev. E*, **58**, 4941
 Chen K., Ruderman M., 1993, *ApJ*, **402**, 264
 Cheng A. F., Ruderman M. A., 1977, *ApJ*, **214**, 598
 Cheng A. F., Ruderman M. A., 1980, *ApJ*, **235**, 576
 Cheng K. S., Zhang L., 1999, *ApJ*, **515**, 337
 Coelho J. G., Malheiro M., 2014, *PASJ*, **66**, 14
 Davies S. R., Coe M. J., Wood K. S., 1990, *MNRAS*, **245**, 268
 Davis L., 1947, *Physical Review*, **72**, 632
 Duncan R. C., Thompson C., 1992, *ApJ*, **392**, L9
 Fahlman G. G., Gregory P. C., 1981, *Nature*, **293**, 202
 Ferrario L., de Martino D., Gänsicke B. T., 2015, *Space Sci. Rev.*, **191**, 111
 Ferraro V. C. A., Bhatia V. B., 1967, *ApJ*, **147**, 220
 Ferraro V. C. A., Unthank H. W., 1949, *MNRAS*, **109**, 462
 Forman W., Jones C., Cominsky L., Julien P., Murray S., Peters G., Tananbaum H., Giacconi R., 1978, *ApJS*, **38**, 357
 García-Berro E., et al., 2012, *ApJ*, **749**, 25
 Gil J., Melikidze G. I., 2002, *ApJ*, **577**, 909
 Gil J. A., Sendyk M., 2000, *ApJ*, **541**, 351
 Gil J., Melikidze G. I., Geppert U., 2003, *A&A*, **407**, 315
 Göhler E., Wilms J., Staubert R., 2005, *A&A*, **433**, 1079
 Gold T., 1962, *Journal of the Physical Society of Japan Supplement*, **17**, A187
 Goldreich P., Julian W. H., 1969, *ApJ*, **157**, 869
 Hulleman F., van Kerkwijk M. H., Kulkarni S. R., 2000, *Nature*, **408**, 689
 Itoh N., Hayashi H., Kohyama Y., 1993, *ApJ*, **418**, 405
 Kaspi V. M., Gavriil F. P., Woods P. M., Jensen J. B., Roberts M. S. E., Chakrabarty D., 2003, *ApJ*, **588**, L93
 Kepler S. O., et al., 2013, *MNRAS*, **429**, 2934
 Kepler S. O., et al., 2015, *MNRAS*, **446**, 4078
 Külebi B., Jordan S., Euchner F., Gänsicke B. T., Hirsch H., 2009, *A&A*, **506**, 1341
 Malheiro M., Rueda J. A., Ruffini R., 2012, *PASJ*, **64**, 56

- Marsch T. R., Gänsicke B. T., Hümmelich S., et al., 2016, *Nature*, **537**, 374
 Paczynski B., 1990, *ApJ*, **365**, L9
 Potekhin A. Y., Chabrier G., 2000, *Phys. Rev. E*, **62**, 8554
 Ruderman M. A., Sutherland P. G., 1975, *ApJ*, **196**, 51
 Rueda J. A., Boshkayev K., Izzo L., Ruffini R., Lorén-Aguilar P., Külebi B., Aznar-Siguán G., García-Berro E., 2013, *ApJ*, **772**, L24
 Thompson C., Duncan R. C., 1995, *MNRAS*, **275**, 255
 Tsai Y.-S., 1974, *Reviews of Modern Physics*, **46**, 815
 Turolla R., Nobili L., 2013, *ApJ*, **768**, 147
 Usov V. V., 1988, *Soviet Astronomy Letters*, **14**, 258
 Usov V. V., 1993, *ApJ*, **410**, 761
 Usov V. V., 1994, *ApJ*, **427**, 984
 Woods P. M., et al., 2004, *ApJ*, **605**, 378
 Zhu W., Kaspi V. M., Dib R., Woods P. M., Gavriil F. P., Archibald A. M., 2008, *ApJ*, **686**, 520

APPENDIX A: HEATING AND COOLING OF PARTICLE INFLUX BOMBARDMENT

We estimate in this appendix the efficiency of the particle bombardment in heating (and re-radiating) the surface area they hit. We follow the discussion in Gil & Melikidze (2002); Gil et al. (2003) for the heat flow conditions in the polar cap surface of neutron stars, and extended it to the present case of magnetized WDs.

The particles arriving to the surface penetrate up to a depth which can be estimated using the concept of *radiation length* (Cheng & Ruderman 1980). For a carbon composition, the radiation length is $\Sigma \approx 43 \text{ g cm}^{-2}$ (Tsai 1974), so an electron would penetrate the WD surface up to a depth

$$\Delta z \approx \frac{\Sigma}{\rho} = 4.3 \times 10^{-3} \text{ cm} \left(\frac{10^4 \text{ g cm}^{-3}}{\rho} \right). \quad (\text{A1})$$

With the knowledge of the thickness of the layer under the surface where the energy deposition occurs we can proceed to estimate the properties of the diffusion and re-radiation

of the kinetic energy of the particle influx using the heat transport and energy balance equations on the star's surface corresponding to the polar cap. The typically small distances [see Eq. (A1)] allow us to introduce a plane-parallel approximation in the direction parallel to the magnetic field lines, say in the direction z orthogonal to the surface.

The energy balance can be simply written as

$$F_{\text{rad}} = F_{\text{heat}} + F_{\text{cond}}, \quad (\text{A2})$$

where $F_{\text{heat}} = e\Delta V\eta\rho_{\text{GJ}}c$, $F_{\text{cond}} = -\kappa\partial T/\partial z$ and $F_{\text{rad}} = \sigma T^4$, with κ the thermal conductivity (along the z -direction).

Let us first estimate the characteristic cooling time. To do this we switch off energy losses and heating terms in the energy balance equation (A2), i.e. the radiation flux is only given by conduction:

$$\sigma T^4 = -\kappa \frac{\partial T}{\partial z}, \quad (\text{A3})$$

which leads to the heat transport equation

$$c_v \frac{\partial T}{\partial t} = \frac{\partial}{\partial z} \left(\kappa \frac{\partial T}{\partial z} \right). \quad (\text{A4})$$

where c_v is the heat capacity per unit volume. We can therefore obtain the characteristic (e -folding) cooling and heating time assuming the quantities are uniform within the penetration depth Δz , i.e.

$$\Delta t_{\text{cool}} = \frac{\Delta z^2 c_v}{\kappa}, \quad \Delta t_{\text{heat}} = \frac{c_v \Delta z}{\sigma T^3}. \quad (\text{A5})$$

We can now introduce the radiation to heating efficiency parameter

$$\epsilon \equiv \frac{F_{\text{rad}}}{F_{\text{heat}}} = \frac{1}{1 + \Delta t_{\text{heat}}/\Delta t_{\text{cool}}} = \frac{1}{1 + \kappa/(\sigma T^3 \Delta z)}, \quad (\text{A6})$$

which shows that in equilibrium, $\Delta t_{\text{heat}} = \Delta t_{\text{cool}}$, we have $\epsilon = 1/2$.

In estimating the spot temperature (8) we have assumed in Eq. (7) full re-radiation of the influx, namely we assumed $\epsilon = 1$. We proceed now to estimate the realistic values of ϵ from Eq. (A6) to check our assumption. We compute the thermal conductivity from Itoh et al. (1993) and the heat capacity from Chabrier & Potekhin (1998); Potekhin & Chabrier (2000). For example, at a density $\rho = 10^3 \text{ g cm}^{-3}$ and $T = 10^6 \text{ K}$, we have $c_v = 2.7 \times 10^{10} \text{ erg cm}^{-3} \text{ K}^{-1}$ and $\kappa \approx 4 \times 10^{11} \text{ erg cm}^{-1} \text{ s}^{-1} \text{ K}^{-1}$, and Eq. (A6) gives $\epsilon \approx 0.86$. At $T = 10^7 \text{ K}$, we have $c_v = 3.8 \times 10^{11} \text{ erg cm}^{-3} \text{ K}^{-1}$ and $\kappa \approx 3.4 \times 10^{13} \text{ erg cm}^{-1} \text{ s}^{-1} \text{ K}^{-1}$ and $\epsilon \approx 1$.

ON THE INDUCED GRAVITATIONAL COLLAPSE SCENARIO OF GAMMA-RAY BURSTS ASSOCIATED WITH SUPERNOVAE

L. BECERRA^{1,2}, C. L. BIANCO^{1,2}, C. L. FRYER³, J. A. RUEDA^{1,2,4}, R. RUFFINI^{1,2,4}

Draft version October 18, 2016

ABSTRACT

Following the induced gravitational collapse (IGC) paradigm of gamma-ray bursts (GRBs) associated with type Ib/c supernovae, we present numerical simulations of the explosion of a carbon-oxygen (CO) core in a binary system with a neutron-star (NS) companion. The supernova ejecta trigger a *hypercritical* accretion process onto the NS thanks to a copious neutrino emission and the trapping of photons within the accretion flow. We show that temperatures 1–10 MeV develop near the NS surface, hence electron-positron annihilation into neutrinos becomes the main cooling channel leading to accretion rates 10^{-9} – $10^{-1} M_{\odot} \text{ s}^{-1}$ and neutrino luminosities 10^{43} – $10^{52} \text{ erg s}^{-1}$ (the shorter the orbital period the higher the accretion rate). We estimate the maximum orbital period, P_{max} , as a function of the NS initial mass, up to which the NS companion can reach by hypercritical accretion the critical mass for gravitational collapse leading to black-hole (BH) formation. We then estimate the effects of the accreting and orbiting NS companion onto a novel geometry of the supernova ejecta density profile. We present the results of a 1.4×10^7 particle simulation which show that the NS induces accentuated asymmetries in the ejecta density around the orbital plane. We elaborate on the observables associated with the above features of the IGC process. We apply this framework to specific GRBs: we find that X-ray flashes (XRFs) and binary-driven hypernovae (BdHNe) are produced in binaries with $P > P_{\text{max}}$ and $P < P_{\text{max}}$, respectively. We analyze in detail the case of XRF 060218.

1. INTRODUCTION

Recently, Ruffini et al. (2016) proposed a binary nature for the progenitors of both long and short GRBs. In this work we focus on long GRBs associated with supernovae. For such systems the *induced gravitational collapse* (IGC) paradigm (see, e.g., Ruffini et al. 2006, 2008; Izzo et al. 2012a; Rueda & Ruffini 2012; Fryer et al. 2014) indicates as progenitor a binary system composed of a CO core and a neutron-star in a tight orbit. Such a binary system emerged first as a necessity for the explanation of a set of observational features of long GRBs associated with type Ic supernovae (Rueda & Ruffini 2012). Besides, it also appears in the final stages of a well defined evolutionary path which includes the presence of interacting binaries responsible for the formation of stripped-envelope stars such as CO cores leading to type Ic supernovae (Rueda & Ruffini 2012; Becerra et al. 2015; Fryer et al. 2015).

The core-collapse of the CO star produces a supernova explosion ejecting material that triggers an accretion process onto the binary neutron-star companion; hereafter indicated as NS. It was advanced in Ruffini et al. (2016) the existence of two classes of long GRBs depending on whether or not a black-hole (BH) is formed in the hypercritical accretion process onto the NS:

- First, there is the subclass of binary-driven hypernovae (BdHNe), long GRBs with isotropic energy $E_{\text{iso}} \gtrsim 10^{52} \text{ erg}$ and rest-frame spectral peak en-

ergy $0.2 \lesssim E_{p,i} \lesssim 2 \text{ MeV}$. Their prompt emission lasts up to $\sim 100 \text{ s}$ and it is at times preceded by an X-ray emission in the 0.3–10 keV band lasting up to 50 s and characterized by a thermal and a power-law component (i.e. Episode 1 in GRB 090618 in Izzo et al. 2012a). They have a long lasting X-ray afterglow generally composed by a spike, a plateau, followed by a common late power-law behavior when measured in the common source rest-frame (Pisani et al. 2013). For all BdHNe at $z \lesssim 1$, an optical supernova with luminosity similar to the one of supernova 1998bw (Galama et al. 1998) has been observed after 10–15 days in the cosmological rest-frame (see, e.g., Melandri et al. 2014). It has been proposed that this class of GRBs occurs when the NS reaches its critical mass through the above accretion process and forms a BH (see Fig. 1). Under these conditions, the GeV emission becomes observable and it has been proposed to originate from the newly formed BH (Ruffini et al. 2016). This GRB subclass occurs in compact binaries with orbital periods as short as $P \sim 5 \text{ min}$ or binary separations $a \lesssim 10^{11} \text{ cm}$ (Fryer et al. 2014).

- Second, there is the subclass of X-ray flashes (XRFs), long GRBs with isotropic energies in the range $E_{\text{iso}} \approx 10^{47}$ – 10^{52} erg ; spectral peak energies $E_{p,i} \approx 4$ – 200 keV (Amati & Della Valle 2013; Ruffini et al. 2015, 2016). Their prompt emission phase lasts $\sim 10^2$ – 10^4 s and it is generally characterized by a spectrum composed by a thermal component (with radii 10^{10} – 10^{12} cm and temperatures 0.1–2 keV, Campana et al. 2006) and power-law component. They have long lasting X-ray afterglows without the characteristic common late power-law behavior encountered in the BdHNe

¹ Dipartimento di Fisica and ICRA, Sapienza Università di Roma, P.le Aldo Moro 5, I-00185 Rome, Italy

² ICRANet, P.zza della Repubblica 10, I-65122 Pescara, Italy

³ CCS-2, Los Alamos National Laboratory, Los Alamos, NM 87545

⁴ ICRANet-Rio, Centro Brasileiro de Pesquisas Físicas, Rua Dr. Xavier Sigaud 150, 22290–180 Rio de Janeiro, Brazil

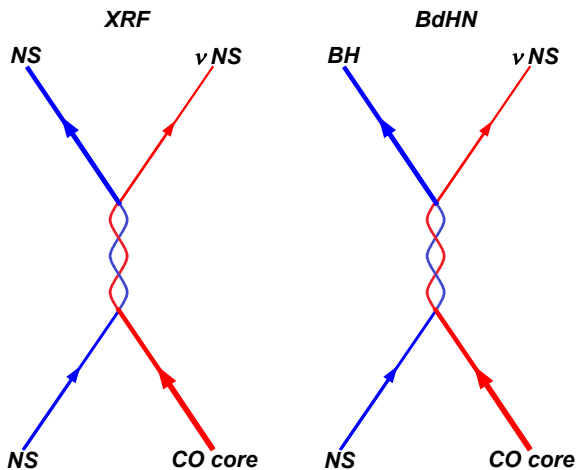


FIG. 1.— Cosmic-matrix of XRFs and BdHNe as introduced in Ruffini (2015a); Ruffini et al. (2015); Ruffini (2015b). See text for details.

(Pisani et al. 2013), nor the characteristic X-ray spike. For all XRFs at $z \lesssim 1$, an optical supernova with luminosity similar to the one of supernova 2010bh (Bufano et al. 2012), has been observed after 10–15 days in the cosmological rest-frame. These sources have been associated within the IGC paradigm to binaries of a CO core and an NS in which there is no BH formation (see Fig. 1): when the accretion is not sufficient to bring the NS to reach the critical mass. This occurs in binaries with orbital periods longer than $P \sim 5$ min or binary separations $a \gtrsim 10^{11}$ cm (Ruffini et al. 2016; Becerra et al. 2015).

The complexity of the above processes leading to two possible outcomes can be summarized schematically within the concept of *Cosmic-Matrix* (*C-matrix*) as first introduced in Ruffini (2015a); Ruffini et al. (2015); Ruffini (2015b). The *C-matrix* describes these systems as a four-body problem in analogy to the case of particle physics (see Fig. 1). The *in-state* is represented by the CO core and the NS companion. The interaction between these two objects given by the hypercritical accretion process triggered by the supernova explosion onto the NS companion, and which is examined in this work, lead to two possible *out-states*: in the case of a BdHN it is formed by the ν NS, i.e. the neutron star left by the supernova explosion of the CO core, and a BH formed from the gravitational collapse of the NS companion of the CO core in the *in-state*. As we have mentioned in XRFs the accretion is not enough to lead to the gravitational collapse of the NS then the *out-state* is a ν NS and another NS (of course more massive than the initial one present in the *in-state*).

It is clear that the observational properties of the IGC binaries are sensitive to the binary parameters which can change the fate of the system. The first estimates of the accretion rate and the possible fate of the accreting NS in an IGC binary were presented in Rueda & Ruffini (2012). To obtain an analytic expression of the accretion rate, such first simple model assumed:

- 1) a pre-supernova homogenous density profile;
- 2) an homologous expansion of the density;

3) constant mass of the NS ($\approx 1.4 M_{\odot}$) and the supernova ejecta ($\approx 4-8 M_{\odot}$). The first application of this model was presented in Izzo et al. (2012a) for the explanation of the Episode 1 of GRB 090618.

In Fryer et al. (2014) there were presented 1D numerical simulations which improved the above model. Specific density and ejection velocity profiles were adopted from numerical simulations of CO core-collapses producing type Ic supernovae. The hydrodynamic evolution of the material entering the NS accretion region was computed on the basis of models of hypercritical accretion in supernova fallback. The integration was followed up to the point where it is finally accreted by the NS on its surface.

In Fryer et al. (2015) the evolution of the gravitational binding energy of the BdHNe was analyzed and it was shown that most of these systems would remain bound after the occurrence of the supernova explosion. This conclusion is in contradiction with the traditional assumption of instantaneous mass ejection which leads to the well-known limit that the system becomes unbound when the binary loses more than half of the total mass. This novel result was obtained by the accurate consideration of two ingredients: the accretion process which changes the mass and the momentum of the binary, and the orbital period which can be as short as the explosion time scale.

In Becerra et al. (2015) the amount of angular momentum transported by the ejecta entering the Bondi-Hoyle region was estimated and how much of it can be transferred to the NS when it is finally accreted. The ejecta density profile was adopted as a power-law in radius and its evolution with time homologous. It is important to recall some of the conclusions obtained in that work:

- 1) the angular momentum the ejecta inside the accretion region is such that it circularizes around the NS forming a disk-like structure;
- 2) the time scale of the disk angular momentum loss is shorter than the time scale at which matter is being captured, so the accretion time scale dominates the evolution;
- 3) for binary periods shorter than some critical value, i.e. $P \lesssim P_{\max}$, the NS can reach either the mass-shedding or secular axisymmetric instability (critical mass point), which induces its gravitational collapse to a BH. In systems with $P > P_{\max}$ the NS gains both mass and angular momentum but not enough to trigger its collapse to a BH. The value of the critical mass has been calculated including the effects of rotation (Cipolletta et al. 2015).

The value of P_{\max} was there computed as a function of the initial NS mass, but only for masses larger than $\approx 1.67 M_{\odot}$, and it was assumed that half of the angular momentum of the disk at the inner disk radius is transferred to the NS.

Although all the above works have already shown that indeed the supernova can induce, by accretion, the gravitational collapse of the NS to a BH, there is still the need of exploring systematically the entire, physically plausible, space of parameters of these systems, as well as to characterize them observationally. The main aims of this work are:

1. To improve the estimate of the accretion rate with respect to the one in Becerra et al. (2015) by includ-

ing effects of the finite size/thickness of the density profile and, for different CO core progenitors leading to different ejected masses.

2. To extend the analysis performed in [Becerra et al. \(2015\)](#) and identify the separatrix of systems in which a BH is formed and the ones where there is not BH formation. This is equivalent to improve the determination of P_{\max} . We extend here the possible range of the initial NS mass and allow for different values of the angular momentum transfer efficiency.
3. To compute the expected luminosity emitted during the hypercritical accretion process onto the NS for a wide range of binary periods shorter (BdHNe) and longer (XRFs) than P_{\max} . With this we can establish the energetic budget that characterizes both XRFs and BdHNe.

In parallel,

- a) We apply the above considerations to specific GRBs by analyzing in detail the specific case of XRF 060218.
- b) We estimate in that specific case the asymmetries created by the orbiting and accreting NS on the ejected matter density profile and the structure of the prompt radiation.
- c) We explore the influence of the prompt X-ray radiation in the late X and optical emission of the supernova and the afterglow.

The article is organized as follows. In [Sec. 2](#) we summarize the framework of the hypercritical accretion of the supernova ejecta onto the NS. [Sec. 3](#) gives details on the computation of the time evolution of both the (gravitational and baryonic) mass and angular momentum of the accreting NS. In [Sec. 4](#) we compute the maximum orbital period, P_{\max} , up to which the induced gravitational collapse of the NS to a BH by accretion can occur. We show in [Sec. 5](#) the asymmetries that the accreting NS produces on the supernova ejecta. In [Sec. 6](#) we summarize the hydrodynamics inside the accretion region, including convective instabilities, and the properties of the neutrino emission. We present in [Sec. 7](#) estimates of the expected luminosities during the hypercritical accretion process. [Sec. 8](#) shows how the radiation from the accretion process as well as the asymmetries in the ejecta influence the supernova emission both in X-rays and in the optical. Finally in [Sec. 9](#) we summarize the results of this work. Additional technical details are presented in a series of appendices.

2. HYPERCRITICAL ACCRETION INDUCED BY THE SUPERNOVA

In order to model the hypercritical accretion process onto the NS, we use the formalism introduced in [Becerra et al. \(2015\)](#). The accretion rate of the ejected material onto the NS is given by ([Hoyle & Lyttleton 1939](#); [Bondi & Hoyle 1944](#); [Bondi 1952](#)):

$$\dot{M}_B = \pi \rho_{\text{ej}} R_{\text{cap}}^2 \sqrt{v_{\text{rel}}^2 + c_{\text{s,ej}}^2}, \quad (1)$$

where R_{cap} is the NS gravitational capture radius

$$R_{\text{cap}} = \frac{2GM_{\text{NS}}}{v_{\text{rel}}^2 + c_{\text{s,ej}}^2}. \quad (2)$$

Here ρ_{ej} and $c_{\text{s,ej}}$ are the density and sound velocity of the ejecta, M_{NS} the NS mass and $\vec{v}_{\text{rel}} = \vec{v}_{\text{ej}} - \vec{v}_{\text{orb}}$, the velocity of the ejecta as seen from an observer at the NS, and G is the gravitational constant. The orbital velocity is $v_{\text{orb}} = \sqrt{GM/a}$, where $M = M_{\text{NS}} + M_{\text{CO}}$ is the total binary mass, $M_{\text{CO}} = M_{\text{env}} + M_{\text{Fe}}$ the total mass of the CO core which is given by the envelope mass M_{env} and the central iron core mass $M_{\text{Fe}} = 1.5 M_{\odot}$. The latter is the mass of the new neutron-star formed in the core-collapse supernova process, hereafter indicated as νNS and its mass $M_{\nu\text{NS}}$, i.e. we adopt $M_{\nu\text{NS}} = M_{\text{Fe}} = 1.5 M_{\odot}$ in agreement with the range of masses predicted under the convective supernova paradigm ([Fryer et al. 2012](#)). For the ejecta velocities, we adopt an homologous explosion model for the supernova expansion, i.e. a velocity proportional to the radius:

$$v_{\text{ej}} = n \frac{r}{t}, \quad (3)$$

where n is the so-called *expansion parameter*. Within this approximation, the density profile evolves as (see, e.g. [Cox 1968](#)):

$$\rho_{\text{ej}}(x, t) = \rho_{\text{ej}}^0(x) \left(\frac{R_{\text{star}}^0}{R_{\text{star}}(t)} \right)^3 \frac{M_{\text{env}}(t)}{M_{\text{env}}^0}, \quad (4)$$

where $x \equiv r/R_{\text{star}}(t)$, M_{env} is the mass ejected (i.e. the mass available to be accreted by the NS), ρ_{ej}^0 is the pre-supernova density profile and R_{star} is the outermost layer of the supernova ejecta. From the velocity profile law we have that R_{star} evolves as:

$$R_{\text{star}}(t) = R_{\text{star}}^0 \left(\frac{t}{t_0} \right)^n, \quad (5)$$

where $t_0 = nR_{\text{star}}^0/v_{\text{star},0}$, being $v_{\text{star},0}$ the velocity of the outermost layer R_{star}^0 .

The pre-supernova density profile of the CO envelope can be well approximated by a power-law profile, i.e.:

$$\rho_{\text{ej}}^0 = \rho_{\text{core}} \left(\frac{R_{\text{core}}}{r} \right)^m, \quad R_{\text{core}} < r < R_{\text{star}}^0. \quad (6)$$

We show in [table 1](#) the properties of the pre-supernova CO cores produced by low-metallicity progenitors with initial zero-age main sequence (ZAMS) masses $M_{\text{ZAMS}} = 15, 20, \text{ and } 30 M_{\odot}$ obtained with the Kepler stellar evolution code ([Woosley et al. 2002](#)).

We now improve the treatment in [Becerra et al. \(2015\)](#) taking into account the finite size of the envelope. We thus modify the above density profile by introducing boundaries to the supernova ejecta through density cut-offs at the outermost and innermost layers of the ejecta, namely:

$$\rho_{\text{ej}}^0 = \hat{\rho}_{\text{core}} \ln \left(\frac{r}{\hat{R}_{\text{core}}} \right) \left(\frac{R_{\text{star}}}{r} - 1 \right)^m, \quad (7)$$

where $\hat{R}_{\text{core}} < r < R_{\text{star}}$. The condition that the modified profile has the same ejecta mass with respect to the unmodified power-law profile implies $\hat{R}_{\text{core}} < R_{\text{core}}$.

TABLE 1
PROPERTIES OF THE PRE-SUPERNOVA CO CORES

Progenitor $M_{\text{ZAMS}} (M_{\odot})$	ρ_{core} (10^8 g cm^{-3})	R_{core} (10^7 cm)	M_{env} (M_{\odot})	R_{star}^0 (10^9 cm)	m
15	3.31	5.01	2.079	4.49	2.771
20	3.02	7.59	3.89	4.86	2.946
30	3.08	8.32	7.94	7.65	2.801

NOTE. — CO cores obtained for the low-metallicity ZAMS progenitors with $M_{\text{ZAMS}} = 15, 20,$ and $30 M_{\odot}$ in Woosley et al. (2002). The central iron core is assumed to have a mass $M_{\text{Fe}} = 1.5 M_{\odot}$, which will be the mass of the νNS , denoted here as $M_{\nu\text{NS}}$, formed out of the supernova process.

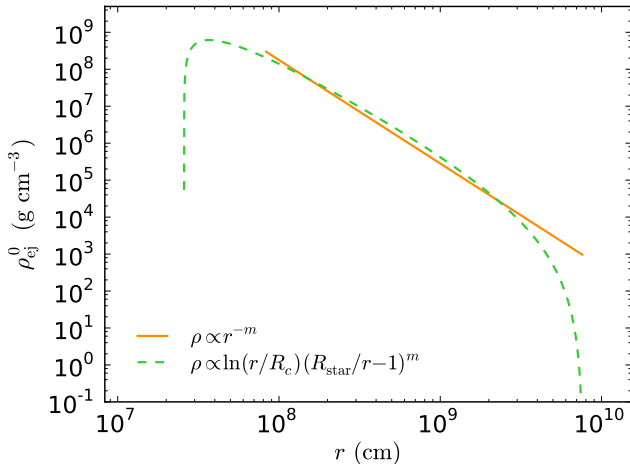


FIG. 2.— Pre-supernova density profile produced by the $M_{\text{ZAMS}} = 30 M_{\odot}$ progenitor of table 1. We compare and contrast the power-law density profile (solid curve) with a modified profile (dashed curve) with density cut-offs at the outermost and innermost ejecta layers following Eqs. (6) and (7). The two profiles have the same envelope mass.

Fig. 2 shows the pre-supernova density profile described by equations (6) and (7) for the $M_{\text{ZAMS}} = 30 M_{\odot}$. For these parameters we have $\hat{R}_{\text{core}} = 0.31 R_{\text{core}}$ and $\hat{\rho}_{\text{core}} = 567.67 \text{ g cm}^{-3}$.

Introducing the homologous expansion for the description of the evolution of the supernova ejecta, equation (1) becomes:

$$\frac{\dot{\mu}_B(\tau)}{(1 - \chi\mu_B(\tau))M_{\text{NS}}^2} = \frac{\tau^{(m-3)n}}{\hat{r}^m} \ln\left(\frac{\hat{r}}{\hat{r}_c\tau^n}\right) \frac{(\hat{r}_s - \hat{r}\tau^{-n})^m}{[1 + \eta\hat{r}/\tau^2]^{3/2}}, \quad (8)$$

where

$$\tau \equiv \frac{t}{t_0}, \quad \mu_B(\tau) \equiv \frac{M_B(\tau)}{\Sigma_B}, \quad \hat{r} \equiv 1 - \frac{R_{\text{cap}}}{a}, \quad (9)$$

and the parameters χ, Σ_B and η depend on the properties of the binary system before the supernova explosion:

$$\Sigma_B = \frac{4\pi\hat{\rho}_c G^2 M_{\odot}^2 t_0}{v_{\text{orb}}^3}, \quad \chi = \frac{\Sigma_B}{M_{\text{env}}^0}, \quad \eta = \left(\frac{na}{t_0 v_{\text{orb}}}\right)^2, \quad (10)$$

where $M_{\text{env}}^0 \equiv M_{\text{env}}(t = t_0) = M_{\text{env}}(\tau = 1)$.

Fig. 3 shows the time evolution of the mass accretion rate onto the NS of initial $1.4 M_{\odot}$ and selected orbital periods. The other binary parameters are: expansion parameter $n = 1$, ejecta outermost layer velocity $v_{\text{star},0} = 2 \times 10^9 \text{ cm s}^{-1}$, and the supernova ejecta profile is the one obtained for the CO core of the $M_{\text{ZAMS}} = 20 M_{\odot}$

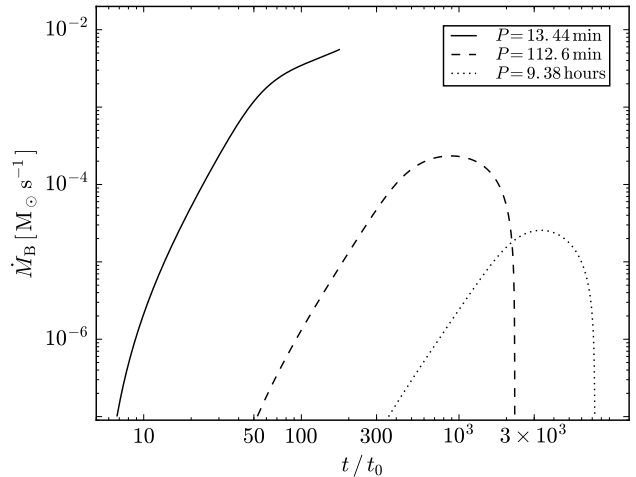


FIG. 3.— Time evolution of the accretion rate onto a NS of initial mass $1.4 M_{\odot}$ for the following binary parameters: expansion parameter $n = 1$, an ejecta outermost layer velocity $v_{\text{star},0} = 2 \times 10^9 \text{ cm s}^{-1}$ and the supernova ejecta profile is the one obtained for the CO core of the $M_{\text{ZAMS}} = 20 M_{\odot}$ progenitor of table 1. For the above progenitor and velocity $t_0 = 2.4 \text{ s}$. Three selected orbital periods are shown: $P = 13.44 \text{ min}$, 112.6 min and 9.38 h which correspond to binary separation distances $a = 2.46 \times 10^{10} \text{ cm}$, $1.01 \times 10^{11} \text{ cm}$, and $2.96 \times 10^{11} \text{ cm}$, respectively. The solid line corresponds to a case in which the NS reaches the critical mass and collapses to a BH (end point of the curve). In the two other cases, owing to the longer orbital period, there is no induced gravitational collapse of the NS to a BH (see Fig. 5 in Sec. 4 for further details).

progenitor of table 1.

We can see from Fig. 3 that the shorter(smaller) the orbital period(separation) the higher the accretion rate and the shorter the time it peaks. In appendix A we derive, following simple arguments, analytic formulas for the peak accretion rate and time which can be useful to get straightforward estimates of these systems.

3. TIME EVOLUTION OF THE ACCRETING NS

Becerra et al. (2015) showed that the supernova ejecta has enough angular momentum to circularize around the NS in a sort of disk-like structure. Thus, the accreted material will transfer both baryonic mass and angular momentum to the NS.

The equilibrium NS configurations form a two-parameter family given by the mass (baryonic or gravitational) and angular momentum (or angular velocity). Namely the NS gravitational mass, M_{NS} , is in general a function of the NS baryonic mass, M_b , and angular momentum, J_{NS} . In a similar way the angular momentum contributes to the mass of a BH (Christodoulou & Ruffini 1971). It is then clear that the evolution of the

NS gravitational mass is given by:

$$\dot{M}_{\text{NS}}(t) = \left(\frac{\partial M_{\text{NS}}}{\partial M_b} \right)_J \dot{M}_b + \left(\frac{\partial M_{\text{NS}}}{\partial J_{\text{NS}}} \right)_{M_b} \dot{J}_{\text{NS}}, \quad (11)$$

We assume that all the (baryonic) mass entering the NS capture region will be accreted by the NS, i.e.:

$$M_b(t) = M_b(t_0) + M_B(t), \quad (12)$$

then $\dot{M}_b \equiv \dot{M}_B$.

For the relation between the NS gravitational mass, the baryonic mass, and the angular momentum for the NS equilibrium configurations, namely the NS gravitational binding energy formula, we use the recent result obtained in [Cipolletta et al. \(2015\)](#):

$$\frac{M_b}{M_\odot} = \frac{M_{\text{NS}}}{M_\odot} + \frac{13}{200} \left(\frac{M_{\text{NS}}}{M_\odot} \right)^2 \left(1 + \frac{1}{137} j_{\text{NS}}^{1.7} \right), \quad (13)$$

where $j_{\text{NS}} \equiv cJ_{\text{NS}}/(GM_\odot^2)$, and which is independent on the nuclear equation of state (EOS).

The torque on the NS by the accreted matter is given by

$$\dot{J}_{\text{NS}} = \xi l(R_{\text{in}}) \dot{M}_B, \quad (14)$$

where R_{in} is the disk inner boundary radius, $l(R_{\text{in}})$ is the angular momentum per unit mass of the material located at $r = R_{\text{in}}$, and $\xi \leq 1$ is a parameter that accounts for the efficiency of the angular momentum transfer. The precise value of ξ depends mainly: 1) on possible angular momentum losses (e.g. by jetted emission during accretion) and 2) on the deceleration of the matter in the disk inner radius zone.

The inner disk radius is given by the maximum between the radius of the last stable circular orbit, r_{lso} , and the NS radius, R_{NS} . Namely, $R_{\text{in}} = \max(r_{\text{lso}}, R_{\text{NS}})$. When the disk extends until the NS surface, $l(R_{\text{in}})$ is given by the Keplerian orbit with radius equal to the NS equatorial radius. On the other hand, if $R_{\text{NS}} < r_{\text{lso}}$, $l(R_{\text{in}})$ is given by the last stable circular orbit. Summarizing:

$$l(R_{\text{in}}) = \begin{cases} l_{\text{K}}(R_{\text{NS}}), & \text{for } R_{\text{NS}} > r_{\text{lso}} \Rightarrow R_{\text{in}} = R_{\text{NS}}, \\ l_{\text{lso}}, & \text{for } R_{\text{NS}} \leq r_{\text{lso}} \Rightarrow R_{\text{in}} = r_{\text{lso}}. \end{cases} \quad (15)$$

We show hereafter the results for three selected NS nuclear EOS: NL3, TM1 and GM1 ([Cipolletta et al. 2015](#)). For these EOS and assuming that the NS is initially non-rotating, we have that $r_{\text{lso}} = 6GM_{\text{NS}}/c^2 > R_{\text{NS}}$ for $M_{\text{NS}} \gtrsim [1.78, 1.71, 1.67] M_\odot$, for the NL3, TM1 and GM1 EOS, respectively.

For the axially symmetric exterior spacetime around a rotating NS, l_{lso} is well approximated by ([Becerra et al. 2015](#)):

$$l_{\text{lso}} \approx 2\sqrt{3} \frac{GM_{\text{NS}}}{c} \left[1 - \frac{1}{10} \left(\frac{j_{\text{NS}}}{M_{\text{NS}}/M_\odot} \right)^{0.85} \right], \quad (16)$$

for co-rotating particles.

On the contrary, for $M_{\text{NS}} \lesssim 1.7 M_\odot$ we have $r_{\text{lso}} < R_{\text{NS}}$ and thus $R_{\text{in}} = R_{\text{NS}}$. We shall adopt for this case the Hartle's slow-rotation approximation. The angular momentum per unit mass of a Keplerian orbit with a radius

equal to the NS radius is, within this approximation, given by ([Boshkayev et al. 2016](#))

$$l_{\text{K}}(u) = \frac{GM_{\text{NS}}}{c\sqrt{u(1-3u)}} \left[1 - j_{\text{NS}} \frac{3u^{3/2}(1-2u)}{1-3u} + j_{\text{NS}}^2 \frac{u^4(3-4u)}{(1-2u)^2(1-3u)} \right], \quad (17)$$

where $u \equiv GM_{\text{NS}}/(c^2 R_{\text{NS}})$. This formula can be also obtained by taking the second order slow rotation limit of the angular momentum of the last stable circular orbit around a Kerr BH ([Rees et al. 1974](#); [Boshkayev et al. 2012, 2016](#)).

Therefore, by solving (numerically) simultaneously equations (8) and (14), with the aid of Eqs. (11–17), it is possible to follow the evolution of the NS mass and angular momentum during the accretion process.

4. INDUCED GRAVITATIONAL COLLAPSE OF THE NS

We proceed now to calculate the binary parameters which discriminate systems in which the NS can reach by accretion its critical mass (M_{crit}) and consequently collapse to a BH, from the systems in which the accretion is not sufficient to induce such a collapse.

The stability of the accreting NS is limited by two main instability conditions: the mass-shedding or Keplerian limit, and the secular axisymmetric instability. Mass-shedding occurs when the centrifugal force balances the gravitational one. Thus, for a given gravitational mass (or central density), it is given by the rotating configuration with angular velocity equal to the Keplerian velocity of test-particles orbiting at the star's equator. In this limit the matter at the surface is marginally bound to the star and small perturbations will cause mass loss to bring the star stable again or otherwise to bring it to a point of dynamical instability point ([Stergioulas 2003](#)).

At the secular axisymmetric instability point the star the star is unstable against axisymmetric perturbations. It is expected to evolve first quasi-stationarily to then find a dynamical instability point where gravitational collapse takes place ([Stergioulas 2003](#)). Using the turning-point method ([Friedman et al. 1988](#)), [Cipolletta et al. \(2015\)](#) computed the critical mass due to this instability point for the NL3, GM1 and TM1 EOS. They showed that the numerical results of the critical NS mass are well fitted, with a maximum error of 0.45%, by the formula

$$M_{\text{NS}}^{\text{crit}} = M_{\text{crit}}^{J=0} (1 + k j_{\text{NS}}^p), \quad (18)$$

where the parameters k and p depends of the nuclear EOS and $M_{\text{crit}}^{J=0}$ is the critical mass in the non-rotating case (see table 2). It can be checked that the latter is, as expected, below the $3.2 M_\odot$ critical mass upper bound by ([Rhoades & Ruffini 1974](#)).

Thus, a NS with initial mass $M_{\text{NS}}(t_0)$ can reach M_{crit} if it accretes an amount of mass $\Delta M_{\text{acc}} = M_{\text{crit}} - M_{\text{NS}}(t_0)$ from the supernova ejecta. Given the initial NS mass, the CO core mass, and the supernova ejecta profile and its velocity, the accretion rate increases for shorter binary separation, namely for shorter orbital periods ([Becerra et al. 2015](#); [Fryer et al. 2014](#)). Therefore, there exists a maximum orbital period, denoted here to as P_{max} , up to

TABLE 2
CRITICAL MASS (AND CORRESPONDING RADIUS) FOR SELECTED PARAMETERIZATIONS OF NUCLEAR EOS OBTAINED IN CIPOLLETTA ET AL. (2015).

EOS	$M_{\text{crit}}^{J=0} (M_{\odot})$	$R_{\text{crit}}^{J=0} (\text{km})$	$M_{\text{max}}^{J \neq 0} (M_{\odot})$	$R_{\text{max}}^{J \neq 0} (\text{km})$	p	k	f_K (kHz)
NL3	2.81	13.49	3.38	17.35	1.68	0.006	1.34
GM1	2.39	12.56	2.84	16.12	1.69	0.011	1.49
TM1	2.20	12.07	2.62	15.98	1.61	0.017	1.40

NOTE. — In the last column we have also reported the rotation frequency of the critical mass configuration in the rotating case. This value corresponds to the frequency of the last configuration along the secular axisymmetric instability line, i.e the configuration that intersects the Keplerian mass-shedding sequence.

which, given $M_{\text{NS}}(t_0)$ (and all the other binary parameters), the NS can accrete this precise amount of mass, ΔM_{acc} .

For example, for a NS with an initial gravitational mass $M_{\text{NS}}(t_0) = 2 M_{\odot}$ accreting the ejected material from the supernova explosion of the $30 M_{\odot}$ ZAMS progenitor (see table 1), $v_{\text{star},0} = 2 \times 10^9 \text{ cm s}^{-1}$, expansion parameter $n = 1$ and angular momentum transfer efficiency $\xi = 0.5$, we find $P_{\text{max}} \approx 26 \text{ min}$. Fig. 4 shows the evolution of such a NS for two different binary periods, $P = 5 \text{ min} < P_{\text{max}}$ and $P = 50 \text{ min} > P_{\text{max}}$. We can see that only for the system with $P < P_{\text{max}}$ the NS accretes enough matter to reach the critical mass for gravitational collapse, given by Eq. (18).

Fig. 5 shows P_{max} , obtained from our numerical simulations, for different values of the NS initial gravitational mass, keeping all the other binary parameters fixed. In this figure we show the results for pre-supernova properties listed in table 1 for the CO progenitors with $M_{\text{ZAMS}} = 20 M_{\odot}$ (left panel) and $30 M_{\odot}$ (right panel), a free expansion for the supernova explosion ($n = 1$), and a velocity of the outermost supernova ejecta layer, $v_{\text{star},0} = 2 \times 10^9 \text{ cm s}^{-1}$.

A few comments on Fig. 5 are in order:

1. The increase of P_{max} with the initial NS mass value $M_{\text{NS}}(0)$ can be easily understood from the fact that the larger $M_{\text{NS}}(0)$ the lower the amount of mass needed to reach the critical NS mass.
2. There is a transition in the behavior at $M_{\text{NS}}(0) \approx 1.7 M_{\odot}$. This occurs because configurations with $M_{\text{NS}}(0) \lesssim 1.7 M_{\odot}$ have the disk extending up to the NS surface, correspondingly we used the angular momentum per unit mass given by equation (17). For larger initial masses, accretion occurs from the last stable orbit and we used equation (16). Thus, the difference around this transition point are attributable to the use of the slow rotation approximation for masses $M_{\text{NS}}(0) < 1.7 M_{\odot}$. We recall that Becerra et al. (2015) considered only initial NS masses $M_{\text{NS}}(0) \gtrsim 1.7 M_{\odot}$ so this transition is not observed there.
3. In Becerra et al. (2015) an angular momentum transfer efficiency parameter $\xi = 0.5$ was adopted. In order to see the effect of such a parameter we adopted here in the simulations the maximum possible value $\xi = 1$. Values of ξ lower than unity account for possible angular momentum losses between the inner disk radius and the NS surface. This implies that the values of P_{max} in Fig. 5 are upper limits to the maximum orbital period for BH

formation. Namely, a value $\xi < 1$ leads to lower values of P_{max} . For instance, in the right panel of Fig. 5 we see that for $M_{\text{NS}}(0) = 1.8 M_{\odot}$ and the NL3 EOS, $P_{\text{max}} \approx 70 \text{ min}$. We checked that, for $\xi = 0.5$, the same initial mass and EOS would instead lead to $P_{\text{max}} \approx 20 \text{ min}$.

4. Because of the highly efficient angular momentum transfer ($\xi = 1$), the NS in the systems of Fig. 5 ends at the mass-shedding limit. In the case of lower values of ξ , the NS might end directly at the secular axisymmetric instability with a lower values of the critical mass with respect to the maximum mass along the Keplerian mass-shedding sequence. We have checked, for instance in the case of $\xi = 0.5$ (the one adopted in Becerra et al. (2015)) and the NL3 EOS, that this occurs when the initial NS mass is close to the non-rotating critical mass value, e.g. for $M_{\text{NS}}(0) \gtrsim 2.2 M_{\odot}$.
5. We recall that in Becerra et al. (2015) only the case of the $M_{\text{ZAMS}} = 30 M_{\odot}$ progenitor was analyzed. We studied here different progenitors. At first sight, it might appear contradictory that the left panel of Fig. 5, which is for a less massive CO core with respect to the one the right panel, shows longer values of the maximum orbital period for BH formation. The reason for this is as follows. First, the binary separation satisfies $a \propto (M_t P^2)^{1/3}$ where M_t is the total binary mass. Thus, for given NS mass and binary period, a less massive CO core implies a less massive binary and a smaller orbit by a factor $a_1/a_2 = (M_{t1}/M_{t2})^{1/3}$. A tighter orbit implies a supernova ejecta density at the NS position higher by a factor $\rho_{\text{ej},1}/\rho_{\text{ej},2} = (a_2/a_1)^3 = M_{t2}/M_{t1}$, hence the accretion rate which is proportional to the density [see equation (1)].

Thus we have shown that in systems with $P \leq P_{\text{max}}$ the induced gravitational collapse of the accreting NS to a BH occurs. These systems explain the BdHNe (Fryer et al. 2015; Becerra et al. 2015; Fryer et al. 2014). We do not simulate in this work the complex process of gravitational collapse rather we assume BH formation at the moment when the NS reaches the critical mass value. We also adopt the mass of the newly formed BH as given by the critical NS mass value.

In systems with $P > P_{\text{max}}$, the NS does not accrete enough matter from the supernova ejecta and the collapse to a BH does not occur. As we show below, these systems explain XRFs (see also Ruffini et al., in preparation, for more details).

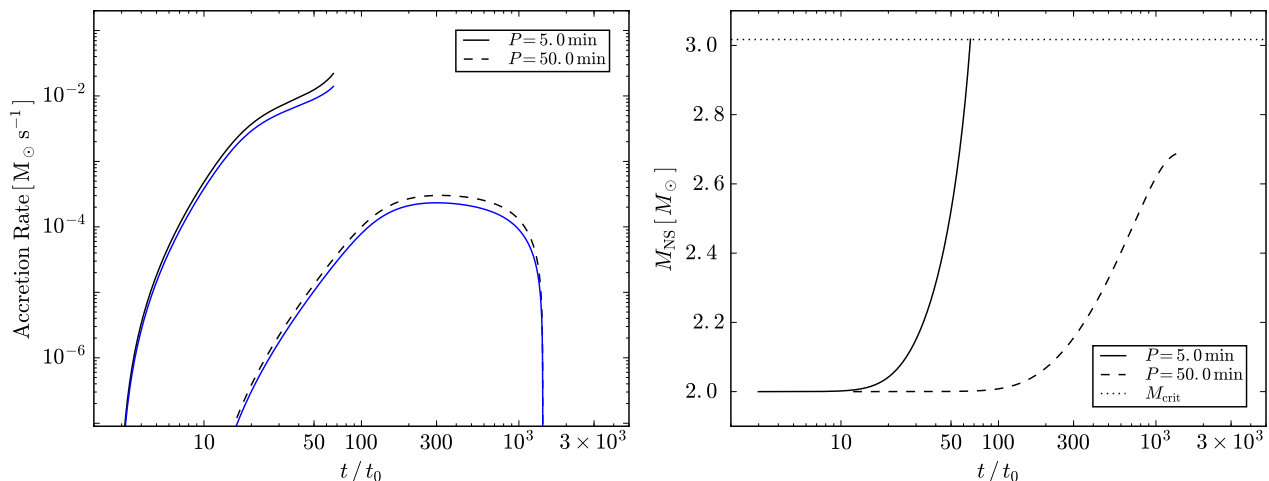


FIG. 4.— Left panel: time evolution of the baryonic mass accretion rate (black curve) obtained from Eq. (8) and rate of increase of the NS gravitational mass obtained from Eq. (11). Right panel: Evolution of the NS gravitational mass. We use here the ejecta from the explosion of a CO core by the $30 M_{\odot}$ ZAMS progenitor, $v_{\text{star},0} = 2 \times 10^9 \text{ cm s}^{-1}$, expansion parameter $n = 1$ and angular momentum transfer efficiency $\xi = 0.5$. Two binary periods are here used: $P = 5 \text{ min} < P_{\text{max}}$ (solid curves) and $P = 50 \text{ min} > P_{\text{max}}$ (dashed curves). For this binary parameters $P_{\text{max}} \approx 26 \text{ min}$. It can be seen only the NS in the system with $P < P_{\text{max}}$ accretes enough matter to reach the critical mass (dotted line) for gravitational collapse.

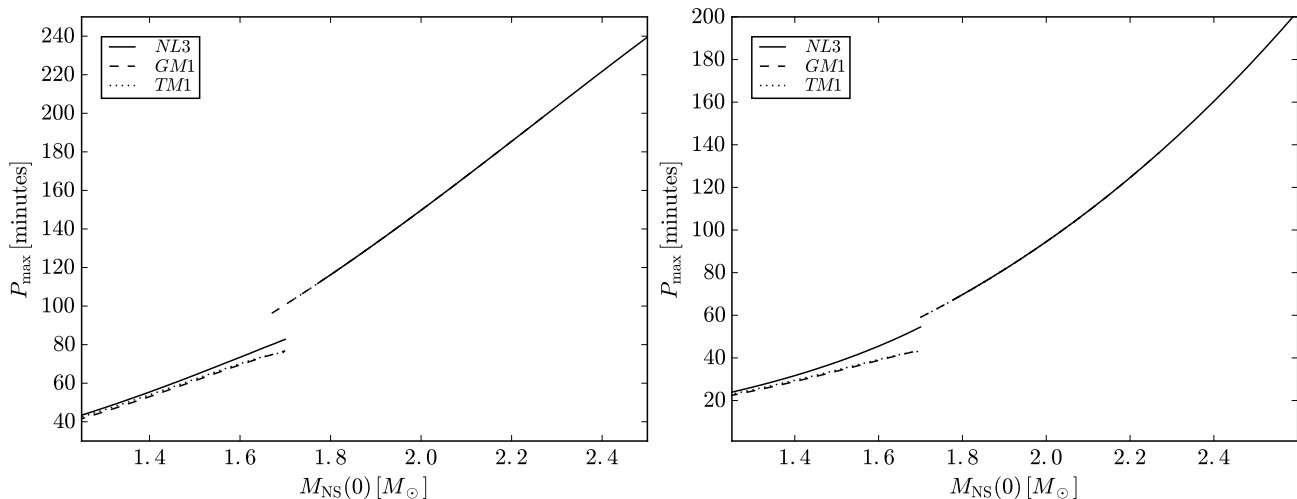


FIG. 5.— Maximum orbital period for which the NS with initial mass $M_{\text{NS}}(0)$ collapses to a BH by accretion of supernova ejecta material. We have adopted a free expansion for the supernova ejecta ($n = 1$), an outermost supernova layer velocity $v_{\text{star},0} = 2 \times 10^9 \text{ cm s}^{-1}$. The left and right panels show the results for CO cores left by $M_{\text{ZAMS}} = 20 M_{\odot}$ and $30 M_{\odot}$ progenitors, respectively (see table 1). The apparent transition at $M_{\text{NS}}(0) \approx 1.7 M_{\odot}$ is explained as follows: configurations with $M_{\text{NS}}(0) \lesssim 1.7 M_{\odot}$ have the disk extending up to the NS surface, correspondingly we used the angular momentum per unit mass given by Eq. (17), instead for larger initial masses the accretion occurs from the last stable orbit and we used equation (16). Thus, the difference around this transition point are attributable to the use of the slow rotation approximation for masses $M_{\text{NS}}(0) < 1.7 M_{\odot}$. See the text for more details.

5. SUPERNOVA EJECTA ASYMMETRIES INDUCED BY THE NS

For isolated supernova explosions, or for very wide binaries with negligible accretion rates, the density of the supernova ejecta would approximately follow the homologous evolution given by equation (4) with constant ejecta mass, i.e. $M_{\text{env}}(t) = M_{\text{env}}^0$, i.e. the density will decrease with time following a simple power-law $\rho_{\text{ej}}(t) \propto t^{-3n}$, with n the expansion parameter, keeping its spherical symmetry about the explosion site (see, e.g., Fig. 6). However, for explosions occurring in close binaries with compact companions such as NSs or BHs, the supernova ejecta is subjected to a strong gravitational field which produces at least two non-negligible effects: 1) an accre-

tion process on the NS that subtracts part of the ejecta mass, and 2) a deformation of the supernova fronts closer to the accreting NS companion. As we show below, the conjunction of these effects can generate large changes in the density profile of the ejecta in a region around the orbital plane.

In order to visualize the above effects we have simulated the evolution of the supernova layers in presence of the NS during the accretion process (see Figs. 6 and 7). Thus, we followed the three-dimensional motion of N particles in the gravitational field of the orbiting NS. Following Becerra et al. (2015), we consider the gravitational field of the NS on the supernova ejecta including the effects of the orbital motion as well as the changes in

the NS gravitational mass as described above in Sec. 2 via the Bondi formalism. The supernova matter is described as formed by point-like particles whose trajectory was computed by solving the Newtonian equation of motion. We plan to do an SPH simulation of this process and expect to present the results in a forthcoming publication.

The initial conditions of the supernova ejecta are computed assuming the supernova layers move via homologous velocity distribution in free expansion (i.e. evolving with $n = 1$). The initial power-law density profile of the CO envelope is simulated by populating the inner layers with more particles, as follows. The total number of particles is $N = N_r \times N_\theta \times N_\phi$ and for symmetry reasons, we simulate only the north hemisphere of the supernova; thus the polar and azimuthal angles are divided as $\Delta\theta = (\pi/2)/N_\theta$ and $\Delta\phi = 2\pi/N_\phi$, respectively. For the radial coordinate we first introduce the logarithmic coordinate $x = \log(r)$ and $\Delta x = (x_s - x_c)/N_r$, where $x_s = \log(R_{\text{star}})$ and $x_c = \log(R_{\text{core}})$. Thus, the thickness of each layer is $\Delta r = r_i(10^{\Delta x} - 1)$, where r_i is the location of the layer. The mass of each particle of the i -layer is: $m_i = 4\pi r_i^3 \ln(10) \Delta x \rho(r_i) / (2N_\theta N_\phi)$.

Let us assume, for the sake of example, the $M_{\text{ZAMS}} = 30 M_\odot$ progenitor of table 1 which gives a CO core with envelope profile $\rho_{\text{ej}}^0 \approx 3.1 \times 10^8 (8.3 \times 10^7 / r)^{2.8} \text{ g cm}^{-3}$ and $R_{\text{star}}^0 = 7.65 \times 10^9 \text{ cm}$. This implies that, for a total number of $N = 10^6$ particles in the simulation, the particles of the innermost radius $r_i = R_{\text{core}} = 8.3 \times 10^7 \text{ cm}$ with density $\rho_{\text{ej}}^0(r_i) = 3.1 \times 10^8 \text{ g cm}^{-3}$ have mass $m_i \approx 2 \times 10^{-5} M_\odot$ while, the particles of the outermost radius $r_i = R_{\text{star}}^0$, would have $m_i \approx 6 \times 10^{-6} M_\odot$. In addition, we assume that particles crossing the Bondi-Hoyle radius are captured and accreted by the NS so we removed them from the system as they reach that region. We removed these particles according to the results obtained from the numerical integration of Eq. (8).

Fig. 6 shows in detail the orbital plane of an IGC binary at selected times of its evolution. The NS has an initial mass of $2.0 M_\odot$; the CO core is the one obtained by the $M_{\text{ZAMS}} = 30 M_\odot$ progenitor (see table 1), which leads to a total ejecta with mass $7.94 M_\odot$ and an iron core that left a νNS of $1.5 M_\odot$. The orbital period of the binary is $P \approx 5 \text{ min}$, i.e. a binary separation $a \approx 1.5 \times 10^{10} \text{ cm}$, and we have adopted an angular momentum transfer efficiency parameter $\xi = 0.5$. The evolution of the accretion rate and the gravitational mass of the NS in this system are the ones shown in Fig. 4. As it can be seen, for the above parameters the NS reaches the critical mass and collapses to form a BH (see also Fig. 5 and conclusion 3 in Sec. 6).

In the simulation shown in Fig. 6 we adopted two millions of particles per solar mass of ejecta so in this simulation we have followed the three-dimensional motion of $N = 2 \times 10^6 (M_{\text{env}}^0 / M_\odot) \approx 1.6 \times 10^7$ particles in the gravitational field of the orbiting NS. To estimate the ejecta density we have chosen a thickness Δz around the orbital plane. For the plots in Fig. 6 we have adopted $\Delta z \approx 0.05a \approx 7.1 \times 10^8 \text{ cm}$.

The left upper panel shows the binary at the initial time of the process, i.e. $t = t_0 = R_{\text{star}}^0 / v_{\text{star},0} = 3.82 \text{ s}$, the first instant of the ejecta radial expansion.

The right upper panel shows the instant at which

the accretion process begins, namely at $t = t_{\text{acc},0} \approx a/v_{0,\text{star}} = 7.7 \text{ s}$. Owing to their fast velocity, the accretion rate of the first layers is low and they escape almost undisturbed, so the supernova ejecta at these times keeps its original spherical symmetry.

The left lower panel shows the binary at the instant in which the accreting NS reaches the critical mass, hence the instant of formation of the BH, at $t = t_{\text{coll}} = 254 \text{ s} \approx 0.85P$. The BH mass is thus set by the critical NS mass, i.e. $M_{\text{BH}} = M_{\text{crit}} \approx 3 M_\odot$ (see Fig. 4). This figure also evidences the asymmetry on the supernova density as induced by the presence of the companion and its increasing gravitational field due to the ongoing accretion process onto it. Indeed, it can be seen how the supernova ‘center’ has been shifted from the explosion site originally at the $(0,0)$ position (see left upper panel), to the approximate position $(0,2)$. Thus, the layers of the ejecta are displaced as a result of the gravitational attraction of the orbiting NS. This can be understood as follows. When the NS passes over the northern hemisphere, it attracts the northern region of the ejecta towards it. Consequently, that part of the ejecta gain velocity in the northern direction. The same effect occurs in the other regions of the orbit, however the effect is asymmetric because, by the time the NS passes, say over the southern hemisphere, it attracts layers moving at slower velocity with respect to the ones it had attracted in the northern hemisphere before. The reason for this is that the southern fastest layers have moved further already while the NS were passing the northern side. This effect is indeed incorporated in our simulation which follows the trajectory of each of the 14 million particles.

It can be also seen in this figure a stream of matter (**one-armed flow**) of negligible mass with respect to the total mass escaping from the system. As we have mentioned above, the NS attracts some layers increasing their velocity. As a result some material can reach escape velocity to leave the binary system forming this unbound debris. The appearance of a one-armed flow (instead of two-armed flows) is because the center-of-mass is located roughly at the CO core position, thus the NS is in practice orbiting the CO core. If the two masses were of comparable masses, (e.g. as in the case of binary NS mergers), they would move around a common center-of-mass lying in between them. In such systems the momentum transfer is more symmetric leading to a symmetric two-armed flow structure. The one-armed flow in our system is, in this sense, more similar to the one that appears in the tidal disruption of a small body by a supermassive BH.

The right lower panel shows the system 100 s after the BH formation, namely at $t = t_{\text{coll}} + 100 \text{ s} = 354 \text{ s} \approx 1.2P$. Thus, this figure shows the new binary system formed by the νNS , out of the supernova, and the BH from the gravitational collapse of the NS. The νNS is at the $(0,0)$ position and it is represented by the white filled circle. The BH is in this instant of time located at the $(0.5, 1.7)$ position and it is represented by the black filled circle. It can be seen the increasing asymmetry of the supernova ejecta around the orbital plane. We note the presence of ejecta in the vicinity of the newly formed BH, the latter sited at the approximate position $(0.5, 1.5)$. It is interesting that part of these ejecta can indeed cause a subsequent accretion process onto the newly formed

BH. The possible outcomes of this process deserve further attention which will be analyzed elsewhere (Ruffini et al., in preparation).

We have shown above the evolution of an IGC binary with very short orbital period of $P \approx 5$ min, for which it occurs the gravitational collapse of the NS of the CO core. Besides the formation of a BH, we have evidenced the asymmetry caused by the presence and accretion onto the NS on the supernova ejecta density. It is natural to ask if these asymmetries also appear for less compact binaries. For comparison, we show in Fig. 7 the results of a numerical simulation for a binary with orbital period $P \approx 50$ min, in which the NS does not reach the critical mass during the entire accretion process (see Sec. 6). The evolution of the accretion rate and the gravitational mass of the NS in this system are shown in Fig. 4.

In these kind of systems, all the ejecta layers passed the NS position. Thus, the total duration of the accretion process, denoted here t_{acc} , is approximately given by the time it takes to the innermost layer of the ejecta to overcome the NS position, i.e. $t_{\text{acc}} \approx a/v_{\text{inner}}$, where $v_{\text{inner}} = (\dot{R}_{\text{core}}/R_{\text{star}}^0)v_{\text{star},0}$ using the homologous expansion assumption. The snapshot corresponds to a time $t = 2667$ s ≈ 44 min $\approx t_{\text{acc}}/4$. To estimate the ejecta density we have chosen in this example $\Delta z = 0.08a \approx 5.3 \times 10^9$ cm. It is interesting that although the NS is in this case farther away from the CO core, it still induces a high asymmetry on the supernova ejecta. We shall investigate elsewhere if this mechanism could explain the asymmetries observed in some type Ibc supernovae (Tanaka et al. 2009; Taubenberger et al. 2009, see, e.g.,). We here constrain ourselves in section 8, instead, to the consequences that the ejecta asymmetries have on the supernova emission (both in X-rays and in the optical).

6. HYDRODYNAMICS INSIDE THE ACCRETION REGION

We turn now to analyze in detail the properties of the system inside the Bondi-Hoyle accretion region. Fig. 3 shows the mass accretion rate onto the NS of initial mass $1.4 M_{\odot}$. We can see that the accretion rate can be as high as $\sim 10^{-1} M_{\odot} \text{ s}^{-1}$. For these high accretion rates we can draw some general properties:

1. We can neglect the effect of the NS magnetic field since for $\dot{M}_B > 2.6 \times 10^{-8} M_{\odot} \text{ s}^{-1}$ the magnetic pressure remains much smaller than the random pressure of the infalling material (Fryer et al. 1996; Rueda & Ruffini 2012).
2. The photons are trapped in the accretion flow. The trapping radius, defined at which the photons emitted diffuse outward at a slower velocity than the one of the infalling material, is (Chevalier 1989):

$$r_{\text{trapping}} = \min\{\dot{M}_B \kappa / (4\pi c), R_{\text{cap}}\}, \quad (19)$$

where κ is the opacity. For the CO core, Fryer et al. (2014) estimated a Rosseland mean opacity roughly $5 \times 10^3 \text{ cm}^2 \text{ g}^{-1}$. For the range of accretion rates, we obtain that $\dot{M}_B \kappa / (4\pi c) \sim 10^{13} - 10^{19}$ cm, a radius much bigger than the NS capture radius

which is in our simulations at most 1/3 of the binary separation. Thus, in our systems the trapping radius extends all the way to the Bondi-Hoyle region, hence the Eddington limit does not apply and hypercritical accretion onto the NS occurs. See Figs. 15 and 16 in appendix B.3 for details.

3. Under these conditions of photons being trapped within the accretion flow, the gain of gravitational energy of the accreted material is mainly radiated via neutrino emission (Zel'dovich et al. 1972; Ruffini & Wilson 1973; Fryer et al. 1996; Rueda & Ruffini 2012; Fryer et al. 2014). See Figs. 15 and 16 in appendix B.3 for details.
4. Fig. 3 shows that the evolution of the accretion rate has a shape composed of a rising part, followed by an almost flat maximum and finally it decreases with time. The rising part corresponds to the passage and accretion of the first layers of the ejecta. The sharpness of the density cut-off of the outermost ejecta layer defines the sharpness of this rising accretion rate. The maximum rate is given by the accretion of the ejecta layers with velocities of the same order as the orbital velocity of the NS. These layers are located very close to the innermost part of the supernova ejecta. Then, the rate start to decrease with the accretion of the innermost layers whose density cut-off determines the sharpness of this decreasing part of the mass accretion rate. See also appendix A for further details.
5. The longer the orbital period/larger binary separation, the lower the accretion rate (see Fig. 11 in appendix A for details.); hence the lower the accretion luminosity and the longer the time at which peak luminosity occurs. These features confirm what advanced in Ruffini et al. (2016); Becerra et al. (2015); Ruffini et al. (2015), namely that less energetic long GRBs correspond to the binaries with wider orbits. Specifically, XRFs correspond to the binaries in which the NS does not reach the point of gravitational collapse to a BH (see below). Since there is a limiting orbital period, P_{max} , up to which the NS can reach the critical mass and collapse to a BH (these systems are the BdHNe Fryer et al. 2015, 2014), the XRFs are the binaries with $P > P_{\text{max}}$ (see Sec. 5 for details).

6.1. Convective instabilities

As the material piles onto the NS and the atmosphere radius, the accretion shock moves outward. The post-shock entropy is a decreasing function of the shock radius position which creates an atmosphere unstable to Rayleigh-Taylor convection during the initial phase of the accretion process (see appendix B for additional details). These instabilities can accelerate above the escape velocity driving outflows from the accreting NS with final velocities approaching the speed of light (Fryer et al. 2006; Fryer 2009). Assuming that radiation dominates, the entropy of the material at the base of the atmosphere

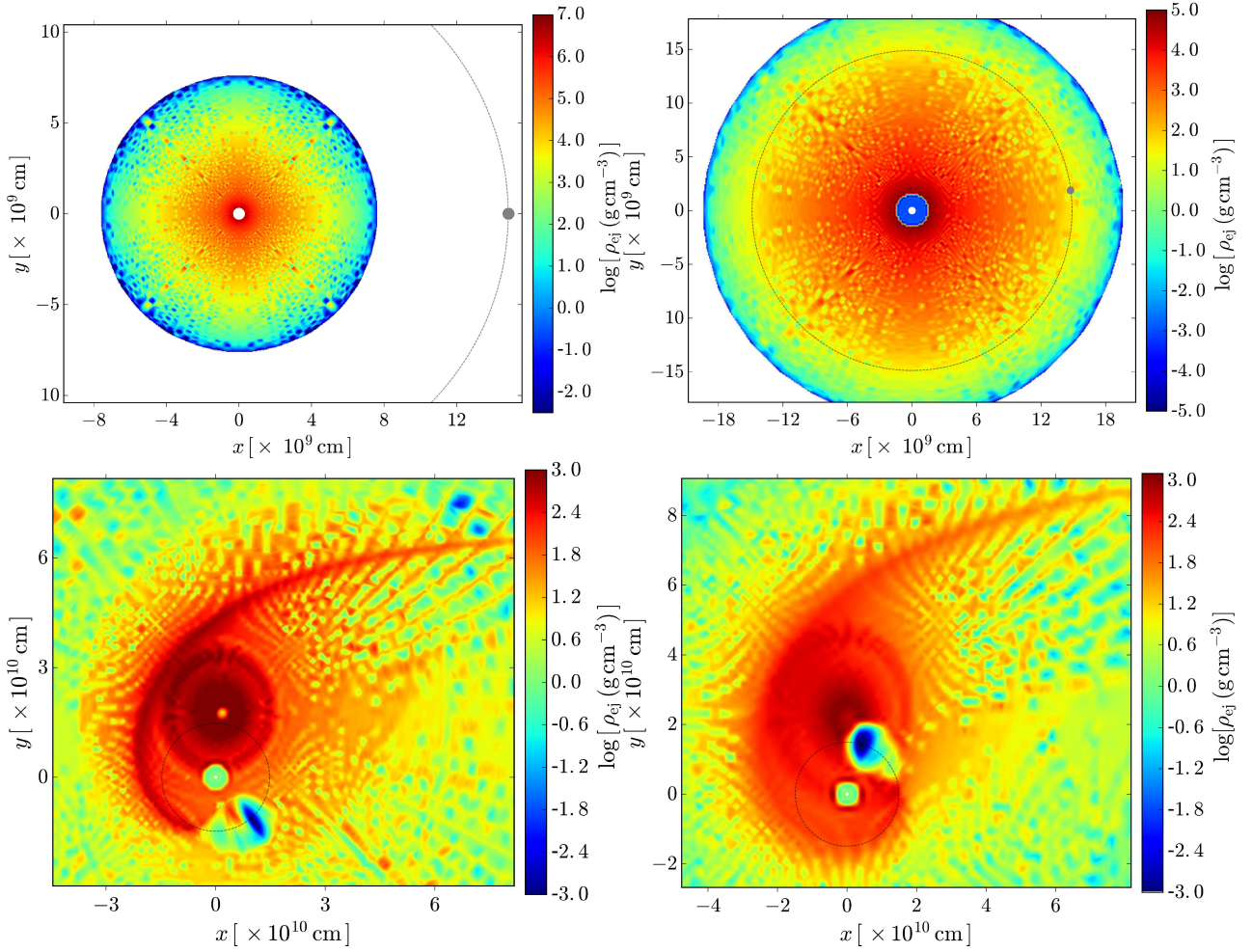


FIG. 6.— Snapshots of the IGC binary system and the supernova ejecta density at selected times of the evolution. In this example we have adopted the $M_{ZAMS} = 30 M_{\odot}$ progenitor with an ejecta mass of $7.94 M_{\odot}$ and a core that left a ν NS of $1.5 M_{\odot}$. We assume homologous evolution of the supernova ejecta with expansion parameter $n = 1$ and ejecta outermost layer velocity $v_{0,\text{star}} = 2 \times 10^9 \text{ cm s}^{-1}$. For the NS we adopt an initial mass $2.0 M_{\odot}$. The binary has an orbital period $P \approx 5 \text{ min}$, i.e. a binary separation distance $a \approx 1.5 \times 10^{10} \text{ cm}$. The evolution of the accretion rate and the gravitational mass of the NS are shown in Fig. 4. The coordinate system is centered on the ν NS born in the supernova: it is here represented with a white-filled circle located at $(0, 0)$. The NS, represented by the gray-filled circle, is orbiting counterclockwise in this time-evolution and we have indicated with a thin-dashed circle its trajectory. The colorbar indicates values of ejecta density. We have chosen a thickness Δz around the orbital plane to estimate the ejecta density: $\Delta z \approx 0.05a \approx 7.1 \times 10^8 \text{ cm}$ for all these figures. We note that, in order to show better the features of the system at different times, we have chosen for each plot different ranges of the x-y scales and of the colorbar. *Left upper panel:* initial time of the process, $t = t_0 = R_{\text{star}}^0/v_{\text{star},0} = 3.82 \text{ s}$. The supernova ejecta starts to expand radially outward and the NS (black filled circle) is located at the position $(a, 0)$. *Right upper panel:* beginning of the accretion process, i.e. passage of the first supernova ejecta layers through the NS gravitational capture region. Thus, this time is $t = t_{\text{acc},0} \approx a/v_{0,\text{star}} = 7.7 \text{ s}$. *Left lower panel:* instant when the NS reaches, by accretion, the critical mass and collapses to a BH. This occurs at $t = t_{\text{coll}} \approx 254 \text{ s} \approx 0.85P$. The BH, here represented by the black-filled circle, has a mass set by the critical NS mass, i.e. $M_{\text{BH}} = M_{\text{crit}} \approx 3 M_{\odot}$ (see Fig. 4). It can be seen here the asymmetry of the supernova ejecta density induced that have been generated by the nearby presence of the NS and the accretion process onto it. We can also see at this stage a stream of matter (of negligible mass) being expelled (i.e. reaching scape velocity) from the system. *Right lower panel:* system 100 s after the BH formation, namely $t = t_{\text{coll}} + 100 \text{ s} = 354 \text{ s} \approx 1.2P$. This figure shows the new binary system composed by the ν NS [white-filled circle at the $(0, 0)$ position] out of the supernova, and a BH [black-filled circle at the $(0.5, 1.7)$ position] out of the gravitational collapse of the NS due to the hypercritical accretion process. The asymmetry of the supernova ejecta is now even larger than the one showed by the left lower panel figure. The asymmetry of the supernova ejecta is such that its ‘center’ has been displaced, from the explosion site originally at the position $(0, 0)$, to the approximate position $(0, 2)$, due to the action of the orbiting NS.

is (Fryer et al. 1996):

$$S_{\text{bubble}} \approx 16 \left(\frac{M_{\text{NS}}}{1.4 M_{\odot}} \right)^{7/8} \left(\frac{\dot{M}_{\text{B}}}{M_{\odot} \text{ s}^{-1}} \right)^{-1/4} \left(\frac{r}{10^6 \text{ cm}} \right)^{-3/8}, \quad (20)$$

in units of k_B per nucleon.

This material will rise and expand, cooling adiabatically, i.e. $T^3/\rho = \text{constant}$, for radiation dominated gas.

If we assume a spherically symmetric expansion, then $\rho \propto 1/r^3$ and we obtain

$$k_B T_{\text{bubble}} = 195 S_{\text{bubble}}^{-1} \left(\frac{r}{10^6 \text{ cm}} \right)^{-1} \text{ MeV}. \quad (21)$$

However, it is more likely that the bubbles expand in the lateral but not in the radial direction (Fryer 2009), thus

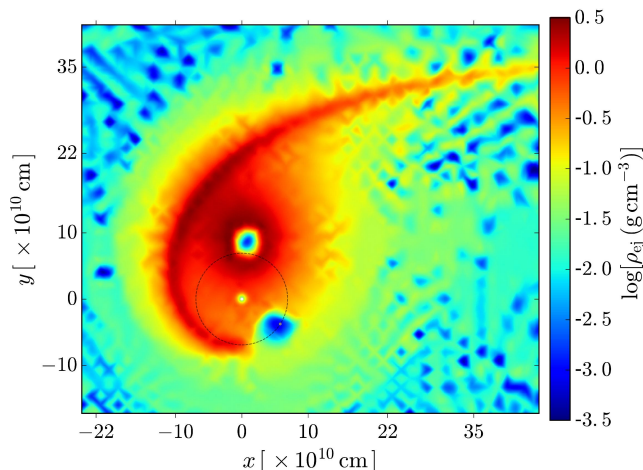


FIG. 7.— Snapshot of an IGC binary system analogous to the one of Fig. 6 but with an orbital period of $P \approx 50$ min (i.e. binary separation $a \approx 7 \times 10^{10}$ cm). In this case the accreting NS (gray-filled circle), which is orbiting counterclockwise (thin-dashed circle), does not collapse to the BH. The ν NS left by the supernova is represented by the white filled circle at the position (0,0). It is clear from this figure the asymmetry of the supernova ejecta: indeed the supernova ‘center’ has been displaced, from the explosion site originally at the position (0,0), to the approximate position (0,9), due to the action of the orbiting NS. The snapshot corresponds to a time $t = 2667$ s ≈ 44 min, which corresponds to roughly 1/4 the total accretion process. To estimate the ejecta density we have adopted $\Delta z = 0.08a \approx 5.3 \times 10^9$ cm.

we have $\rho \propto 1/r^2$, i.e.

$$T_{\text{bubble}} = T_0(S_{\text{bubble}}) \left(\frac{r_0}{r}\right)^{2/3}, \quad (22)$$

where $T_0(S_{\text{bubble}})$ is given by equation (21) evaluated at $r = r_0 \approx R_{\text{NS}}$.

This temperature implies a bolometric blackbody flux at the source from the bubbles

$$F_{\text{bubble}} = \sigma T_{\text{bubble}}^4 \approx 2 \times 10^{40} \left(\frac{M_{\text{NS}}}{1.4 M_{\odot}}\right)^{-7/2} \left(\frac{\dot{M}_B}{M_{\odot} \text{ s}^{-1}}\right) \times \left(\frac{R_{\text{NS}}}{10^6 \text{ cm}}\right)^{3/2} \left(\frac{r_0}{r}\right)^{8/3} \text{ erg s}^{-1} \text{ cm}^{-2}, \quad (23)$$

where σ is the Stefan-Boltzmann constant.

In Fryer et al. (2014) it was shown that the above thermal emission from the rising bubbles produced during the hypercritical accretion process can explain the early ($t \lesssim 50$ s) thermal X-ray emission observed in GRB 090618 (Izzo et al. 2012b,a). In that case T_{bubble} drops from 50 keV to 15 keV expanding from $r \approx 10^9$ cm to 6×10^9 cm, for an accretion rate $10^{-2} M_{\odot} \text{ s}^{-1}$.

From the above formulas we can explain the blackbody emission observed in XRF 060218 (Campana et al. 2006). The observed temperature ($k_B T \approx 0.2$ keV) and radius of the emitter (a few 10^{11} cm) are consistent with the temperature and surface radius of the above bubbles formed in a system with a NS of initial mass $1.4 M_{\odot}$, supernova-progenitor of $20 M_{\text{ZAMS}}$, and orbital period 2.5 h: it can be easily checked via equation (22) that for $r \sim 10^{11}$ cm and an accretion rate of the order of $10^{-6} M_{\odot} \text{ s}^{-1}$, the bubbles would have a temperature consistent with the one observed in XRF 060218. Further details on this specific case and additional examples

will be presented elsewhere (Ruffini et al., in preparation).

It is worth mentioning the possibility that, as discussed in Fryer et al. (2006), r-process nucleosynthesis occurs in these outflows. This implies that long GRBs can be also r-process sites with specific signatures from the decay of the produced heavy elements, possibly similar as in the case of the *kilonova* emission in short GRBs (see, e.g., Tanvir et al. 2013, and references therein). The signatures of this phenomenon in XRFs and BdHNe, and its comparison with kilonovae, deserves to be explored. However, this is out of the scope of the present work and it will be presented elsewhere.

6.2. Neutrino emission during hypercritical accretion

Most of the energy from the accretion is lost through neutrino emission and the neutrino luminosities are proportional to the accretion rate (see appendix B.2 for details). For the accretion rate conditions characteristic of our models $\sim 10^{-4}$ – $10^{-2} M_{\odot} \text{ s}^{-1}$ (see Sec. 2 and appendix A), pair annihilation dominates the neutrino emission and electron neutrinos remove the bulk of the energy (see Fryer 2009, and Figs. 15 and 16 in appendix B.3 for details). The temperature of these neutrinos can be roughly approximated by assuming that the inflowing material generally flows near to the NS surface before shocking and emitting neutrinos (see appendix B.1 and B.2). The pressure from this shock is given by (Fryer et al. 2006):

$$P_{\text{shock}} = \frac{1}{2}(\gamma + 1)\rho_{\text{acc}}v_{\text{acc}}^2 \quad (24)$$

where, if we assume the accretion occurs nearly at free-fall,

$$v_{\text{acc}} = \left(\frac{2GM_{\text{NS}}}{R_{\text{NS}}}\right)^{1/2} \quad (25)$$

and

$$\rho_{\text{acc}} = \frac{\dot{M}_{\text{acc}}}{4\pi R_{\text{NS}}^2 v_{\text{acc}}} \quad (26)$$

where $\dot{M}_{\text{acc}} = \dot{M}_B$ is the accretion rate onto the NS. The equation of state $\gamma = 4/3$ for the radiation-dominated conditions in this material, leads to the temperature of this material:

$$T_{\text{acc}} = \left(\frac{3P_{\text{shock}}}{4\sigma/c}\right)^{1/4} = \left(\frac{7}{8} \frac{\dot{M}_{\text{acc}} v_{\text{acc}} c}{4\pi R_{\text{NS}}^2 \sigma}\right)^{1/4}. \quad (27)$$

The electron-positron pairs producing the neutrinos are thermalized at this temperature and the resulting neutrino temperature can be estimated by this formula. For accretion rates lying between $\sim 10^{-4}$ – $10^{-2} M_{\odot} \text{ s}^{-1}$, we estimate neutrino temperatures lying between 1.7–5.2 MeV (i.e. neutrino energies $E_{\nu} \approx 3k_B T \approx 5$ –15 MeV; see appendix B.2), predicting energies only slightly below those produced by detailed calculations (Fryer 2009). A detailed study of the neutrino emission will be presented elsewhere (Ruffini et al., in preparation; see also appendix B.1 and B.2).

As we show in appendix B.2, for the developed temperatures (say $k_B T \sim 1$ –10 MeV) near the NS surface

(see Figs. 13 and 14), the dominant neutrino emission process is the electron-positron annihilation leading to neutrino-antineutrino. This process produces a neutrino emissivity proportional to the ninth power of the temperature [see Eq. (B20)]. The accretion atmosphere near the NS surface is characterized by a temperature gradient (see Fig. 13 in appendix B.1) with a typical scale height $\Delta r_{\text{ER}} \approx 0.7 R_{\text{NS}}$, obtained from Eq. (B19). Owing to the aforementioned strong dependence of the neutrino emission on temperature, most of the neutrino emission occurs in the region Δr_{ER} above the NS surface.

These conditions lead to the neutrinos to be efficient in balancing the gravitational potential energy gain, as indicated in Eq. (B18), allowing the hypercritical accretion rates. We show in appendix B.3 (see Figs. 15 and 16) photons are trapped within the flow the Eddington limit does not apply in this system. As discussed in Fryer et al. (1996), the neutrinos can balance efficiently the gravitational energy gain. The effective accretion onto the NS can be estimated as:

$$\dot{M}_{\text{eff}} \approx \Delta M_{\text{ER}} \frac{L_{\text{ER}}}{E_{\text{ER}}}, \quad (28)$$

where ΔM_{ER} , L_{ER} are the mass and neutrino luminosity in the emission region (i.e. Δr_{ER}), and E_{ER} is half the gravitational potential energy gained by the material falling from infinity to the $R_{\text{NS}} + \Delta r_{\text{ER}}$. Since $L_{\text{ER}} \approx 2\pi R_{\text{NS}} \Delta r_{\text{ER}} \epsilon_{e^-e^+}$ with $\epsilon_{e^-e^+}$ the electron-positron pair annihilation process emissivity given by Eq. (B20), and $E_{\text{ER}} = (1/2)GM_{\text{NS}}\Delta M_{\text{ER}}/(R_{\text{NS}} + \Delta r_{\text{ER}})$, it can be checked that for $M_{\text{NS}} = 1.4 M_{\odot}$ this accretion rate leads to values $\dot{M}_{\text{eff}} \approx 10^{-9}-10^{-1} M_{\odot} \text{ s}^{-1}$ for temperatures $k_B T = 1-10 \text{ MeV}$.

The neutrino signal from this accretion can be similar to the one from accretion in supernovae with fallback. Fallback begins immediately after the launch of the supernova explosion and, after peaking, decays with time ($t^{-5/3}$; Chevalier 1989). Depending upon the total fallback mass, the fallback accretion rate can remain above $10^{-4} M_{\odot} \text{ s}^{-1}$ for 10^3-10^4 s (Wong et al. 2014).

7. ACCRETION LUMINOSITY

In order to make a comparison with observed light-curves we need to estimate the luminosity produced during the accretion process. The gain of gravitational potential energy in the accretion process is the total one available to be released e.g. by neutrinos and photons. The total energy released in the star in a time-interval dt during the accretion of an amount of mass dM_b with angular momentum lM_b , is given by (see, e.g., Sibgatullin & Sunyaev 2000; Becerra et al. 2015):

$$\begin{aligned} L_{\text{acc}} &= (\dot{M}_b - \dot{M}_{\text{NS}})c^2 \\ &= \dot{M}_b c^2 \left[1 - \left(\frac{\partial M_{\text{NS}}}{\partial J_{\text{NS}}} \right)_{M_b} l - \left(\frac{\partial M_{\text{NS}}}{\partial M_b} \right)_{J_{\text{NS}}} \right], \end{aligned} \quad (29)$$

where we have used Eq. (11). This upper limit to the energy released is just the amount of gravitational energy gained by the accreted matter by falling to the NS surface and which is not spent in changing the gravitational binding energy of the NS. The total energy releasable during the accretion process, $\Delta E_{\text{acc}} \equiv \int L_{\text{acc}} dt$, is thus

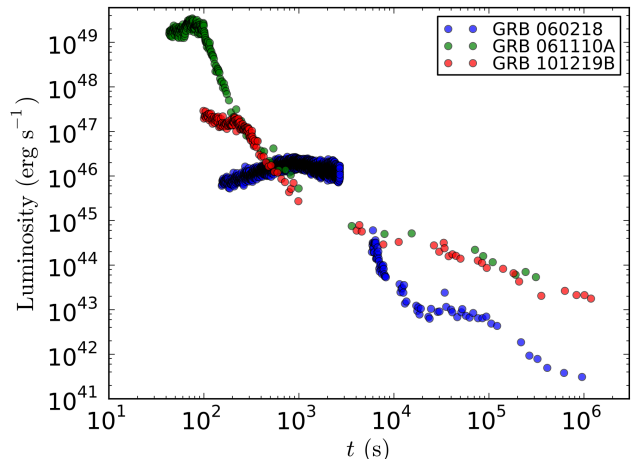


FIG. 8.— Observed 0.3–10 keV XRT light-curves of some XRFs.

given by the difference in binding energies of the initial and final NS configurations. The typical luminosity will be $L_{\text{acc}} \approx \Delta E_{\text{acc}}/\Delta t_{\text{acc}}$ where Δt_{acc} is the duration of the accretion process.

The duration of the accretion process is given approximately by the flow time of the slowest layers of the supernova ejecta to the NS. If the velocity of these layers is v_{inner} , then $\Delta t_{\text{acc}} \sim a/v_{\text{inner}}$, where a is the binary separation. For $a \sim 10^{11} \text{ cm}$ and $v_{\text{inner}} \sim 10^8 \text{ cm s}^{-1}$ we obtain $\Delta t_{\text{acc}} \sim 10^3 \text{ s}$, while for shorter binary separation, e.g. $a \sim 10^{10} \text{ cm}$ ($P \sim 5 \text{ min}$), $\Delta t_{\text{acc}} \sim 10^2 \text{ s}$, as validated by the results of our numerical integrations shown e.g. in Figs. 3 and 4. See also appendix A.

We have shown in Fig. 4 the evolution of both the baryonic mass \dot{M}_b and the gravitational mass \dot{M}_{NS} for a specific example. We have seen that these two quantities show a similar behavior, therefore we should expect the difference between them, which gives the available energy to be released (29), evolves with time analogously. Besides, we can see that the NS in the system with $P = 5 \text{ min}$ accretes $\approx 1 M_{\odot}$ in $\Delta t_{\text{acc}} \approx 100 \text{ s}$. With the aid of Eq. (13) we can estimate the difference in binding energies between a $2 M_{\odot}$ and a $3 M_{\odot}$ NS, i.e. $\Delta E_{\text{acc}} \approx 13/200(3^2 - 2^2) M_{\odot} c^2 \approx 0.32 M_{\odot} c^2$ leading to a maximum luminosity $L_{\text{acc}} \approx 3 \times 10^{-3} M_{\odot} c^2 \approx 0.1 \dot{M}_b c^2$.

Such an accretion power could lead to signatures observable in long GRBs (see, e.g., Izzo et al. 2012a; Fryer et al. 2014) since it could be as high as $L_{\text{acc}} \sim 0.1 \dot{M}_b c^2 \sim 10^{47}-10^{51} \text{ erg s}^{-1}$ for accretion rates in the range $\dot{M}_b \sim 10^{-6}-10^{-2} M_{\odot} \text{ s}^{-1}$. Fig. 8 shows a few examples of light-curves of XRFs. It can be shown that the accretion luminosity can explain the observed early emission ($t \lesssim 10^3 \text{ s}$) in these examples (see Sec. 8 and Becerra et al., in preparation).

8. INFLUENCE OF THE HYPERCRITICAL ACCRETION ON THE SUPERNOVA EMISSION

The duration of the accretion is shorter than the one of the long-lasting X-ray emission (at times $t \sim 10^3-10^6 \text{ s}$). We shall show below (see Sec. 8 and Becerra et al., in preparation) such a long-lasting emission can be explained from the supernova powered by the prompt radiation, i.e. the X-ray radiation occurring during the

accretion process onto the NS. In the case of the tightest binaries leading to BdHNe, the supernova is in addition powered by the prompt radiation following the BH formation.

We now analyze the emission of the supernova at early stages. Traditionally, the supernova shock breaks out of the star producing a burst of X-ray emission which, in a spherically symmetric model, behaves as a sharp rise and equally fast decay as the forward shock cools. However, in our models, the supernova shock has distinct asymmetries caused by the accretion onto the NS (see Figs. 6–7 in Sec. 5). In addition, the X-rays emitted from this hypercritical accretion add energy to the explosion. To calculate the shock breakout luminosity, we use the simplified light-curve code described in Bayless et al. (2015) and De La Rosa (2016). This code assumes homologous outflow for the ejecta velocities, modeling the radiative transport using a single group diffusion scheme with prescriptions for recombination opacities and energies. Energy released in the accretion onto the neutron star is injected as an energy source at the base of the explosion. Because these calculations are 1-dimensional, we mimic the asymmetry in the explosion by modeling a series of spherical explosions with different densities. Each of these densities produces a different light-curve with the more massive models producing later shock breakout times.

In Fig. 9 we compare and contrast the luminosity expected from the accretion process given by equation (29) and from the accretion-powered supernova, with the observed X-ray luminosity of XRF 060218. The parameters characterizing the binary are: orbital period of 2.5 h, supernova velocity $v_{\text{star},0} = 2 \times 10^9 \text{ cm s}^{-1}$, a pre-supernova core obtained from the $M_{\text{ZAMS}} = 20 M_{\odot}$ evolution which leads to a CO core envelope mass $\sim 4 M_{\odot}$ (see table 1), and initial NS mass $M_{\text{NS}}(t_0) = 1.4 M_{\odot}$. For these binary parameters, the NS does not collapse to a BH, in agreement with the fact that XRFs, as XRF 060218, should be explained by these kind of binaries.

For this burst, our model assumes an initial explosion energy of 2×10^{51} erg, ranging the spherical equivalent-mass from $0.05\text{--}4 M_{\odot}$. Fig. 9 shows light-curves rising quickly at $t \lesssim 10^4$ s for the lowest mass to $\sim 10^5$ s for the $4 M_{\odot}$ explosion. This maximum mass corresponds to the ejecta mass from our supernova. The corresponding CO core mass of our progenitor is this ejecta mass plus the mass of the νNS , roughly $5.4 M_{\odot}$. It is possible that the mass is slightly larger for our progenitors, and the emission from the breakout could be longer, but peak X-ray emission from shock breakout beyond a few times 10^5 s will be difficult to achieve. The observed emission would come from the sum of this full range of explosions. The close match of our models (fitted to our expected progenitor mass) to this X-ray plateau demonstrates that this sequence of shock breakouts is certainly a viable and natural explanation for this emission (see Fig. 9).

We have shown that the X-ray plateau in the afterglow is powered almost entirely by a sequence of shock breakouts and the expanding photosphere. We turn now to the optical emission which is more complex. The optical emission can be powered by the expanding photosphere, ^{56}Ni decay and the energy deposited by the accreting NS. For XRF 060218, the light-curve in the optical and UV exhibits a double-peaked structure suggestive of multiple

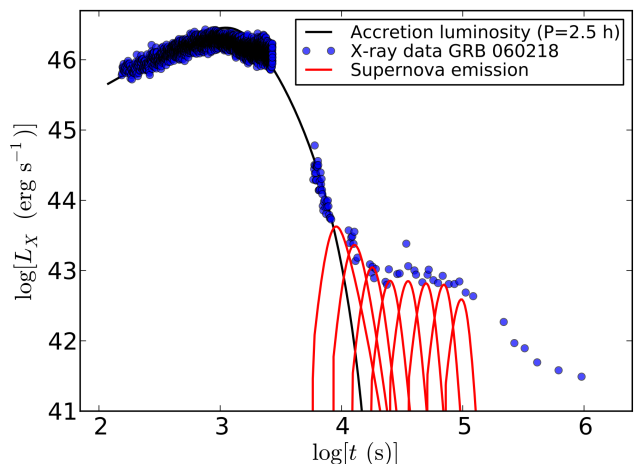


FIG. 9.— Comparison of the accretion luminosity given by equation (29) and the supernova luminosity with the observed X-ray luminosity of XRF 060218. The binary system has the following parameters: supernova velocity $v_{\text{star},0} = 2 \times 10^9 \text{ cm s}^{-1}$, a pre-supernova core obtained from the $M_{\text{ZAMS}} = 20 M_{\odot}$ evolution (see table 1), initial NS mass $M_{\text{NS}}(t_0) = 1.4 M_{\odot}$, and orbital period of 2.5 h. In this example the initial explosion energy is 2×10^{51} erg, ranging the spherical equivalent-mass from $0.05\text{--}4 M_{\odot}$. It can be seen that at early times $t \lesssim 10^4$ s the luminosity is dominated by the accretion process. The supernova X-ray light-curves rise quickly at $t \approx 10^4$ s for the lowest mass, to $t \sim 10^5$ s for the $4 M_{\odot}$ explosion, which corresponds to total ejecta mass from our supernova.

power sources and, using our light-curve code, we can test out different scenarios. Just like the X-ray, geometry effects will modify the optical light-curve. Here we merely probe the different emission mechanisms to determine the viability of each to explain the XRF 060218 optical light-curve.

Fig. 10 shows the V and B band light-curves for XRF 060218 (Pian et al. 2006). The light-curve in both bands peaks first near 50,000 s and then again at 500,000 s. Using our $1 M_{\odot}$ 1D model from our X-ray emission, we simulate the V and B band light-curves. Without either ^{56}Ni decay or accretion energy, the supernova explosion only explains the first peak. However, if we include the energy deposition from the accretion onto the NS (for our energy deposition, we use $4 \times 10^{46} \text{ erg s}^{-1}$ over a 2500 s duration), our simulations produce a second peak at roughly 500,000 s. A second peak can also be produced by increasing the total ^{56}Ni yield. However, even if we assume half of the total ejecta is ^{56}Ni , the second peak remains too dim to explain the observations.

The accretion energy in our model provides a natural explanation for the double-peaked features observed in the optical emission of XRF 060218. However, our simple model makes a series of approximations: e.g., we use gray transport, estimating the V and B emission assuming a blackbody, we assume the opacities are dominated by electron scattering, etc. Our simplified picture cannot reproduce accurately the first slowly rising part of the optical data which can be due to a combination of 1) the low-energy tail of the X-ray bubbles and 2) the geometry asymmetries which, just like for the X-rays, cause 1D effective mass ejecta to be lower along some lines of sight leading to some optical emission. The simulation of these details are out of the scope of the present article

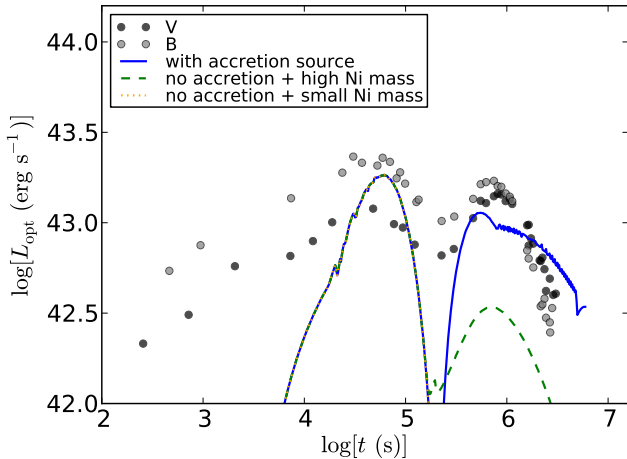


FIG. 10.— Optical and UV luminosity of XRF 060218 (Pian et al. 2006). The light-curve shows a double-peaked structure. The red dotted curve shows the supernova optical emission without either ^{56}Ni decay or accretion energy; it can be seen that it explains only the first peak. The blue solid curve includes the energy deposition from the accretion onto the NS (which is a power source of 4×10^{46} erg s^{-1} over a 2500 s duration). This simulation reproduces both the first peak at $\sim 50,000$ s as well as the second peak at $\sim 500,000$ s. The dashed green curve shows that a second peak can also be produced without accretion power by increasing the total ^{56}Ni yield. However, even if we assume half of the total ejecta is ^{56}Ni , the produced second peak cannot explain the observational data.

and will be the subject of future simulations. We have shown that, although approximate, the accretion mechanism can power the observed XRF 060218 light-curve.

9. CONCLUSIONS

We have analyzed in detail the IGC paradigm of GRBs associated with supernovae. The progenitor is a binary system composed of CO core and a NS in which the explosion of the CO core as supernova triggers a hypercritical accretion process onto the NS. For the given supernova parameters (total CO core mass, density profile, ejecta mass and velocity) and an initial mass of the NS, the fate of the NS depends only on the binary separation/orbital period. The picture that arises from the simulation of the accretion process as a function of the orbital period is as follows.

1. Since the accretion rate decreases for increasing values of the orbital period, there exists a specific value of it over which BH formation is not possible because the NS does not accrete sufficient matter to reach the critical mass. We denoted this maximum period for gravitational collapse as P_{max} and computed it as a function of the initial NS mass for selected pre-supernova CO cores (see Fig. 5). Therefore, in systems with $P \leq P_{\text{max}}$ BH formation occurs and these systems, within the IGC paradigm, can explain BdHNe (Fryer et al. 2015; Becerra et al. 2015; Fryer et al. 2014). In systems with $P > P_{\text{max}}$, the NS does not accrete enough matter from the supernova ejecta and the collapse to a BH does not occur: these systems, within the IGC paradigm, are used to explain the nature of XRFs.
2. We have shown that the early emission ($t \lesssim 10^3$ s) of an IGC binary is powered by the accretion lumi-

nosity. This luminosity explains the prompt emission of XRFs as presented here in the case of XRF 060218 (see Fig. 9). We are planning to extend this conclusion to additional XRFs (Ruffini et al., in preparation).

3. We have shown that convection instabilities arising from the NS accretion atmosphere can drive hot outflows emitting X-rays observable in the early emission of GRBs. It has been shown in Fryer et al. (2014) that the emission from such an outflows is consistent with the early ($t \lesssim 50$ s) thermal X-ray emission observed in the BdHN GRB 090618 (Izzo et al. 2012a,b). We have shown here the consistency with the thermal emission of XRF 060218. The observational verification in the case of additional XRFs will be presented elsewhere (Ruffini et al., in preparation). Details of the structure of the accretion region are presented in appendix B.
4. Neutrino emission is the main energy sink of the system, allowing the hypercritical accretion to occur. We have given estimates of the neutrino flux and energy. Typical neutrino energies are in the range 1–15 MeV. A detailed study of the neutrino emission will be presented elsewhere (Ruffini et al., in preparation). Details are also presented in appendix B.2.
5. We have shown that the presence of the NS in very compact orbit produces large asymmetries in the supernova ejecta around the orbital plane (see Figs. 6 and 7). These asymmetries are the combined effect of the accretion and of the action of the gravitational field of the NS on the supernova layers.
6. The above supernova asymmetries lead to observable effects in the supernova emission. The shocked material becomes transparent at different times with different luminosities along different directions owing to the asymmetry created in the supernova ejecta by the orbiting and accreting NS (see Figs. 6 and 7). The sequence of shock breakout luminosities are thus influenced by the asymmetries in the explosion: the light-curve produced along the more massive directions produce later shock breakout times. We have shown that the observed long-lasting, $t > t_{\text{acc}}$, afterglow X-ray emission observed in XRFs can be powered by this mechanism and presented as an example XRF 060218 (see Fig. 9). The specific example is here presented for XRF 060218 and evidence that this mechanism is also observed in additional XRFs will be presented elsewhere (Ruffini et al., in preparation).
7. We have exemplified the above mechanism for late time X-ray emission observed in XRF 060218. The supernova ejecta asymmetries are even more pronounced in more compact binaries in which the NS, by accretion, reaches the critical mass and collapses to a BH (see Fig. 6). This implies that this mechanism is also at work in the X-ray afterglow of BdHNe with specific additional features in the spike, in the plateau and in the late power-law emission (Ruffini et al., in preparation).

8. We have shown that not only asymmetries caused by the close accreting NS modify the classic picture of supernova emission. The X-rays emitted from the accretion add energy to the supernova explosion. We have simulated the optical emission of the supernova and compared and contrasted our theoretical expectation with the optical luminosity of XRF 060218 which shows a peculiar double-peaked shape. We have shown that without either ^{56}Ni decay or accretion energy, the supernova explosion can explain only the first peak. We then showed that the inclusion of ^{56}Ni decay produces indeed a double-peaked light-curve but with a second peak which is too dim to explain the observed optical emission. This conclusion holds even adopting unphysical high amounts of ^{56}Ni mass of up to half of the ejecta mass. Instead, we demonstrated that the source of energy given by the hypercritical accretion onto the NS provides a double-peaked light-curve consistent with the observational data. See Fig. 10 and Ruffini et al. (in preparation), for details.
9. We have shown how the radiation during the continuous accretion process affects the supernova emission both in X-rays and in the optical. We have simulated this effect for binaries in which the NS does not collapse to a BH, namely for XRFs (e.g. XRF 060218). For systems with shorter orbital periods in which a BH is formed, namely for BdHNe, besides the initial interaction of the supernova with the radiation from the accretion process, the supernova interacts with the radiation from the prompt radiation following the BH formation. The interaction of the electron-positron pairs (moving with Lorentz factor $\Gamma \sim 10^2$) with the supernova material at a distance of $r \sim 10^{12}$ cm and moving at $\Gamma \sim 1$ can originate the flare observed around $t \sim 100$ s after the GRB trigger time in the X-ray data of BdHNe. The theoretical and observational details of this process will be presented elsewhere (Ruffini et al., in preparation).

It is interesting that in parallel to the above conclusions we can also draw some inferences on the astrophysics of NS-NS binaries. Our results suggest that the systems in which the accreting NS does not reach the critical mass (i.e the XRFs) are natural candidates to produce such binaries (Ruffini et al. 2016). We have shown that this will occur for CO-NS binaries with long orbital periods; thus it is possible that many of these systems become unbound by the supernova explosion produced by the CO core. The XRF to BdHN occurrence rate ratio can shed light on the ratio of bound/unbound IGC binaries Fryer et al. (2015). The short orbital periods $P < P_{\text{max}}$ needed for BdHNe obtained from our theoretical model imply that XRF must be much more common than BdHNe, as it is indeed observed (see, e.g., Guetta & Della Valle 2007; Ruffini et al. 2016, and references therein). The few systems which will keep bound become NS-NS binaries where at least one of the components can be massive and with a rotation period in the millisecond region. If the NS accretes from the LSO, then at the end of the process it will have an angular momentum $J_{\text{NS}} \sim 2\sqrt{3}GM_{\text{acc}}M_{\text{NS}}/c \approx 4.3 \times 10^{48} [M_{\text{acc}}/(0.1M_{\odot})][M_{\text{NS}}/(1.4M_{\odot})]$ g cm² s⁻², where M_{acc} is the total accreted mass. Thus, the NS will have a rotation period $P = 2\pi I_{\text{NS}}/J_{\text{NS}} \approx 1.6 (0.1M_{\odot}/M_{\text{acc}})(R_{\text{NS}}/10^6 \text{ cm})^2$ ms, where $I_{\text{NS}} \sim 2/5 M_{\text{NS}} R_{\text{NS}}^2$ is the NS moment of inertia. That known binary millisecond pulsars could be formed in XRFs is a very exciting result that deserves further scrutiny (Ruffini et al., in preparation).

We thank the referee for the comments and suggestions. L.B. acknowledges the support given by the International Relativistic Astrophysics Ph. D Program (IRAP-PhD). J.A.R. acknowledges the support by the International Cooperation Program CAPES-ICRANet financed by CAPES, Brazilian Federal Agency for Support and Evaluation of Graduate Education within the Ministry of Education of Brazil. J.A.R. acknowledges partial support of the project No. 3101/GF4 IPC-11/2015 and the target program of the Ministry of Education and Science of the Republic of Kazakhstan.

APPENDIX

ANALYTIC APPROXIMATION FOR THE PEAK ACCRETION RATE

We can see from Fig. 3 that the shorter(smaller) the orbital period(separation) the higher the peak accretion rate \dot{M}_{peak} and the shorter the peak time, t_{peak} . Indeed, we can derive such a feature from simple arguments. The accretion rate (1) increases for higher densities and lower velocities, so we should expect as indeed shown in Fig. 3, it increases with time as the inner ejecta layers, which are denser and slower [see Eqs. (4) and (3)], reach and passed the accretion region. The accretion rate starts to peak at the passage of the innermost densest layer, r_{inner} , through the capture region. Such a layer moves with velocity $v_{\text{inner}} = (r_{\text{inner}}/R_{\text{star}}^0)v_{\text{star},0}$ as given by the homologous expansion assumption.

Thus, the accretion rate peaks around the peak time:

$$t_{\text{peak}} = \frac{a - R_{\text{cap}}}{v_{\text{inner}}} = \frac{(a - R_{\text{cap}})R_{\text{star}}^0}{r_{\text{inner}}v_{\text{star},0}}, \quad (\text{A1})$$

namely the time when r_{inner} reaches the capture region which is located at a distance $r = a - R_{\text{cap}}$ from the CO core center.

The radius r_{inner} is the maximum of the density profile (7), namely the root of the equation:

$$r_{\text{inner}} - R_{\text{star}}^0 + R_{\text{star}}^0 m \ln \left(\frac{r_{\text{inner}}}{\hat{R}_{\text{core}}} \right) = 0, \quad (\text{A2})$$

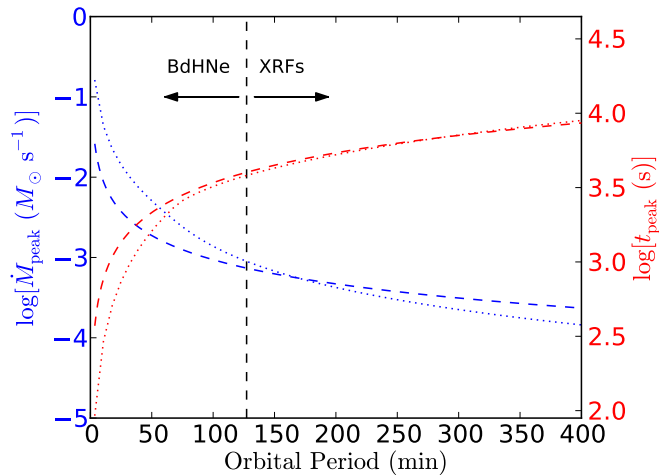


FIG. 11.— (Color online) Peak accretion rate (\dot{M}_{peak} , blue curves and left y-scale) and peak time (t_{peak} , red curves and right y-scale) as a function of the orbital period. The dashed curves give the analytic peak accretion rate and time (A5) and (A4), respectively, while the dotted curves correspond to the values obtained from the numerical integration of the equations in Sec. 2. This example corresponds to the following binary parameters: a CO core from the $M_{\text{ZAMS}} = 20 M_{\odot}$ progenitor of table 1, an initial NS mass $2.0 M_{\odot}$, and a velocity of the outermost ejecta layer $v_{\text{star},0} = 2 \times 10^9 \text{ cm s}^{-1}$. For these parameters we have $\eta \approx 0.41$ from equation (A3). The black dashed vertical line marks the maximum orbital period (for these system parameters, $P_{\text{max}} \approx 127 \text{ min}$) for which the NS reaches, by accretion, the critical mass and collapses to a BH (see Fig. 5 in Sec. 4). We recall that within the IGC interpretation systems with $P < P_{\text{max}}$ lead to BdHNe while systems with $P > P_{\text{max}}$ lead to XRFs.

where we recall $\hat{R}_{\text{core}} \approx 0.31 R_{\text{core}}$. Since $r_{\text{inner}} \approx \hat{R}_{\text{core}}$, we can obtain the approximate solution:

$$r_{\text{inner}} \approx \eta R_{\text{core}}, \quad \eta \equiv \frac{R_{\text{star}}^0}{R_{\text{core}}} \frac{1+m}{1+m(R_{\text{star}}^0/\hat{R}_{\text{core}})}. \quad (\text{A3})$$

Since $v_{\text{inner}} < v_{\text{orb}}$, we can approximate the relative velocity as given only by the orbital one, i.e. $v_{\text{rel}} \approx v_{\text{orb}}$, and within this approximation, the capture radius reduces to $R_{\text{cap}} \approx (2M_{\text{NS}}/M)a$. Then, equation (A1) becomes

$$t_{\text{peak}} \approx \left(1 - \frac{2M_{\text{NS}}}{M}\right) \left(\frac{GM}{4\pi^2}\right)^{1/3} \left(\frac{R_{\text{star}}^0}{\eta R_{\text{core}}}\right) \frac{P^{2/3}}{v_{\text{star},0}}. \quad (\text{A4})$$

We can now evaluate equation (1) at the above $t = t_{\text{peak}}$ and applying the same approximations, we obtain for the peak accretion rate

$$\dot{M}_{\text{peak}} \approx 2\pi^2 \frac{(2M_{\text{NS}}/M)^{5/2}}{(1-2M_{\text{NS}}/M)^3} \eta^{3-m} \rho_{\text{core}} \frac{R_{\text{core}}^3}{P}, \quad (\text{A5})$$

where we recall $M = M_{\text{CO}} + M_{\text{NS}}$ is the total binary mass, being $M_{\text{CO}} = M_{\text{env}} + M_{\nu\text{NS}}$ the total mass of the CO core given by the envelope mass and the central iron core mass leading to the formation of the νNS .

Fig. 11 shows the behavior of Eqs. (A5) and (A4) as a function of the orbital period and compare them with the corresponding values obtained from the numerical integration of the accretion equations presented in Sec. 2. This example is for the binary parameters: a CO core from the $M_{\text{ZAMS}} = 20 M_{\odot}$ progenitor of table 1, an initial NS mass $2.0 M_{\odot}$, and a velocity of the outermost ejecta layer $v_{\text{star},0} = 2 \times 10^9 \text{ cm s}^{-1}$. For these parameters, $\eta \approx 0.41$ from equation (A3). It can be seen that the accuracy of the above simple analytic formulas increases for the systems with $P > P_{\text{max}}$. This is expected since, as we have mentioned, only for these systems the innermost ejecta layers passed the NS position. In systems with $P < P_{\text{max}}$, the NS collapses to a BH before the passage of the innermost layers. In those cases, the maximum accretion rate is not reached at the passage of r_{inner} but at the passage of a layer located at $r_{\text{max}} > r_{\text{inner}}$, hence with velocity $v_{\text{max}} = v(r = r_{\text{max}}) > v_{\text{inner}}$, and thus $v_{\text{max}} \gtrsim v_{\text{orb}}$. In any case, it is clear the above formulas for \dot{M}_{peak} and t_{peak} remain valid to obtain typical (order-of-magnitude) estimates of the accretion process in these binaries. The consistency of the numerical and analytic results (within their range of validity) shown here serves as well as an indicator of the reliability of the numerical results (see also appendix C).

PHYSICS INSIDE THE ACCRETION REGION

In this appendix we analyze the NS accretion zone following the theoretical framework established for supernova fallback accretion (Chevalier 1989; Houck & Chevalier 1991; Fryer et al. 1996). Fig. 12 shows schematically the structure of the NS atmosphere: the supernova material entering the NS capture region shocks as it piles up onto the NS surface. As the atmosphere compresses, it becomes sufficiently hot to emit neutrinos allowing the matter to reduce its entropy and be incorporated into the NS.

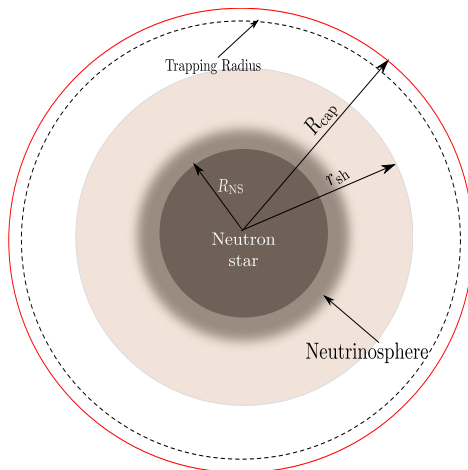


FIG. 12.— Structure of the NS accretion atmosphere. The ejecta from the supernova enter the NS capture region (red circle) at a distance $r = R_{\text{cap}}$ [see equation (2)] from the NS center and start to fall to the NS surface. The material shocks as it piles on top the NS surface. The shock decelerates the material while it moves towards the NS and near the surface, at the *neutrinosphere*, it loses energy by the emission of neutrinos. The neutrino emission allows the material to reduce its entropy to be finally accreted by the NS.

Accretion zone structure and equation of state

In order to model the evolution of the NS accretion zone, we assume that it passes through a sequence of quasi-steady state envelopes, each characterized by the mass accretion rate \dot{M} , the NS mass, M_{NS} and its radius R_{NS} . The spacetime outside the NS is described by the Schwarzschild metric:

$$ds^2 = -\left(1 - \frac{r_{\text{sch}}}{r}\right) dt^2 + \left(1 - \frac{r_{\text{sch}}}{r}\right)^{-1} dr^2 + r^2 (d\theta^2 + \sin^2 \theta d\phi^2), \quad (\text{B1})$$

where $r_{\text{sch}} = 2GM_{\text{NS}}/c^2$ is the Schwarzschild radius. The steady-state relativistic fluid equations for mass, momentum and energy conservation in this geometry are:

$$\frac{1}{r^2} \frac{d}{dr} (r^2 \rho u) = 0, \quad (\text{B2})$$

$$\frac{1}{2} \frac{d}{dr} \left(\frac{u}{c}\right)^2 + \frac{r_{\text{sch}}}{2r} + \frac{1}{w} \frac{dP}{dr} \left[\left(\frac{u}{c}\right)^2 + 1 - \frac{r_{\text{sch}}}{r}\right] = 0, \quad (\text{B3})$$

$$\frac{d}{dr} (\rho c^2 + U) - \frac{w}{\rho} \frac{d\rho}{dr} + \frac{Q_\nu}{u} = 0, \quad (\text{B4})$$

where u is the radial component of the four-velocity, Q_ν is the total energy loss rate per unit volume by neutrino cooling, $w = \rho c^2 + U + P$ is the relativistic enthalpy, ρ is the mass density, P is the pressure and U is the internal energy density.

The boundary conditions are determined by the conservation of mass, momentum and energy flows through the shock front at $r = R_s$. These one are expressed by the Rankine-Hugoniot conditions (Landau & Lifshitz 1959):

$$\rho_p u_p - \rho_{\text{sh}} u_{\text{sh}} = 0, \quad (\text{B5})$$

$$w_p u_p^t u_p - w_{\text{sh}} u_{\text{sh}}^t u_{\text{sh}} = 0, \quad (\text{B6})$$

$$w_p u_p^2 + P_p - w_{\text{sh}} u_{\text{sh}}^2 - P_{\text{sh}} = 0, \quad (\text{B7})$$

where u^t is the time component of the four-velocity, determined by the condition $g_{\mu\nu} u^\mu u^\nu = -c^2$. The indexes ‘ p ’ and ‘sh’ denote the quantities in the pre-shock and post-shock zone, respectively. Outside the shock front, the material is in approximate free fall, thus:

$$u_p = \sqrt{\frac{2GM_{\text{ns}}}{r}}, \quad \rho_p = \frac{\dot{M}}{4\pi r^2 v_p}, \quad P_p = \frac{1}{2} \rho_p v_p^2. \quad (\text{B8})$$

We consider a gas of electrons, positrons, ions and photons. Then, the total pressure and density energy are:

$$P_{\text{tot}}(\rho, T) = P_\gamma + P_{\text{ion}} + P_{e^-} + P_{e^+}, \quad (\text{B9})$$

$$U_{\text{tot}}(\rho, T) = U_\gamma + U_{\text{ion}} + U_{e^-} + U_{e^+}. \quad (\text{B10})$$

For the pressure and the internal energy of the radiation field, we adopt a blackbody in thermodynamical equilibrium:

$$P_\gamma = \frac{1}{3} a T^4, \quad U_\gamma = 3P_\gamma, \quad (\text{B11})$$

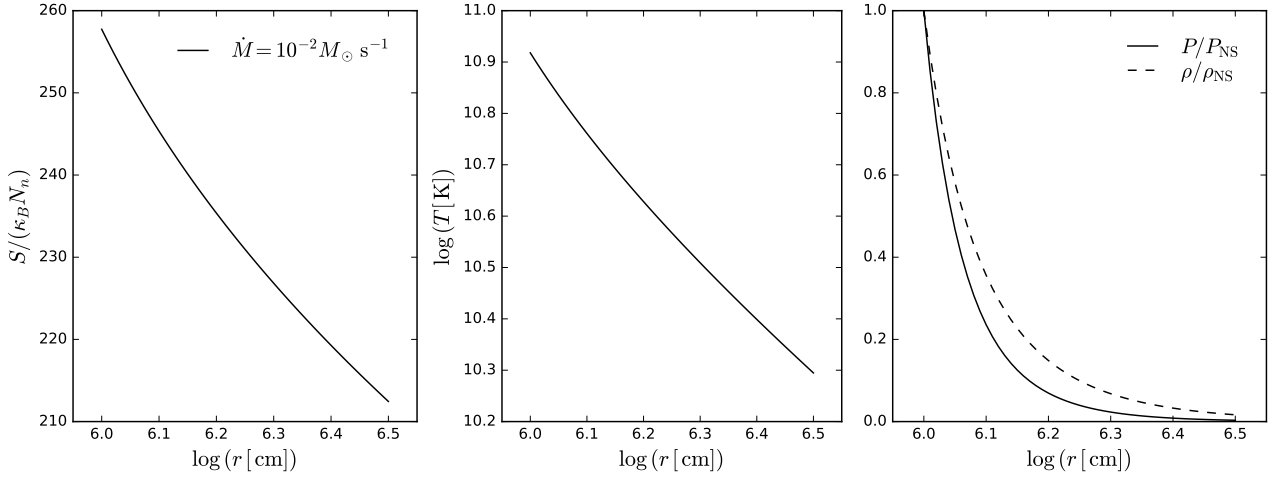


FIG. 13.— Entropy, temperature, density and pressure profile for a NS accreting atmosphere for $\dot{M} = 10^{-2} M_{\odot} \text{ s}^{-1}$. The pressure and density are normalized to $P_{\text{NS}} \approx 3.28 \times 10^{29} \text{ dyn cm}^{-2}$ and $\rho_{\text{NS}} \approx 7.5 \times 10^8 \text{ g cm}^{-3}$, respectively.

with $a = 4\sigma/c = 7.56 \times 10^{-15} \text{ erg cm}^{-3} \text{ K}^{-4}$, where σ is the Stefan-Boltzmann constant.

For the ion gas, we assume a perfect gas:

$$n_{\text{ion}} = \frac{\rho}{Am_u}, \quad P_{\text{ion}} = n_{\text{ion}}\kappa_B T, \quad U_{\text{ion}} = \frac{3}{2}P_{\text{ion}}, \quad (\text{B12})$$

where n_{ion} is the ion number density, $m_u = 1.6604 \times 10^{-24} \text{ g}$ is the atomic mass unit and κ_B is the Boltzmann constant.

Finally, the electrons and positrons are described by the Fermi-Dirac distributions:

$$n_{e^{\pm}} = \frac{m_e^3 c^3}{\pi^2 \hbar^3} \sqrt{2} \beta^{3/2} [\mathcal{F}_{1/2}(\eta_{e^{\pm}}, \beta) + \beta \mathcal{F}_{3/2}(\eta_{e^{\pm}}, \beta)], \quad (\text{B13})$$

$$P_{e^{\pm}} = \frac{8 m_e^4 c^5}{3\sqrt{2} \pi^2 \hbar^3} \beta^{5/2} \left[\mathcal{F}_{3/2}(\eta_{e^{\pm}}, \beta) + \frac{1}{2} \beta \mathcal{F}_{5/2}(\eta_{e^{\pm}}, \beta) \right], \quad (\text{B14})$$

$$U_{e^{\pm}} = \frac{m_e c^2}{\pi^2} \frac{2\sqrt{2} m_e^3 c^3}{\hbar^3} \beta^{5/2} [\mathcal{F}_{3/2}(\eta_{e^{\pm}}, \beta) + \beta \mathcal{F}_{5/2}(\eta_{e^{\pm}}, \beta)], \quad (\text{B15})$$

where $\mathcal{F}_k(\eta, \beta) \equiv \int_0^{\infty} \frac{x^k (1+0.5x\beta)^{1/2} dx}{e^{x-\eta} + 1}$ is the relativistic Fermi-Dirac integral, $\beta \equiv \kappa_B T / (m_e c^2)$ is the relativity parameter and $\eta \equiv (\mu - m_e c^2) / \kappa_B T$ is the degeneracy parameter, with μ the chemical potential. Since the electrons and positrons are in equilibrium with radiation ($e^+ + e^- \rightarrow \gamma + \gamma$), their chemical potentials are related by $\mu_{e^-} + \mu_{e^+} = 0$ and then $\eta_{e^+} = -\eta_{e^-} - 2/\beta$. Finally, for each value of density and temperature, η_{e^-} is determined from the charge neutrality condition:

$$n_{e^-} - n_{e^+} = \frac{Z}{A} \frac{\rho}{m_u} = Zn_{\text{ion}}. \quad (\text{B16})$$

As an example, we show in Fig. 13 the entropy, temperature, density and pressure profile from the NS surface (we have assumed a NS of $M_{\text{NS}} = 2.0 M_{\odot}$ with $R_{\text{NS}} = 10^6 \text{ cm}$) to the shock radius for a specific value of the mass accretion rate $10^{-2} M_{\odot} \text{ s}^{-1}$. For the ions we adopt here $Z = 6$ and $A = 12$. It can be seen here that the entropy gradient of the NS atmosphere is negative, and it is thus subjected to convective instabilities (see Sec. 6.1).

Neutrino emission and shock position

We turn now to discuss the neutrino emission processes taken into account in our calculations. We follow the results reported in Itoh et al. (1996) for the neutrino energy loss rates computed within the Weinberg-Salam theory (Weinberg 1967; Salam 1968). We use here the formulas which fit the numerical results in the following regime of density and temperature: $10^9 \text{ g cm}^{-3} < \rho < 10^{14} \text{ g cm}^{-3}$ and $10^7 \text{ K} < T < 10^{11} \text{ K}$ (Itoh et al. 1996).

We consider the following channels of neutrino emission. i) Pair annihilation: $e^+ + e^- \rightarrow \nu + \bar{\nu}$ (Munakata et al. 1985; Itoh et al. 1989); this neutrino energy loss rate is here denoted by $\epsilon_{e^-e^+}$. ii) Photo-neutrino process: $\gamma + e^{\pm} \rightarrow e^{\pm} + \nu + \bar{\nu}$ (Munakata et al. 1985; Itoh et al. 1989), denoted by ϵ_{γ} . iii) Plasmon decay: $\bar{\gamma} \rightarrow \nu + \bar{\nu}$ (Kohyama et al. 1986, 1994), denoted by ϵ_{pl} . iv) Bremsstrahlung processes (Itoh & Kohyama 1983; Itoh et al. 1984b,a,c), denoted by ϵ_{BR} , which can be due to electron-nucleon interaction $e^{\pm} + N \rightarrow N + \nu + \bar{\nu}$ or to nucleon-nucleon interaction $N + N \rightarrow N + N + \nu + \bar{\nu}$. It is important to mention that two different expressions for the total Bremsstrahlung emission are shown in Itoh et al. (1996) depending if the Coulomb parameter, $\Gamma \equiv (Ze)^2 / (r_i k_B T)$ where $r_i = [3 / (4\pi n_{\text{ion}})]^{1/3}$, is higher or lower than

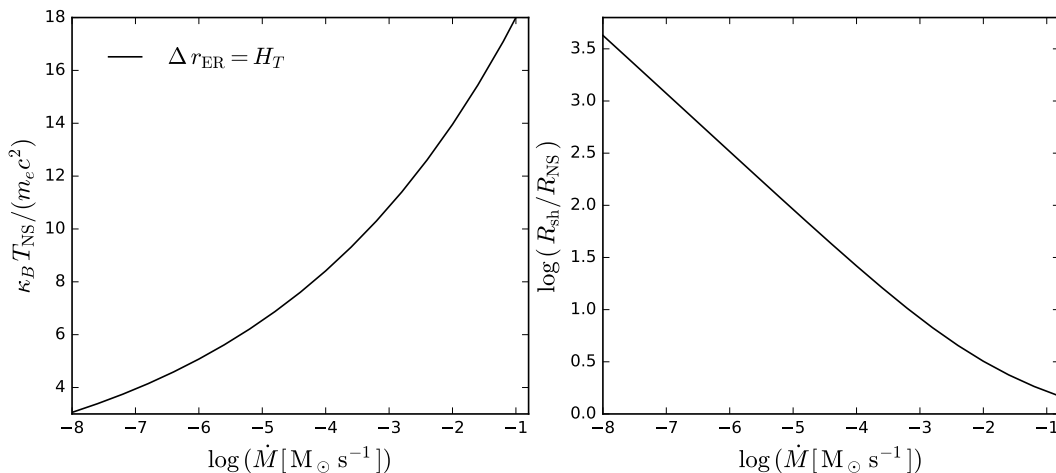


FIG. 14.— Temperature of the NS surface (left panel) and ratio between the shock radius and the NS radius (right plot) as a function of the mass accretion rate in the range $\dot{M} = 10^{-8}$ – $10^{-1} M_\odot \text{ s}^{-1}$.

the critical value $\Gamma \approx 180$, over which the system crystallizes. So the total energy loss rate per unit volume due to neutrino emission is $Q_\nu = \epsilon_{e^-e^+} + \epsilon_\gamma + \epsilon_{\text{pl}} + \epsilon_{\text{BR}}$.

Since the infalling material is strongly decelerated by the accretion shock, the post-shock kinetic energy is much less than the internal and gravitational energy. Then, assuming a polytropic gas [$P = (\gamma - 1)U \propto \rho^\gamma$] and subsonic velocities inside the shock radius, $(v/c)^2 \ll 1$, Eqs. (B4) can be solved for the radial dependence of the fluid variables ρ , P and u as (Houck & Chevalier 1991):

$$\rho = \rho_{\text{sh}} f(r)^{\frac{1}{\gamma-1}}, \quad P = P_{\text{sh}} f(r)^{\frac{\gamma}{\gamma-1}}, \quad u = \frac{u_{\text{sh}}}{r^2} f(r)^{\frac{1}{1-\gamma}} \quad f(r) \equiv \frac{\left(1 - \frac{r_{\text{sch}}}{r}\right)^{-1/2} - 1}{\left(1 - \frac{r_{\text{sch}}}{R_{\text{NS}}}\right)^{-1/2} - 1}. \quad (\text{B17})$$

The approximation of a polytropic equation of state was validated by numerical simulations in Fryer et al. (1996), who showed the infall NS atmosphere is well approximated by a polytropic gas of index $\gamma = 1.4$.

Since neutrinos are the main energy sink of the system (see below), the position of the shock can be estimated from the balance between the neutrino emission and the release of the potential gravitational energy due to the accretion process, i.e.:

$$\left(\frac{4\pi R_{\text{NS}}^2 \Delta r_{\text{ER}}}{\sqrt{1 - \frac{2GM_{\text{NS}}}{c^2 R_{\text{NS}}}}} \right) Q_\nu \approx c^2 \dot{M} \left[\left(1 - \frac{2GM_{\text{NS}}}{c^2 R_{\text{NS}}} \right)^{-1/2} - 1 \right], \quad (\text{B18})$$

where we have assumed the rate at which gravitational energy is released as the kinetic energy gained in the free fall from infinity, and we have considered the proper volume of the cooling region and the proper cooling rate. We have also introduced the thickness of the neutrino emission region at the base of the atmosphere, Δr_{ER} , which in view of the strong dependence of the neutrino emission processes on the temperature, can be estimated as one temperature scale height, i.e.:

$$\Delta r_{\text{ER}} \approx H_T = \frac{T}{|(dT/dr)|}, \quad \frac{dT}{dr} = \left(\frac{\partial \ln T}{\partial \ln \rho} \right)_P \frac{d \ln \rho}{dr} + \left(\frac{\partial \ln T}{\partial \ln P} \right)_\rho \frac{d \ln P}{dr}. \quad (\text{B19})$$

Fig. 14 shows the NS surface temperature and the shock position as a function of the mass accretion rate. The thickness of the neutrino emission region is very poorly dependent on the accretion rate; indeed equation (B19) gives $\Delta r_{\text{ER}} \approx 0.76$ – $0.77 R_{\text{NS}}$ for $\dot{M} = 10^{-8}$ – $10^{-1} M_\odot \text{ s}^{-1}$.

Under the conditions (non-degenerate, relativistic, hot plasma) of our hypercritically accreting NS, the most efficient neutrino emission is given by the e^+e^- pair annihilation (see Fig. 16). In these T - ρ conditions, $\epsilon_{e^-e^+}$ reduces to the simple expression (Yakovlev et al. 2001):

$$\epsilon_{e^-e^+} = 1.39 \times 10^{25} \left(\frac{k_B T}{1 \text{ MeV}} \right)^9 \text{ erg cm}^{-3} \text{ s}^{-1}. \quad (\text{B20})$$

Neutrino and photon optical depth

We have assumed that the neutrinos produced at the base of the NS surface are the main sink of the gravitational potential energy gained by the infalling material. We proceed now to assess the validity of this statement through the calculation of the neutrino opacity.

The total neutrino opacity is:

$$\kappa_\nu = \kappa_{\nu,\text{abs}} + \kappa_{\nu,\text{scat}}, \quad (\text{B21})$$

where $\kappa_{\nu,\text{abs}}$ and $\kappa_{\nu,\text{scat}}$ correspond to the opacity produced by absorption and scattering processes. In general, the opacity can be written as

$$\kappa = \frac{\sigma_i n_i}{\rho}, \quad (\text{B22})$$

where n_i is the particle density and σ_i is the process cross section. We adopt the following scattering and absorption process:

Scattering processes: neutrinos transfer momentum to the matter by the scattering off nuclei and electrons and positrons:

- Coherent neutrino nucleus scattering: $\nu + (A, Z) \rightarrow \nu + (A, Z)$ (Tubbs & Schramm 1975)

$$\sigma_A = \frac{1}{16} \sigma_0 \left(\frac{E_\nu}{m_e c^2} \right)^2 A^2 \left[1 - \frac{Z}{A} + (4 \sin^2 \theta_w - 1) \frac{Z}{A} \right]^2 \quad \text{with} \quad \sigma_0 = \frac{4G_F^2 (m_e c^2)^2}{\pi (\hbar c)^4} \approx 1.71 \times 10^{-44} \text{ cm}^2 \quad (\text{B23})$$

where G_F is the Fermi weak neutrino coupling constant and θ_w is the Weinberg angle, $\sin^2 \theta_w = 0.23$. The scattering is coherent in the sense that nucleus acts as a single particle and the initial and final neutrino energy are nearly equal.

- Neutrino-electron scattering (Bowers & Wilson 1982; Burrows & Thompson 2002):

$$\sigma_e(E) = \frac{3}{8} \sigma_0 \beta \frac{E}{m_e c^2} \left(1 + \frac{\eta_e}{4} \right) \left[(C_v + C_a)^2 + \frac{1}{3} (C_v + C_a)^2 \right] \quad (\text{B24})$$

where $C_v = 1/2 + 2 \sin^2 \theta_w$ for electron neutrino and antineutrino types, $C_a = 1/2$ for neutrino and $C_a = -1/2$ for antineutrinos.

Absorption processes: Since we have shown that the most efficient neutrino cooling process near the NS surface is the electron-positron annihilation, the inverse process namely the annihilation of neutrinos, $\nu + \bar{\nu} \rightarrow e^- + e^+$, represents the main source of opacity. The total average cross sections are given by (Goodman et al. 1987):

$$\sigma_\nu(E_\nu) = \frac{4}{3} K_{\nu\bar{\nu}} \sigma_0 \langle E_\nu \rangle \langle E_{\bar{\nu}} \rangle, \quad \sigma_{\bar{\nu}}(E_{\bar{\nu}}) = \frac{4}{3} K_{\nu\bar{\nu}} \sigma_0 \langle E_{\bar{\nu}} \rangle \langle E_\nu \rangle, \quad (\text{B25})$$

where $K_{\nu\bar{\nu}} = (1 + 4 \sin^2 \theta_w + 8 \sin^4 \theta_w)/12 = 0.195$. The energy of the neutrino and antineutrinos are calculated assuming they are described by the Fermi-Dirac distribution with zero chemical potential:

$$\langle E_\nu \rangle = \langle E_{\bar{\nu}} \rangle = \frac{U_\nu}{n_\nu} = \frac{\mathcal{F}_3(0,0)}{\mathcal{F}_2(0,0)} k_B T = 3.15 k_B T, \quad \langle E_\nu^2 \rangle = \frac{\mathcal{F}_4(0,0)}{\mathcal{F}_2(0,0)} (k_B T)^2 = 12.93 (k_B T)^2. \quad (\text{B26})$$

Then, the total neutrino opacity is:

$$\kappa_\nu = \left[\sigma_A \left(\frac{\rho}{A m_u} \right) + \sigma_e(E_\nu) n_{e^-} + \sigma_\nu(E_\nu) n_\nu \right] / \rho, \quad (\text{B27})$$

The neutrino optical depth can then be obtained as:

$$d\tau_\nu = \kappa_\nu \rho dr = \frac{dr}{\lambda_\nu}, \quad (\text{B28})$$

where λ_ν is the neutrino mean free path:

$$\lambda_\nu = \frac{1}{\kappa_\nu \rho}. \quad (\text{B29})$$

Thus, the optical depth at the base of the neutrino emission region can be estimated as: $\tau_{\nu,\text{ER}} \approx \kappa_\nu \rho_{\text{NS}} \Delta r_{\text{ER}} = \Delta r_{\text{ER}} / \lambda_{\nu,\text{ER}}$. Large values for the optical depth means ($\tau_\nu \gg 1$) implies that the neutrinos are reabsorbed by the matter and cannot freely scape from the system.

In order to verify that photons are trapped in the infalling material, we evaluate the photon mean free path and photon emissivity:

$$\tau_\gamma = \kappa_R \rho \Delta r_{\text{ER}}, \quad \dot{q}_\gamma \approx \frac{1}{\Delta r_{\text{ER}}} \frac{\sigma T^4}{\tau_\gamma}, \quad (\text{B30})$$

where σ is the Stefan-Boltzmann constant, τ_γ is the photon optical depth, and κ_R is the Rosseland mean opacity:

$$\kappa_R = 0.4 + 0.64 \times 10^{23} \left(\frac{\rho}{\text{g cm}^{-3}} \right) \left(\frac{T}{\text{K}} \right)^{-3} \text{ g}^{-1} \text{ cm}^2, \quad (\text{B31})$$

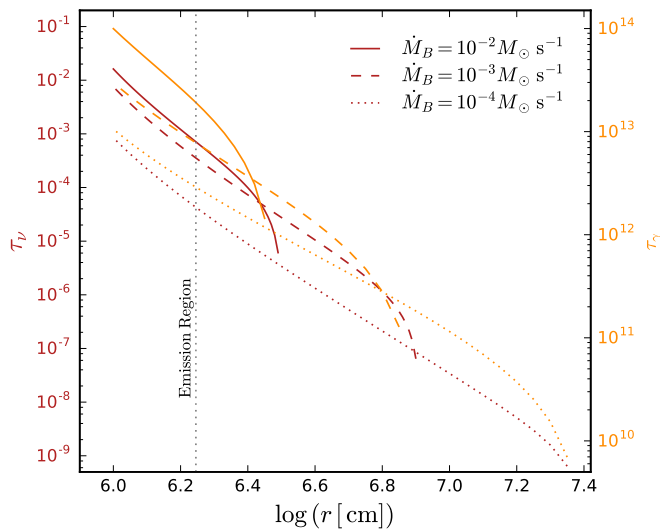


FIG. 15.— Neutrino (left y-scale, τ_ν) and photon (right y-scale, τ_γ) optical depths in the NS star accretion region (from the shock radius to the NS surface) for selected accretion rates.

being the first term due to the electron scattering and the second one to the free-free absorption.

We show in Fig. 15 the neutrino and photon optical depth profile in the NS accretion region for three different values of the mass accretion rate. We can see the photon optical depth is much higher than unity for photons, implying they are indeed trapped at any radius. On the contrary, the neutrino optical depth is much lower than unity, implying they efficiently cool the atmosphere which allows the system to proceed the accretion at hypercritical rates.

We show in Fig. 16 the T - ρ diagram of the NS surface for accretion rates $\dot{M} = 10^{-8}$ – $10^{-1} M_\odot \text{ s}^{-1}$ which covers both XRFs and BdHNe (see, e.g., Fig. 11). Higher temperatures and densities correspond to higher accretion rates. We show contours indicating where the neutrino emissivities of the different neutrino emission processes are equal. It can be seen from these two figures that: 1) pair annihilation neutrino process are highly dominant over the other neutrino emission mechanisms; 2) neutrinos can efficiently escape taking away most of the energy (high emissivity); 3) photons are trapped hence they have negligible emissivity; 4) even for the largest accretion rates the neutrino optical depth in the accretion zone is below unity and so the system is not opaque to neutrinos.

CONVERGENCE TESTS

We proceed now to perform a convergence test of the results of our numerical integration. We will perform the test for four important quantities, as a function of the dimensionless time $\tau = t/t_0$: the NS accreted mass $M_{\text{acc}}(\tau)$, gravitational mass $M_{\text{NS}}(\tau)$, angular momentum $J_{\text{NS}}(\tau)$ and gravitational capture radius measured from the supernova center normalized to the binary separation, i.e. $\hat{r} = 1 - R_{\text{cap}}(\tau)/a$.

We use for the numerical integration the Adams method implemented in the Python library SciPy version 0.17.1. This requires that the user sets, besides the system of ordinary differential equations, a minimum and a maximum integration stepsize. For the integration we set both to the same value, say $\Delta\tau$. To perform this test we select five values of the stepsize: $\Delta\tau_i \equiv \tau_{\text{acc},0}/N_i$ with $N_i = 1, 20, 50, 200, 500$ for $i = 1, \dots, 5$ and $\tau_{\text{acc},0} = t_{\text{acc},0}/t_0$ is the dimensionless time at which the accretion process starts, i.e. the instant at which the first ejecta layer reaches the NS capture radius. We denote as $A_{\Delta\tau_i}$ the numerical value of the quantity A computed with the stepsize $\Delta\tau_i$, and then compute the relative error with respect to the computed value using a reference stepsize, i.e.: $\text{Er}(A) \equiv |A_{\Delta\tau_{\text{ref}}} - A_{\Delta\tau_i}|/A_{\Delta\tau_{\text{ref}}}$. Fig. 17 shows the convergence test for a binary system with the following parameters: the CO core of the $M_{\text{ZAMS}} = 20 M_\odot$ progenitor, an initial NS mass of $2 M_\odot$, and an orbital period $P = 3$ h. For these parameters we have $\tau_{\text{acc},0} \approx 29$ and so the stepsizes are: $\Delta\tau_i = 0.0581, 0.1453, 0.5812, 9.6874, 29.062$, respectively for $i = 1, \dots, 5$. The stepsize of reference in this test is $\Delta\tau_{\text{ref}} = \Delta\tau_3 = 0.5812$. We can see that, as expected, the relative error increases for stepsizes higher than $\Delta\tau_3$ and decreases for stepsizes lower than it, indicating convergence. All the results shown in this article are for $\Delta\tau_3$, which corresponds to a different numerical value for different binary systems, since the value of $\tau_{\text{acc},0}$ is specific to each system.

REFERENCES

- Amati, L., & Della Valle, M. 2013, *International Journal of Modern Physics D*, 22, 1330028
- Bayless, A. J., Even, W., Frey, L. H., et al. 2015, *ApJ*, 805, 98
- Becerra, L., Cipolletta, F., Fryer, C. L., Rueda, J. A., & Ruffini, R. 2015, *ApJ*, 812, 100
- Bondi, H. 1952, *MNRAS*, 112, 195
- Bondi, H., & Hoyle, F. 1944, *MNRAS*, 104, 273
- Boshkayev, K., Quevedo, H., & Ruffini, R. 2012, *Phys. Rev. D*, 86, 064043
- Boshkayev, K. A., Quevedo, H., Abutalip, M. S., Kalymova, Z. A., & Suleymanova, S. S. 2016, *International Journal of Modern Physics A*, 31, 1641006
- Bowers, R. L., & Wilson, J. R. 1982, *ApJS*, 50, 115
- Bufano, F., Pian, E., Sollerman, J., et al. 2012, *ApJ*, 753, 67

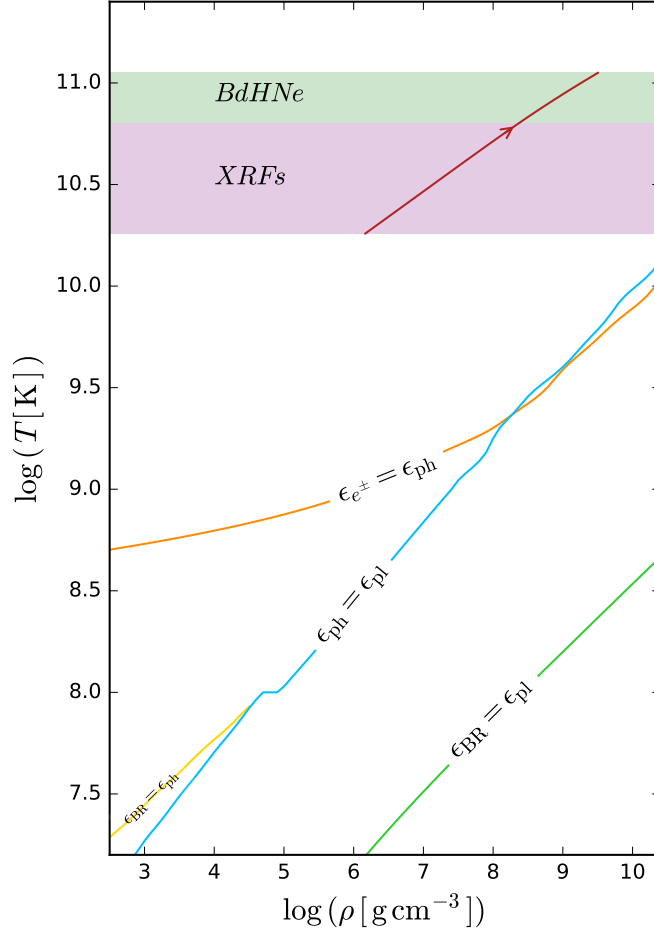


FIG. 16.— Temperature-density diagram of the accreting atmosphere equation of state. In order to see the dominant neutrino processes, we show contours at which the emissivities of the different neutrino processes become equal: ϵ_{e^\pm} correspond to the pair annihilation process, ϵ_γ to the photo-neutrino emission, ϵ_{pl} to the plasmon decay and ϵ_{BR} to the Bremsstrahlung emission. The solid red curve shows the corresponding T - ρ values of the NS surface in the range of accretion $\dot{M} = 10^{-8}$ – $10^{-1} M_\odot \text{ s}^{-1}$ which covers typical rates achieved in XRFs and BdHNe (see Fig. 11). The arrow indicates the direction of increasing accretion rate. Thus, while accreting, the NS moves from the left lower part of the red curve to the right upper part of it. It is clear that in this regime of XRFs and BdHNe, the electron-positron pair annihilation dominates the neutrino emission.

- Burrows, A., & Thompson, T. A. 2002, ArXiv Astrophysics e-prints
 Campana, S., Mangano, V., Blustin, A. J., et al. 2006, *Nature*, 442, 1008
 Chevalier, R. A. 1989, *ApJ*, 346, 847
 Christodoulou, D., & Ruffini, R. 1971, *Phys. Rev. D*, 4, 3552
 Cipolletta, F., Cherubini, C., Filippi, S., Rueda, J. A., & Ruffini, R. 2015, *Phys. Rev. D*, 92, 023007
 Cox, J. P. 1968, *Principles of stellar structure - Vol.1: Physical principles; Vol.2: Applications to stars* (New York: Gordon and Breach, 1968)
 De La Rosa. 2016, Submitted to *ApJ*
 Friedman, J. L., Ipser, J. R., & Sorkin, R. D. 1988, *ApJ*, 325, 722
 Fryer, C. L. 2009, *ApJ*, 699, 409
 Fryer, C. L., Belczynski, K., Wiktorowicz, G., et al. 2012, *ApJ*, 749, 91
 Fryer, C. L., Benz, W., & Herant, M. 1996, *ApJ*, 460, 801
 Fryer, C. L., Herwig, F., Hungerford, A., & Timmes, F. X. 2006, *ApJ*, 646, L131
 Fryer, C. L., Oliveira, F. G., Rueda, J. A., & Ruffini, R. 2015, *Physical Review Letters*, 115, 231102
 Fryer, C. L., Rueda, J. A., & Ruffini, R. 2014, *ApJ*, 793, L36
 Galama, T. J., Vreeswijk, P. M., van Paradijs, J., et al. 1998, *Nature*, 395, 670
 Goodman, J., Dar, A., & Nussinov, S. 1987, *ApJ*, 314, L7
 Guetta, D., & Della Valle, M. 2007, *ApJ*, 657, L73
 Houck, J. C., & Chevalier, R. A. 1991, *ApJ*, 376, 234
 Hoyle, F., & Lyttleton, R. A. 1939, *Proceedings of the Cambridge Philosophical Society*, 35, 405
 Itoh, N., Adachi, T., Nakagawa, M., Kohyama, Y., & Munakata, H. 1989, *ApJ*, 339, 354
 Itoh, N., Hayashi, H., Nishikawa, A., & Kohyama, Y. 1996, *ApJ*, 102, 411
 Itoh, N., & Kohyama, Y. 1983, *ApJ*, 275, 858
 Itoh, N., Kohyama, Y., Matsumoto, N., & Seki, M. 1984a, *ApJ*, 280, 787
 —. 1984b, *ApJ*, 285, 304
 Itoh, N., Matsumoto, N., Seki, M., & Kohyama, Y. 1984c, *ApJ*, 279, 413
 Izzo, L., Rueda, J. A., & Ruffini, R. 2012a, *A&A*, 548, L5
 Izzo, L., Ruffini, R., Penacchioni, A. V., et al. 2012b, *A&A*, 543, A10
 Kohyama, Y., Itoh, N., & Munakata, H. 1986, *ApJ*, 310, 815
 Kohyama, Y., Itoh, N., Obama, A., & Hayashi, H. 1994, *ApJ*, 431, 761
 Landau, L. D., & Lifshitz, E. M. 1959, *Fluid mechanics* (Oxford: Pergamon Press, 1959)
 Melandri, A., Pian, E., D’Elia, V., et al. 2014, *A&A*, 567, A29
 Munakata, H., Kohyama, Y., & Itoh, N. 1985, *ApJ*, 296, 197
 Pian, E., Mazzali, P. A., Masetti, N., et al. 2006, *Nature*, 442, 1011
 Pisani, G. B., Izzo, L., Ruffini, R., et al. 2013, *A&A*, 552, L5
 Rees, M., Ruffini, R., & Wheeler, J. A. 1974, *Black holes, gravitational waves and cosmology* (New York: Gordon and Breach Science Publishers Inc.)
 Rhoades, C. E., & Ruffini, R. 1974, *Physical Review Letters*, 32, 324
 Rueda, J. A., & Ruffini, R. 2012, *ApJ*, 758, L7

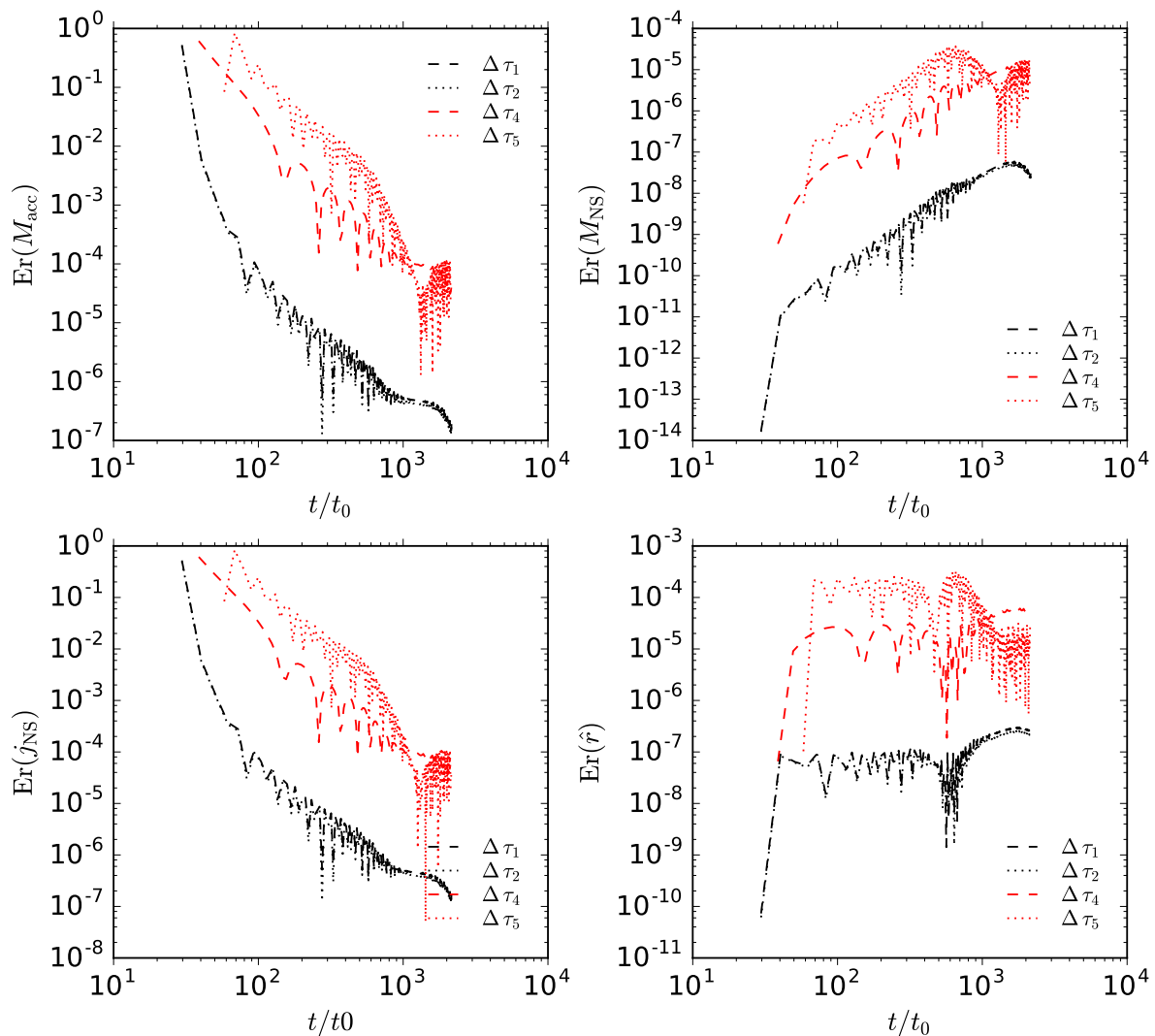


FIG. 17.— Convergence test for the NS accreted mass $M_{\text{acc}}(\tau)$, gravitational mass $M_{\text{NS}}(\tau)$, angular momentum $J_{\text{NS}}(\tau)$ and the gravitational capture radius measured from the supernova center normalized to the binary separation, i.e. $\hat{r} = 1 - R_{\text{cap}}(\tau)/a$. We select here five values of the stepsize: $\Delta\tau_i = 0.0581, 0.1453, 0.5812, 9.6874, 29.062$ for $i = 1, \dots, 5$. The parameters of the binary system in this example are: the CO core of the $M_{\text{ZAMS}} = 20 M_{\odot}$ progenitor, an initial NS mass of $2 M_{\odot}$, and an orbital period $P = 3$ h. The relative error increases for stepsizes higher than $\Delta\tau_3$ and decreases for stepsizes lower than it, which indicates convergence.

Ruffini, R. 2015a, in Thirteenth Marcel Grossmann Meeting: On Recent Developments in Theoretical and Experimental General Relativity, Astrophysics and Relativistic Field Theories, ed. K. Rosquist, 242–314

Ruffini, R. 2015b, *Astronomy Reports*, 59, 591

Ruffini, R., Bernardini, M. G., Bianco, C. L., et al. 2006, in The Tenth Marcel Grossmann Meeting. Proceedings of the MG10 Meeting held at Brazilian Center for Research in Physics (CBPF), Rio de Janeiro, Brazil, 20–26 July 2003, Eds.: Mário Novello; Santiago Perez Bergliaffa; Remo Ruffini. Singapore: World Scientific Publishing, in 3 volumes, ISBN 981-256-667-8 (set), ISBN 981-256-980-4 (Part A), ISBN 981-256-979-0 (Part B), ISBN 981-256-978-2 (Part C), 2006, XLVIII + 2492 pp.: 2006, p.369, ed. M. Novello, S. Perez Bergliaffa, & R. Ruffini, 369

Ruffini, R., & Wilson, J. 1973, *Physical Review Letters*, 31, 1362

Ruffini, R., Bernardini, M. G., Bianco, C. L., et al. 2008, in The Eleventh Marcel Grossmann Meeting On Recent Developments in Theoretical and Experimental General Relativity, Gravitation and Relativistic Field Theories, ed. H. Kleinert, R. T. Jantzen, & R. Ruffini, 368–505

Ruffini, R., Wang, Y., Enderli, M., et al. 2015, *ApJ*, 798, 10

Ruffini, R., Rueda, J. A., Muccino, M., et al. 2016, *ArXiv e-prints*

Salam, A. 1968, *Elementary Particle Physics* (Stockholm: Almquist and Wiksells)

Sibgatullin, N. R., & Sunyaev, R. A. 2000, *Astronomy Letters*, 26, 772

Stergioulas, N. 2003, *Living Reviews in Relativity*, 6

Tanaka, M., Kawabata, K. S., Maeda, K., et al. 2009, *ApJ*, 699, 1119

Tanvir, N. R., Levan, A. J., Fruchter, A. S., et al. 2013, *Nature*, 500, 547

Taubenberger, S., Valenti, S., Benetti, S., et al. 2009, *MNRAS*, 397, 677

Tubbs, D. L., & Schramm, D. N. 1975, *ApJ*, 201, 467

Weinberg, S. 1967, *Physical Review Letters*, 19, 1264

Wong, T.-W., Fryer, C. L., Ellinger, C. I., Rockefeller, G., & Kalogera, V. 2014, *ArXiv e-prints*

Woolsey, S. E., Heger, A., & Weaver, T. A. 2002, *Reviews of Modern Physics*, 74, 1015

Yakovlev, D. G., Kaminker, A. D., Gnedin, O. Y., & Haensel, P. 2001, *Phys. Rep.*, 354, 1

Zel'dovich, Y. B., Ivanova, L. N., & Nadezhin, D. K. 1972, *Soviet Ast.*, 16, 209

ON THE CLASSIFICATION OF GRBS AND THEIR OCCURRENCE RATES

R. RUFFINI^{1,2,3,4}, J. A. RUEDA^{1,2,4}, M. MUCCINO^{1,2}, Y. AIMURATOV^{1,2}, L. M. BECERRA^{1,2}, C. L. BIANCO^{1,2}, M. KOVACEVIC^{1,2,3}, R. MORADI^{1,2}, F. G. OLIVEIRA^{1,2,3}, G. B. PISANI^{1,2}, Y. WANG^{1,2}

¹Dip. di Fisica and ICRA, Sapienza Università di Roma, Piazzale Aldo Moro 5, I-00185 Rome, Italy.

²ICRANet, Piazza della Repubblica 10, I-65122 Pescara, Italy.

³Université de Nice Sophia Antipolis, CEDEX 2, Grand Château Parc Valrose, Nice, France.

⁴ICRANet-Rio, Centro Brasileiro de Pesquisas Físicas, Rua Dr. Xavier Sigaud 150, 22290-180 Rio de Janeiro, Brazil.

ABSTRACT

There is mounting evidence for the binary nature of the progenitors of gamma-ray bursts (GRBs). For a long GRB, the induced gravitational collapse (IGC) paradigm proposes as progenitor, or “in-state”, a tight binary system composed of a carbon-oxygen core (CO_{core}) undergoing a supernova (SN) explosion which triggers hypercritical accretion onto a neutron star (NS) companion. For a short GRB, a NS-NS merger is traditionally adopted as the progenitor. We divide long and short GRBs into two sub-classes, depending on whether or not a black hole (BH) is formed in the merger or in the hypercritical accretion process exceeding the NS critical mass. For long bursts, when no BH is formed we have the sub-class of X-ray flashes (XRFs), with isotropic energy $E_{iso} \lesssim 10^{52}$ erg and rest-frame spectral peak energy $E_{p,i} \lesssim 200$ keV. When a BH is formed we have the sub-class of binary-driven hypernovae (BdHNe), with $E_{iso} \gtrsim 10^{52}$ erg and $E_{p,i} \gtrsim 200$ keV. In analogy, short bursts are similarly divided into two sub-classes. When no BH is formed, short gamma-ray flashes (S-GRFs) occur, with $E_{iso} \lesssim 10^{52}$ erg and $E_{p,i} \lesssim 2$ MeV. When a BH is formed, the authentic short GRBs (S-GRBs) occur, with $E_{iso} \gtrsim 10^{52}$ erg and $E_{p,i} \gtrsim 2$ MeV. We give examples and observational signatures of these four sub-classes and their rate of occurrence. From their respective rates it is possible that “in-states” of S-GRFs and S-GRBs originate from the “out-states” of XRFs. We indicate two additional progenitor systems: white dwarf-NS and BH-NS. These systems have hybrid features between long and short bursts. In the case of S-GRBs and BdHNe evidence is given of the coincidence of the onset of the high energy GeV emission with the birth of a Kerr BH.

Keywords: gamma ray bursts – hypercritical accretion – black holes – high energy emission

1. INTRODUCTION

On February 1974, at the same AAAS meeting in San Francisco where the discovery of GRBs by the Vela satellites was publicly announced (Strong et al. 1975), the possible relation of GRBs with the “moment of gravitational collapse” leading to a BH formation was advanced (see Gursky & Ruffini 1975). Damour & Ruffini (1975) considered, for definiteness, the vacuum polarization process occurring in an overcritical Kerr-Newman BH (KNBH). Evidence was given for: a) the formation of a vast amount of e^+e^- -baryon plasma; b) the energetics of GRBs of the order of $E_{\max} \approx 10^{54} M_{\text{BH}}/M_{\odot}$ erg, where M_{BH} is the BH mass, implying their cosmological origin; c) the ultra-high energy cosmic rays with energy up to $\sim 10^{20}$ eV originating from such an extreme electro-dynamical process. Soon after, the role of an e^+e^- plasma for the origin of GRBs was also considered by Cavallo & Rees (1978). It took almost thirty years to clarify some of the analogies and differences between these two processes of e^+e^- -pair creation leading, respectively, to the alternative concepts of “fireball” and “fireshell” (Aksenov et al. 2007, 2009).

Already in 1989, well before the establishment of the GRB cosmological nature and energetics, Eichler et al. (1989) gave support to the cosmological interpretation of GRBs and indicated in merging NS binaries their possible origin. They also pointed out the relevance of such NS-NS mergers for the occurrence of r-process, as well as for the emission of gravitational radiation, indicating the uncertainty in the determination of their rate of occurrence.

Following the launch of the Compton satellite and the observations by the BATSE detector (Meegan et al. 1992), a phenomenological classification based on the prompt T_{90} duration was advanced: GRBs were classified into long GRBs for $T_{90} > 2$ s, and short GRBs for $T_{90} < 2$ s (Klebesadel 1992; Dezalay et al. 1992; Kouveliotou et al. 1993; Tavani 1998).

Shortly after Narayan et al. (1992) indicated the possible cosmological origin of short GRBs originating in binary NS mergers. They also introduced the clear indication of the role of $\nu\bar{\nu}$ annihilation leading to the formation of an e^+e^- plasma. This paper was followed by a large number of theoretical works including the gravitational wave emission in Newtonian, post-Newtonian, and general relativistic treatments (see, e.g., Rasio & Shapiro 1999), as well as the $\nu\bar{\nu}$ annihilation leading to an e^+e^- plasma (see, e.g., Salmonson & Wilson 2002 and Rosswog et al. 2003 and references therein).

Soon after the paper by Narayan et al. (1992), Woosley (1993) also supported the cosmological origin of GRBs and introduced the concept of BH-Accretion-Disks, produced by the collapse of a very massive star. Such a system was indicated by its author as a *collapsar* and was assumed to be the origin of ultrarelativistic jets expected to occur by the same author in long GRBs. For a recent review see MacFadyen & Woosley (1999); MacFadyen et al. (2001); Woosley & Bloom (2006).

After the determination of the cosmological nature of GRBs (Costa et al. 1997; Metzger et al. 1997; van Paradijs et al. 1997) and the confirmation of their outstanding energy ($\approx 10^{54}$ erg), we returned to our GRB scenario (Damour & Ruffini 1975). In a period of four years, from 1997 to 2001, we developed a fully relativistic GRB theoretical model examining, as well, the dynamics of the e^+e^- plasma originating the GRB emission (the fireshell model, see, e.g., Preparata et al. 1998; Ruffini et al. 1999, 2000, 2001a,b,c, and Section 2). The fireshell model applies to both short and long GRBs.

The origin of short GRBs from NS–NS (or NS–BH) binaries as “in-states” has been confirmed by strong observational and theoretical evidences (see, e.g., Goodman 1986; Paczynski 1986; Eichler et al. 1989; Narayan et al. 1991, 1992; Meszaros & Rees 1997; Rosswog et al. 2003; Lee et al. 2004; Berger 2014). In this article we address specifically some of the latest results within the fireshell model (Muccino et al. 2013; Ruffini et al. 2015b) on the possible presence or absence of a BH formation in NS–NS mergers, the consequent classification of short bursts into S-GRFs, when no BH is formed (see Section 6), and S-GRBs, when a BH is formed (see Section 7), and the computation of their occurrence rate (see Section 10).

The application of the fireshell model to the case of long GRBs followed a longer path for reaching a proper understanding of the overall phenomenon. The first application of our model to a long GRB was implemented on GRB 991216 (Ruffini et al. 2001a,b,c, 2002, 2004, 2006a). In these papers a clear difference between the thermal component observed at the transparency of the e^+e^- plasma, the Proper GRB (P-GRB) emission (Ruffini et al. 1999, 2000), and the non-thermal remaining part, later called prompt emission (Ruffini et al. 2001b), was evidenced. This fully relativistic approach was not readily accepted by the GRB community, also in view of its objective technical complexity and novelties in the theoretical physics scenario. Some authors attempted to describe the GRB phenomenon by simplified Newtonian approaches, e.g., those based on the concept of *magnetars* (Usov 1992; Dai & Lu 1998a,b; Kluźniak & Ruderman 1998; Zhang & Mészáros 2001). As the detailed observations of the X-ray afterglow by the *Swift*-XRT (Evans et al. 2007) were obtained, as well as the high energy emission by the Fermi-LAT (Atwood et al. 2009), our model has correspondingly evolved pointing out the precise common power-law behavior of the rest-frame 0.3–10 keV X-ray luminosity light curves (Pisani et al. 2013), as well as the nesting properties (Ruffini et al. 2014b). As pointed out in the present article, the concept of long GRBs has evolved into XRFs and BdHNe, depending on the possible presence or absence of a BH in their formation process (see also Ruffini et al. 2015a).

It is appropriate to recall that the quest for having progenitors for the collapsar hypothesized by Woosley (1993) led to an interesting direction of research dealing with a binary system composed of two very massive stars of $\approx 50 M_{\odot}$ each. The large masses involved in these systems were introduced in order to form a BH at the end of their evolution. Similarly, the large amount of angular momentum of the system would guarantee the formation of an accretion disks needed in the collapsar model (Fryer et al. 1999). Up to six different scenarios were there envisaged leading to a *collapsar*, as well as a few leading, alternatively, to a variety of binary compact systems. The need for choosing low-metallicity massive stars followed from the expectation of the formation large BHs in their evolution (Fryer et al. 1999). The elimination of H from metal-rich massive stars would follow naturally, but the formation of a BH was not expected in their final stage of evolution (Woosley 1993).

The spatial and temporal coincidence of a long GRB explosion with an optical SN, first observed in the association between GRB 980425 and SN 1998bw, created a profound conceptual turmoil in the GRB community. Woosley and collaborators postulated the birth of a SN out of a collapsar (see, e.g., Woosley & Bloom 2006, and references therein).

In our approach, GRBs were supposed to originate from the BH formation, while SNe were expected to lead only to NSs (see, e.g., Ruffini 2015, and references therein). We consequently introduced a new paradigm to explain the coincidence of these two qualitative and quantitative different astrophysical events in space and time: the birth of a SN and the occurrence of a GRB. The induced gravitational collapse (IGC) paradigm was then introduced (see, e.g.,

Ruffini et al. 2001a, 2006b, 2007, 2008; Izzo et al. 2012b; Rueda & Ruffini 2012; Fryer et al. 2014). This approach differs from alternative descriptions of the GRB-SN coincidences occurring, e.g., in the *magnetars* and the *collapsar* models, where the two events are coming from a single progenitor star, and takes full advantage of the recent observations of SNe Ibc in interacting binary systems (Smartt 2009).

In a first formulation we considered a finely tuned process: the GRB triggering the explosion of a binary companion star very close to the onset of the SN (Ruffini et al. 2001a). This scenario soon led to the alternative IGC paradigm in which a CO_{core} undergoes a SN explosion in presence of a NS companion in a tight binary system. This is also by itself an unlikely event which in order to occur needs a fine tuning of the initial conditions of the binary system. This scenario was shown to be consistent with population synthesis analysis (Fryer et al. 1999, 2015). The SN explosion induces a hypercritical accretion of its ejecta onto the companion NS, leading to the formation of a more massive NS (MNS), when the NS critical mass M_{crit} is not reached, or to the formation of a BH with the associated GRB emission in the opposite case (see, e.g., Rueda & Ruffini 2012; Fryer et al. 2014). The IGC scenario was first tested and verified in GRB 090618 (Izzo et al. 2012c,b). It soon became clear that the occurrence of a GRB is far from being a single event, but it is part of an authentic laboratory composed of a variety of astrophysical relativistic phenomena preceding and following the prompt GRB emission.

We adopted as progenitor of our CO_{core}-NS binary system the massive binaries independently considered in Fryer et al. (1999) and Nomoto et al. (1994, 1995). In our case, the late evolution of such massive binary systems do not lead to a collapsar, nor to an hypernova, but to a much richer and vast number of possibilities, made possible by our IGC paradigm. Consistently with the considerations by Sakamoto et al. (2005), indicating that XRFs, X-ray rich bursts, and all long GRBs are part of a same population which we show to originate in the hypercritical accretion process of the SN ejecta onto a binary companion NS.

In agreement with the considerations by Soderberg et al. (2006); Guetta & Della Valle (2007); Liang et al. (2007) for a sub-classification of long bursts into low-luminous and high-luminous GRBs, we have divided the long bursts into two different scenarios depending on the distance between the CO_{core} and the NS binary companion (Becerra et al. 2015). Correspondingly two different sub-classes of long bursts, both originating in the hypercritical accretion process of the IGC scenario, have been shown to exist (Ruffini et al. 2015a; Becerra et al. 2015): the XRFs, which clearly include low-luminous GRBs, such as GRB 060218 (Campana et al. 2006), when no BH is formed (see Section 4), and the BdHNe, such as GRB 130427A (Ruffini et al. 2015a), when a BH is formed (see Section 5). Their occurrence rates have been computed (see Section 10). Instead of proposing just a new classification, we also give the description of its underlying physical origin: the hypercritical accretion process of the SN ejecta onto a binary companion NS, with the full associated theoretical treatments at the basis of the IGC paradigm.

To the above four sub-classes of long and short bursts, we have recently added a new hybrid sub-class of ultrashort GRBs (U-GRBs) which, as recently pointed out in Fryer et al. (2015), can originate during the further evolution of the BdHNe out-states. Indeed, nearly 100% of the NS-BH binaries which are the outcome of BdHNe remain bound. Their orbital velocities are high and even large kicks are unlikely to unbind these systems. They represent a new family of NS-BH binaries unaccounted for in current standard population synthesis analyses (see, e.g., Fryer et al. 2015, and Section 8).

The above considerations based on the IGC paradigm and the NS-NS paradigm as progenitors encompass and classify into sub-classes most of the known astrophysical systems related to GRBs. We finally recall the existence of a class of long GRBs occurring in a low density circumburst medium (CBM) with density $\sim 10^{-3} \text{ cm}^{-3}$, with hybrid short/long burst properties in their γ -ray light curves: 1) an initial spike-like harder emission and 2) a prolonged softer emission observed up to a hundred seconds. These bursts do not have an associated SN, even though in the case of a low value of the cosmological redshift its detection would not be precluded. The prototype of such systems is GRB 060614 (Della Valle et al. 2006). The progenitor for this class of long bursts has been identified in a binary system composed of a NS and a white dwarf (WD) (Caito et al. 2009). Their merger leads to a MNS with additional orbiting material, but not to an authentic GRB. We refer to these systems, historically addressed as disguised short GRB, as gamma-ray flashes (GRFs), see, e.g., GRB 060614, Caito et al. 2009 and GRB 071227, Caito et al. 2010).

In the following we adopt the term *burst* only for those systems leading to the BH formation, namely to S-GRBs, U-GRBs and BdHNe. We refer to the term *flash*, instead, only for those systems not leading to the BH formation, namely to S-GRFs, GRFs and XRFs (see Fig. 7).

The main topic addressed in the present article is to estimate the rates of occurrence of the XRFs, BdHNe, S-GRFs, S-GRBs, U-GRBs, and GRFs and to give a general description of these GRB sub-classes. In Section 2 we present a short summary on the fireshell model. In Section 3 we discuss the 10^{52} erg lower limit in binary systems leading to BH formation. After describing the observational properties of the above sub-classes, their interpretation within the

Extended wording	Acronym
Binary-driven hypernova	BdHN
Black hole	BH
Carbon-oxygen core	CO _{core}
Circumburst medium	CBM
EQuiTemporal Surfaces	EQTS
Gamma-ray burst	GRB
Gamma-ray flash	GRF
Induced gravitational collapse	IGC
Kerr-Newman black hole	KNBH
Massive neutron star	MNS
Neutron star	NS
New neutron star	ν NS
Proper gamma-ray burst	P-GRB
Short gamma-ray burst	S-GRB
Short gamma-ray flash	S-GRF
Supernova	SN
Ultrashort gamma-ray burst	U-GRB
White dwarf	WD
X-ray flash	XRF

Table 1. Alphabetic ordered list of the acronyms used in this work.

IGC paradigm, the NS-NS merger scenario and the fireshell scenario, we present some prototypes (see Sections 4, 5, 6, 7, 8, and 9, respectively). We then proceed in Section 10 to estimate their observed occurrence rates and to compare and contrast our results with those outlined in the literature (see, e.g., Soderberg et al. 2006; Guetta & Della Valle 2007; Liang et al. 2007; Virgili et al. 2009, 2011; Rangel Lemos et al. 2010; Wanderman & Piran 2010, 2015; Kovacevic et al. 2014; Sun et al. 2015). We then draw some general conclusions in Section 11.

A standard flat Λ CDM cosmological model with $\Omega_M = 0.27$, $\Omega_\Lambda = 0.73$, and $H_0 = 71 \text{ km s}^{-1} \text{ Mpc}^{-1}$ is adopted throughout the paper. A summary of acronyms used throughout the paper is shown in Table 1.

2. SUMMARY OF THE FIRESHELL MODEL

The fireshell model for GRBs (see, e.g. Ruffini et al. 2001a,b,c) has been introduced to explain the GRB phenomenon as originating in the gravitational collapse leading to the formation of a BH (Damour & Ruffini 1975). The GRB emission results by taking into proper account relativistic magneto-hydrodynamical effects, quantum-electrodynamical process, and relativistic space-time transformations.

The role of the relativistic magneto-hydrodynamical effects arising in the gravitational collapse of a globally neutral magnetized plasma has been first considered in Ruffini & Wilson (1975), where the occurrence of a local charge separation, during a globally neutral accretion process, led to the development of overcritical electric fields at the onset of a KNBH formation.¹ These overcritical fields and, consequently, the vacuum polarization process leading to the creation of an e^+e^- plasma, have been considered in Damour & Ruffini (1975), for the sake of definiteness in a KNBH, as the energy source of GRBs:² the pair creation process is fully reversible and as a result a highly efficient energy extraction mechanism occurs, which may deliver as much as $E_{\text{max}} \approx 10^{54} M_{\text{BH}}/M_\odot \text{ erg}$.

Later on, the concept of *dyadotorus* for a KNBH (Cherubini et al. 2009; Ruffini 2009) has been introduced to describe the region where pair creation occurs, leading to the formation of a BH. The dynamics of an optically thick *fireshell* of e^+e^- plasma of total energy $E_{e^+e^-}^{\text{tot}}$, i.e., its expansion and self-acceleration due to its own internal pressure, has been described in Ruffini et al. (1999). The effect of baryonic contamination, i.e., the remnant of the collapsed object, on the dynamics of the fireshell has been then considered in Ruffini et al. (2000), where it has been shown that even after the engulfment of a baryonic mass M_B , quantified by the baryon load $B = M_B c^2 / E_{e^+e^-}^{\text{tot}}$, the fireshell remains still

¹ Overcritical electric fields are defined as larger than the critical value $E_c = m_e^2 c^3 / (\hbar e)$, where m_e is the electron mass, c the speed of light in the vacuum, \hbar the reduced Planck constant, and e the electron charge.

² The role of an e^+e^- plasma for the origin of GRBs was also considered independently by Cavallo & Rees (1978).

optically thick and continues its self-acceleration up to ultrarelativistic velocities (Aksenov et al. 2007, 2009). When the fireshell reaches transparency condition, a flash of thermal radiation termed P-GRB is emitted (Ruffini et al. 1999, 2000). The dynamics of the fireshell up to the transparency condition is fully described by $E_{e^+e^-}^{\text{tot}}$ and B : solutions with $B \leq 10^{-2}$ are characterized by regular relativistic expansion; for $B > 10^{-2}$ turbulence and instabilities occur (Ruffini et al. 2000).

The P-GRB emission is followed by the prompt emission (Ruffini et al. 2001b). The prompt emission originates in the collisions of the accelerated baryons left over after transparency, moving at Lorentz factor $\Gamma \approx 100\text{--}1000$, with interstellar clouds of CBM (Ruffini et al. 2002, 2004, 2005). These interactions give rise to a modified blackbody spectrum in the co-moving frame (Patricelli et al. 2012). The resulting observed spectral shape, once the constant arrival time effect is taken into account in the EQuiTemporal Surfaces (EQTS, see Bianco & Ruffini 2005a,b), is in general non-thermal, as the result of the convolution of a large number of modified thermal spectra with different Lorentz factors and temperatures. To reproduce the prompt emission light curve and spectra three additional parameters, all related to the properties of the CBM, are required: the CBM density profile n_{CBM} , the filling factor \mathcal{R} that accounts for the size of the effective emitting area, and a low-energy power-law index α of the modified black body spectrum (Patricelli et al. 2012). These parameters are obtained by running a trial-and-error simulation of the observed prompt emission light curves and spectra.

To describe the dynamics of such an e^+e^- -baryon plasma from the vicinity of a BH all the way up to ultrarelativistic velocities at the infinity, both in the P-GRB and the prompt emission, the appropriate relative spacetime transformation paradigm has been discussed in Ruffini et al. (2001c). It relates the observed GRB signal to its past light cone, defining the events on the worldline of the source that is essential for the interpretation of the data. Particular attention has been there given to the explicit equations relating the comoving time, the laboratory time, the arrival time, and the arrival time at the detector corrected by the cosmological effects, consistently with the equation of motion of the system (see also Bianco & Ruffini 2004, 2005a,b, 2006), compared and contrasted with the corresponding treatments in the literature (see, e.g., Sari 1997, 1998; Waxman 1997; Panaitescu & Meszaros 1998; Panaitescu & Mészáros 1999; Rees & Meszaros 1998; Granot et al. 1999; Chiang & Dermer 1999).

As recalled above, the evolution of a baryon-loaded pair plasma, is generally described in terms of $E_{e^+e^-}^{\text{tot}}$ and B and it is independent of the way the pair plasma is created. Given this generality, in addition to the specific case of the dyadotorus mentioned above, these concepts can be applied as well in the case of a pair plasma created via $\nu\bar{\nu} \leftrightarrow e^+e^-$ mechanism in a NS merger as described in Narayan et al. (1992), Salmonson & Wilson (2002), and Rosswog et al. (2003), or in the hyper-accretion disks around BHs as described in Woosley (1993) and Zalamea & Beloborodov (2011), assuming that the created pair plasma is optically thick. The relative role of neutrino and weak interactions vs. the electromagnetic interactions in building the dyadotorus is currently topic of intense research.

In conclusion, the deeper understanding of the GRB phenomenon, occurring under very different initial conditions, has highlighted the possibility of using the general description of the dyadosphere (dyadotorus) to any source of an optically thick baryon-loaded e^+e^- plasma and, consequently, to apply the above fireshell treatment in total generality.

The generality of the fireshell approach clearly differs from alternative treatments purporting late activity from a central engine (see, e.g., the *collapsar* model in Woosley 1993, Popham et al. 1999, Woosley & Bloom 2006 and references therein, and the Newtonian *magnetar* model in Zhang & Mészáros 2001, Dai et al. 2006, Metzger et al. 2011, Bucciantini et al. 2012, Giacomazzo & Perna 2013, Lü & Zhang 2014, and references therein), and proposes a different explanation for the afterglow observations in long GRBs (see Pisani et al. 2013, and Aimuratov et al., in preparation).

3. ON THE 10^{52} ERG LOWER LIMIT IN BINARY SYSTEMS LEADING TO BH FORMATION

During the hypercritical accretion process onto the NS the total energy available to be released, e.g. in form of neutrinos and photons, is given by the gain of gravitational potential energy of the matter being accreted by the NS (Zel'dovich et al. 1972; Ruffini & Wilson 1973; Rueda & Ruffini 2012; Fryer et al. 2014). The total energy released in the star in a time-interval dt during the accretion of an amount of mass dM_b with angular momentum $l\dot{M}_b$ is given by (see, e.g., Sibgatullin & Sunyaev 2000; Becerra et al. 2015):

$$L_{\text{acc}} = \left(\dot{M}_b - \dot{M}_{\text{NS}}\right) c^2 = \dot{M}_b c^2 \left[1 - \left(\frac{\partial M_{\text{NS}}}{\partial J_{\text{NS}}}\right)_{M_b} l - \left(\frac{\partial M_{\text{NS}}}{\partial M_b}\right)_{J_{\text{NS}}} \right], \quad (1)$$

where J is the NS angular momentum. The last two terms of the above equation take into due account the change of binding energy of the NS while accreting both matter and angular momentum. We assume, as a norm, a typical NS mass of $\approx 1.4 M_{\odot}$, a value observed in galactic NS binaries (Zhang et al. 2011; Antoniadis 2015) and characteristic

of the XRFs (Becerra et al. 2016). We also assume a NS critical mass M_{crit} in the range from $2.2 M_{\odot}$ up to $3.4 M_{\odot}$ depending on the equations of state and angular momentum (see Becerra et al. 2016, 2015; Cipolletta et al. 2015, for details). L_{acc} is clearly a function both of the NS mass and of M_{crit} .

Since $L_{acc} \propto \dot{M}_b$, it evolves with time similarly to \dot{M}_B . We have shown that the accretion luminosity can be as high as $L_{acc} \sim 0.1 \dot{M}_b c^2 \sim 10^{47} - 10^{51}$ erg s $^{-1}$ for accretion rates $\dot{M}_b \sim 10^{-6} - 10^{-2} M_{\odot}$ s $^{-1}$ (see Becerra et al. 2016, 2015, for details). The duration of the accretion process is given approximately by the flow time of the slowest layers of the SN ejecta to the NS companion. If the velocity of these layers is v_{inner} , then $\Delta t_{acc} \sim a/v_{inner}$, where a is the binary separation. For $a \sim 10^{11}$ cm and $v_{inner} \sim 10^8$ cm s $^{-1}$ we obtain $\Delta t_{acc} \sim 10^3$ s, while for shorter binary separation, e.g. $a \sim 10^{10}$ cm ($P \sim 5$ min), $\Delta t_{acc} \sim 10^2$ s. These estimates are validated by our numerical simulations (see, e.g., Becerra et al. 2016, 2015; Fryer et al. 2015, 2014). From the above results we obtain that for systems with the above short orbital periods the NS collapses to a BH, namely BdHNe (Becerra et al. 2016), and a total energy larger than the separatrix energy of $\approx 10^{52}$ erg is released during the hypercritical accretion process. For systems with larger separations, in which the hypercritical accretion is not sufficient to induce the collapse of the NS into a BH, namely the XRFs (Becerra et al. 2016), the value of $\approx 10^{52}$ erg represents a theoretical estimate of the upper limit to the energy emitted by norm in the hypercritical accretion process. These considerations are derived from theoretical expectations based on the above mentioned masses for the accreting NSs and M_{crit} . Indeed, they are in satisfactory agreement with the observations of 20 XRFs and 233 BdHNe (considered up to the end of 2014) which we have used in our sample (see Table 2 and 3, respectively). The upper limit for the XRFs is $(7.3 \pm 0.7) \times 10^{51}$ erg (see Sec. 4.1), while the lower limit for the BdHNe is $(9.2 \pm 1.3) \times 10^{51}$ erg (see Sec. 5.1).

The same arguments apply to the fusion process of two NSs in a binary NS merger (Ruffini et al. 2015b). Therefore, from these general arguments, we can conclude that the energy emitted during the merger process leading to the formation of a BH should be larger than $\approx 10^{52}$ erg. Indeed, we find the upper limit for the S-GRFs of $(7.8 \pm 1.0) \times 10^{51}$ erg (see Sec. 6.1) and the lower limit for the S-GRBs of $(2.44 \pm 0.22) \times 10^{52}$ erg (see Sec. 7.1).

Such a separatrix energy is clearly a function of the initial NS mass undergoing accretion, by norm assumed to be $\approx 1.4 M_{\odot}$. It is also a function of the yet unknown precise value of M_{crit} for which only an absolute upper limit of $3.2 M_{\odot}$ has been established for the non-rotating case (Rhoades & Ruffini 1974). As already pointed out in Ruffini et al. (2015b) for the case of binary NS mergers, the direct observation of the separatrix energy between S-GRFs and S-GRBs, and also (in this case) between BdHNe and XRFs, gives fundamental informations for the determination of the actual value of M_{crit} , for the minimum mass of the newly-formed BH, and for the mass of the accreting NS. It is appropriate to notice that a value of the mass of the accreting NS binary, larger than $\approx 1.4 M_{\odot}$, is *a priori* possible and would give interesting observational properties: an exceptional accreting NS with mass close to M_{crit} would lead to a BdHN with a value of the energy lower than the theoretical separatrix of $\approx 10^{52}$ erg. Conversely, the accretion on a NS with mass smaller than $\approx 1.4 M_{\odot}$ should lead to an XRF with energy larger than $\approx 10^{52}$ erg. These rare possibilities will be precious in further probing the implications of the IGC paradigm, in estimating the NS masses, as well as in deriving more stringent limits on M_{crit} directly from observations.

Our theory of the hypercritical accretion, applied in the GRB analysis through the IGC paradigm in binary systems, introduces substantial differences with respect to the traditional ones. To appreciate these differences and gain familiarity in this novel approach, we recommend the reading of all the references quoted in this section.

4. THE X-RAY FLASHES

4.1. General properties

The observational features of long bursts with energy below $\approx 10^{52}$ erg are listed below and summarized in Fig. 1. These bursts are interpreted within the theoretical framework of the IGC as a new class which we indicate as XRFs.

The upper limit on the energetic of the XRFs is $(7.3 \pm 0.7) \times 10^{51}$ erg as measured in GRB 110106B.

The isotropic energies are in the range $(6.4 \pm 1.6) \times 10^{47} \lesssim E_{iso} \lesssim (7.3 \pm 0.7) \times 10^{51}$ erg (see Fig. 8 and Amati & Della Valle 2013; Ruffini et al. 2015a).

The spectral peak energies are in the range $4 \lesssim E_{p,i} \lesssim 200$ keV (see Fig. 8 and Amati & Della Valle 2013; Ruffini et al. 2015a) and increase monotonically with E_{iso} .

The cosmological redshifts are in the range $0.0085 \leq z \leq 1.096$, with an average value of ≈ 0.43 (see Table 2).

The prompt emission phase has a duration ranging between $\sim 10^2 - 10^4$ s (see Fig. 1 (a)) with a spectrum generally characterized by a thermal component and power-law component. The radii of the thermal emitter are in the range of $10^{10} - 10^{12}$ cm and the temperatures vary in the range of 0.1–2 keV (see, e.g., Campana et al. 2006, and Fig. 1 (c)), depending on the values of the binary period and separation of the progenitor systems.

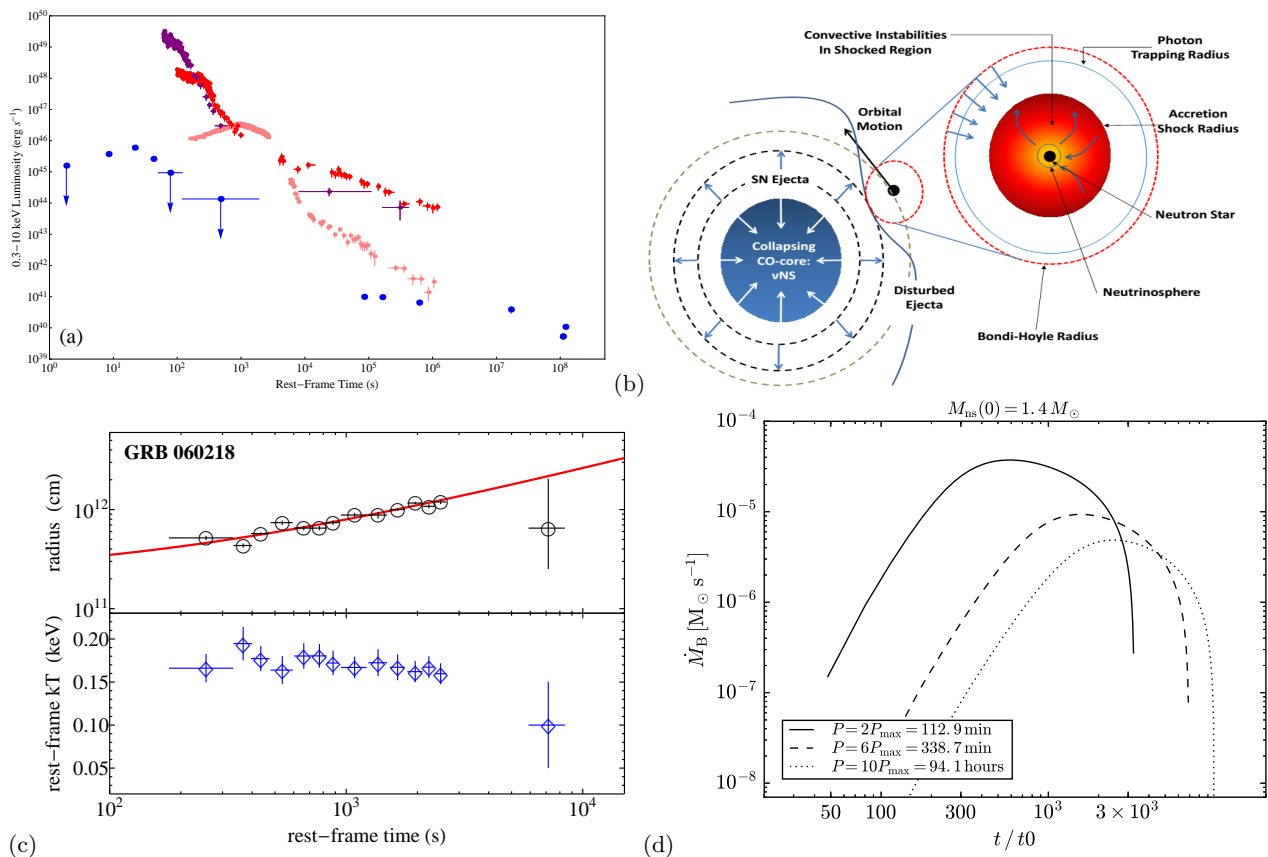


Figure 1. (a) Rest-frame 0.3–10 keV luminosity light curves of four selected XRFs: GRB 980425 (blue), GRB 060218 (pink), GRB 070419A (purple), and GRB 101219B (red). (b) A sketch of the CO_{core}-NS binary progenitor and the hypercritical accretion process in the IGC scenario (reproduced from Fryer et al. 2014). (c) Upper panel: the evolution of the radius of the thermal component detected in GRB 060218 (black circles) and its linear fit (solid red curve). Lower panel: the decay of the corresponding rest-frame temperature (blue diamonds). Reproduced from Campana et al. (2006). (d) Mass accretion rate \dot{M}_B of the SN ejecta onto a NS companion of initial mass $1.4 M_\odot$, as function of time. Three cases are plotted for various selected orbital periods $P > P_{\max}$ (see legend).

The long lasting X-ray afterglow does not exhibit any specific common late power-law behavior (see Fig. 1 (a)).

For all XRFs at $z \lesssim 1$, an optical SN with a luminosity similar to the one of SN 2010bh (Bufano et al. 2012), occurs after 10–15 days in the cosmological rest-frame.

No high energy emission has ever been observed.

In view of the observed values of $E_{p,i}$ which occur in the X-ray domain and also because of the low values of their $E_{\text{iso}} < 10^{52}$ erg, we adopted the name XRFs for these soft and less energetic long bursts, a terminology already used in the literature on purely morphological grounds (see, e.g., Heise 2003; Amati et al. 2004; Soderberg et al. 2006).

4.2. Theoretical interpretation of XRFs within the IGC paradigm

In the IGC paradigm an XRF occurs when the CO_{core}-NS binary separation a is so large (typically $a > 10^{11}$ cm, see e.g., Becerra et al. 2015) that the accretion of the SN ejecta onto the NS is not sufficient for the NS to reach M_{crit} . Correspondingly, there is a critical or maximum value of the orbital period P_{\max} (e.g. $P_{\max} \approx 28$ min for a NS with initial mass of $1.4 M_\odot$) for which the NS collapses to a BH, namely for $P > P_{\max}$ the accretion rate is not sufficient to induce the gravitational collapse of the companion NS into a BH (see Figs. 1 (d)).

The hypercritical accretion of the SN ejecta onto the NS binary companion occurs at rates $< 10^{-2} M_\odot \text{ s}^{-1}$ and can last from several hundreds of seconds all the way up to $\sim 10^4$ s, until the whole SN ejecta flies beyond the NS binary orbit (see Fig. 1 (a)). The photons are trapped in the accreting material and the accretion energy is lost through a large associated neutrino emission (see, e.g., Zel'dovich et al. 1972; Ruffini & Wilson 1973; Rueda & Ruffini 2012; Fryer et al. 2014, and references therein). The upper limit of 10^{52} erg of these sources is explainable by estimating the gravitational energy of the matter accreted onto the NS reaching a mass below M_{crit} at the end of the accretion process (see Sec. 3).

GRB	z	$E_{\text{iso}}/(10^{50} \text{ erg})$	GRB	z	$E_{\text{iso}}/(10^{50} \text{ erg})$
970508	0.835	65 ± 13	081007	0.5295	17 ± 2
980425	0.0085	0.0064 ± 0.0016	100316D	0.059	0.59 ± 0.05
980613	1.096	50 ± 10	100816A	0.8049	71 ± 9
990712	0.434	69 ± 13	101219B	0.55	63 ± 6
020819B	0.41	69 ± 18	110106B	0.618	$73 \pm$
020903	0.251	0.24 ± 0.06	120121B	0.017	0.0139 ± 0.0002
031203	0.105	0.99 ± 0.10	120422A	0.283	2.4 ± 0.8
050416A	0.6528	11 ± 2	120714B	0.3984	8.0 ± 2.0
060218	0.033	0.54 ± 0.05	130702A	0.145	6.5 ± 1.0
070419	0.97	24 ± 10	130831A	0.4791	46 ± 2

Table 2. List of the XRFs considered in this work up to the end of 2014. For each source (first columns) the values of z and $E_{\text{iso}} \lesssim 10^{52}$ erg (second and third columns, respectively) are listed.

The resulting emission, dubbed Episode 1, exhibits a spectrum composed of a thermal component, possibly originating from the outflow within the NS atmosphere driven out by Rayleigh-Taylor convection instabilities, and a power-law component. The shorter the binary period, the larger the accretion rate (see Figs. 1 (f)) and the values of E_{iso} and $E_{\text{p,i}}$, and correspondingly the shorter the prompt emission duration (see Fig. 1 (a)). The excess of angular momentum of the system necessarily leads to a jetted emission, manifested in the power-law spectral component (Becerra et al. 2015). Indeed in the IGC simulations the typical radii inferred from the evolving thermal component coincide with the observed ones of 10^{10} – 10^{12} cm.

In the IGC paradigm the in-state is represented by an exploding CO_{core} and a companion NS. The out-state is multiple system composed of a MNS, resulting from the accretion of part of the SN ejecta onto the binary companion NS, a νNS , originating from the SN event, and the remaining part of the SN ejecta shocked by the hypercritical accretion emission of the XRF. This energy injection into the SN ejecta leads to the occurrence of a broad-lined SN Ic (*hypernova*, see, e.g., Maeda & Nomoto 2003) with a kinetic energy larger than that of the traditional SNe Ic. The presence of ^{56}Ni in the SN ejecta leads to the observed SN emission after ≈ 10 – 15 days in the cosmological rest-frame which is observable for sources at $z \lesssim 1$.

Clearly the absence of hard γ -ray and GeV emissions is implicit in the nature of the hypercritical accretion process not leading to a BH and the corresponding rate of neutrino emission (see also Appendix A).

4.3. Prototypes

In Fig. 1(a) we reproduce the rest-frame 0.3–10 keV luminosity light curves of four selected XRFs: GRB 980425 (Pian et al. 2000; Kouveliotou et al. 2004; Pian et al. 2004), associated with SN 1998bw (Galama et al. 1998), GRB 060218 associated with SN 2006aj (Campana et al. 2006; Soderberg et al. 2006), GRB 070419A (Evans et al. 2007, 2009) with an optical SN bump (Hill et al. 2007), and GRB 101219B (Evans et al. 2007, 2009) associated with SN 2010ma (Sparre et al. 2011). Their prompt emissions are represented by the above mentioned Episode 1. In Fig. 1 (c) we plot the evolution of both temperature and radius inferred from the thermal component observed in the Episode 1 emission of GRB 060218. The increasing radius and almost constant temperature are obtained from the thermal component observed in GRB 060218 (Campana et al. 2006). Details will appear in forthcoming publications (Pisani et al., and Becerra et al., in preparation). A complete list of XRFs is shown in Table 2.

5. THE BINARY-DRIVEN HYPERNOVAE

5.1. General properties

The observational features of long bursts with energy above $\approx 10^{52}$ erg are listed below and summarized in Fig. 2. These bursts are interpreted within the theoretical framework of the IGC as a new class which we indicate as BdHNe.

The lower limit on the energetic of the BdHNe is $(9.2 \pm 1.3) \times 10^{51}$ erg as measured in GRB 070611.

The observed isotropic energies are in the range $(9.2 \pm 1.3) \times 10^{51} \lesssim E_{\text{iso}} \lesssim (4.07 \pm 0.86) \times 10^{54}$ erg (see Fig. 8 and Amati & Della Valle 2013; Ruffini et al. 2015a) and are in principle dependent on the NS mass which we have assumed, as an example, $\approx 1.4 M_{\odot}$ (see sec. 3).

The spectral peak energies are in the range $0.2 \lesssim E_{\text{p,i}} \lesssim 2$ MeV (see Fig. 8 and Amati & Della Valle 2013; Ruffini et al. 2015a) and increase monotonically with E_{iso} .

The cosmological redshifts are in the range $0.169 \leq z \leq 9.3$, with an average value of ≈ 2.42 (see Table 3).

The prompt emission phase of BdHNe exhibits a more complex structure than that of XRFs. Indeed three different regimes are found:

- a) A thermal emission with a decreasing temperature following a broken power-law behavior, and an additional non-thermal spectral component (a power-law), dominate the early emission in selected BdHNe (see, e.g., Izzo et al. 2012c, and Fig. 2 (a)). The existence of this thermal component was first identified in the GRB BATSE data by Ryde (2004, 2005). It has been then shown to occur in the case of BdHNe as GRB 090618 (Izzo et al. 2012c, and Fig. 2 (a)), GRB 101023 (Penacchioni et al. 2012), GRB 110709B (Penacchioni et al. 2013), and GRB 970828 Ruffini et al. (2015c). The characteristic radii inferred from the cooling thermal component are of the order of 10^9 – 10^{10} cm and the average expansion speed is $\sim 10^8$ – 10^9 cm s $^{-1}$ (Izzo et al. 2012c; Penacchioni et al. 2012, 2013; Ruffini et al. 2015c).
- b) This early emission is followed by the characteristic GRB emission (see Fig. 2 (d)), encompassing a thermal precursor, the P-GRB (Ruffini et al. 1999, 2000), followed by the prompt emission (Ruffini et al. 2002, 2004, 2005).
- c) The prompt emission is followed by a steep decay, then by a plateau and a late power-law decay. These features have been first reported in Nousek et al. (2006) and Zhang et al. (2006).

The late decay has typical slopes of $-1.7 \lesssim \alpha_X \lesssim -1.3$ (Pisani et al. 2013) and shows a characteristic power-law behavior both in the optical and in X-rays. When computed in the source cosmological rest-frame, the late power-law decay in X-rays exhibits new features: overlapping and nesting (see Fig. 2 (c)). Overlapping has been proven in a sample of six BdHNe: GRBs 060729, 061007, 080319B, 090618, 091127, and 111228, (Izzo et al. 2012a; Pisani et al. 2013). The nested property of the BdHNe has been discussed in Ruffini et al. (2014b), where it has been shown that the duration (the luminosity) of the plateau phase is inversely (directly) proportional to the energy of the GRB emission: the more energetic the source, the smaller (higher) the duration (the luminosity) of the plateau.

For all BdHNe at $z \lesssim 1$, an optical SN with a luminosity similar to the one of SN 1998bw (Galama et al. 1998), occurs after 10–15 days in the cosmological rest-frame.

A distinctive high energy emission observed up to 100 GeV shows a luminosity light curve following a precise power-law behavior with index ≈ -1.2 (Fig. 2 (d) and Nava et al. 2014). The turn-on of this GeV emission occurs after the P-GRB emission and during the prompt emission phase.

5.2. Theoretical interpretation of BdHNe within the IGC paradigm

In the IGC paradigm a BdHN occurs when the CO_{core}-NS binary is more tightly bound ($a \lesssim 10^{11}$ cm, see e.g., Becerra et al. 2015). The larger accretion rate of the SN ejecta, e.g., $\gtrsim 10^{-2}$ – $10^{-1} M_{\odot}$ s $^{-1}$, leads the companion NS to easily reach its critical mass M_{crit} (Rueda & Ruffini 2012; Fryer et al. 2014; Becerra et al. 2015), leading to the formation of a BH. The electro-dynamical conditions encountered in the final accretion phase explain the existence of a vacuum polarization process leading to the creation of an e^+e^- plasma and to the formation of a KNBH with a large variety of new astrophysical phenomena. For the sake of clarity and independence on the physical regime encountered, in the IGC paradigm we have divided the activities of the BdHNe in a numbered set of distinct Episodes.

Episode 1 of BdHNe originates in the same hypercritical accretion process as the corresponding one of XRFs. The corresponding spectrum again exhibits an expanding thermal component and a power-law function (Izzo et al. 2012c; Ruffini et al. 2015c). The typical radii inferred from the thermal component are of the order of 10^9 – 10^{10} cm and the average expansion speed is $\sim 10^8$ – 10^9 cm s $^{-1}$ (see Fig. 2 (a) and Izzo et al. 2012c; Ruffini et al. 2015c).

Episode 2 corresponds to the authentic long GRB emission (see Fig. 2 (b)), stemming from the collapse of the companion NS to a BH. For its theoretical description we adopt the traditional fireshell model (see Ruffini et al. 2001a,b,c, and Section 2). The GRB emission occurs at Lorentz factor at the transparency of $\Gamma = 10^2$ – 10^3 (Izzo et al. 2012c; Ruffini et al. 2015c) and the spatial extension of the interaction of the fireshell with the circumburst medium goes all the way up to $\sim 10^{16}$ – 10^{17} cm, reached at the end of Episode 2 (Izzo et al. 2012c). The BdHNe have $E_{\text{iso}} \gtrsim 10^{52}$ erg and their $E_{p,i} \gtrsim 200$ keV is in the hard γ -ray domain.

Episode 3 in BdHNe originates from the SN ejecta (Ruffini et al. 2015a). In this case an extra energy injection is delivered by the interaction of the GRB outflow with the SN ejecta resulting in an isotropic energy emission of 10^{51} – 10^{52} erg. This interaction produces a flare at the beginning of Episode 3 (typically at a rest-frame time of $\sim 10^2$ s) with the typical signature of an expanding thermal component in its spectrum. The radii inferred from this thermal

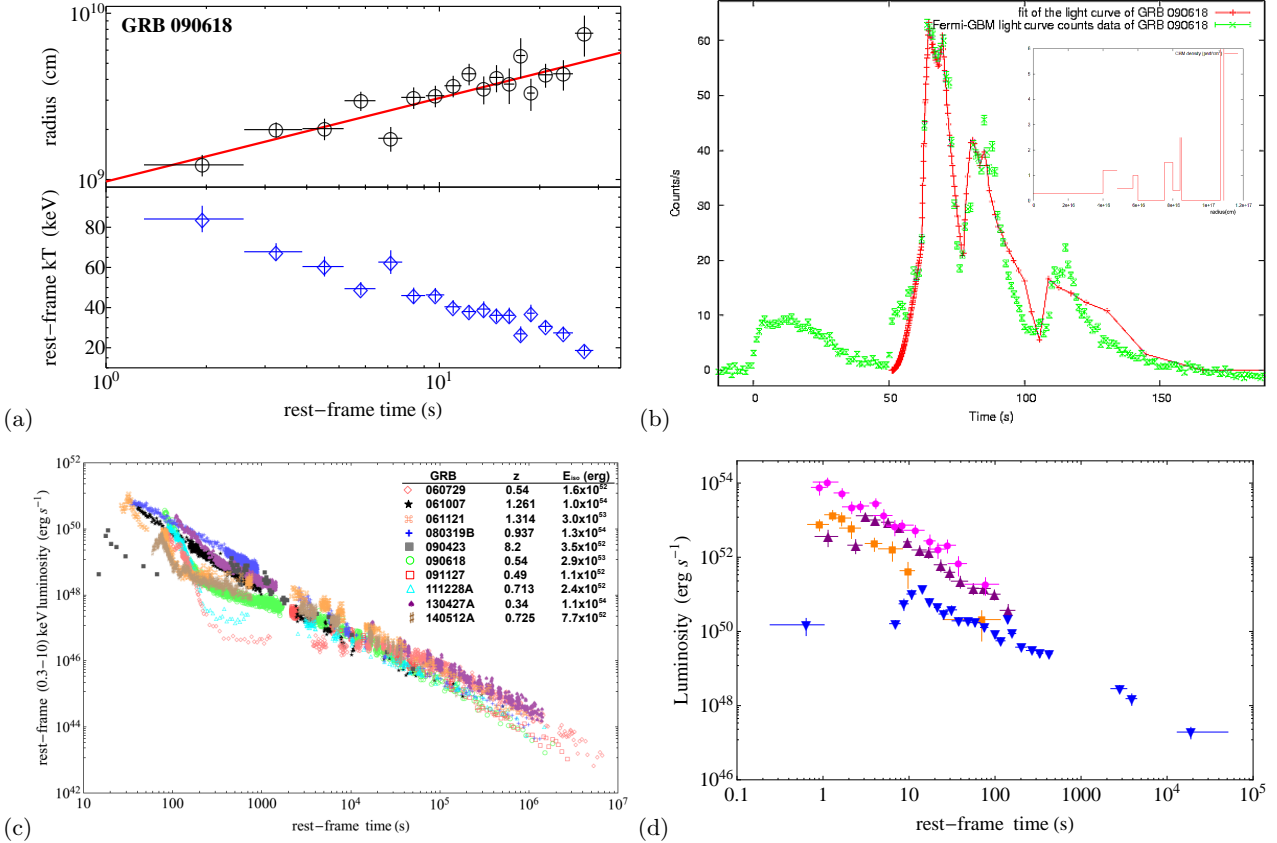


Figure 2. (a) Upper panel: the evolution of the radius of the thermal component detected in the Episode 1 of GRB 090618 (black circles) and its linear fit (solid red curve). Lower panel: the decay of the corresponding rest-frame temperature (blue diamonds). Reproduced from Izzo et al. (2012c). (b) The fireshell simulation (red line) of the light curve of Episode 2 of the prototype GRB 090618 (green data). The small inset reproduces the CBM profile required for the simulation. Reproduced from Izzo et al. (2012c). (c) The rest-frame 0.3–10 keV luminosity light curves of selected BdHNe. All these sources exhibit the overlapping of the late power-law decay, outlined in Pisani et al. (2013), and a nested structure, as outlined in Ruffini et al. (2014b). (d) The rest-frame 0.1–100 GeV luminosity light curves of selected BdHNe (reproduced from Ackermann et al. 2013): GRB 080916C (magenta circles), GRB 090902B (purple triangles), GRB 110731A (orange squares), GRB 130427A (blue reversed triangles).

component are $\sim 10^{12}$ – 10^{13} cm and their evolution reveals a mildly relativistic expansion at $\Gamma \approx 2$ (Ruffini et al. 2014b, 2015a). The rest-frame 0.3–10 keV luminosity light is then followed by a plateau phase and a late power-law decay. The late decay has been shown to exhibit a common power-law behavior and a nested structure (see, e.g., Pisani et al. 2013; Ruffini et al. 2014b, and Fig. 2 (c)). The possibility of using the late X-ray emission as a distance indicator has been explored by inferring the redshifts of GRBs 101023 and 110709B (Penacchioni et al. 2012, 2013), and has been applied to predict the occurrence of the SN associated to GRB 130427A after ~ 10 – 15 days in the cosmological rest-frame before its discovery (Ruffini et al. 2013), later confirmed by the observations (de Ugarte Postigo et al. 2013; Levan et al. 2013; Watson et al. 2013; Xu et al. 2013).

Episode 4, as predicted in the IGC paradigm and in analogy to XRFs, corresponds to the optical SN emission observable in all BdHNe at $z \lesssim 1$ after ≈ 10 – 15 days in the cosmological rest-frame. It is remarkable that these SNe have a standard luminosity, like the one of SN 1998bw (see, e.g., Melandri et al. 2014).

A new Episode 5, here introduced, is identified with the long-lived GeV emission. This emission is conceptually distinct in its underlying physical process from that of Episode 3. When LAT data are available, the majority of BdHNe observed by the *Fermi* satellite (Atwood et al. 2009) exhibit such an emission, similar to the one observed in S-GRBs (see Section 6). In Ruffini et al. (2015a) the further accretion of matter onto the newly-formed BH has been indicated as the origin of this GeV emission. An outstanding exception is GRB 151027A (Kovacevic et al., in preparation).

Also for BdHNe the in-state is composed of an exploding CO_{core} and a companion NS. The out-state is again multiple system. First, there is a GRB composed of the P-GRB and its prompt emission. Then there is a newly-formed BH,

produced by the hypercritical accretion of part of the SN ejecta onto the binary companion NS reaching M_{crit} . Again, there is a νNS originating from the SN explosion. Finally, there is the remaining part of the SN ejecta shocked by the GRB emission. The energy injection into the SN ejecta from both the hypercritical accretion phase and the GRB emission leads also in this case to the occurrence of a broad-lined SN Ic (*hypernova*, see, e.g., [Maeda & Nomoto 2003](#)) with a kinetic energy larger than that of the traditional SNe Ic.

5.3. Prototypes

In the following selected prototypes of BdHNe are given and illustrated in Fig. 2.

The first systematic time-resolved spectral analysis of an Episode 1 of a BdHN has been performed for GRB 090618 ([Izzo et al. 2012c](#)). In this source the typical radii inferred from the cooling thermal component are of the order of 10^9 – 10^{10} cm and the average expansion speed is $\sim 10^8$ – 10^9 cm s $^{-1}$ (see Fig. 2(a)). Similar results have been obtained for GRB 101023 ([Penacchioni et al. 2012](#)), GRB 110907B ([Penacchioni et al. 2013](#)), and GRB 980828 ([Ruffini et al. 2015c](#)).

The selected prototypes of Episode 2 emission have isotropic energies ranging from $E_{\text{iso}} = 1.60 \times 10^{53}$ erg in GRB 970828 ([Ruffini et al. 2015c](#)), to $E_{\text{iso}} = 1.32 \times 10^{54}$ erg in GRB 080319B ([Patricelli et al. 2012](#)). The amount of baryonic matter loaded before the P-GRB emission, the baryon load $B \equiv M_B c^2 / E_{e^+e^-}^{\text{tot}}$, where $E_{e^+e^-}^{\text{tot}}$ is the pair plasma energy and M_B the engulfed baryon mass, is in the range from $B = 1.98 \times 10^{-3}$ for GRB 090618 ([Izzo et al. 2012c](#)), to $B = 7.0 \times 10^{-3}$ in GRB 970828 ([Ruffini et al. 2015c](#)). Correspondingly, their transparency emission occurs at Lorentz factors at the transparency ranging from $\Gamma = 143$ in GRB 970828 ([Ruffini et al. 2015c](#)), to $\Gamma = 490$ in GRB 090618, ([Izzo et al. 2012c](#)). The average density of the circumburst medium in these prototypes, inferred from description of the the interaction with the fireshell after its transparency ([Ruffini et al. 2002, 2004, 2005](#)), vary from 0.6 cm $^{-3}$ in GRB 090618 ([Izzo et al. 2012c](#)), to $\approx 10^3$ cm $^{-3}$ in GRB 970828 ([Ruffini et al. 2015c](#)). The size of the corresponding emitting region, $\sim 10^{16}$ – 10^{17} cm, is clearly incompatible with the radii inferred from Episode 1 and 3. This points to the different origins in the emission mechanisms of the above three Episodes.

The radii inferred from the expanding thermal components observed in the spectra of the flares at the beginning of Episode 3 are typically $\sim 10^{12}$ – 10^{13} cm. This has been found in the cases of GRB 090618, (see, e.g., [Starling et al. 2010; Ruffini et al. 2014b](#)), and GRB 130427A ([Ruffini et al. 2015a](#)). In both these sources, the expansion of the thermal emitter of Episode 3 proceeds at $\Gamma \approx 2$ ([Ruffini et al. 2014b, 2015a](#)). After the initial emission in the spike of Episode 3, the rest-frame 0.3–10 keV luminosity light curve is then followed by a plateau phase and a late power-law decay. The overlapping of the late power-law decay and the nested structure are reproduced in Fig. 2 (c) for selected sources: GRB 060729, GRB 061007, GRB 080319B, GRB 090618, GRB 091127B, and GRB 111228A (considered in [Pisani et al. 2013](#)), GRB 061121 and GRB 130427A (considered in [Ruffini et al. 2014b, 2015a](#)), GRB 090423 ([Ruffini et al. 2014a](#)), and GRB 140512A (introduced here).

Episode 4 has been spectroscopically identified for the two closest BdHNe, e.g., GRB 091127–SN 2009 nz ([Cobb et al. 2010](#)) and GRB 130427A–SN 2013cq ([Xu et al. 2013](#)). In the cases of GRB 060729 ([Cano et al. 2011](#)), GRB 080319B ([Kann et al. 2008](#)), GRB 090618 ([Cano et al. 2011](#)), and GRB 111228A ([D’Avanzo et al. 2012](#)), at $z \lesssim 1$, the identification was possible through the detection of bumps in their Episode 3 optical light curves.

Turning now to the Episode 5 of BdHNe, the GeV emission has been studied in detail in the case of GRB 130427A ([Ruffini et al. 2015a](#)), as well as in other selected BdHNe (see Fig. 2 (d) and [Ackermann et al. 2013](#)). The turn-on has been identified as the on-set of the emission from the newly-formed BH ([Ruffini et al. 2015a](#)).

A complete list of BdHNe is shown in Table 3.

The ultra long GRBs ([Levan et al. 2014; Boër et al. 2015](#)) are certainly BdHNe on the ground of their late x-ray rest frame luminosity ([Pisani et al.](#), submitted to ApJ).

Table 3. List of the BdHNe considered in this work up to the end of 2014. For each source (first columns) the values of z and E_{iso} (second and third columns, respectively) are listed.

GRB	z	$E_{\text{iso}}/(10^{52} \text{ erg})$	GRB	z	$E_{\text{iso}}/(10^{52} \text{ erg})$
970228	0.695	1.65 ± 0.16	081008	1.969	10.0 ± 1.0
970828	0.958	30.4 ± 3.6	081028	3.038	18.3 ± 1.8
971214	3.42	22.1 ± 2.7	081029	3.8479	12.1 ± 1.4
980329	3.5	267 ± 53	081109	0.9787	1.81 ± 0.12
980703	0.966	7.42 ± 0.74	081118	2.58	12.2 ± 1.2

Table 3. continued.

GRB	z	$E_{\text{iso}}/(10^{52} \text{ erg})$	GRB	z	$E_{\text{iso}}/(10^{52} \text{ erg})$
990123	1.6	241 ± 39	081121	2.512	32.4 ± 3.7
990506	1.3	98.1 ± 9.9	081203A	2.05	32 ± 12
990510	1.619	18.1 ± 2.7	081221	2.26	31.9 ± 3.2
990705	0.842	18.7 ± 2.7	081222	2.77	27.4 ± 2.7
991208	0.706	23.0 ± 2.3	090102	1.547	22.6 ± 2.7
991216	1.02	69.8 ± 7.2	090205	4.6497	1.12 ± 0.16
000131	4.5	184 ± 32	090313	3.375	4.42 ± 0.79
000210	0.846	15.4 ± 1.7	090323	3.57	438 ± 53
000418	1.12	9.5 ± 1.8	090328	0.736	14.2 ± 1.4
000911	1.06	70 ± 14	090418A	1.608	17.2 ± 2.7
000926	2.07	28.6 ± 6.2	090423	8.1	8.8 ± 2.1
010222	1.48	84.9 ± 9.0	090424	0.544	4.07 ± 0.41
010921	0.45	0.97 ± 0.10	090429B	9.3	6.7 ± 1.3
011121	0.36	8.0 ± 2.2	090516	4.109	72 ± 14
011211	2.14	5.74 ± 0.64	090519	3.85	24.7 ± 2.8
020124	3.2	28.5 ± 2.8	090529	2.625	2.56 ± 0.30
020127	1.9	3.73 ± 0.37	090530	1.266	1.73 ± 0.19
020405	0.69	10.6 ± 1.1	090618	0.54	28.6 ± 2.9
020813	1.25	68 ± 17	090715B	3.0	23.8 ± 3.7
021004	2.3	3.47 ± 0.46	090809	2.737	1.88 ± 0.26
021211	1.01	1.16 ± 0.13	090812	2.452	47.5 ± 8.2
030226	1.98	12.7 ± 1.4	090902B	1.822	292 ± 29.2
030323	3.37	2.94 ± 0.92	090926	2.106	228 ± 23
030328	1.52	38.9 ± 3.9	090926B	1.24	4.14 ± 0.45
030329	0.169	1.62 ± 0.16	091003	0.897	10.7 ± 1.8
030429	2.65	2.29 ± 0.27	091020	1.71	8.4 ± 1.1
030528	0.78	2.22 ± 0.27	091024	1.092	18.4 ± 2.0
040912	1.563	1.36 ± 0.36	091029	2.752	7.97 ± 0.82
040924	0.859	0.98 ± 0.10	091109A	3.076	10.6 ± 1.4
041006	0.716	3.11 ± 0.89	091127	0.49	1.64 ± 0.18
050126	1.29	2.47 ± 0.25	091208B	1.063	2.06 ± 0.21
050315	1.95	6.15 ± 0.30	100219A	4.6667	3.93 ± 0.61
050318	1.444	2.30 ± 0.23	100302A	4.813	1.33 ± 0.17
050319	3.243	4.63 ± 0.56	100414A	1.368	55.0 ± 5.5
050401	2.898	37.6 ± 7.3	100513A	4.8	6.75 ± 0.53
050502B	5.2	2.66 ± 0.22	100621A	0.542	2.82 ± 0.35
050505	4.27	16.0 ± 1.1	100728A	1.567	86.8 ± 8.7
050525A	0.606	2.30 ± 0.49	100728B	2.106	3.55 ± 0.36
050603	2.821	64.1 ± 6.4	100814A	1.44	15.3 ± 1.8
050730	3.969	11.8 ± 0.8	100901A	1.408	4.22 ± 0.50
050802	1.71	5.66 ± 0.47	100906A	1.727	29.9 ± 2.9
050814	5.3	9.9 ± 1.1	101213A	0.414	2.72 ± 0.53
050820	2.615	103 ± 10	110128A	2.339	1.58 ± 0.21
050904	6.295	133 ± 14	110205A	2.22	48.3 ± 6.4
050908	3.347	1.54 ± 0.16	110213A	1.46	5.78 ± 0.81

Table 3. continued.

GRB	z	$E_{\text{iso}}/(10^{52} \text{ erg})$	GRB	z	$E_{\text{iso}}/(10^{52} \text{ erg})$
0509220	2.199	5.6 ± 1.8	110213B	1.083	8.3 ± 1.3
051022	0.8	56.0 ± 5.6	110422A	1.77	79.8 ± 8.2
051109A	2.346	6.85 ± 0.73	110503A	1.613	20.8 ± 2.1
051111	1.55	15.4 ± 1.9	110715A	0.82	4.36 ± 0.45
060115	3.533	5.9 ± 3.8	110731A	2.83	49.5 ± 4.9
060124	2.296	43.8 ± 6.4	110801A	1.858	10.9 ± 2.7
060202	0.785	1.20 ± 0.09	110818A	3.36	26.6 ± 2.8
060206	4.056	4.1 ± 1.9	111008A	4.9898	24.7 ± 1.2
060210	3.91	32.2 ± 3.2	111107A	2.893	3.76 ± 0.55
060306	3.5	7.6 ± 1.0	111209A	0.677	5.14 ± 0.62
060418	1.489	13.5 ± 2.7	111228A	0.716	2.75 ± 0.28
060510B	4.9	19.1 ± 0.8	120119A	1.728	27.2 ± 3.6
060522	5.11	6.47 ± 0.63	120326A	1.798	3.27 ± 0.33
060526	3.22	2.75 ± 0.37	120327A	2.813	14.42 ± 0.46
060605	3.773	4.23 ± 0.61	120404A	2.876	4.18 ± 0.34
060607A	3.075	11.9 ± 2.8	120624B	2.197	319 ± 32
060707	3.424	4.3 ± 1.1	120711A	1.405	180 ± 18
060708	1.92	1.06 ± 0.08	120712A	4.175	21.2 ± 2.1
060714	2.7108	7.67 ± 0.44	120716A	2.486	30.2 ± 3.0
060814	1.923	56.7 ± 5.7	120802A	3.796	12.9 ± 2.8
060906	3.6856	7.81 ± 0.51	120811C	2.671	6.41 ± 0.64
060908	1.884	7.2 ± 1.9	120815A	2.358	1.65 ± 0.27
060926	3.2086	2.29 ± 0.37	120909A	3.93	87 ± 10
060927	5.46	12.0 ± 2.8	121024A	2.298	4.61 ± 0.55
061007	1.262	90.0 ± 9.0	121027A	1.773	3.29 ± 0.17
061110B	3.4344	17.9 ± 1.6	121128A	2.2	8.66 ± 0.87
061121	1.314	23.5 ± 2.7	121201A	3.385	2.52 ± 0.34
061126	1.1588	31.4 ± 3.6	121229A	2.707	3.7 ± 1.1
061222A	2.088	30.0 ± 6.4	130408A	3.758	35.0 ± 6.4
070110	2.3521	4.98 ± 0.30	130418A	1.218	9.9 ± 1.6
070125	1.547	84.1 ± 8.4	130420A	1.297	7.74 ± 0.77
070306	1.4959	8.26 ± 0.41	130427A	0.334	92 ± 13
070318	0.84	3.64 ± 0.17	130427B	2.78	5.04 ± 0.48
070411	2.954	8.31 ± 0.45	130505A	2.27	347 ± 35
070508	0.82	7.74 ± 0.29	130514A	3.6	52.4 ± 9.2
070521	1.35	10.8 ± 1.8	130518A	2.488	193 ± 19
070529	2.4996	12.8 ± 1.1	130606A	5.91	28.3 ± 5.1
070611	2.0394	0.92 ± 0.13	130610A	2.092	6.99 ± 0.46
070721B	3.6298	24.2 ± 1.4	130701A	1.155	2.60 ± 0.09
071003	1.604	38.3 ± 4.5	130907A	1.238	304 ± 19
071010B	0.947	2.32 ± 0.40	130925A	0.347	18.41 ± 0.37
071020	2.145	10.0 ± 4.6	131105A	1.686	34.7 ± 1.2
071031	2.6918	4.99 ± 0.97	131117A	4.042	1.02 ± 0.16
071117	1.331	5.86 ± 2.7	140206A	2.74	35.93 ± 0.73
080207	2.0858	16.4 ± 1.8	140213A	1.2076	9.93 ± 0.15

Table 3. continued.

GRB	z	$E_{\text{iso}}/(10^{52} \text{ erg})$	GRB	z	$E_{\text{iso}}/(10^{52} \text{ erg})$
080210	2.6419	4.77 ± 0.29	140226A	1.98	5.8 ± 1.1
080310	2.4274	8.58 ± 0.90	140304A	5.283	13.7 ± 1.1
080319B	0.937	118 ± 12	140311A	4.954	11.6 ± 1.5
080319C	1.95	14.9 ± 3.0	140419A	3.956	186 ± 77
080325	1.78	9.55 ± 0.84	140423A	3.26	65.3 ± 3.3
080411	1.03	16.2 ± 1.6	140428A	4.7	1.88 ± 0.31
080413A	2.433	8.6 ± 2.1	140430A	1.6	1.54 ± 0.23
080413B	1.1	1.61 ± 0.27	140506A	0.889	1.12 ± 0.06
080514B	1.8	18.1 ± 3.6	140508A	1.027	23.24 ± 0.26
080603B	2.69	6.0 ± 3.1	140509A	2.4	3.77 ± 0.44
080604	1.4171	1.05 ± 0.12	140512A	0.725	7.76 ± 0.18
080605	1.64	28 ± 14	140515A	6.32	5.41 ± 0.55
080607	3.036	200 ± 20	140518A	4.707	5.89 ± 0.59
080710	0.8454	1.68 ± 0.22	140614A	4.233	7.3 ± 2.1
080721	2.591	134 ± 23	140629A	2.275	6.15 ± 0.90
080804	2.205	12.0 ± 1.2	140703A	3.14	1.72 ± 0.09
080805	1.5042	5.05 ± 0.22	140801A	1.32	5.69 ± 0.05
080810	3.35	47.8 ± 5.5	140808A	3.29	11.93 ± 0.75
080905B	2.3739	4.55 ± 0.37	140907A	1.21	2.29 ± 0.08
080913	6.695	9.2 ± 2.7	141026A	3.35	7.17 ± 0.90
080916A	0.689	0.98 ± 0.10			
080916C	4.35	407 ± 86			
080928	1.692	3.99 ± 0.91			

6. THE SHORT GAMMA-RAY FLASHES

6.1. General properties

The observational features of short bursts with energy below $\approx 10^{52}$ erg are listed below and summarized in Fig. 3. These bursts are interpreted within the theoretical framework of the NS-NS merger paradigm in the fireshell model as a new class which we indicate as S-GRFs.

The upper limit on the energetic of the S-GRFs is $(7.8 \pm 1.0) \times 10^{51}$ erg as measured in GRB 100117A.

The isotropic energies are in the range $(8.5 \pm 2.2) \times 10^{48} \lesssim E_{\text{iso}} \lesssim (7.8 \pm 1.0) \times 10^{51}$ erg (see Fig. 8 and Zhang et al. 2012; Calderone et al. 2015; Ruffini et al. 2015b).

The spectral peak energies are in the range $0.2 \lesssim E_{\text{p},i} \lesssim 2$ MeV (see Fig. 8 and Zhang et al. 2012; Calderone et al. 2015; Ruffini et al. 2015b) and increase monotonically with E_{iso} .

The cosmological redshifts are in the range $0.111 \leq z \leq 2.609$, with an average value of ≈ 0.71 (see Table 4).

The prompt emission phase has a duration of a few seconds, and is expected to crucially be a function of the masses of the binary neutron stars.

The long lasting X-ray afterglow does not exhibit any specific common late power-law behavior (see Fig. 3 (a)).

For all S-GRFs no SN association is expected, nor observed.

No high energy GeV emission is expected nor observed in absence of BH formation.

6.2. Theoretical interpretation of S-GRFs within the NS-NS merger paradigm in the fireshell model

As noted in the Introduction, current paradigms indicate mergers of NS-NS or NS-BH binaries as progenitors.

The extension of the IGC paradigm considerations to NS-NS mergers has led to a new classification of short bursts into two sub-classes depending upon the mass of the merged core, namely whether or not a BH is formed out of the merger (see Fig. 3 (d) and Ruffini et al. 2015b). This, in turn, depends on the NS equation of state and on the adoption of a global neutrality model, as opposed to the case of absence of electromagnetic structures when local

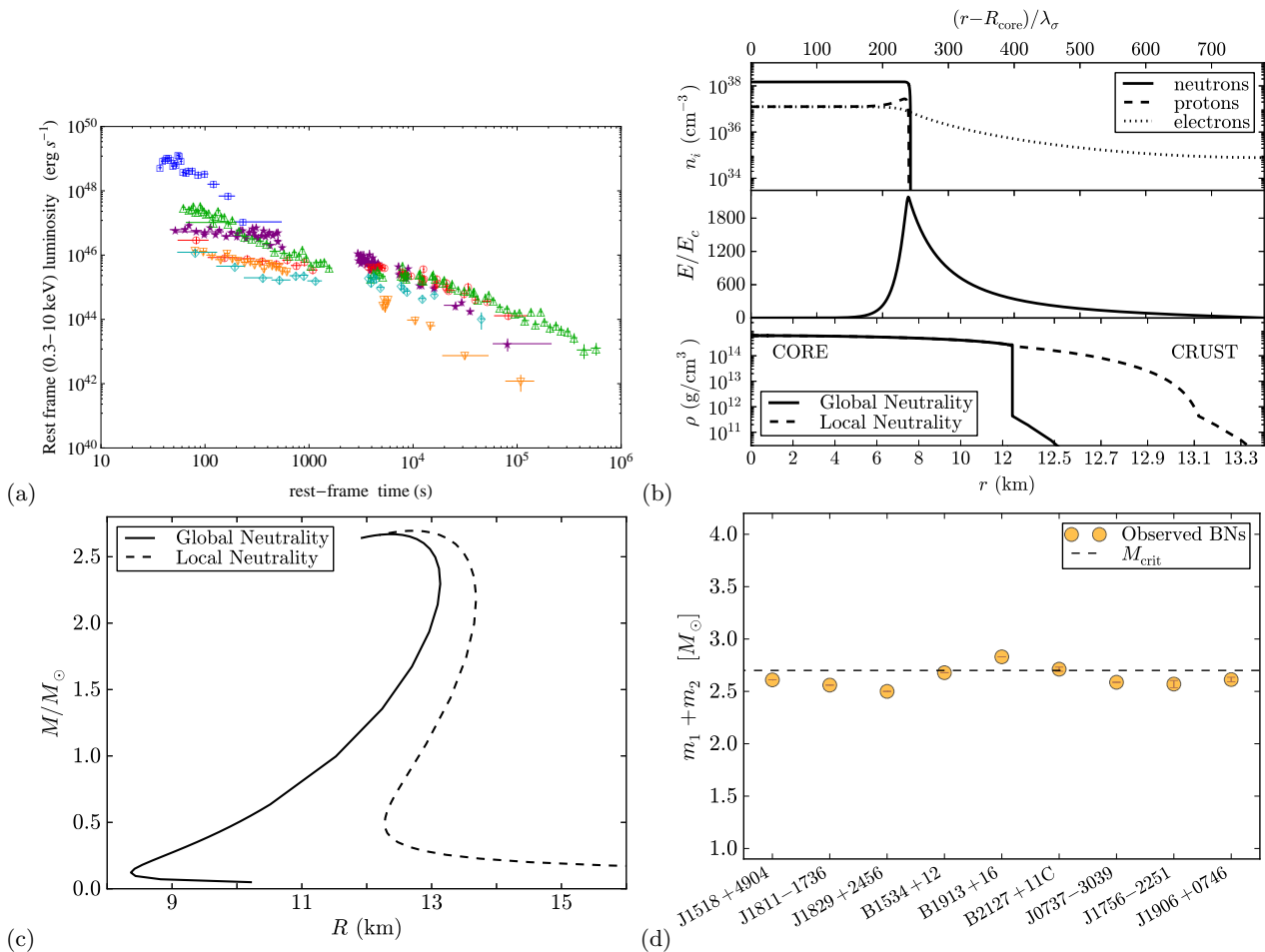


Figure 3. (a) Rest-frame 0.3–10 keV luminosity light curves of some selected S-GRFs: GRB 051210 (blue squares), GRB 051221 (green triangles), GRB 061201 (orange reversed triangles), GRB 070809 (light blue diamonds), GRB 130603B (purple stars), and GRB 140903A (red circles). See Table 4 for details on the sources. (b) Upper panel: particle density profiles in the NS core-crust boundary interface. Middle panel: electric field in the core-crust transition layer in units of E_c . Lower panel: density profile inside a NS star with central density $\rho \sim 5\rho_{\text{nuc}}$, where ρ_{nuc} is the nuclear density, from the solution of the TOV equations (locally neutral case) and the globally neutral solution presented in Belvedere et al. (2012). Here the density at the edge of the crust is the neutron drip density $\rho_{\text{drip}} = 4.3 \times 10^{11} \text{ g cm}^{-3}$ and $\lambda_\sigma = \hbar/(m_\sigma c) \sim 0.4 \text{ fm}$ denotes the σ -meson Compton wavelength. Reproduced from Oliveira et al. (2014) with their kind permission. (c) Mass-radius relation obtained with the local and the new global neutrality equilibrium configurations, by applying the NL3 nuclear model, with a critical mass of $2.67 M_\odot$ for non-rotating NS (Belvedere et al. 2012). Figure reproduced from (Belvedere et al. 2012). (d) Plot of the galactic binary NSs with known total masses ($m_1 + m_2$, in solar masses). The horizontal dashed line marks the NS critical mass: systems beyond this value lead to BH formation. Reproduced from Ruffini et al. (2015b).

charge neutrality is imposed (see, e.g., Belvedere et al. 2012, and references therein, and Fig. 3 (c)). Also relevant is the very different density distribution in the crust and in the core between these two treatments, which could play an important role in the NS–NS mergers (see Fig. 3 (d) and Oliveira et al. 2014).

S-GRFs originate from NS–NS mergers with initial total mass $m_1 + m_2$ leading to merged core with mass smaller than M_{crit} , therefore their outcomes are a MNS with additional orbiting material, or even a binary NS or WD companion (see, e.g., Bildsten & Cutler 1992, and references therein), due to the energy and momentum conservation laws (Ruffini et al. 2015b). As discussed in Sec. 2, even though a BH is not formed out of the merger, also for these systems the general description of the fireshell model can be applied. A viable mechanism for S-GRFs can be the creation of a pair plasma via $\nu\bar{\nu} \rightarrow e^+e^-$ in a NS–NS merger (see, e.g., Narayan et al. 1992; Salmonson & Wilson 2002; Rosswog et al. 2003), where the maximum energy attainable in the process is $\approx 10^{52}$ erg, which represents indeed the upper limit to the energetic of these systems. Their energies are very similar to those emitted in XRFs. However, S-GRFs have $E_{p,i}$ as high as $\sim 2 \text{ MeV}$ (see, e.g., Ruffini et al. 2015b; Calderone et al. 2015; Zhang et al. 2012), therefore, in view of the hardness of their spectra, we adopted the name of S-GRFs to distinguish them from the corresponding XRFs.

GRB	z	$E_{\text{iso}}/(10^{50} \text{ erg})$	GRB	z	$E_{\text{iso}}/(10^{50} \text{ erg})$
050509B	0.225	0.085 ± 0.022	090927	1.37	27.6 ± 3.5
050709	0.161	0.80 ± 0.08	100117A	0.915	78 ± 10
051221A	0.546	26.3 ± 3.3	100206A	0.408	4.67 ± 0.61
060502B	0.287	4.33 ± 0.53	100625A	0.453	7.50 ± 0.30
061201	0.111	1.51 ± 0.73	100724A	1.288	16.4 ± 2.4
061217	0.827	42.3 ± 7.2	101219A	0.718	48.8 ± 6.8
070429B	0.902	4.75 ± 0.71	111117A	1.3	34 ± 13
070724A	0.457	0.60 ± 0.14	120804A	1.3	70 ± 15
070729	0.8	11.3 ± 4.4	130603B	0.356	21.2 ± 2.3
070809	0.473	2.76 ± 0.37	131004A	0.717	12.7 ± 0.9
080123	0.495	11.7 ± 3.9	140622A	0.959	0.70 ± 0.13
080905A	0.122	6.58 ± 0.96	140903A	0.351	1.41 ± 0.11
090426	2.609	44.5 ± 6.6	141004A	0.573	21.0 ± 1.9
090515	0.403	0.094 ± 0.014			

Table 4. List of the S-GRFs considered in this work up to the end of 2014. For each source (first columns) the values of z and E_{iso} (second and third columns, respectively) are listed.

S-GRFs coincide with the majority of the systems extensively discussed in Berger (2014). All S-GRFs have an extended X-ray afterglow (Berger 2014; Ruffini et al. 2015b). Similarly to XRFs, the rest-frame 0.3–10 keV luminosity light curve does not exhibit either a late common power-law behavior, or the nesting discovered in the BdHNe (see Fig. 3(a)). At the moment, there are still a large number of possible candidates for the description of the origin of the late X-ray afterglow emission: a) the interaction of the MNS with orbiting material or with a less massive binary NS or WD companion, b) the accelerated baryons interacting with the circumburst medium after the P-GRB emission, or c) the possible radioactive decay of heavy elements synthesized in the ejecta of a compact binary merger (Li & Paczyński 1998). In this light we recall the possibility of a *macronova* emission, a near-infrared/optical transient (a bump) in the late afterglow (see the case of GRB 130603B in Berger et al. 2013 and Tanvir et al. 2013).

As a general conclusion, in Ruffini et al. (2015b) the necessary absence of a SN was indicated. It has been predicted there that, since no BH is produced in the merger, S-GRFs should never exhibit high energy GeV emission, which is expected to originate in the newly-born BH (Ruffini et al. 2015b). No counterexample has been found as of today. In Ruffini et al. (2016) it has been shown that the absence of detection of GeV emission, necessary within the fireshell model, is indeed supported by the observations. The entire section 6.5 of that paper is dedicated to the GeV emission of S-GRFs and S-GRBs. As evidenced there, it is concluded that S-GRFs, due to the upper limits of the LAT observations, have, if any, GeV fluxes necessarily 10^5 – 10^6 times weaker than those of S-GRBs, although their E_{iso} is only a factor 10^2 smaller (see also Appendix A).

6.3. Prototypes

In Table 4 we indicate selected the prototypes of S-GRFs. For each of them, we list the values of E_{iso} and z used in order to evaluate their rate.

7. THE SHORT GRBS

7.1. General properties

The observational features of short bursts with energy above $\approx 10^{52}$ erg are listed below and summarized in Fig. 4. These bursts are interpreted within the theoretical framework of the NS-NS merger paradigm in the fireshell model as a new class which we indicate as S-GRBs.

The lower limit on the energetic of the S-GRBs is $(2.44 \pm 0.22) \times 10^{52}$ erg as measured in GRB 081024B.

The isotropic energies are in the range $(2.44 \pm 0.22) \times 10^{52} \lesssim E_{\text{iso}} \lesssim (2.83 \pm 0.15) \times 10^{53}$ erg (see Fig. 8 and Zhang et al. 2012; Muccino et al. 2013; Calderone et al. 2015; Ruffini et al. 2015b).

The spectral peak energies are in the range $2 \lesssim E_{\text{p},i} \lesssim 8$ MeV (see Fig. 8 and Zhang et al. 2012; Muccino et al. 2013; Calderone et al. 2015; Ruffini et al. 2015b) and increase monotonically with E_{iso} .

The cosmological redshifts are in the range $0.903 \leq z \leq 5.52$, with an average value of ≈ 2.48 (see Table 5).

GRB	z	$E_{\text{iso}}/(10^{52} \text{ erg})$	GRB	z	$E_{\text{iso}}/(10^{52} \text{ erg})$
060801	1.13	3.27 ± 0.49	090510	0.903	3.95 ± 0.21
081024B	3.05	2.44 ± 0.22	140402A	5.52	4.7 ± 1.1
090227B	1.61	28.3 ± 1.5	140619B	2.67	6.03 ± 0.79

Table 5. List of the S-GRBs considered in this work up to the end of 2014. For each source (first columns) the values of z and E_{iso} (second and third columns, respectively) are listed.

The P-GRB and the prompt emission components have a total duration of a few seconds, which is expected to crucially be a function of the masses of the binary neutron stars. (see Fig. 4 (a) and (b)).

Only in the case of GRB 090510 an X-ray afterglow has been observed not conforming to any known afterglow (see Fig. 4 (c)).

For all S-GRBs no SN association is expected nor observed.

In all S-GRBs an extremely high energy GeV emission has been observed (see Fig. 4 (d)). It is interesting that even in one case, which was outside the nominal *Fermi*-LAT field of view, evidence for high energy emission has been found (Ruffini & Wang, in preparation, and Ackermann et al. 2013).

7.2. Theoretical interpretation of S-GRBs within the NS-NS merger paradigm in the fireshell model

S-GRBs originate from NS-NS mergers with initial total mass $m_1 + m_2$ leading to a merged core with mass larger than M_{crit} so that a BH is formed (Ruffini et al. 2015b). In order to conserve energy and momentum, the outcome of such S-GRBs is a KNBH with additional orbiting material, or a binary companion (Bildsten & Cutler 1992; Ruffini et al. 2015b). If we compare and contrast the different Episodes encountered in the description of the BdHNe (see Section 5) with those of S-GRBs, we find some remarkable analogies but also some differences in view of the simplicity of the underlying physical system of S-GRBs, which unlike the BdHNe, do not exhibit any of the extremely complex activities related to the SN (see Section 5).

Episode 1 corresponds here to the activity of the NS-NS merger before the gravitational collapse into a BH. Because of the compactness of the systems this process at times is not observable or it possibly corresponds to faint precursors observed in some short bursts (see, e.g., Troja et al. 2010 and Ruffini et al. 2016).

Episode 2 corresponds to the GRB emission stemming from the NS-NS merger. It is described within the fireshell model as composed of two components (see Sec. 2): the P-GRB emission, with a mainly thermal spectrum (see Fig. 4 (a)), and the prompt emission, with a characteristic non-thermal spectrum (see Fig. 4 (b)). Typically in all S-GRBs so far analyzed (see, e.g., GRB 090227B, Muccino et al. 2013, and GRB 140619B, Ruffini et al. 2015b) the baryon load is standard, e.g., $B \approx 10^{-5}$, and is consistent with the crustal masses of NS-NS mergers (Belvedere et al. 2014; Ruffini et al. 2015b). The average densities of the circumburst medium where S-GRBs occur are $\langle n_{\text{CBM}} \rangle \approx 10^{-5} \text{ cm}^{-3}$, typical of the halos of GRB host galaxies (see, e.g., Muccino et al. 2013; Ruffini et al. 2015b). Most remarkable is that this model gives the theoretical explanation for the fulfillment of the $E_{\text{p},i} - E_{\text{iso}}$ relation for the short bursts (see Fig. 8 and Zhang et al. 2012; Calderone et al. 2015; Ruffini et al. 2015b).

Episode 3, which corresponds to the traditional X-ray afterglow, is missing here in view of the absence of the SN and of all the characteristic processes originating from the interaction between the GRB and the SN ejecta, as in the case of BdHNe (see Section 5). At times S-GRBs have nonprominent X-ray or optical emissions (see Fig. 4 (c)).

Episode 4, identified with the optical emission of a SN, is here missing.

Episode 5 coincides with the long-lived GeV emission. All S-GRBs consistently exhibit this emission, which appears to be strictly correlated to the one observed in the BdHNe. By analogy with BdHNe, we assume that the GeV emission originate from the activity of the newly-born KNBH produced in the merger (Ruffini et al. 2015b). Indeed the presence of a BH is the only commonality between BdHNe and S-GRBs. By comparing and contrasting Figs. 2 (d) and 4 (d), we see that the turn-on of the GeV emission in S-GRBs occurs earlier and is energetically more prominent than the corresponding one of the BdHNe. To emphasize this point in Fig. 4 (d) we have represented by a dashed line the minimal turn-on time of the GeV emission of BdHNe (see Ruffini et al. 2016, and Ruffini et al., in preparation). The very high angular momentum, expected to occur in NS-NS mergers, and the very high luminosities of the S-GRBs, originating in the corresponding BH formation, offer the great opportunity to analyze some of the features expected in a KNBH.

7.3. Prototypes

In Table 5 we list all the S-GRBs identified so far.

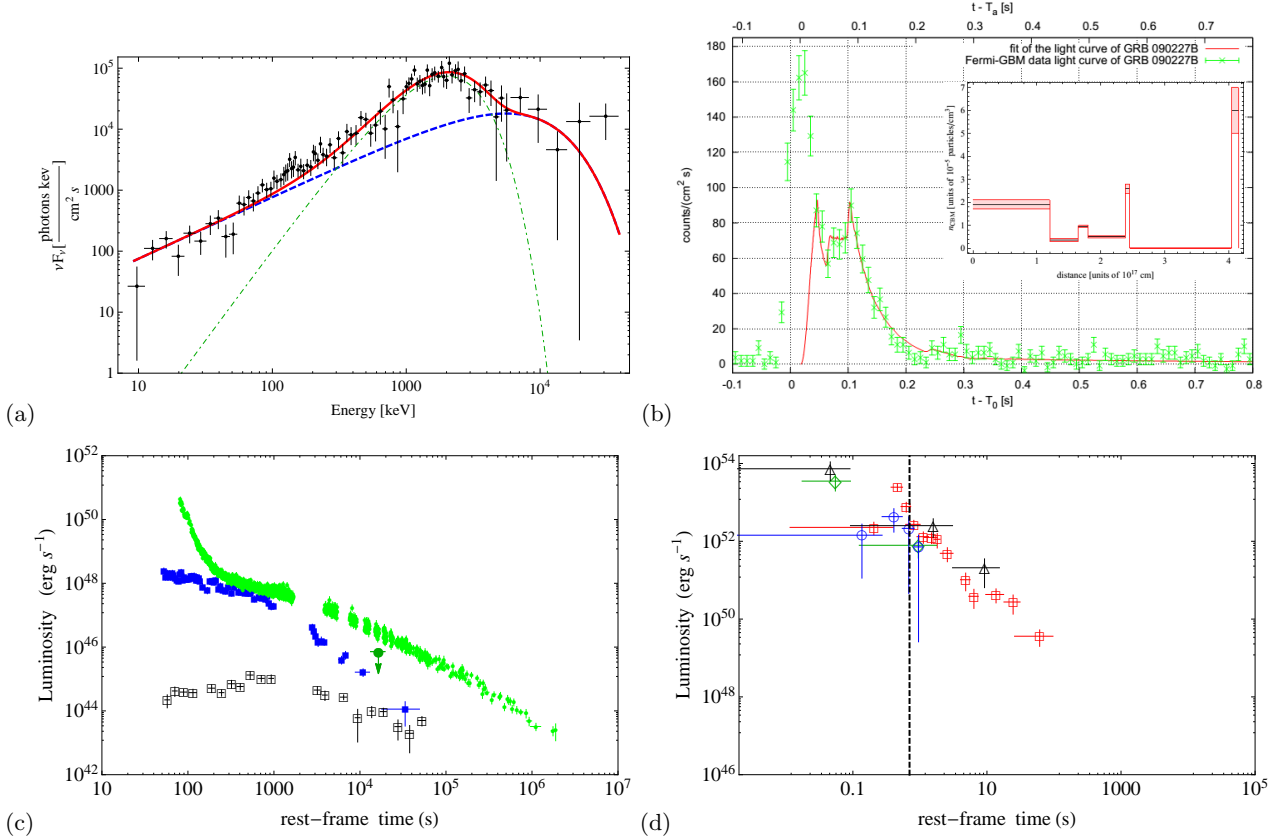


Figure 4. (a) The simulation of the observed P-GRB spectrum of the prototypical S-GRB 090227B: the dashed-dotted green line represents the BB emission, the dashed blue line corresponds to the early on-set of the prompt emission within the P-GRB computed from the fireshell simulation in the energy band 8–40000 keV; the sum of the two components is shown as a solid red line. Reproduced from [Muccino et al. 2013](#). (b) The NaI-n2 light curve of the prompt emission of the S-GRB 090227B (green data) and the simulation within the fireshell model (red curve). The small inset reproduces the CBM profile required for the simulation. Reproduced from [Muccino et al. 2013](#). (c) The available X-ray and optical luminosities of S-GRBs: the X-ray rest-frame 0.3–10 keV (blue filled squares) and the optical rest-frame 2–7 eV (black empty squares, taken from [De Pasquale et al. 2010](#)) luminosity light curves of GRB 090510, and the X-ray rest-frame 0.3–10 keV upper limit of GRB 140619B (green filled circle, see, e.g., [Ruffini et al. 2015b](#)). For comparison the rest-frame 0.3–10 keV luminosity light curve of one of the prototypes of BdHNe, GRB 090618 (green circles) is shown. (d) The rest-frame 0.1–100 GeV luminosity light curves of the S-GRBs 081024B (green diamonds), 090510 (red squares), 140402A (black triangles), 140619B (blue circles). The dashed vertical line marks the minimal turn-on time of the GeV emission of BdHNe. It is clear that in the case of S-GRBs the GeV emission turns on at shorter time scales and exhibits larger luminosities.

The first identified S-GRB 090227B has been analyzed by [Muccino et al. \(2013\)](#). The analysis of its P-GRB emission has found a baryon load $B = 4.13 \times 10^{-5}$ and a Lorentz factor at the transparency condition $\Gamma = 1.44 \times 10^4$. The fit of the light curve of the prompt emission allowed the determination of the average number density of the circumburst medium, i.e., $\langle n_{CBM} \rangle = 1.9 \times 10^{-5} \text{ cm}^{-3}$, which is typical of galactic halos where NS–NS mergers migrate, owing to natal kicks imparted to the binaries at birth (see, e.g., [Berger 2014](#)). These values are strikingly similar to those inferred for other S-GRBs: GRB 081024B ($B = 4.80 \times 10^{-5}$, $\Gamma = 1.07 \times 10^4$, and $\langle n_{CBM} \rangle = 5.0 \times 10^{-6} \text{ cm}^{-3}$, [Aimuratov et al., in preparation](#)), GRB 090510 ($B = 5.54 \times 10^{-5}$, $\Gamma = 1.04 \times 10^4$, and $\langle n_{CBM} \rangle = 8.7 \times 10^{-6} \text{ cm}^{-3}$, [Ruffini et al. 2016](#)), and GRB 140619B ($B = 5.52 \times 10^{-5}$, $\Gamma = 1.08 \times 10^4$, and $\langle n_{CBM} \rangle = 4.7 \times 10^{-5} \text{ cm}^{-3}$, [Ruffini et al. 2015b](#)).

With the exception of GRB 090227B, which was outside the nominal *Fermi*-LAT field of view ([Ackermann et al. 2013](#)), the GeV luminosity light curves of the above four S-GRBs and that of the additional example recently identified, GRB 140402A ([Ruffini et al., in preparation](#)) follow a common behavior when computed in the source rest-frame (see [Fig. 4 \(d\)](#)).

8. ULTRASHORT GRBS

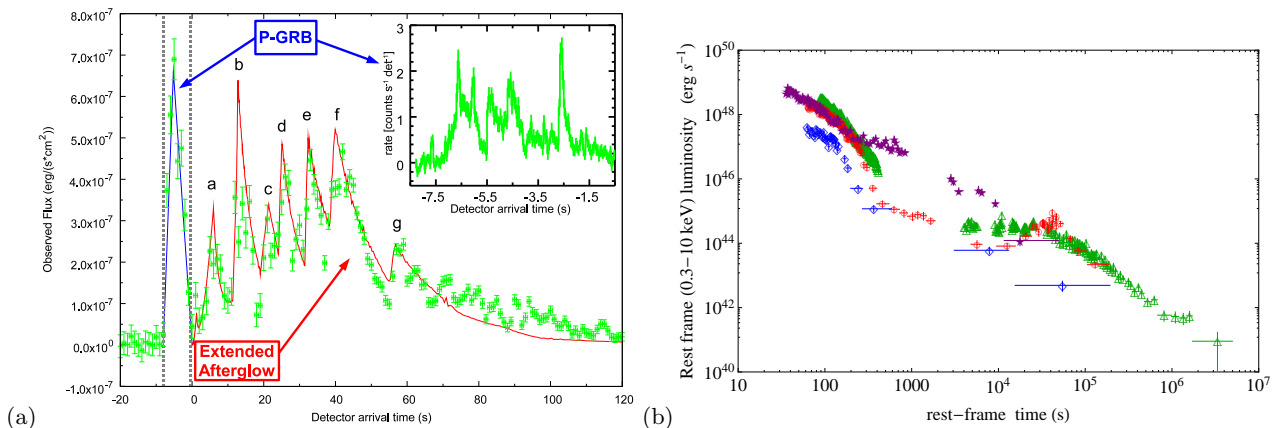


Figure 5. (a) The fireshell simulation of the *Swift*-BAT prompt emission of GRB 060614 (taken from [Caito et al. 2009](#)). (b) The rest-frame 0.3–10 keV luminosity light curves of selected GRFs: GRB 050724 (red circles), GRB 060614 (green triangles), GRB 070714B (purple stars), and GRB 071227 (blue diamonds).

As pointed out in the introduction, U-GRBs originate from the NS-BH binaries produced in the BdHNe and nearly 100% of these binaries remain bound ([Fryer et al. 2015](#)). The lack of any observed source to date is mainly due to the extremely short duration of these systems ([Fryer et al. 2015](#)).

Interesting considerations, which may be of relevance for describing the U-GRB sub-class, can be found in [Popham et al. \(1999\)](#).

9. THE GAMMA-RAY FLASHES

9.1. General properties

The observational features of short bursts followed by an extended emission with energy below $\approx 10^{52}$ erg are listed below and summarized in Fig. 5. These bursts are interpreted within the theoretical framework of a binary merger of a NS and a massive WD ([della Valle et al. 1992, 1994](#)) in the fireshell model as a new class which we indicate as GRFs. The upper limit on the energetic of the GRFs is $(9.8 \pm 2.4) \times 10^{51}$ erg as measured in GRB 070714B.

The isotropic energies are in the range $(8.9 \pm 1.6) \times 10^{49} \lesssim E_{\text{iso}} \lesssim (9.8 \pm 2.4) \times 10^{51}$ erg.

The spectral peak energies are in the range $0.2 \lesssim E_{\text{p},i} \lesssim 2$ MeV.

The cosmological redshifts are in the range $0.089 \leq z \leq 2.31$, with an average value of ≈ 0.54 (see Table 6).

The γ -ray emission is composed of: 1) an initial spike-like harder emission and 2) a prolonged softer emission observed up to a hundred seconds (see Fig. 5(a)).

The long lasting X-ray afterglow does not exhibit any specific common late power-law behavior (see Fig. 5(b)).

No SN association is expected, nor observed also in the case of nearby sources ([Della Valle et al. 2006](#)).

No high energy GeV emission is expected nor observed in absence of BH formation.

9.2. Theoretical interpretation of GRFs within the NS-WD merger paradigm in the fireshell model

As we mentioned, the mergers of NS–WD binaries, notoriously very common astrophysical systems ([Cadelano et al. 2015](#)), can be the progenitors of another GRB sub-class: the GRFs. Possible evolutionary scenarios leading to NS–WD mergers have been envisaged e.g. in [Lazarus et al. \(2014\)](#); [Tauris et al. \(2000\)](#). Another less likely but yet possible scenario is the merger of a NS–WD binary produced, as recalled in Section 6.2, from an S-GRF. Namely, the merger of a not mass-symmetric NS–NS binary with total mass $m_1 + m_2$ smaller than M_{crit} , that produce a MNS with a low-mass WD companion (see, e.g., [Bildsten & Cutler 1992](#), and references therein), due to the energy and momentum conservation laws ([Ruffini et al. 2015b](#)).

With the term GRFs we dubbed a class of long GRBs occurring in a CBM environment with low density, e.g., $\sim 10^{-3} \text{ cm}^{-3}$, with a light curve in γ -rays composed of an initial spike-like hard emission, identified with the P-GRB, and prolonged softer emission, explained as the prompt emission (see Fig. 5 (a) and [Caito et al. 2009, 2010](#)). No associated SN has been ever observed, although in the case of the low value of the cosmological redshift its detection would not have been precluded ([Della Valle 2006](#)). The prototype of such systems is GRB 060614 ([Caito et al. 2009](#)).

Apart from the absence of any associated SN to a GRF, the identification of NS-WD binaries as progenitor systems of the GRFs comes from the following observational and theoretical evidences: a) the initial spike-like emission fulfills the $E_{\text{p},i} - E_{\text{iso}}$ relation for S-GRFs and S-GRBs ([Zhang et al. 2012](#); [Calderone et al. 2015](#); [Ruffini et al. 2015b](#)), both

GRB	z	$E_{\text{iso}}/(10^{50} \text{ erg})$	GRB	z	$E_{\text{iso}}/(10^{50} \text{ erg})$
050724	0.257	6.19 ± 0.74	061021	0.3462	50 ± 11
050911	0.165	0.89 ± 0.16	061210	0.409	0.24 ± 0.06
060505	0.089	2.35 ± 0.42	070506	2.31	51.3 ± 5.4
060614	0.125	21.7 ± 8.7	070714B	0.923	98 ± 24
061006	0.438	17.9 ± 5.6	071227	0.381	8.0 ± 1.0

Table 6. List of the GRFs considered in this work up to the end of 2014. For each source (first columns) the values of z and E_{iso} (second and third columns, respectively) are listed.

originating in NS–NS mergers (Ruffini et al. 2015b); b) the value of the baryon load, $B \approx 10^{-3}$ (Caito et al. 2009, 2010) points to a system more baryon-contaminated than the simpler and more compact NS–NS merger ($B \approx 10^{-5}$, see, e.g., Ruffini et al. 2015b); c) the fit of the prompt emission within the fireshell model provides CBM with low density, e.g., $\sim 10^{-3} \text{ cm}^{-3}$, typical of the halos of the GRB host galaxies (Caito et al. 2009, 2010); d) the presence of a macronova emission in the optical afterglow of the prototype GRF 060614 (Jin et al. 2015).

In summary, we list below the different Episodes observed (or not) in GRFs.

Episode 1 does not exist due to the compactness of the NS–WD merger.

Episode 2 corresponds to the γ -ray emission stemming from the NS–WD merger. The fireshell theory still applies to these systems in view of the considerations presented in Section 2. Also in this case a viable mechanism consists in the pair creation via $\nu\bar{\nu} \rightarrow e^+e^-$ during a NS–WD merger (see, e.g., Paschalidis et al. 2011). This is in line with the upper limit to the energetic of these systems in γ -rays is $E_{\text{iso}} \approx 10^{52} \text{ erg}$.

Episode 3 in GRFs, like in the cases of XRFs and S-GRFs, does not exhibit either a late common power-law behavior, or the nesting discovered in the rest-frame 0.3–10 keV luminosity light curves of BdHNe (see Fig. 5(b)). Also for GRFs, possible candidates for the explanation of the late X-ray afterglow emission are: a) the accelerated baryons interacting with the CBM after the P-GRB emission, or b) the possible radioactive decay of heavy elements synthesized in the ejecta of a compact binary merger (Li & Paczyński 1998).

Episode 4 is missing in view of the absence of the SN.

Episode 5, namely the GeV emission, does not occur for NS–WD mergers. This fact, together to the energetics of these systems, $E_{\text{iso}} < 10^{52} \text{ erg}$, implies that both of these necessary and sufficient conditions for the BH formation are not fulfilled. Therefore, in a NS–WD merger, in view of the limited mass of the WD component, the NS critical mass is never reached in the accretion process during the merger.

9.3. Prototypes

In Table 6 we list all the GRFs identified so far.

The prototype of GRFs is GRB 060614 and has been analyzed by Caito et al. (2009). From the analysis of its P-GRB emission a baryon load $B = 2.8 \times 10^{-3}$ and a Lorentz factor at the transparency condition $\Gamma = 346$ have been found. From the fit of the light curve of the prompt emission it has been inferred that this burst occurred in a CBM with density $n_{\text{CBM}} = 2.3 \times 10^{-5}$ – $4.8 \times 10^{-3} \text{ cm}^{-3}$, which is typical of galactic halos where NS–NS and NS–WD mergers occur (see, e.g., Berger 2014). Analogous results were obtained for the GRF 071227: $B = 2.0 \times 10^{-4}$ and $n_{\text{CBM}} = 1.0 \times 10^{-4}$ – $1.0 \times 10^{-2} \text{ cm}^{-3}$ (Caito et al. 2010).

Further analyses on other GRF examples will be presented elsewhere.

10. THE OBSERVED RATES OF SHORT AND LONG BURSTS

The observed GRB occurrence rate is defined by the convolution of both (likely redshift-dependent) luminosity function, which describes the fraction of bursts with isotropic equivalent luminosities in the interval $\log L$ and $\log L + d \log L$, and cosmic GRB occurrence rate, which gives the number of sources at different redshifts. The definition of both of these functions is still an open issue and depends on *a priori* assumptions and some investigations have been carried out in the literature (see, e.g., Soderberg et al. 2006; Guetta & Della Valle 2007; Liang et al. 2007; Virgili et al. 2009; Rangel Lemos et al. 2010; Wanderman & Piran 2010; Guetta et al. 2011; Kovacevic et al. 2014, for long bursts, Virgili et al. 2011; Wanderman & Piran 2015, for short bursts, and Sun et al. 2015, for both long and short bursts). To complicate the matter, also the instrumental sensitivity threshold, the field of view Ω_i , and the operational time T_i of the various detectors i observing GRBs introduce additional uncertainties to the problem.

In the following we ignore the possible redshift-evolution of the luminosity function. Thus, if ΔN_i events are detected by various detectors in a finite logarithmic luminosity bin from $\log L$ to $\log L + \Delta \log L$, the total local event rate density

of bursts between observed minimum and maximum luminosities, L_{\min} and L_{\max} respectively, is defined as (see Sun et al. 2015)

$$\rho_0 \simeq \sum_i \sum_{\log L_{\min}}^{\log L_{\max}} \frac{4\pi}{\Omega_i T_i} \frac{1}{\ln 10} \frac{1}{g(L)} \frac{\Delta N_i}{\Delta \log L} \frac{\Delta L}{L}, \quad (2)$$

where

$$g(L) = \int_0^{z_{\max}(L)} \frac{f(z)}{1+z} \frac{dV(z)}{dz} dz, \quad (3)$$

and the comoving volume is given by

$$\frac{dV(z)}{dz} = \frac{c}{H_0} \frac{4\pi d_L^2}{(1+z)^2 [\Omega_M(1+z)^3 + \Omega_\Lambda]^{1/2}}, \quad (4)$$

where d_L is the luminosity distance. The dimensionless function $f(z)$ describes the GRB cosmic redshift-dependent event rate density. In the following we assume no redshift dependency, therefore we set $f(z) = 1$. The maximum redshift $z_{\max}(L)$ in Eq. (3) defines the maximum volume inside which an event with luminosity L can be detected. This redshift can be computed from the 1 s-bolometric peak luminosity L , k -corrected from the observed detector energy band into the burst cosmological rest-frame energy band 1–10⁴ keV (Schaefer 2007), and the corresponding 1 s-threshold peak flux f_{th} , which is the limiting peak flux to allow the burst detection (see Band 2003, for details). Therefore, z_{\max} can be defined via (see, e.g., Zhang et al. 2009; Ruffini et al. 2014a)

$$f_{\text{th}} = \frac{L}{4\pi d_L^2(z_{\max})k}, \quad (5)$$

where we duly account for the k -correction.

Within the assumptions that the GRB luminosity function does not evolve with redshift and that $f(z) = 1$, we investigate the evolution with the redshift of the GRB rates by separating the bursts into several redshift bins. As suggested in Sun et al. (2015), this can be done in each redshift interval $z_j \leq z \leq z_{j+1}$ by changing the integration limits of Eq. (3) into z_j and $\min[z_{j+1}, z_{\max,j}(L)]$, where $z_{\max,j}(L)$ is the maximum redshift for the j^{th} redshift bin. Finally, from Eq. (2) we derive an event rate ρ_0^z in each redshift bin around z .

In the following we adopt the following fields of view and operational times for various detectors: *Beppo-SAX*, $\Omega_{\text{BS}} = 0.25$ sr, $T_{\text{BS}} = 7$ y; *BATSE*, $\Omega_{\text{B}} = \pi$ sr, $T_{\text{B}} = 10$ y, *HETE-2*, $\Omega_{\text{H}} = 0.8$ sr, $T_{\text{H}} = 7$ y; *Swift-BAT*, $\Omega_{\text{S}} = 1.33$ sr, $T_{\text{S}} = 10$ y; *Fermi-GBM*, $\Omega_{\text{F}} = 9.6$ sr, $T_{\text{F}} = 7$ y. We assume no beaming correction in computing the rates of the GRB sub-classes.

10.1. Rate of S-GRFs

The local rate of S-GRFs, obtained from the sample of sources listed in Table 4, is $\rho_0 = 3.6_{-1.0}^{+1.4}$ Gpc⁻³ y⁻¹ and it is in agreement with the estimates obtained from the whole short burst population detected by the *Swift-BAT* detector (and, therefore, including also S-GRBs and GRFs) and reported in the literature (1–10 Gpc⁻³ y⁻¹, see, e.g., Clark et al. 2015, and references therein). In particular our local rates with $f(z) = 1$ agrees with recent more precise estimates: a) $4.1_{-1.9}^{+2.3}$ Gpc⁻³ y⁻¹ for $L_{\min} = 5 \times 10^{49}$ erg/s and for $f(z)$ described by a power law merger delay model (Wanderman & Piran 2015); b) $4.2_{-1.0}^{+1.3}$, $3.9_{-0.9}^{+1.2}$, and $7.1_{-1.7}^{+2.2}$ Gpc⁻³ y⁻¹ for $L_{\min} = 7 \times 10^{49}$ erg/s and $f(z)$ described as Gaussian, log-normal and power law merger delay models, respectively (Sun et al. 2015).

The evolution of the S-GRF rate in various redshift bins is shown in Fig. 6 (c). This rate decreases as a power law from the local value in the interval $0.1 \leq z \leq 0.4$ to a value of $0.042_{-0.025}^{+0.046}$ Gpc⁻³ y⁻¹ in the interval $1.0 \leq z \leq 2.7$. Also in the case of S-GRFs the increasing sampled comoving Universe volume and the threshold of the detectors play a fundamental role in the observed decrease of their rate at larger distances.

10.2. Rate of S-GRBs

Previously we have identified and described four S-GRBs in Ruffini et al. (2015b), e.g., GRB 081024B, GRB 090227B, GRB 090510, and GRB 140619B. Here we present two additional new members of this class: GRB 060801 (at $z \approx 1.13$ and with $z_{\max} \approx 2.04$, in this work) and GRB 140402A (at $z \approx 5.52$ and with $z_{\max} \approx 7.16$, Ruffini et al. in preparation). From these six S-GRBs detected by the *Fermi* and the *Swift* satellites, we obtain via Eqs. (2)–(3) a local rate $\rho_0 = (1.9_{-1.1}^{+1.8}) \times 10^{-3}$ Gpc⁻³ y⁻¹.

With only six sources, we could not build the evolution with the redshift of such systems.

10.3. Rate of XRFs

In [Kovacevic et al. \(2014\)](#), we have estimated an updated observed rate for the XRFs at $z < 0.1$ based on the method outlined in [Soderberg et al. \(2006\)](#) and [Guetta & Della Valle \(2007\)](#). In this work, we consider the complete list of XRFs shown in [Table 2](#) and the method outlined in [Sun et al. \(2015\)](#). From [Eq. \(2\)–\(3\)](#) the local rate of XRFs is $\rho_0 = 100_{-34}^{+45} \text{Gpc}^{-3} \text{y}^{-1}$, where the attached errors are determined from the 95% confidence level of the Poisson statistic ([Gehrels 1986](#)). Within the extent of our different classification criteria and different choices for $f(z)$, our estimate is in agreement with those reported for low-luminous long GRBs in [Liang et al. \(2007\)](#) and [Virgili et al. \(2009\)](#), and in particular with the value of $164_{-65}^{+98} \text{Gpc}^{-3} \text{y}^{-1}$, obtained by [Sun et al. \(2015\)](#) with the same method.

In the IGC scenario the XRF out-states are NS–NS binary systems. For a reasonable sets of binary initial conditions, populations synthesis simulations performed by [Fryer et al. \(1999\)](#) provide a NS–NS formation rate (0.2–1600) $\text{Gpc}^{-3} \text{y}^{-1}$. NS–NS formation rate accounts for other possible channels in the population synthesis models, in addition to the one we considered from the XRFs. It is interesting, nevertheless, that our predicted rate is consistent with that obtained by [Fryer et al. \(1999\)](#) obtained.

For the same above reason, our rate of XRFs can be also compared with the NS–NS merger rate proposed by [Eichler et al. \(1989\)](#). In this historical paper, the NS–NS merger rate is derived from the strong assumption that each merger ejects always the same amount of material r-process classified and the heavy r-process material. [Eichler et al. \(1989\)](#) obtain a rough estimate of (140–14000) $\text{Gpc}^{-3} \text{y}^{-1}$, which is marginally consistent to the upper value of the local XRF rate.

The evolution of the XRF rate in various redshift bins is shown in [Fig. 6 \(a\)](#). It decreases from a value of $95_{-63}^{+123} \text{Gpc}^{-3} \text{y}^{-1}$ in the interval $0 \leq z \leq 0.1$ to a value of $0.8_{-0.5}^{+1.1} \text{Gpc}^{-3} \text{y}^{-1}$ in the interval $0.7 \leq z \leq 1.1$. This effect is mainly due to the intrinsic low luminosities of the bulk of the XRF population (10^{46} – 10^{48} erg/s, see, e.g., [Bromberg et al. 2011](#)) and to the threshold of the detectors: at increasing sampled Universe comoving volumes, these low luminous XRFs become undetectable, therefore at higher redshifts the total XRF rate decreases.

10.4. Rate of BdHNe

We proceed now in estimating the rate of BdHNe from the total sample of 233 sources (see [Table 3](#)). From [Eq. \(2\)–\(3\)](#) the local rate of BdHNe is $\rho_0 = 0.77_{-0.08}^{+0.09} \text{Gpc}^{-3} \text{y}^{-1}$. Our estimate is in agreement with two recent estimates obtained from long bursts with $L \geq 10^{50}$ erg/s and by assuming $f(z) \neq 1$: a) the value of $1.3_{-0.7}^{+0.6} \text{Gpc}^{-3} \text{y}^{-1}$ obtained by [Wanderman & Piran \(2010\)](#), even though limited to the *Swift* long bursts and including long some bursts with $E_{\text{iso}} < 10^{52}$ erg, obtained from a GRB inferred cosmic rate independent on the star formation rate; b) the value of $0.8_{-0.1}^{+0.1} \text{Gpc}^{-3} \text{y}^{-1}$ obtained by [Sun et al. \(2015\)](#) with the same method and including the star formation rate dependence.

In the IGC scenario the BdHNe out-states are NS–BH binary systems. Following again the work by [Fryer et al. \(1999\)](#), populations synthesis simulations (which accounts also for alternative scenarios to that of the IGC model) provide a NS–BH formation rate of (0.02–1000) $\text{Gpc}^{-3} \text{y}^{-1}$. Also in this case, even though a straightforward comparison is not possible, the BdHNe rate is consistent with the NSBH formation rate obtained by [Fryer et al. \(1999\)](#).

The evolution of the BdHNe rate in various redshift bins is shown in [Fig. 6 \(b\)](#). It slightly decreases from the local value in the interval $0.1 \leq z \leq 0.4$ to a value of $0.17_{-0.04}^{+0.05} \text{Gpc}^{-3} \text{y}^{-1}$ in the interval $3.6 \leq z \leq 9.3$. As stated for the case of XRFs, this effect occurs because for increasing sampled Universe comoving volumes, only the most luminous BdHNe are detectable, even though in a less marked way than the case of the XRFs.

10.5. Rate of U-GRBs

As pointed out in [Section 8](#), nearly 100% of the BdHNe leads to bound NS–BH binaries, which are the progenitor systems of U-GRBs ([Fryer et al. 2015](#)). If we include the possibility of other channels of formation for these NS–BH binaries, we can safely assume the BdHNe local rate as a lower limit for these U-GRBs, e.g., $\rho_0 = 0.77_{-0.08}^{+0.09} \text{Gpc}^{-3} \text{y}^{-1}$. From this consideration, it appears that the U-GRBs have the second higher rate among the short bursts after the S-GRFs.

10.6. Rate of GRFs

We proceed now in estimating the rate of GRFs from the total sample of 10 sources (see [Table 6](#)). From [Eq. \(2\)–\(3\)](#) we obtain a local rate $\rho_0 = 1.02_{-0.46}^{+0.71} \text{Gpc}^{-3} \text{y}^{-1}$, and represent the first estimate for these kind for bursts originating from NS–WD mergers.

Due to the limited number of sources in our sample, we limited the study of the GRF rate evolution in two redshift bins, as shown in [Fig. 6 \(d\)](#). The rate starts from a value consistent with the above local rate, in the redshift interval

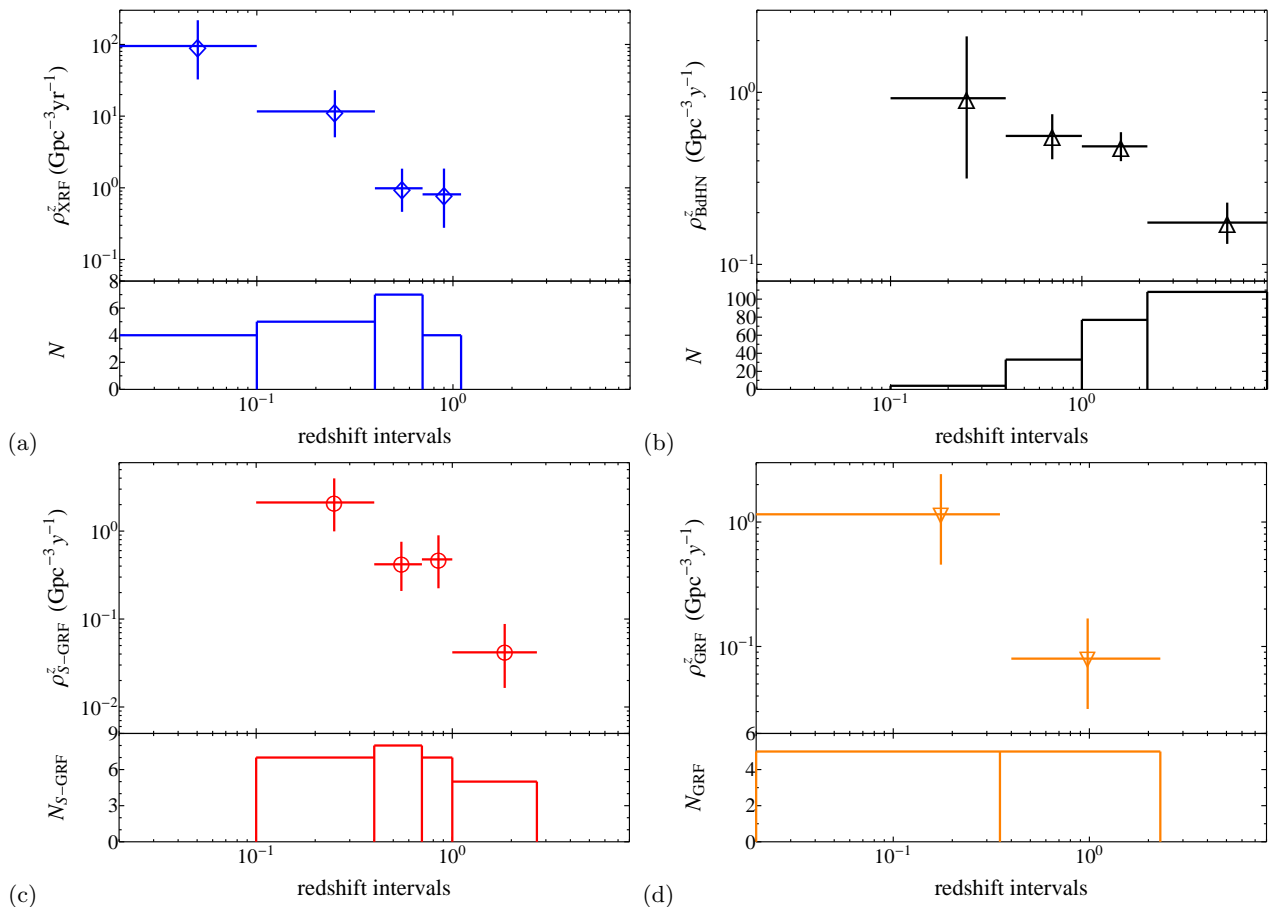


Figure 6. The evolution of the rate with the redshift for the considered GRB sub-classes: (a) the XRF, (b) the BdHNe, (c) the S-GRFs, (d) the GRFs. In each plot the upper panel shows the evolution rate with the redshift, while the lower panel displays the number of observed sources in each redshift bin. Because of the limited amount of sources, for S-GRBs no redshift bin evolution is shown. In the case of U-GRBs, there are no current detections.

$0 \leq z \leq 0.35$, to a value of $0.080_{-0.048}^{+0.088} \text{Gpc}^{-3} \text{y}^{-1}$, in the interval $0.35 \leq z \leq 2.31$. Also for GRFs, the cutoff in the rate at higher redshift occurs because for increasing sampled Universe comoving volumes only the most luminous sources are detectable. However this effect, as in the case of S-GRFs, is more pronounced due to their intrinsically weaker luminosities, when compared to those of S-GRBs.

11. CONCLUSIONS

The remarkable progress reached in understanding the GRB phenomenon has been made possible by the outstanding spectral and temporal information acquired from X-rays, γ -rays and high energy observatories, as well as from optical and radio data obtained by telescopes all over the planet. At the same time this result has been fostered by a novel deeper theoretical understanding in the physics and astrophysics of WD (see, e.g., Boshkayev et al. 2013), NS (see, e.g., Belvedere et al. 2014; Cipolletta et al. 2015) and BH (see, e.g., Ruffini et al. 2010). Consequently the understanding of the GRB phenomenon has evolved from an elementary paradigm based on a single jetted emission process as postulated in the fireball model (see, e.g., Sari et al. 1998; Piran 2005; Meszaros 2006; Gehrels et al. 2009, and reference therein) to an authentic astrophysical laboratory involving many-body interactions between different astrophysical systems encountering previously unexplored regimes and observational evidence.

In the Introduction we review the increasing number of GRB observations which have led likewise to the theoretical progress in the understanding of the GRB phenomena. While the role of NS–NS (or NS–BH) binaries as “in-states” of short GRBs has been widely accepted and confirmed by strong observational and theoretical evidence (see, e.g., Goodman 1986; Paczynski 1986; Eichler et al. 1989; Narayan et al. 1991, 1992; Meszaros & Rees 1997; Rosswog et al. 2003; Lee et al. 2004; Berger 2014; Ruffini et al. 2015b), the identification of the progenitor systems for long GRBs followed a more difficult path. Initially, theoretical models based on a single progenitor were proposed: a *collapsar* (Woosley 1993), or a *magnetar* (see, e.g., Zhang & Mészáros 2001). Then, the role of binary progenitor systems

composed of two very massive stars for long GRBs was recognized by (Fryer et al. 1999), where several different scenarios were there envisaged leading to a *collapsar* (Woosley 1993), as well as a few leading, alternatively, to a variety of binary compact systems. These considerations were addressed by our group in a set of papers assuming that the birth of a SN and the occurrence of a GRB were qualitatively and quantitatively different astrophysical events in space and time. This led to the necessity of introducing the IGC paradigm (see, e.g., Ruffini et al. 2001a, 2006b, 2007, 2008; Izzo et al. 2012b; Rueda & Ruffini 2012; Fryer et al. 2014; Ruffini et al. 2015a). In the IGC paradigm the long GRB-SN coincidence originates from CO_{core}-NS binary progenitors system. This approach differs from alternative descriptions, e.g., the *magnetars* and the *collapsar* models, where the two events are coming from a single progenitor star.

In Section 2, we review the fireshell model for GRBs (see, e.g. Ruffini et al. 2001a,b,c) and its general description which can be applied to any source of an optically thick baryon-loaded e^+e^- plasma, i.e., in the quantum-electrodynamical process expected in the formation of a BH (see, e.g., Preparata et al. 1998; Ruffini et al. 1999, 2000; Cherubini et al. 2009; Ruffini 2009), as well as in the case of a pair plasma created via $\nu\bar{\nu} \leftrightarrow e^+e^-$ mechanism in a NS-NS merger (Narayan et al. 1992; Salmonson & Wilson 2002; Rosswog et al. 2003), or in the hyper-accretion disks around BHs (Woosley 1993; Zalamea & Beloborodov 2011).

In Section 3, we discuss the role of the 10^{52} erg energy critical value introduced to discriminate between binary systems leading to the formation of a MNS (XRFs, S-GRFs and GRFs), with energy lower than the above critical value, and those leading to the formation of a BH (BdHNe, S-GRBs and U-GRBs), with energy larger than the above critical value. The value of 10^{52} erg is derived by considering the hypercritical accretion process onto a NS leading to an energy release in form of neutrinos and photons, given by the gain of gravitational potential energy of the matter accreted in the NS. This includes the change of binding energy of the NS while accreting both matter and angular momentum (Becerra et al. 2016). A typical NS mass of $\approx 1.4 M_\odot$ has been assumed, as observed in galactic NS binaries (Zhang et al. 2011; Antoniadis 2015). A NS critical mass in the range of $2.2 M_\odot$ up to $3.4 M_\odot$ depending on the equations of state and angular momentum (see Becerra et al. 2016, 2015; Cipolletta et al. 2015, for details) has been assumed.

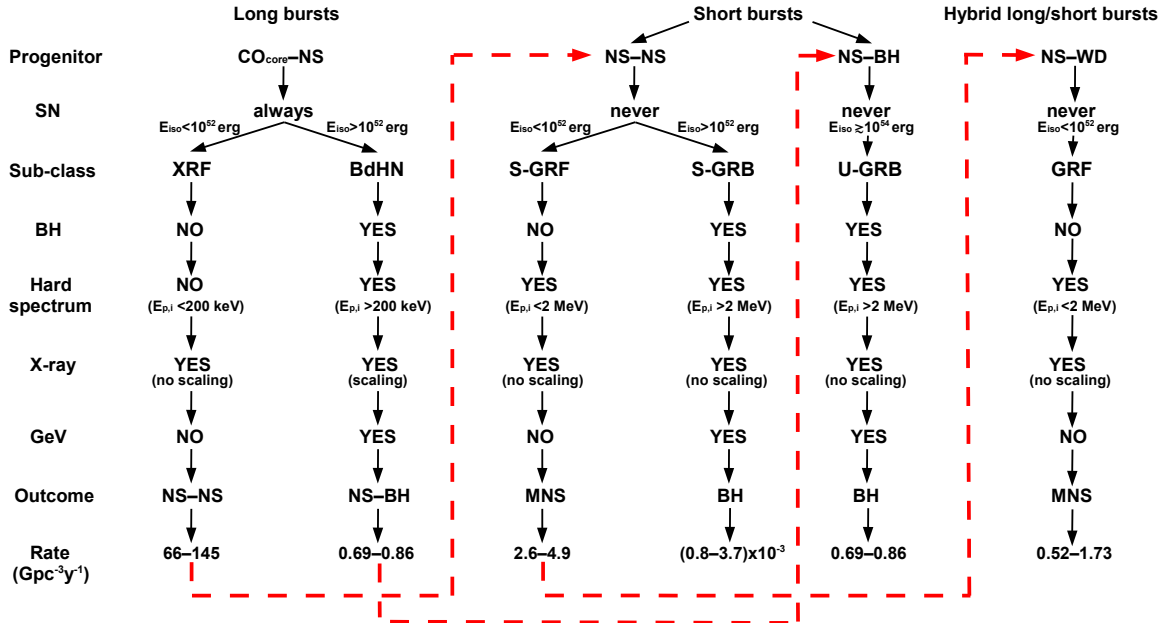


Figure 7. Summary of the properties of long, short and hybrid long/short burst sub-classes discussed in the Introduction. The red dashed lines indicate the evolutionary tracks linking the out-states and the in-states of some of the sub-classes considered in this work.

In Section 4, we describe the properties of XRFs (see Fig. 8). In these systems the distance between the CO_{core} and the NS companion is $a > 10^{11}$ cm. The hypercritical accretion process is not sufficient to push the NS beyond its M_{crit} and an MNS is formed (see, e.g., Becerra et al. 2015, 2016). In Table 2 we list the XRFs considered in this work, as well as the spectral, temporal and luminosity analysis of selected prototype, e.g., GRB 060218. The complete

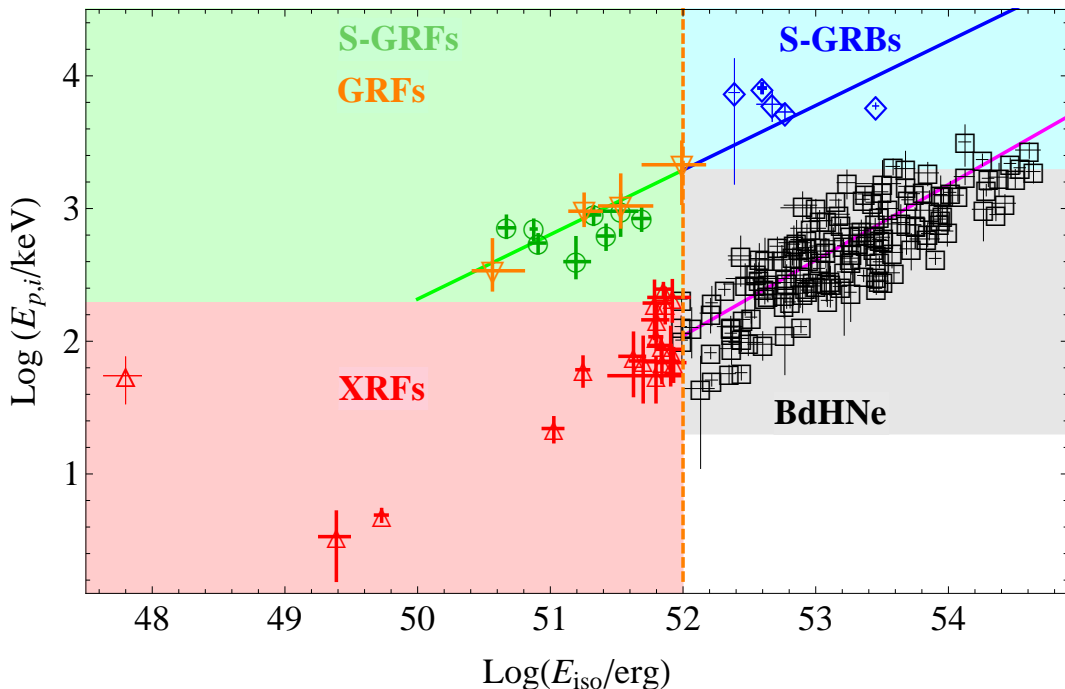


Figure 8. The $E_{p,i}$ - E_{iso} plane for XRFs, BdHNe, S-GRBs, S-GRFs, and the initial spike-like emission of the GRFs. The XRFs (red triangles) cluster in the red shaded region ($E_{p,i} \lesssim 200$ keV and $E_{iso} \lesssim 10^{52}$ erg), while the BdHNe (black squares) in the gray shaded one ($E_{p,i} \gtrsim 200$ keV and $E_{iso} \gtrsim 10^{52}$ erg); the Amati relation (Amati & Della Valle 2013) fulfilled by the BdHNe is plotted with a magenta solid line. The S-GRFs (green circles) and the initial spike-like emission of the GRFs (orange reverse triangles) cluster in the green shaded region ($E_{p,i} \lesssim 2$ MeV and $E_{iso} \lesssim 10^{52}$ erg), while the S-GRBs (blue diamonds) in the blue shaded one ($E_{p,i} \gtrsim 2$ MeV and $E_{iso} \gtrsim 10^{52}$ erg); the relation for short bursts (Ruffini et al. 2015b; Calderone et al. 2015; Zhang et al. 2012) is plotted with a green solid line for the S-GRFs and the GRFs, and in blue for the S-GRBs.

theoretical simulation of this prototype is presented in Becerra et al. (2016).

In Section 5 we consider the BdHNe, for which the binary separation between the CO_{core} and the NS binary companion is $a < 10^{11}$ cm and the hypercritical accretion process trigger the gravitational collapse of the NS into a BH (see, e.g., Becerra et al. 2015, 2016). We show here an updated list of BdHNe (see Table 3), as well as a diagram summarizing some of the key properties and prototypes (see Fig. 8), analyzed within the IGC paradigm and the fireshell model (see, e.g., GRB 090618 and GRB 130427A).

In Section 6, we outline the properties of S-GRFs listed in Table 4 and shown in Fig. 8. These systems coincide with the short bursts considered in Berger (2014). They originate in NS-NS mergers leading to the formation of a MNS and possibly a binary companion, in order to fulfill the conservation of energy and momentum (Ruffini et al. 2015b).

In Section 7 we present S-GRBs originating in NS-NS mergers leading to the formation of a BH (see Fig. 8). We give, in Table 5, their updated list. We then describe their prototypes, analyzed within the fireshell model (see, e.g., GRB 090227B and GRB 140619B), and outline the key role of the P-GRB identification for their description, as well as the analysis of the GeV emission.

In Section 8, motivated by the results obtained by Fryer et al. (2015), where it was shown that nearly 100% of the NS-BH binaries, namely the out-states of the BdHNe, remain bound, we add the description of this not yet observed, but theoretically predicted sub-class of U-GRBs, unaccounted for in current standard population synthesis analyses.

In Section 9, we review the properties of the GRFs listed in Table 6 and shown in Fig. 8. We recall and describe the results obtained from the sources analyzed within the fireshell model (see, e.g., GRB 060614, Caito et al. 2009 and GRB 071227, Caito et al. 2010).

The most important result of the present article is the estimate the rates of occurrence of the XRFs, BdHNe, S-GRFs, S-GRBs, U-GRBs, and GRFs sub-classes. In Section 10, we introduce the procedure outlined in Sun et al. (2015) for estimating the local rates and their evolution with the redshift of the above sub-classes of long and short bursts, assuming no beaming (note: the recent observation of the absence of GeV emission associated to a BdHN may limit this assumption). By ignoring possible redshift-evolution of the GRB sub-classes luminosity functions and assuming that the GRB cosmic event rate density is redshift-independent (e.g., $f(z) = 1$), the above method duly

takes into account observational constraints, i.e., the detector solid angle coverage of the sky Ω and sensitivities which in turn define a maximum volume of observation depending on the intrinsic luminosity of the sources (see Section 10 and Soderberg et al. 2006; Guetta & Della Valle 2007; Liang et al. 2007; Virgili et al. 2009, 2011; Rangel Lemos et al. 2010; Wanderman & Piran 2010, 2015; Kovacevic et al. 2014; Sun et al. 2015 for details). We obtain:

- an S-GRF local rate of $\rho_0 = 3.6_{-1.0}^{+1.4} \text{ Gpc}^{-3} \text{ y}^{-1}$ (see Section 10.1);
- an S-GRB local rate of $\rho_0 = (1.9_{-1.1}^{+1.8}) \times 10^{-3} \text{ Gpc}^{-3} \text{ y}^{-1}$ (see Section 10.2);
- an XRF local rate of $\rho_0 = 100_{-34}^{+45} \text{ Gpc}^{-3} \text{ y}^{-1}$ (see Section 10.3);
- a BdHN local rate of $\rho_0 = 0.77_{-0.08}^{+0.09} \text{ Gpc}^{-3} \text{ y}^{-1}$ (see Section 10.4; for the above reason this rate coincides with that of the U-GRBs, see Section 10.5);
- a GRF local rate of $\rho_0 = 1.02_{-0.46}^{+0.71} \text{ Gpc}^{-3} \text{ y}^{-1}$ (see Section 10.6).

The local rates of S-GRFs, XRFs, and BdHNe, are in agreement, within the extent of the different classification criteria, with those reported in the literature. The local rates of S-GRBs and GRFs are, instead, new ones following from the classification proposed in this work. The evolution with the redshift of the rates of XRFs, BdHNe, S-GRFs, and GRFs is shown in Fig. 6. It is certainly of interest to compare and contrast these results obtained from the direct observations of the sources in our new classification with the results computed from population synthesis models. Any possible disagreement will give the opportunity to identify possible missing links in the evolutionary phases within population synthesis analysis.

We are now in a position to apply the above rates of S-GRFs, S-GRBs and U-GRBs to assess the detectability and the expected number of gravitational wave detections by LIGO from NS-NS and NS-BH binaries (Ruffini et al., in preparation). We are also ready to apply the above BdHN rate to give an estimate of the contribution of GRBs to cosmic rays (Ruffini et al., in preparation).

Before concluding, in support of the classification proposed in this article, we recall that the luminosity light curves of the GeV emission is uniquely observed in both BdHNe and S-GRBs. In both cases it follow a precise power-law behavior with time $\propto t^{-1.2}$ (see Nava et al. 2014, Ruffini et al. 2016 and Fig. 9). An outstanding conclusion of this paper is that in both BdHNe and S-GRBs, where the presence of the BH is predicted, the turn-on of this GeV emission occurs after the P-GRB emission and at the beginning of the prompt emission phase (see Figs. 2 (d) and 4 (d)). This commonality, in such different systems, as well as their energy requirements (see Tab. 7 and Fig. 9) are naturally explained if we assume, as indicated in Ruffini et al. (2015a,b), that this GeV emission originates by accretion processes in the newly-born BH. We have pointed out in Ruffini et al. (2016) how the total energy of the GeV emission can be expressed in term of the gravitational binding energy of matter accretion into Kerr BHs (see Ruffini & Wheeler 1969, in problem 2 of § 104 in Landau & Lifshitz 2003). This energetics requirement could not be fulfilled in the case of accretion onto a NS, in view of the much smaller value of the gravitational binding energy when compared to the case of a rotating BH (see e.g. Sibgatullin & Sunyaev 2000). On the general issue of the origin of the jetted GeV emission, and not just of its energetics, we refer to the last paragraph of the conclusions of the paper by Ruffini et al. (2016).

We have added a Table. 7 with the values of the GeV emission for both the case of S-GRBs and BdHNe. These energy releases up to $\approx 10^{54}$ erg can be explained by the occurrence of accretion onto a rotating BH with mass in the range of 3–10 M_{\odot} . It is also clear from Fig. 9 that S-GRBs and BdHNe have GeV emission sharing a common luminosity pattern and originating, in both cases, from a newly-born Kerr BH (Ruffini et al. 2015a,b). This picture includes also the first scenario of an IGC considered in Ruffini et al. (2001a) where an exploding CO_{core} is in a close binary system with an already formed BH companion. In view of the hypercritical accretion process of the SN ejecta onto an already formed BH, these systems have $E_{\text{iso}} \gtrsim 10^{54}$ erg and $E_{\text{p,i}} \gtrsim 2$ MeV. Their out-states are a binary composed of a more massive BH and a νNS . Such systems, which we refer to as BH-SNe, are expected to be the late evolutionary stages of X-ray binaries such as Cyg X-1 or Cyg X-3 (see, e.g., Giacconi & Ruffini 1978).

In conclusion we have computed the occurrence rate of short and long bursts following a new classification and obtaining figures in good agreement with the ones derived from population synthesis models. Essential to the classification have been the following new considerations:

- 1) the binary nature of the progenitors and their separation;
- 2) the essential role of the hypercritical accretion process onto a NS member of a close binary system. The possible reaching of M_{crit} by the accretion process and the formation of a BH;

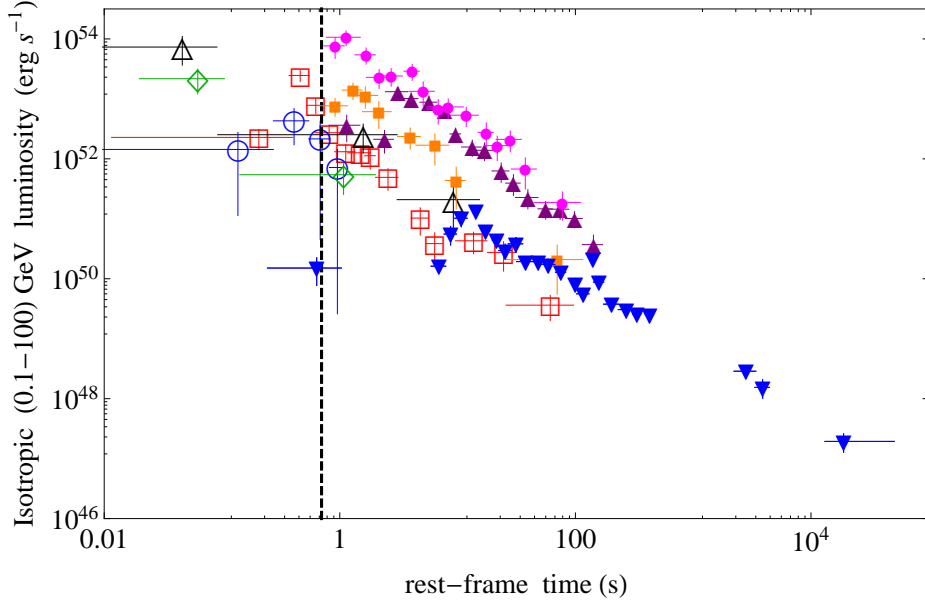


Figure 9. The rest-frame 0.1–100 GeV isotropic luminosity light curves of selected BdHNe (filled symbols) and all S-GRBs with available LAT data (empty symbols). BdHNe: GRB 080916C (magenta circles), GRB 090902B (purple triangles), GRB 110731A (orange squares), GRB 130427A (blue reversed triangles). S-GRBs: GRB 081024B (green diamonds), GRB 090510 (red squares), GRB 140402A (black triangles), GRB 140619B (blue circles). Also in this case the dashed vertical line marks the minimal turn-on time of the GeV emission of BdHNe.

source	z	$E_{p,i}$ (MeV)	E_{iso} (10^{52} erg)	E_{LAT} (10^{52} erg)
S-GRBs				
081024B	2.6 ± 1.6	8.7 ± 4.9	2.44 ± 0.22	2.70 ± 0.93
090510	0.903	7.89 ± 0.76	3.95 ± 0.21	5.78 ± 0.60
140402A	5.52 ± 0.93	6.1 ± 1.6	4.7 ± 1.1	16.6 ± 5.3
140619B	2.67 ± 0.37	5.34 ± 0.79	6.03 ± 0.79	2.34 ± 0.91
BdHNe				
080916C	4.35	2.76 ± 0.37	407 ± 86	440 ± 47
090902B	1.822	2.19 ± 0.22	292 ± 29	110 ± 5
110731A	2.83	1.16 ± 0.12	49.5 ± 4.9	42.5 ± 7.4
130427A	0.3399	1.25 ± 0.15	92 ± 13	19.9 ± 2.9

Table 7. List of the prompt and GeV emission properties of selected BdHNe and S-GRBs. We listed z , $E_{p,i}$, E_{iso} (in the rest-frame energy band 1–10000 keV), and E_{LAT} (in the rest-frame energy band 0.1–100 GeV).

- 3) the activity of the newly-born BHs originating the energetic prominent GeV emission, which can be explained in terms of the gravitational energy release by accreting matter onto a Kerr BH.

This classification is now open to a verification by the addition of new GRBs sources and offer new possibilities of theoretical and observational activities including:

- 1) the reaching of new observational constraints on the value of the NS critical mass M_{crit} and the minimum mass of a BH, which play a fundamental role in defining the separatrix among the different classes of our classification.
- 2) having elucidated the role of the activities of the newly-born BH in explaining the energetics of the GeV emission, in order to identify its microphysical process, the study of fundamental issues of general relativistic quantum electrodynamical processes appears to be open to further lines of inquiry (see, e.g., [Ruffini et al. 2010](#), and references therein);

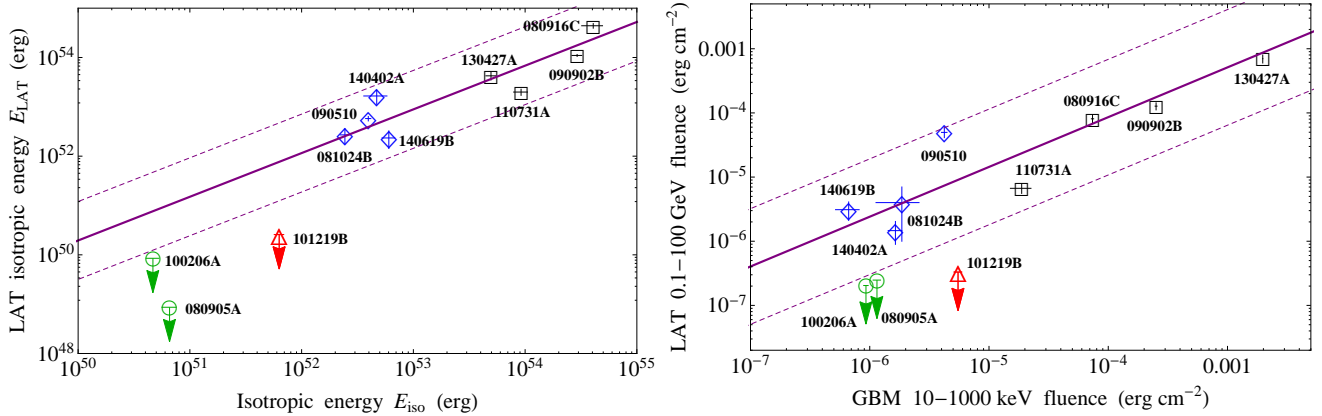


Figure A1. For the sources in Tab. 7 (BdHNe as black squares and S-GRBs as blue diamonds), as well as for 2 S-GRFs (green circles) and 1 XRF (red triangle) which did not exhibit GeV emission although they were in the optimal position ($< 65^\circ$ from the LAT boresight) for its detection, we plot: (Left:) the relation between E_{iso} of the prompt emission observed by the *Fermi*-GBM instrument and the total isotropic energy in the 0.1–100 GeV energy band observed by the *Fermi*-LAT instrument (or the corresponding upper limit if not detected); and (Right:) the relation between the 10–1000 keV fluence observed by the *Fermi*-GBM instrument and the total 0.1–100 GeV fluence observed by the *Fermi*-LAT instrument (or the corresponding upper limit if not detected). The purple solid line is the relation between the plotted quantities of BdHNe and S-GRBs, and the dashed lines are the corresponding dispersion.

- 3) it is conceivable that the sizable enlargement of the database of GRBs and of their spectral and luminosity time variability may open the possibility of further enlarging the above classification.

We thank the Editor and the Referee for their comments which helped to improve the presentation and the contextualization of our results. This work made use of data supplied by the UK Swift Science Data Center at the University of Leicester. J.A.R. acknowledges the support by the International Cooperation Program CAPES-ICRANet financed by CAPES-Brazilian Federal Agency for Support and Evaluation of Graduate Education within the Ministry of Education of Brazil. M.K. and Y. A. are supported by the Erasmus Mundus Joint Doctorate Program Grant N. 2013–1471 and 2014-0707, respectively, from EACEA of the European Commission. M.M. acknowledges the partial support of the project N 3101/GF4 IPC-11, and the target program F.0679 of the Ministry of Education and Science of the Republic of Kazakhstan.

APPENDIX

A. ON THE NON-OBSERVED GEV EMISSION IN S-GRFS AND XRFs

In Fig. A1 we compare and contrast the sources in Tab. 7, all exhibiting a GeV emission, with 2 S-GRFs and 1 XRF which, as theoretically expected within the fireshell model, do not exhibit any GeV emission. All these sources were in the optimal position ($< 65^\circ$ from the LAT boresight) for the detection of the GeV emission.

In the Left panel we plot the values of E_{iso} and of the isotropic energy in the *Fermi*-LAT energy band or the corresponding upper limits if not observed. These upper limits were obtained by using the unbinned likelihood analysis which was performed assuming an integration time of 100 s after the flash trigger, a radius of the source region of 10° and a zenith angle cut of 100° . This plot observationally supports the theoretical expectation, made in Ruffini et al. (2016) and quoted in section 6.2 above, that S-GRFs have, if any, GeV fluxes necessarily 10^5 – 10^6 times weaker than those of S-GRBs, although their E_{iso} is only a factor 10^2 smaller.

Motivated by a request of the Referee, we also plotted in the Right panel, the values of the fluence observed by *Fermi*-GBM and by *Fermi*-LAT or the corresponding upper limits if not observed (computed as above).

From both plots it is clear that the upper limits to the GeV emission of S-GRFs and XRFs are much lower than what one may expect from the extrapolation to lower energies of the one observed in BdHNe and S-GRBs. This is a further clear observational support to the absence, theoretically implied by the fireshell model, of any GeV emission associated to S-GRFs and XRFs (see sections 4.2 and 6.2 above).

REFERENCES

- Ackermann, M., Ajello, M., Asano, K., et al. 2013, *ApJS*, 209, 11
- Aksenov, A. G., Ruffini, R., & Vereshchagin, G. V. 2007, *Physical Review Letters*, 99, 125003
- 2009, *PhRvD*, 79, 043008
- Amati, L., & Della Valle, M. 2013, *International Journal of Modern Physics D*, 22, 30028
- Amati, L., Frontera, F., in't Zand, J. J. M., et al. 2004, *A&A*, 426, 415
- Antoniadis, J. 2015, *Astrophysics and Space Science Proceedings*, 40, 1
- Atwood, W. B., Abdo, A. A., Ackermann, M., et al. 2009, *ApJ*, 697, 1071
- Band, D. L. 2003, *ApJ*, 588, 945
- Becerra, L., Bianco, C. L., Fryer, C. L., Rueda, J. A., & Ruffini, R. 2016, *ArXiv e-prints*
- Becerra, L., Cipolletta, F., Fryer, C. L., Rueda, J. A., & Ruffini, R. 2015, *ApJ*, 812, 100
- Belvedere, R., Boshkayev, K., Rueda, J. A., & Ruffini, R. 2014, *Nuclear Physics A*, 921, 33
- Belvedere, R., Pugliese, D., Rueda, J. A., Ruffini, R., & Xue, S.-S. 2012, *Nuclear Physics A*, 883, 1
- Berger, E. 2014, *ARA&A*, 52, 43
- Berger, E., Fong, W., & Chornock, R. 2013, *ApJL*, 774, L23
- Bianco, C. L., & Ruffini, R. 2004, *ApJL*, 605, L1
- 2005a, *ApJL*, 633, L13
- 2005b, *ApJL*, 620, L23
- 2006, *ApJL*, 644, L105
- Bildsten, L., & Cutler, C. 1992, *ApJ*, 400, 175
- Boër, M., Gendre, B., & Stratta, G. 2015, *ApJ*, 800, 16
- Boshkayev, K., Rueda, J. A., Ruffini, R., & Siutsou, I. 2013, *ApJ*, 762, 117
- Bromberg, O., Nakar, E., & Piran, T. 2011, *ApJL*, 739, L55
- Bucciantini, N., Metzger, B. D., Thompson, T. A., & Quataert, E. 2012, *MNRAS*, 419, 1537
- Bufano, F., Pian, E., Sollerman, J., et al. 2012, *ApJ*, 753, 67
- Cadelano, M., Pallanca, C., Ferraro, F. R., et al. 2015, *ApJ*, 812, 63
- Caito, L., Amati, L., Bernardini, M. G., et al. 2010, *A&A*, 521, A80+
- Caito, L., Bernardini, M. G., Bianco, C. L., et al. 2009, *A&A*, 498, 501
- Calderone, G., Ghirlanda, G., Ghisellini, G., et al. 2015, *MNRAS*, 448, 403
- Campana, S., Mangano, V., Blustin, A. J., et al. 2006, *Nature*, 442, 1008
- Cano, Z., Bersier, D., Guidorzi, C., et al. 2011, *MNRAS*, 174
- Cavallo, G., & Rees, M. J. 1978, *MNRAS*, 183, 359
- Cherubini, C., Geralico, A., J. A. Rueda, H., & Ruffini, R. 2009, *Physical Review D*, 79, 124002
- Chiang, J., & Dermer, C. D. 1999, *ApJ*, 512, 699
- Cipolletta, F., Cherubini, C., Filippi, S., Rueda, J. A., & Ruffini, R. 2015, *PhRvD*, 92, 023007
- Clark, J., Evans, H., Fairhurst, S., et al. 2015, *ApJ*, 809, 53
- Cobb, B. E., Bloom, J. S., Perley, D. A., et al. 2010, *ApJL*, 718, L150
- Costa, E., Frontera, F., Heise, J., et al. 1997, *Nature*, 387, 783
- Dai, Z. G., & Lu, T. 1998a, *A&A*, 333, L87
- 1998b, *Physical Review Letters*, 81, 4301
- Dai, Z. G., Wang, X. Y., Wu, X. F., & Zhang, B. 2006, *Science*, 311, 1127
- Damour, T., & Ruffini, R. 1975, *Physical Review Letters*, 35, 463
- D'Avanzo, P., Melandri, A., Palazzi, E., et al. 2012, *GRB Coordinates Network*, 13069, 1
- De Pasquale, M., Schady, P., Kuin, N. P. M., et al. 2010, *ApJL*, 709, L146
- de Ugarte Postigo, A., Xu, D., Leloudas, G., et al. 2013, *GRB Coordinates Network*, 14646, 1
- Della Valle, M. 2006, in *American Institute of Physics Conference Series*, Vol. 836, *Gamma-Ray Bursts in the Swift Era*, ed. S. S. Holt, N. Gehrels, & J. A. Nousek, 367
- della Valle, M., Bianchini, A., Livio, M., & Orio, M. 1992, *A&A*, 266, 232
- della Valle, M., Rosino, L., Bianchini, A., & Livio, M. 1994, *A&A*, 287, 403
- Della Valle, M., Chincarini, G., Panagia, N., et al. 2006, *Nature*, 444, 1050
- Dezalay, J.-P., Barat, C., Talon, R., et al. 1992, in *American Institute of Physics Conference Series*, Vol. 265, *American Institute of Physics Conference Series*, ed. W. S. Paciesas & G. J. Fishman, 304–309
- Eichler, D., Livio, M., Piran, T., & Schramm, D. N. 1989, *Nature*, 340, 126
- Evans, P. A., Beardmore, A. P., Page, K. L., et al. 2007, *A&A*, 469, 379
- 2009, *MNRAS*, 397, 1177
- Fryer, C. L., Oliveira, F. G., Rueda, J. A., & Ruffini, R. 2015, *Physical Review Letters*, 115, 231102
- Fryer, C. L., Rueda, J. A., & Ruffini, R. 2014, *ApJ*, 793, L36
- Fryer, C. L., Woosley, S. E., & Hartmann, D. H. 1999, *ApJ*, 526, 152
- Galama, T. J., Vreeswijk, P. M., van Paradijs, J., et al. 1998, *Nature*, 395, 670
- Gehrels, N. 1986, *ApJ*, 303, 336
- Gehrels, N., Ramirez-Ruiz, E., & Fox, D. B. 2009, *ARA&A*, 47, 567
- Giacconi, R., & Ruffini, R., eds. 1978, *Physics and astrophysics of neutron stars and black holes*
- Giacomazzo, B., & Perna, R. 2013, *ApJL*, 771, L26
- Goodman, J. 1986, *ApJL*, 308, L47
- Granot, J., Piran, T., & Sari, R. 1999, *ApJ*, 513, 679
- Guetta, D., & Della Valle, M. 2007, *ApJL*, 657, L73
- Guetta, D., Pian, E., & Waxman, E. 2011, *A&A*, 525, A53
- Gursky, H., & Ruffini, R., eds. 1975, *Astrophysics and Space Science Library*, Vol. 48, *Neutron stars, black holes and binary X-ray sources; Proceedings of the Annual Meeting, San Francisco, Calif., February 28, 1974*
- Heise, J. 2003, in *American Institute of Physics Conference Series*, Vol. 662, *Gamma-Ray Burst and Afterglow Astronomy 2001: A Workshop Celebrating the First Year of the HETE Mission*, ed. G. R. Ricker & R. K. Vanderspek, 229–236
- Hill, J., Garnavich, P., Kuhn, O., et al. 2007, *GRB Coordinates Network*, 6486, 1
- Izzo, L., Pisani, G. B., Muccino, M., et al. 2012a, *ArXiv e-prints*
- Izzo, L., Rueda, J. A., & Ruffini, R. 2012b, *A&A*, 548, L5
- Izzo, L., Ruffini, R., Penacchioni, A. V., et al. 2012c, *A&A*, 543, A10
- Jin, Z.-P., Li, X., Cano, Z., et al. 2015, *ApJL*, 811, L22
- Kann, D. A., Schulze, S., & Updike, A. C. 2008, *GRB Coordinates Network*, 7627, 1
- Klebesadel, R. W. 1992, in *Gamma-Ray Bursts - Observations, Analyses and Theories*, ed. C. Ho, R. I. Epstein, & E. E. Fenimore (Cambridge University Press), 161–168
- Kluźniak, W., & Ruderman, M. 1998, *ApJL*, 505, L113
- Kouveliotou, C., Meegan, C. A., Fishman, G. J., et al. 1993, *ApJL*, 413, L101
- Kouveliotou, C., Woosley, S. E., Patel, S. K., et al. 2004, *ApJ*, 608, 872
- Kovacevic, M., Izzo, L., Wang, Y., et al. 2014, *A&A*, 569, A108
- Landau, L. D., & Lifshitz, E. M. 2003, *The classical theory of fields* (Butterworth-Heinemann (Oxford), 4th rev. engl. ed.)
- Lazarus, P., Tauris, T. M., Knispel, B., et al. 2014, *MNRAS*, 437, 1485
- Lee, W. H., Ramirez-Ruiz, E., & Page, D. 2004, *ApJL*, 608, L5

- Levan, A. J., Fruchter, A. S., Graham, J., et al. 2013, GRB Coordinates Network, 14686, 1
- Levan, A. J., Tanvir, N. R., Starling, R. L. C., et al. 2014, *ApJ*, 781, 13
- Li, L.-X., & Paczyński, B. 1998, *ApJL*, 507, L59
- Liang, E., Zhang, B., Virgili, F., & Dai, Z. G. 2007, *ApJ*, 662, 1111
- Lü, H.-J., & Zhang, B. 2014, *ApJ*, 785, 74
- MacFadyen, A. I., & Woosley, S. E. 1999, *ApJ*, 524, 262
- MacFadyen, A. I., Woosley, S. E., & Heger, A. 2001, *ApJ*, 550, 410
- Maeda, K., & Nomoto, K. 2003, *ApJ*, 598, 1163
- Meegan, C. A., Fishman, G. J., Wilson, R. B., et al. 1992, *Nature*, 355, 143
- Melandri, A., Pian, E., D’Elia, V., et al. 2014, *A&A*, 567, A29
- Meszáros, P. 2006, *Reports on Progress in Physics*, 69, 2259
- Meszáros, P., & Rees, M. J. 1997, *ApJL*, 482, L29
- Metzger, B. D., Giannios, D., Thompson, T. A., Bucciantini, N., & Quataert, E. 2011, *MNRAS*, 413, 2031
- Metzger, M. R., Djorgovski, S. G., Kulkarni, S. R., et al. 1997, *Nature*, 387, 878
- Muccino, M., Ruffini, R., Bianco, C. L., Izzo, L., & Penacchioni, A. V. 2013, *ApJ*, 763, 125
- Narayan, R., Paczyński, B., & Piran, T. 1992, *ApJL*, 395, L83
- Narayan, R., Piran, T., & Shemi, A. 1991, *ApJL*, 379, L17
- Nava, L., Vianello, G., Omodei, N., et al. 2014, *ArXiv e-prints*
- Nomoto, K., Yamaoka, H., Pols, O. R., et al. 1994, *Nature*, 371, 227
- Nomoto, K. I., Iwamoto, K., & Suzuki, T. 1995, *PhR*, 256, 173
- Nousek, J. A., Kouveliotou, C., Grupe, D., et al. 2006, *ApJ*, 642, 389
- Oliveira, F. G., Rueda, J. A., & Ruffini, R. 2014, *ApJ*, 787, 150
- Paczynski, B. 1986, *ApJL*, 308, L43
- Panaitescu, A., & Meszaros, P. 1998, *ApJL*, 493, L31
- Panaitescu, A., & Mészáros, P. 1999, *ApJ*, 526, 707
- Paschalidis, V., Liu, Y. T., Etienne, Z., & Shapiro, S. L. 2011, *PhRvD*, 84, 104032
- Patricelli, B., Bernardini, M. G., Bianco, C. L., et al. 2012, *ApJ*, 756, 16
- Penacchioni, A. V., Ruffini, R., Bianco, C. L., et al. 2013, *A&A*, 551, A133
- Penacchioni, A. V., Ruffini, R., Izzo, L., et al. 2012, *A&A*, 538, A58
- Pian, E., Amati, L., & Antonelli et al., L. A. 2000, *ApJ*, 536, 778
- Pian, E., Giommi, P., Amati, L., et al. 2004, *Advances in Space Research*, 34, 2711
- Piran, T. 2005, *Rev. Mod. Phys.*, 76, 1143
- Pisani, G. B., Izzo, L., Ruffini, R., et al. 2013, *A&A*, 552, L5
- Popham, R., Woosley, S. E., & Fryer, C. 1999, *ApJ*, 518, 356
- Preparata, G., Ruffini, R., & Xue, S. 1998, *A&A*, 338, L87
- Rangel Lemos, L. J., Bianco, C. L., Mosquera Cuesta, H. J., Rueda, J. A., & Ruffini, R. 2010, in *25th Texas Symposium on Relativistic Astrophysics*, 204
- Rasio, F. A., & Shapiro, S. L. 1999, *Classical and Quantum Gravity*, 16, R1
- Rees, M. J., & Meszaros, P. 1998, *ApJL*, 496, L1
- Rhoades, C. E., & Ruffini, R. 1974, *Physical Review Letters*, 32, 324
- Rosswog, S., Ramirez-Ruiz, E., & Davies, M. B. 2003, *MNRAS*, 345, 1077
- Rueda, J. A., & Ruffini, R. 2012, *ApJL*, 758, L7
- Ruffini, R. 2009, *The ergosphere and Dyadosphere of black holes*, ed. D. L. Wiltshire, M. Visser, & S. Scott (Cambridge University Press)
- . 2015, *Astronomy Reports*, 59, 591
- Ruffini, R., Bernardini, M. G., Bianco, C. L., et al. 2005, in *American Institute of Physics Conference Series*, Vol. 782, *XIth Brazilian School of Cosmology and Gravitation*, ed. M. Novello & S. E. Perez Bergliaffa, 42
- Ruffini, R., Bernardini, M. G., Bianco, C. L., et al. 2006a, *Advances in Space Research*, 38, 1291
- Ruffini, R., Bernardini, M. G., Bianco, C. L., et al. 2006b, in *The Tenth Marcel Grossmann Meeting*, ed. M. Novello, S. Perez Bergliaffa, & R. Ruffini (Singapore: World Scientific), 369
- Ruffini, R., Bernardini, M. G., & Bianco et al., C. L. 2008, in *The Eleventh Marcel Grossmann Meeting*, ed. H. Kleinert, R. T. Jantzen, & R. Ruffini, 368–505
- Ruffini, R., Bianco, C. L., Chardonnet, P., Frascchetti, F., & Xue, S. 2002, *ApJL*, 581, L19
- Ruffini, R., Bianco, C. L., Frascchetti, F., Xue, S.-S., & Chardonnet, P. 2001a, *ApJL*, 555, L117
- . 2001b, *ApJL*, 555, L113
- . 2001c, *ApJL*, 555, L107
- Ruffini, R., Bianco, C. L., Xue, S.-S., et al. 2004, *International Journal of Modern Physics D*, 13, 843
- Ruffini, R., Salmonson, J. D., Wilson, J. R., & Xue, S. 2000, *A&A*, 359, 855
- Ruffini, R., Salmonson, J. D., Wilson, J. R., & Xue, S.-S. 1999, *A&A*, 350, 334
- Ruffini, R., Vereshchagin, G., & Xue, S. 2010, *PhR*, 487, 1
- Ruffini, R., & Wilson, J. 1973, *Physical Review Letters*, 31, 1362
- Ruffini, R., & Wilson, J. R. 1975, *PhRvD*, 12, 2959
- Ruffini, R., Bernardini, M. G., Bianco, C. L., et al. 2007, in *ESA Special Publication*, Vol. 622, *ESA Special Publication*, 561
- Ruffini, R., Bianco, C. L., Enderli, M., et al. 2013, *GRB Coordinates Network*, 14526, 1
- Ruffini, R., Izzo, L., Muccino, M., et al. 2014a, *A&A*, 569, A39
- Ruffini, R., Muccino, M., Bianco, C. L., et al. 2014b, *A&A*, 565, L10
- Ruffini, R., Wang, Y., Enderli, M., et al. 2015a, *ApJ*, 798, 10
- Ruffini, R., Muccino, M., Kovacevic, M., et al. 2015b, *ApJ*, 808, 190
- Ruffini, R., Izzo, L., Bianco, C. L., et al. 2015c, *Astronomy Reports*, 59, 626
- Ruffini, R., Muccino, M., Aimuratov, Y., et al. 2016, *ArXiv e-prints*
- Ryde, F. 2004, *ApJ*, 614, 827
- . 2005, *ApJL*, 625, L95
- Sakamoto, T., Lamb, D. Q., Kawai, N., et al. 2005, *ApJ*, 629, 311
- Salmonson, J. D., & Wilson, J. R. 2002, *ApJ*, 578, 310
- Sari, R. 1997, *ApJL*, 489, L37
- . 1998, *ApJL*, 494, L49
- Sari, R., Piran, T., & Narayan, R. 1998, *ApJL*, 497, L17
- Schaefer, B. E. 2007, *ApJ*, 660, 16
- Sibgatullin, N. R., & Sunyaev, R. A. 2000, *Astronomy Letters*, 26, 772
- Smartt, S. J. 2009, *ARA&A*, 47, 63
- Soderberg, A. M., Kulkarni, S. R., Nakar, E., et al. 2006, *Nature*, 442, 1014
- Sparre, M., Sollerman, J., Fynbo, J. P. U., et al. 2011, *ApJL*, 735, L24
- Starling, R. L. C., Wiersema, K., Levan, A. J., et al. 2010, *ArXiv e-prints*
- Strong, I. B., Klebesadel, R. W., & Evans, W. D. 1975, in *Annals of the New York Academy of Sciences*, Vol. 262, *Seventh Texas Symposium on Relativistic Astrophysics*, ed. P. G. Bergman, E. J. Fenyves, & L. Motz, 145–158
- Sun, H., Zhang, B., & Li, Z. 2015, *ApJ*, 812, 33
- Tanvir, N. R., Levan, A. J., Fruchter, A. S., et al. 2013, *Nature*, 500, 547
- Tauris, T. M., van den Heuvel, E. P. J., & Savonije, G. J. 2000, *ApJL*, 530, L93

- Tavani, M. 1998, *ApJL*, 497, L21
- Troja, E., Rosswog, S., & Gehrels, N. 2010, *ApJ*, 723, 1711
- Usov, V. V. 1992, *Nature*, 357, 472
- van Paradijs, J., Groot, P. J., Galama, T., et al. 1997, *Nature*, 386, 686
- Virgili, F. J., Liang, E.-W., & Zhang, B. 2009, *MNRAS*, 392, 91
- Virgili, F. J., Zhang, B., O'Brien, P., & Troja, E. 2011, *ApJ*, 727, 109
- Wanderman, D., & Piran, T. 2010, *MNRAS*, 406, 1944
- . 2015, *MNRAS*, 448, 3026
- Watson, A. M., Butler, N., Kutyrev, A., et al. 2013, GRB Coordinates Network, 14666, 1
- Waxman, E. 1997, *ApJL*, 491, L19
- Woosley, S. E. 1993, *ApJ*, 405, 273
- Woosley, S. E., & Bloom, J. S. 2006, *ARA&A*, 44, 507
- Xu, D., de Ugarte Postigo, A., Kruehler, T., et al. 2013, GRB Coordinates Network, 14597, 1
- Zalamea, I., & Beloborodov, A. M. 2011, *MNRAS*, 410, 2302
- Zel'dovich, Y. B., Ivanova, L. N., & Nadezhin, D. K. 1972, *Soviet Ast.*, 16, 209
- Zhang, B., Fan, Y. Z., Dyks, J., et al. 2006, *ApJ*, 642, 354
- Zhang, B., & Mészáros, P. 2001, *ApJL*, 552, L35
- Zhang, B., Zhang, B., Virgili, F. J., et al. 2009, *ApJ*, 703, 1696
- Zhang, C. M., Wang, J., Zhao, Y. H., et al. 2011, *A&A*, 527, A83
- Zhang, F.-W., Shao, L., Yan, J.-Z., & Wei, D.-M. 2012, *ApJ*, 750, 88

ON THE RATE AND ON THE GRAVITATIONAL WAVE EMISSION OF SHORT AND LONG GRBS

R. RUFFINI^{1,2,3,4}, J. RODRIGUEZ^{1,2}, M. MUCCINO^{1,2}, J. A. RUEDA^{1,2,4}, Y. AIMURATOV^{1,2}, U. BARRES DE ALMEIDA^{4,5},
L. BECERRA^{1,2}, C. L. BIANCO^{1,2}, C. CHERUBINI^{6,7}, S. FILIPPI^{6,7}, D. GIZZI¹, M. KOVACEVIC^{1,2,3}, R. MORADI^{1,2},
F. G. OLIVEIRA^{1,2,3}, G. B. PISANI^{1,2}, Y. WANG^{1,2}

(Dated: October 26, 2016)
Draft version October 26, 2016

ABSTRACT

GRBs, traditionally classified as “long” and “short”, have been often assumed, till recently, to originate from a single black hole (BH) with an ultrarelativistic jetted emission. There is evidence that both long and short bursts have as progenitors merging and/or accreting binaries, each composed by a different combination of carbon-oxygen cores (CO_{core}), neutron stars (NSs), BHs and white dwarfs (WDs). Consequently, the traditional long bursts have been sub-classified as (I) X-ray flashes (XRFs), (II) binary-driven hypernovae (BdHNe), and (III) BH-supernovae (BH-SNe). They are framed within the induced gravitational collapse (IGC) paradigm which envisages as progenitor a tight binary composed of a CO_{core} and a NS or BH companion. The SN explosion of the CO_{core}, originating a new NS (ν NS), triggers a hypercritical accretion process onto the companion NS or BH. If the accretion is not sufficient for the NS to reach its critical mass, an XRF occurs, leading to a ν NS-NS system. Instead, when the BH is already present or formed by the hypercritical accretion, a BdHN occurs, leading to a ν NS-BH system. Similarly, the traditional short bursts, originating in NS-NS mergers, are sub-classified as (IV) short gamma-ray flashes (S-GRFs) and (V) short GRBs (S-GRBs), respectively when the merging process does not lead or leads to BH formation. Two additional families are (VI) ultra-short GRBs (U-GRBs) and (VII) gamma-ray flashes (GRFs), respectively formed in ν NS-BH and NS-WD mergers. We use the estimated occurrence rate of the above sub-classes to assess the gravitational wave emission in the merging process and its detectability by Advanced LIGO, Advanced Virgo, eLISA, and resonant bars.

Subject headings: gamma-ray burst: general — gravitational waves — black hole physics — stars: neutron — white dwarfs — binaries: general

1. INTRODUCTION

Thanks to the extensive observations carried out by γ -ray telescopes, such as AGILE, BATSE, BeppoSAX, *Fermi*, *HETE-II*, *INTEGRAL*, Konus/WIND and *Swift*, our understanding of “long” and “short” gamma-ray burst (GRB) progenitor systems has greatly improved. This has led also to a vast literature devoted to the estimate of their relative occurrence rates, all in general agreement. For long bursts see, e.g., Soderberg et al. (2006); Guetta & Della Valle (2007); Liang et al. (2007); Virgili et al. (2009); Rangel Lemos et al. (2010); Wanderman & Piran (2010); Guetta et al. (2011); Kovacevic et al. (2014); for short bursts see, e.g., Virgili et al. (2011); Wanderman & Piran (2015); and for both long and short bursts see, e.g., Sun et al. (2015); Ruffini et al. (2016).

Our aim in this article is to use the rate of the GRB occurrence to assess the detectability of their associated

gravitational wave (GW) emission by the ground-based interferometers Advanced LIGO (hereafter aLIGO) and Advanced Virgo (hereafter AdV), by the space-based interferometer eLISA, as well as by the resonant bars. In order to do this we have to identify the different kinds of GRB progenitors. GRBs, traditionally classified as long and short, have been often assumed, till recently, to originate from a single black hole (BH) with an ultrarelativistic jetted emission. There is today clear evidence (see Ruffini et al. 2016) that both long and short bursts have as progenitors merging and/or accreting binary systems, each composed by a different combination of carbon-oxygen cores (CO_{core}), neutron stars (NSs), black holes (BHs) and white dwarfs (WDs). For each system the initial state and the final state are respectively here referred to as “*in-state*” and “*out-state*”.

For the traditional long GRBs, the induced gravitational collapse (IGC) paradigm (Ruffini et al. 2006, 2007, 2008; Izzo et al. 2012; Rueda & Ruffini 2012; Fryer et al. 2014; Ruffini et al. 2015a) proposes as *in-state* a tight binary system composed of a CO_{core} undergoing a supernova (SN) explosion and a companion compact object, e.g. a NS or a BH. The SN explosion triggers hypercritical accretion onto the companion (Ruffini et al. 2016). They are classified into three sub-classes (Ruffini et al. 2016):

- I. X-ray flashes (XRFs) with isotropic energy $E_{\text{iso}} \lesssim 10^{52}$ erg and rest-frame spectral peak energy $E_{p,i} \lesssim 200$ keV. This class occurs in CO_{core}-NS binaries when the hypercritical accretion onto the NS com-

¹ Dipartimento di Fisica and ICRA, Sapienza Università di Roma, P.le Aldo Moro 5, I-00185 Rome, Italy

² ICRANet, P.zza della Repubblica 10, I-65122 Pescara, Italy

³ Université de Nice Sophia Antipolis, CEDEX 2, Grand Château Parc Valrose, Nice, France

⁴ ICRANet-Rio, Centro Brasileiro de Pesquisas Físicas, Rua Dr. Xavier Sigaud 150, 22290-180 Rio de Janeiro, Brazil

⁵ Centro Brasileiro de Pesquisas Físicas, Rua Dr. Xavier Sigaud 150, 22290-180 Rio de Janeiro, Brazil

⁶ Unit of Nonlinear Physics and Mathematical Modeling, Università Campus Bio-Medico di Roma, Via A. del Portillo 21, I-00128 Rome, Italy

⁷ ICRA, Università Campus Bio-Medico di Roma, Via A. del Portillo 21, I-00128 Rome, Italy

Table 1

Summary of the astrophysical aspects of the different GRB sub-classes and of their observational properties. In the first four columns we indicate the GRB sub-classes and their corresponding *in-states* and the *out-states*. In columns 5–8 we list the ranges of $E_{p,i}$ and E_{iso} (rest-frame 1–10⁴ keV), $E_{\text{iso,X}}$ (rest-frame 0.3–10 keV), and $E_{\text{iso,Gev}}$ (rest-frame 0.1–100 GeV). Columns 9 and 10 list, for each GRB sub-class, the maximum observed redshift and the local observed rate ρ_{GRB} obtained in Ruffini et al. (2016).

	Sub-class	<i>In-state</i>	<i>Out-state</i>	$E_{p,i}$ (MeV)	E_{iso} (erg)	$E_{\text{iso,X}}$ (erg)	$E_{\text{iso,Gev}}$ (erg)	z_{max}	ρ_{GRB} (Gpc ⁻³ yr ⁻¹)
I	XRFs	CO _{core} -NS	ν NS-NS	$\lesssim 0.2$	$\sim 10^{48}\text{--}10^{52}$	$\sim 10^{48}\text{--}10^{51}$	–	1.096	100^{+45}_{-34}
II	BdHNe	CO _{core} -NS	ν NS-BH	$\sim 0.2\text{--}2$	$\sim 10^{52}\text{--}10^{54}$	$\sim 10^{51}\text{--}10^{52}$	$\lesssim 10^{53}$	9.3	$0.77^{+0.09}_{-0.08}$
III	BH-SN	CO _{core} -BH	ν NS-BH	$\gtrsim 2$	$> 10^{54}$	$\sim 10^{51}\text{--}10^{52}$	$\gtrsim 10^{53}$	9.3	$\lesssim 0.77^{+0.09}_{-0.08}$
IV	S-GRFs	NS-NS	MNS	$\lesssim 2$	$\sim 10^{49}\text{--}10^{52}$	$\sim 10^{49}\text{--}10^{51}$	–	2.609	$3.6^{+1.4}_{-1.0}$
V	S-GRBs	NS-NS	BH	$\gtrsim 2$	$\sim 10^{52}\text{--}10^{53}$	$\lesssim 10^{51}$	$\sim 10^{52}\text{--}10^{53}$	5.52	$(1.9^{+1.8}_{-1.1}) \times 10^{-3}$
VI	U-GRBs	ν NS-BH	BH	$\gtrsim 2$	$> 10^{52}$	–	–	–	$\gtrsim 0.77^{+0.09}_{-0.08}$
VII	GRFs	NS-WD	MNS	$\sim 0.2\text{--}2$	$\sim 10^{51}\text{--}10^{52}$	$\sim 10^{49}\text{--}10^{50}$	–	2.31	$1.02^{+0.71}_{-0.46}$

panion is not enough to induce gravitational collapse into a BH (Becerra et al. 2016, 2015). Thus, the *out-states* of XRFs are binaries composed of a newly-formed $\sim 1.4\text{--}1.5 M_{\odot}$ NS (hereafter ν NS) born in the SN explosion, and a massive NS (MNS) which accreted matter from the SN ejecta. Their occurrence rate is $\rho_{\text{XRF}} = 100^{+45}_{-34} \text{ Gpc}^{-3} \text{ yr}^{-1}$ (Ruffini et al. 2016), which is in agreement with those for low-luminous long GRBs (Liang et al. 2007; Virgili et al. 2009; Sun et al. 2015).

II. Binary-driven hypernovae (BdHNe) with $E_{\text{iso}} \gtrsim 10^{52}$ erg and $E_{p,i} \gtrsim 200$ keV. BdHNe occur in more compact CO_{core}-NS binaries which leads to a more massive hypercritical accretion onto the NS, hence leading to BH formation. Therefore, the *out-states* of BdHNe are ν NS-BH binaries (Becerra et al. 2016; Fryer et al. 2015; Becerra et al. 2015). Their occurrence rate is $\rho_{\text{BdHN}} = 0.77^{+0.09}_{-0.08} \text{ Gpc}^{-3} \text{ yr}^{-1}$ (Ruffini et al. 2016), which is in agreement with those for high-luminous long GRBs (Wanderman & Piran 2010; Sun et al. 2015).

III. BH-SN with $E_{\text{iso}} \gtrsim 10^{54}$ erg and $E_{p,i} \gtrsim 2$ MeV. BH-SN occur in close CO_{core}-BH binaries (Ruffini et al. 2001) in which the hypercritical accretion produces, as *out-states*, a more massive BH and a ν NS. Such BH-SN systems correspond to the late evolutionary stages of X-ray binaries, as Cyg X-1 and Cyg X-3 (Giacconi & Ruffini 1978), or microquasars (Mirabel & Rodríguez 1998). These systems are here considered a sub-set of the BdHNe. Therefore, in the following we assume the rate of BdHNe as an upper limit to the rate of BH-SNe, i.e. $\rho_{\text{BH-SN}} \lesssim 0.77^{+0.09}_{-0.08} \text{ Gpc}^{-3} \text{ yr}^{-1}$ (Ruffini et al. 2016).

Similarly, for the traditional short GRBs, the *in-states* are NS-NS or NS-BH merging binaries, as commonly adopted also within the traditional models (see, e.g., Goodman 1986; Paczynski 1986; Eichler et al. 1989; Narayan et al. 1991; Meszaros & Rees 1997; Rosswog et al. 2003; Lee et al. 2004; Berger 2014). They are divided into three sub-classes (Fryer et al. 2015; Ruffini et al. 2015b, 2016):

IV. Short gamma-ray flashes (S-GRFs), with $E_{\text{iso}} \lesssim 10^{52}$ erg and $E_{p,i} \lesssim 2$ MeV, occur when no BH

is formed in the NS-NS merger, i.e. they lead to a MNS. Their occurrence rate is $\rho_{\text{S-GRF}} = 3.6^{+1.4}_{-1.0} \text{ Gpc}^{-3} \text{ yr}^{-1}$ (Ruffini et al. 2016), which is in agreement with the estimates obtained from the whole short burst population reported in the literature (Wanderman & Piran 2015; Sun et al. 2015).

V. Authentic short GRBs (S-GRBs), with $E_{\text{iso}} \gtrsim 10^{52}$ erg and $E_{p,i} \gtrsim 2$ MeV, occur when a BH is formed in the NS-NS merger. Their occurrence rate is $\rho_{\text{S-GRB}} = (1.9^{+1.8}_{-1.1}) \times 10^{-3} \text{ Gpc}^{-3} \text{ yr}^{-1}$ (Ruffini et al. 2016).

VI. Ultra-short GRBs (U-GRBs), a new sub-class of short bursts originating from ν NS-BH merging binaries. Such systems are yet unobserved and present a great challenge not only in the present case of high-energy but also possibly in the radio band where they would manifest themselves as pulsar-BH binaries (see, e.g., Tauris et al. 2015, and references therein). They can originate from BdHNe (see II above) or from BH-SN events (see III above). We recall that in Fryer et al. (2015) it is shown that the majority of BdHN *out-states* remain bound. We thus assume as an ansatz that $\rho_{\text{U-GRB}} \approx \rho_{\text{BdHN}} = 0.77^{+0.09}_{-0.08} \text{ Gpc}^{-3} \text{ yr}^{-1}$ (Ruffini et al. 2016).

VII. Gamma-ray flashes (GRFs) have $10^{51} \lesssim E_{\text{iso}} \lesssim 10^{52}$ erg and $0.2 \lesssim E_{p,i} \lesssim 2$ MeV. This sub-class of sources originates in NS-WD mergers (Ruffini et al. 2016). These binaries are notoriously very common astrophysical systems (Cadelano et al. 2015) and possible evolutionary scenarios leading to such mergers have been envisaged (see, e.g., Lazarus et al. 2014; Tauris et al. 2000). GRFs form a MNS and not a BH (see Ruffini et al. 2016, for details). Their rate of occurrence is $\rho_{\text{GRF}} = 1.02^{+0.71}_{-0.46} \text{ Gpc}^{-3} \text{ yr}^{-1}$ (Ruffini et al. 2016).

Interestingly, it has been shown in Ruffini et al. (2016); Fryer et al. (2015); Becerra et al. (2015) that the *out-states* of long GRBs can become the *in-states* of short GRBs. Since $\rho_{\text{XRF}} > \rho_{\text{S-GRF}}$ and $\rho_{\text{XRF}} > \rho_{\text{S-GRB}}$, the *out-states* of XRFs (ν NS-NS) could be the *in-states* of S-GRFs (NS-NS mergers leading to a MNS) and S-GRBs (NS-NS mergers leading to a BH).

There is also an additional evolutionary scenario concerning the NS-WD merger, namely that they are produced from an S-GRF (Ruffini et al. 2016). The merger of a mass-asymmetric NS-NS binary with total mass $m_1 + m_2$ smaller than M_{crit} can produce a MNS with a low-mass WD companion (see Bildsten & Cutler 1992, and references therein), a type of binary of great current interest (see, e.g., Lazarus et al. 2014; Tauris et al. 2000).

The rate of occurrence of the above GRB sub-classes has been recently estimated in Ruffini et al. (2016) assuming the absence of beaming. We show in Table 1 a summary of the astrophysical aspects related to the GRB sub-classes and their observational properties. With this knowledge of the compact object binary progenitors associated with each GRB sub-class and their corresponding rate of occurrence, we can now proceed to estimate their GW emission in order to evaluate its possible detectability by aLIGO and bar detectors.

2. GW EMISSION AND DETECTABILITY

In the introduction we have recalled that the evolution of the binary progenitors of both short and long GRBs lead to compact binaries which will eventually merge in a characteristic timescale and emit GWs. We turn now to assess the detectability of the GW emission by these merging binaries by aLIGO.

In order to do this, we make the following drastic gedanken assumptions:

1. Although it is manifest that the release of gravitational energy of the system in the merger phase is dominated by the X, gamma-ray and GeV emission (see Table 1), we assume in Sec. 2.2 that the binary dynamics is only driven by the GW emission.
2. Consistent with the above GW emission dominance assumption, we further assume that the GW waveform is known and thus one can use the matched filter technique to estimate the signal-to-noise ratio (see Sec. 2.1). The actual GW waveform under the realistic conditions of electromagnetic emission dominance is still unknown.
3. To estimate the maximum distance of GW detectability we adopt in Sec. 3 that the source is optimally oriented with respect to the detector.

The above assumptions are made with the only aim of establishing an absolute upper limit to the GW emission and its putative detectability under the most optimistic conditions. Similarly, we assume that the binarity of the system does not compromise the structure of the NS (see Sec. 2.3).

The minimum GW frequency detectable by the broadband aLIGO interferometer is $f_{\text{min}}^{\text{aLIGO}} \approx 10$ Hz (LIGO Scientific Collaboration et al. 2015). Since during the binary inspiral the GW frequency is twice the orbital one (see below Sec. 2.2), the above implies a binary is inside the aLIGO band for orbital periods $P_{\text{orb}} \lesssim 0.2$ s. Thus, we can conclude that CO_{core}-NS binaries, *in-states* of XRFs and BdHNe, and CO_{core}-BH binaries, *in-states* of BH-SN, are not detectable by aLIGO since they have orbital periods $P_{\text{orb}} \gtrsim 5$ min $\gg 0.2$ s. Concerning their *out-states* after the corresponding hypercritical accretion

processes, namely ν NS-NS, *out-states* of XRFs, and ν NS-BH, *out-states* of BdHNe and BH-SNe, they are not detectable by aLIGO at their birth but only when approaching the merger. In the case of NS-WD binaries, the WD large radius and its very likely tidal disruption by the NS make their GW emission hard to be detected (see, e.g., Paschalidis et al. 2009). Thus, we do not consider NS-WD binaries in the following discussion.

It is clear that the analysis of GW emission during the final coalescence and merger of the ν NS-NS binaries produced by XRFs is included in the analysis of the S-GRF and S-GRB sub-classes, and the merger of ν NS-BH binaries produced in BdHNe and BH-SNe is included in the one of U-GRBs.

In order to define the possible masses of the components of the binary systems, we need information on the NS structure. In particular, we have to establish the maximum stable NS mass, i.e., the critical mass for gravitational collapse to a BH. The critical mass lies within the range 2.2–3.4 M_{\odot} depending on the equation of state (EOS) and on the NS angular momentum (see Cioffalo et al. 2015; Becerra et al. 2015; Belvedere et al. 2014 for details). These quoted values are for EOS based on relativistic nuclear mean-field models (in this case the NL3, TM1 and GM1 models) and for a NS angular momentum from $J = 0$ up to $J_{\text{max}} \approx 0.7GM^2/c$ (Cioffalo et al. 2015). Hereafter, we adopt the stiffest model, namely the NL3 EOS, which leads to the largest NS critical mass: from $M_{\text{crit}} \approx 2.7 M_{\odot}$ at $J = 0$, that, as expected, is lower than the non-rotating critical mass upper limit of 3.2 M_{\odot} established by Rhoades & Ruffini (1974), to $M_{\text{crit}} \approx 3.4 M_{\odot}$ at J_{max} (Cioffalo et al. 2015).

For S-GRFs, we consider the simple case of symmetric binary (NS-NS) mergers, $m_1 = m_2 = m$. The precise value of the merging NS masses leading to a BH is still poorly known, thus we have chosen it as roughly half the maximum NS critical mass. Thus, for the sake of completeness we explore mass values from $m \approx 1 M_{\odot}$ to $m \approx 1.7 M_{\odot}$.

For S-GRBs, we also consider non-spinning symmetric binary components with values starting from the upper edge of the S-GRF progenitors, i.e. $m \approx 1.7 M_{\odot}$, up to the maximum non-rotating stable mass, i.e. $m \approx 2.8 M_{\odot}$.

For the U-GRBs which are *out-states* of BdHN we adopt $m_1 = 1.5 M_{\odot}$ for the ν NS mass and $m_{\text{BH}} = 2.7$ – $3.4 M_{\odot}$ for the BH mass. For the U-GRBs which are *out-states* of BH-SN we adopt $m_1 = 1.5 M_{\odot}$ for the ν NS mass and $m_{\text{BH}} = 3.4$ – $10 M_{\odot}$ for the BH mass.

2.1. Signal-to-noise ratio

We first recall the main ingredients needed to estimate the detectability of the aforementioned merging binaries associated with the different GRB classes. The signal $h(t)$ induced in the detector is:

$$h(t) = F_+(\theta, \phi, \psi)h_+(t, \iota, \beta) + F_{\times}(\theta, \phi, \psi)h_{\times}(t, \iota, \beta), \quad (1)$$

where h_+ and h_{\times} are the two polarizations of the GW; ι and β are the polar and azimuthal angles of the unit vector from the source to the detector, relative to a coordinate system centered in the source. The detector pattern functions F_+ and F_{\times} depend on the localization of the source with respect to the detector, i.e. they depend on the spherical polar angles θ and ϕ of the source

relative to a coordinate system centered in the detector. The pattern functions also depend on the polarization angle ψ .

Since the GW signal might be deep inside the noise, the signal-to-noise ratio, denoted hereafter by ρ , is usually computed using the matched filter technique, i.e. (Flanagan & Hughes 1998):

$$\rho^2 = 4 \int_0^\infty \frac{|\tilde{h}(f)|^2}{S_n(f)} df, \quad (2)$$

where f is the GW frequency in the detector's frame, $\tilde{h}(f)$ is the Fourier transform of $h(t)$ and $\sqrt{S_n(f)}$ is the one-sided amplitude spectral density (ASD) of the aLIGO noise. We recall that in the detector's frame the GW frequency is redshifted by a factor $1+z$ with respect to the one in the source's frame, f_s , i.e. $f = f_s/(1+z)$.

The exact position of the binary relative to the detector and the orientation of the binary rotation plane are usually unknown, thus it is a common practice to estimate the signal-to-noise ratio averaging over all the possible locations and orientations, i.e.:

$$\langle \rho^2 \rangle = 4 \int_0^\infty \frac{\langle |\tilde{h}(f)|^2 \rangle}{S_n(f)} df = 4 \int_0^\infty \frac{h_c^2(f)}{f^2 S_n(f)} df, \quad (3)$$

with $h_c(f)$ the characteristic strain (Flanagan & Hughes 1998)

$$h_c = \frac{(1+z)}{\pi d_l} \sqrt{\frac{\langle F_+^2 \rangle}{2} \frac{G}{c^3} \frac{dE}{df_s} [(1+z)f]}, \quad (4)$$

where

$$d_l = \frac{(1+z)c}{H_0} \int_0^z [\Omega_M(1+x)^3 + \Omega_\Lambda]^{-1/2} dx, \quad (5)$$

is the source luminosity distance and we have used the fact that $\langle F_+^2 \rangle = \langle F_\times^2 \rangle$ and $\langle F_+ F_\times \rangle = 0$. We recall that $\langle F_+^2 \rangle = 1/5$ for an interferometer and $\langle F_+^2 \rangle = 4/15$ for a resonant bar (see, e.g., Maggiore 2007). We adopt a Λ CDM cosmology with $H_0 = 71 \text{ km s}^{-1} \text{ Mpc}^{-1}$, $\Omega_M = 0.27$ and $\Omega_\Lambda = 0.73$ (Rigault et al. 2015). It is important to recall that, as we have mentioned, we are interested in estimating the GW detectability under the most optimistic conditions. Thus, to estimate the maximum distance of GW detectability we adopt in Sec. 3 the ansatz of optimally oriented sources with respect to the detector. The above averaging procedure is here used with the only aim of giving an estimate of the GW strain amplitude, h_c , compared and contrasted below in Sec. 2.4 with the strain noise of the detectors.

2.2. GW energy spectrum

A binary system, by emitting GWs, evolves in time through two regimes: the first is the *inspiral regime* and the second, which we refer hereafter to as *merger regime*, is composed in the most general case of the final plunge, of the merger, and of the ringdown (oscillations) of the newly formed object.

During the inspiral regime the system evolves describing quasi-circular orbits and it is well described by the traditional point-like quadrupole approximation (Peters & Mathews 1963; Peters 1964; Rees et al. 1974; Landau

& Lifshitz 1975). The GW frequency is twice the orbital frequency ($f_s = 2f_{\text{orb}}$) and grows monotonically. The energy spectrum during the inspiral regime is:

$$\frac{dE}{df_s} = \frac{1}{3} (\pi G)^{2/3} M_c^{5/3} f_s^{-1/3}, \quad (6)$$

where $M_c = \mu^{3/5} M^{2/5} = \nu^{3/5} M$ is the called *chirp mass*, $M = m_1 + m_2$ is the total binary mass, $\mu = m_1 m_2 / M$ is the reduced mass, and $\nu \equiv \mu / M$ is the symmetric mass-ratio parameter. A symmetric binary ($m_1 = m_2$) corresponds to $\nu = 1/4$ and the test-particle limit is $\nu \rightarrow 0$. The total energy emitted during this regime can be estimated as the binding energy of the binary at the last stable circular orbit (LSO). For a test-particle in the Schwarzschild background, the LSO is located at $r_{\text{LSO}} = 6GM/c^2$ and the binding energy is:

$$\Delta E_{\text{insp}} = (1 - 2\sqrt{2}/3) \mu c^2. \quad (7)$$

The GW spectrum of the merger regime is characterized by a GW burst (see, e.g., Davis et al. 1971; Shibata & Taniguchi 2011; Bernuzzi et al. 2015a). Thus, to estimate whether this part of the signal contributes to the signal-to-noise ratio, it is sufficient to estimate the location of the GW burst in the frequency domain and its energy content. We recall that, in general, the merger regime is composed of plunge+merger+ringdown. The frequency range spanned by the GW burst is $\Delta f = f_{\text{qnm}} - f_{\text{merger}}$, where f_{merger} is the frequency at which the merger starts and f_{qnm} is the frequency of the ringing modes of the newly formed object after the merger, and the energy emitted is ΔE_{merger} . With these quantities defined, we can estimate the typical value of the merger regime spectrum as:

$$\left(\frac{dE}{df_s} \right)_{\text{merger}} \sim \frac{\Delta E_{\text{merger}}}{\Delta f}. \quad (8)$$

2.3. GW energy and frequency in the merger regime

2.3.1. NS-NS merger

Numerical relativity simulations (e.g. Shibata & Taniguchi 2011; Bernuzzi et al. 2015a) show that finite size effects might end the inspiral regime before the LSO. After this point, the GW spectrum damps exponentially. For the case of NS-NS the merger starts in an orbit larger than the LSO, and for the case of a NS-BH, as we will see below, the merger can occur below the LSO making the spectrum similar to a BH-BH merger. When the merger occurs well before the LSO, there is not the plunge. Therefore, the emitted energy will be less than the case when the plunge is present. We can therefore obtain an upper limit to ΔE_{merger} by adopting the energy emitted during the plunge-merger-ringdown of a BH-BH merger (Detweiler & Szedenits 1979; Nagar et al. 2007)

$$\Delta E_{\text{merger}} \approx 0.5 \nu^2 M c^2. \quad (9)$$

To complete the estimate of the merger regime spectrum, we have to estimate the value of Δf in the different cases of interest. The approach to the merger point, $r = r_{\text{merger}}$, depends on the nature of the binary system. Typically, the merger is assumed to start at the point of maximum GW strain (see, e.g., Bernuzzi et al.

Table 2

Properties of the GW emission of S-GRFs, S-GRBs and U-GRBs. We have made the drastic gedanken assumption that the binary evolution is only driven by GW emission, although it is manifest that the gravitational energy of the system in the merger phase is dominated by the radio, optical, X, gamma-ray and GeV emission (see Table 1). This assumption is made with the only aim of establishing an absolute upper limit to the GW emission and its detectability under the most optimistic conditions. Column 1: GRB sub-class. Column 2: energy emitted in GWs during the inspiral regime ΔE_{insp} given by Eq. (7). Column 3: energy emitted in GWs during the merger regime (plunge+merger+ringdown) ΔE_{merger} given by Eq. (9). Columns 4: GW frequency at merger. Column 5: GW frequency of the ringdown regime. Column 6: lowest cosmological redshift value $z_{\text{min}}^{\text{obs}}$ at which each sub-class has been observed. Column 7: luminosity distance corresponding to $z_{\text{min}}^{\text{obs}}$, $d_{l,\text{min}}$, estimated from Eq. (5). Columns 8 and 9: GW horizon calculated with the sensitivity of the first run of aLIGO (O1) and the expected final sensitivity (2022+), respectively. It can be seen that the current GW horizon is much smaller than the observed distances of GRBs, impeding a positive detection by aLIGO. Only in the case of U-GRB (BH-SN) it is foreseen a possible detection during the run 2022+. See also Table 3. We have used for S-GRFs ($1.4+1.4$) M_{\odot} , for S-GRBs ($2.0+2.0$) M_{\odot} and, for U-GRBs ($1.5+3.0$) M_{\odot} and ($1.5+10.0$) M_{\odot} respectively for the *out-states* of BdHNe and of BH-SN. Even if no U-GRB has yet been identified, we use here the values of $z_{\text{min}}^{\text{obs}}$ and $d_{l,\text{min}}$ corresponding to the closest BdHN observed.

	ΔE_{insp} (erg)	ΔE_{merger} (erg)	f_{merger} (kHz)	f_{qnm} (kHz)	$z_{\text{min}}^{\text{obs}}$	$d_{l,\text{min}}$ (Mpc)	d_{GW} (Mpc)	
							O1	2022+
S-GRF	7.17×10^{52}	1.60×10^{53}	1.20	3.84	0.111	508.70	168.43	475.67
S-GRB	1.02×10^{53}	2.28×10^{53}	1.43	2.59	0.903	5841.80	226.62	640.18
U-GRB	1.02×10^{53}	2.03×10^{52}	0.98	2.30	0.169	804.57	235.62	665.72
U-GRB (BH-SN)	1.34×10^{53}	1.35×10^{53}	0.38	0.90	0.169	804.57	362.27	1023.43

2015a, and references therein). However, since the transition from a binary system to a single merged object is not sharply definable, there can be found different definitions of the merger point in the literature (see, e.g., Kawaguchi et al. 2015). For our purpose it is sufficient to estimate the frequency at “contact”, namely the frequency at a binary separation $r_{\text{contact}} \approx r_1 + r_2$ where r_i is the radius of the i -component. This certainly sets a lower limit to the frequency at maximum strain at merger, i.e. $r_{\text{contact}} \gtrsim r_{\text{merger}}$. Thus, we adopt for these systems:

$$f_{\text{merger}}^{\text{NS-NS}} \approx f_{\text{contact}}^{\text{NS-NS}} = \frac{1}{\pi} \frac{c^3}{GM} \left[\frac{\mathcal{C}_1 \mathcal{C}_2 (1+q)}{\mathcal{C}_1 + q \mathcal{C}_2} \right]^{3/2}, \quad (10)$$

where $q = m_2/m_1$ is the mass-ratio which is related to the symmetric mass-ratio parameter by $\nu = q/(1+q)^2$, and $\mathcal{C}_i \equiv Gm_i/c^2 r_i$ is the compactness of the i -component.

For a mass symmetric NS-NS binary, we have that $f_{\text{contact}}^{\text{NS-NS}} \approx (1/\pi)(c^3/G)\mathcal{C}_{\text{NS}}^{3/2}/M$, where $\mathcal{C}_{\text{NS}} \equiv \mathcal{C}_1 = \mathcal{C}_2$ is the compactness parameter of the initial NS. For example, for the NL3 EOS, the NS compactness lies in the range $\mathcal{C}_{\text{NS}} \approx 0.14\text{--}0.3$ for a NS mass $1.4\text{--}2.8 M_{\odot}$ (see, e.g., Cipolletta et al. 2015). Thus, using the same EOS we have, for an $M = (1.4 + 1.4) M_{\odot} = 2.8 M_{\odot}$ binary, $f_{\text{contact}}^{\text{NS-NS}} \approx 1.34$ kHz, and for an $M = (2.0 + 2.0) M_{\odot} = 4.0 M_{\odot}$ binary, $f_{\text{contact}}^{\text{NS-NS}} \approx 1.43$ kHz.

In the merger regime either a BH or a MNS can be formed. If a BH is formed, the $l = 2$ multipole (quadrupole) quasi-normal oscillations lead to a spectrum that peaks at a frequency (Davis et al. 1971, 1972)

$$f_{\text{qnm}}^{\text{BH}} \approx \frac{0.32}{2\pi} \frac{c^3}{GM}, \quad (11)$$

i.e. $f_{\text{qnm}} \approx 3.4$ kHz for a Schwarzschild BH of $3 M_{\odot}$. In the case of a rotating BH, namely a Kerr BH, the peak frequency shifts to higher values (Detweiler 1980). Thus, the value of $f_{\text{qnm}}^{\text{BH}}$ for a non-rotating BH can be considered as a lower bound to the peak frequency.

When the merger does not lead to a BH, the merger frequency is dominated by the oscillations of a MNS. This

last frequency is of the order of

$$f_{\text{qnm}}^{\text{MNS}} \approx \frac{1}{\pi} \left(\frac{GM}{R^3} \right)^{1/2} = \frac{1}{\pi} \left(\frac{c^3}{G} \right) \frac{\mathcal{C}_{\text{MNS}}^{3/2}}{M}, \quad (12)$$

where R is the radius of the MNS and $\mathcal{C}_{\text{MNS}} \equiv GM/(c^2 R)$ is its compactness. In either case of BH or MNS formation, it is satisfied $f_{\text{qnm}} > f_{\text{contact}}$. It can be checked that the above frequency estimates are consistent with values obtained from full numerical relativity simulations (see, e.g., Rodriguez et al. 2016; Anninos et al. 1995; Bernuzzi et al. 2015a).

2.3.2. NS-BH merger

For a NS-BH merger, the approach to merger is different since general relativistic effects avoid the objects to go all the way to the “contact” point following circular orbits. For example, let us assume $m_1 = m_{\text{BH}} \approx 3 M_{\odot}$ and $m_2 = M_{\text{NS}} \approx 1.5 M_{\odot}$, so $M = 1.5 + 3.0 M_{\odot} = 4.5 M_{\odot}$. In this case $r_1 = 2Gm_{\text{BH}}/c^2$ (for a Schwarzschild BH) and $r_2 = Gm_2/(c^2 \mathcal{C}_2)$, so $r_{\text{contact}} \approx 3.3GM/c^2$. Within the test-particle limit, the LSO around a Schwarzschild BH occurs at $r_{\text{LSO}} = 6Gm_{\text{BH}}/c^2 \approx 6GM/c^2 > r_{\text{contact}}$. Taking into account finite-mass and tidal effects does not change this conclusion (on the contrary, the LSO becomes bigger; see Bernuzzi et al. 2015b). Thus, we have that $r_{\text{contact}} < r_{\text{LSO}}$ which suggests that a NS-BH binary, similar to the case of a BH-BH one, can pass from the inspiral regime, to the plunge from $r_{\text{plunge}} = r_{\text{LSO}}$ to merger at $r_{\text{merger}} \approx r_{\text{contact}}$, to the ringing of the newly formed BH. At r_{plunge} , the GW frequency is

$$f_{\text{plunge}}^{\text{NS-BH}} \approx \frac{1}{\pi} \left(\frac{GM}{r_{\text{LSO}}^3} \right)^{1/2} = \frac{1}{\pi 6^{3/2}} \left(\frac{c^3}{GM} \right), \quad (13)$$

and as in the previous case of BH formation from a NS-NS merger, the NS-BH post-merger GW spectrum will be dominated by frequencies given by Eq. (11). Namely, for the present example $f_{\text{plunge}}^{\text{NS-BH}} \approx 980$ Hz and $f_{\text{qnm}}^{\text{BH}} \approx 2.3$ kHz.

In the above analysis we have neglected the possibility that the NS can be tidally disrupted by the BH before it reaches $r = r_{\text{LSO}}$. The NS is disrupted by the

BH if $r_{\text{LSO}} < r_{\text{td}}$, where r_{td} is the tidal disruption radius. Numerical simulations of NS-BH binary mergers suggest $r_{\text{td}} \lesssim 0.45q^{-1/3}R_{\text{NS}}$ (see Shibata & Taniguchi 2011, and references therein), where $q \equiv m_2/m_1 \leq 1$ is the binary mass-ratio. To evaluate whether $r_{\text{LSO}} < r_{\text{td}}$ or $r_{\text{LSO}} > r_{\text{td}}$, we need to compute the LSO accounting for tidal effects on the NS, since they make the effective potential more attractive with respect to the point-like one (Bernuzzi et al. 2015b). From simulations of NS-BH binaries (with $m_{\text{BH}} = 3 M_{\odot}$ and for $q \leq 1$) via the effective one-body formalism at 4th post-Newtonian order including the tidal potential, we have obtained $r_{\text{LSO}} \approx 5(GM/c^2)q^{2/5}$ (Gizzi & Rueda 2016). This implies tidal disruption for values of the NS compactness $\mathcal{C}_{\text{NS}} < \mathcal{C}_{\text{NS,td}} = 0.09q^{4/15}/(1+q)$. For $1.5 + 3.0 M_{\odot}$ and $1.5 + 10.0 M_{\odot}$ ν NS-BH binaries, we have $\mathcal{C}_{\text{NS}} \approx 0.15$ and $\mathcal{C}_{\text{NS,td}} \approx 0.05$, thus tidal disruption of the NS by the BH seems to be unlikely in both cases, as we have supposed.

2.4. Characteristic strain and detectors sensitivity

From Eqs. (6) and (8) and with the knowledge of the energy released in GWs (9) and the spanned frequencies in the merger regime (see Table 2), we can estimate the characteristic strain (4) which can be compared and contrasted with the strain noise of GW detectors.

Fig. 1 shows the GW signal ASD produced by S-GRFs, S-GRBs and U-GRBs, obtained with the aid of Eq. (4). In this figure we adopt: a $(1.4+1.4) M_{\odot}$ ν NS-NS merger for S-GRFs, a $(2.0+2.0) M_{\odot}$ ν NS-NS merger for S-GRBs, a $(1.5 + 3.0) M_{\odot}$ ν NS-BH merger for U-GRBs produced by *out-states* of BdHNe, and a $(1.5 + 10.0) M_{\odot}$ ν NS-BH merger for U-GRBs produced by *out-states* of BH-SNe. We have assumed in this plot that these sources are located at the closest luminosity distance d_l at which each sub-class has been observed (see Table 2 for details). We show the noise ASD of aLIGO in the current run (O1) and in the expected 2022+ run (Abbott et al. 2016); the expected noise ASD of AdV (BNS-optimized; Abbott et al. 2016); the expected noise ASD of the space-based interferometer eLISA for the N2A1, N2A2 and N2A5 configurations (see, e.g., Klein et al. 2016); and the noise ASD of the NAUTILUS bar detector for a 1 ms GW burst (Astone et al. 2006, 2008). Narrow-band resonant bar detectors (such as ALLEGRO, AURIGA, EXPLORER, NAUTILUS and NIOBE) are sensitive within a bandwidth of ~ 1 –10 Hz around the resonant frequency which is typically $f_0 \sim 1$ kHz (see, e.g., Table 2 in Camp & Cornish 2004, for a summary of the properties of the bar detectors). The bar detector with the wider bandwidth is NAUTILUS with a minimum strain spectral noise $\sqrt{S_n} = 10^{-21} \text{ Hz}^{-1/2}$ at $f_0 = 935$ Hz and $\sqrt{S_n} \leq 10^{-20} \text{ Hz}^{-1/2}$ in a bandwidth ~ 30 Hz around f_0 (Astone et al. 2008). This implies that a 1 ms GW burst would be detected by this instrument if it has a strain amplitude $h \gtrsim 3 \times 10^{-19}$ (Astone et al. 2006, 2008).

From this figure we can conclude for the NS-NS and NS-BH binaries associated with S-GRFs, S-GRBs and U-GRBs:

1. *Before merging*: they transit, during their inspiral regime which spans the frequency range $f < f_{\text{merger}}/(1+z)$ (see in Table 2 the frequencies and redshift), first the eLISA frequency band to then enter the aLIGO and AdV ones in the final orbits

prior the merging process (when $P_{\text{orb}} < 0.2$ s). The narrow bandwidth of the bar detectors does not cover these frequencies. For the adopted distances we see that the characteristic strain generated by all these sources is below the sensitivity of eLISA. S-GRFs are below the sensitivity of aLIGO (O1), AdV and NAUTILUS, but inside the sensitivity of aLIGO (2022+). S-GRBs are below the sensitivity of aLIGO (all runs), AdV and NAUTILUS. U-GRBs from *out-states* of BdHNe are below the sensitivity of aLIGO (O1), AdV and NAUTILUS, but inside the sensitivity of aLIGO (2022+). U-GRBs from *out-states* of BH-SNe are below the sensitivity of aLIGO (O1) and NAUTILUS, inside the sensitivity of aLIGO (2022+), and marginally inside the sensitivity of AdV.

2. *Merging*: the merging regime, which expands frequencies from $f_{\text{contact}}/(1+z)$ to $f_{\text{qnm}}/(1+z)$ (see in Table 2 the frequencies and redshift), is outside the eLISA frequency band but inside the aLIGO, AdV and bar detectors ones. The characteristic strain in this final merger phase $h \sim 10^{-24}$ – 10^{-23} is, unfortunately, well below the sensitivity of all of them (see also Kobayashi & Mészáros 2003 for similar conclusions for aLIGO).

From the above it can be seen that the most interesting instrument for the possible detection of the GW emission from binaries associated with GRBs is aLIGO. Therefore, we estimate in the next section the expected detection rates by aLIGO (see Fig. 2 and Table 3).

3. GW DETECTION RATE

We assume a threshold for the aLIGO single detector $\rho_0 = 8$ (Abbott et al. 2016). This minimum ρ_0 defines a maximum detection distance or GW horizon distance, which is denoted as d_{GW} . This horizon corresponds to the most optimistic case when the binary is just above the detector and the binary plane is parallel to the detector plane, i.e. $\theta = \phi = \iota = 0$ (Allen et al. 2012):

$$d_{\text{GW}} = \frac{2A}{\rho_0} \left(\int_0^{\infty} \frac{f^{-7/3}}{S_n(f)} df \right)^{1/2}, \quad (14)$$

where $A = 5/(24\pi^{4/3})^{1/2}(GM_{\odot}/c^3)^{5/6}c$. We show in Table 2 GW horizon for S-GRFs, S-GRBs and U-GRBs. Since not all the sources are optimally aligned with the detector, the number of detected sources inside a sphere of radius d_{GW} will be a fraction \mathcal{F}^3 of the total. This fraction determines the range of the detector $\mathcal{R} = \mathcal{F}d_{\text{GW}}$, with $\mathcal{F}^{-1} = 2.2627$ (Finn & Chernoff 1993). In order to give an estimate of the annual number of detectable binaries associated with GRBs we use the *search volume* as computed in (Abbott et al. 2016), $\mathcal{V}_s = V_{\text{max}}^{\text{GW}}\mathcal{T}$, where $V_{\text{max}}^{\text{GW}} = (4\pi/3)\mathcal{R}^3$ and \mathcal{T} is the observing time. We use here the lower and upper values of \mathcal{V}_s for a $(1.4+1.4) M_{\odot}$ NS binary for the different observational campaigns reported in (Abbott et al. 2016): 2015/2016 (O1) with $\mathcal{T} = 3$ months, $\mathcal{V}_s = (0.5\text{--}4) \times 10^5 \text{ Mpc}^3 \text{ yr}$, 2017/2018 (O3) with $\mathcal{T} = 9$ months, $\mathcal{V}_s = (3\text{--}10) \times 10^6 \text{ Mpc}^3 \text{ yr}$, and the one by the entire network including LIGO-India at design sensitivity (2022+) with $\mathcal{T} = 1$ yr, $\mathcal{V}_s = 2 \times 10^7 \text{ Mpc}^3 \text{ yr}$. The

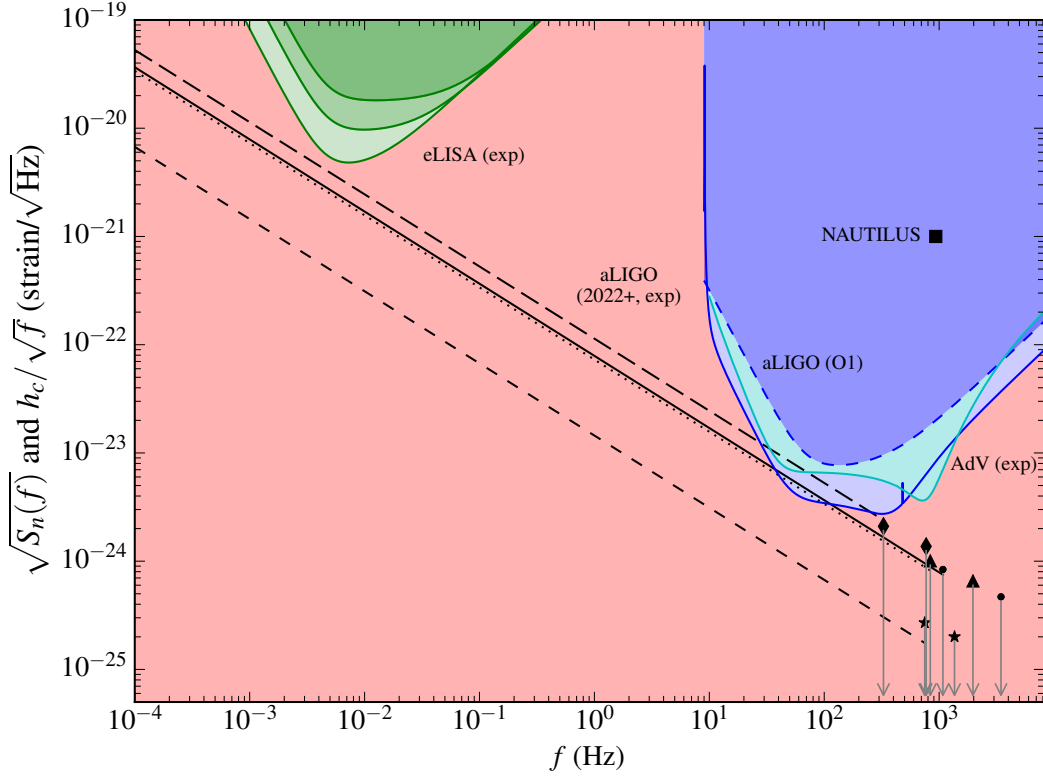


Figure 1. Comparison of the signal's ASD h_c/\sqrt{f} of S-GRFs, S-GRBs and U-GRBs with the noise's ASD $\sqrt{S_n(f)}$, where S_n is the power spectrum density of the detector's noise of eLISA, of aLIGO and of the bar detector NAUTILUS. The green lines, from top to bottom, are the expected noise's ASD of the N2A1, N2A2 and N2A5 configurations of eLISA (Klein et al. 2016). The dashed and continuous blue lines correspond to the noise's ASD respectively of aLIGO O1 run (2015/2016) and of the expected aLIGO 2022+ run (Abbott et al. 2016), and the cyan line is the expected noise's ASD of AdV (BNS-optimized; Abbott et al. 2016). The filled square indicates the noise's ASD of the NAUTILUS resonant bar for a 1 ms GW burst (Astone et al. 2006, 2008). The red filled area indicates the region of undetectability by any of the above instruments. We recall that in this plot the GW frequency is redshifted by a factor $1+z$ with respect to the source frame value, i.e. $f = f_s/(1+z)$, for which we use the cosmological redshift and corresponding luminosity distance of the closest observed source of each sub-class (see Table 2). The following three curves correspond to the inspiral regime of the coalescence: S-GRFs with $(1.4 + 1.4) M_\odot$ (solid curve), S-GRBs with $(2.0 + 2.0) M_\odot$ (short-dashed curve), U-GRB with $(1.5 + 3.0) M_\odot$ (dotted curve) from *out-states* of BdHNe, and U-GRB with $(1.5 + 10.0) M_\odot$ (long dashed curve) from *out-states* of BH-SNe. The dot, star, triangle and diamond correspond to h_c in the merger regime for S-GRFs, S-GRBs, U-GRBs from *out-states* of BdHNe, and U-GRBs from *out-states* of BH-SNe, respectively. The first point is located at $f_{\text{merger}}/(1+z)$ and the second at $f_{\text{qnm}}/(1+z)$ (see Table 2). The down-arrows indicate that these estimates have to be considered as upper limits since we have assumed that all the energy release in the system goes in GWs, which clearly overestimates the GW energy output in view of the dominance of the electromagnetic emission (see Table 3). We have also overestimated the GW energy in the merger regime by using Eq. (9) which is the expected GW energy emitted in the plunge+merger+ringdown phases of a BH-BH merger. For binary mergers involving NSs, as we have discussed in Sec. 2.3, the energy released in GWs must be necessarily lower than this value.

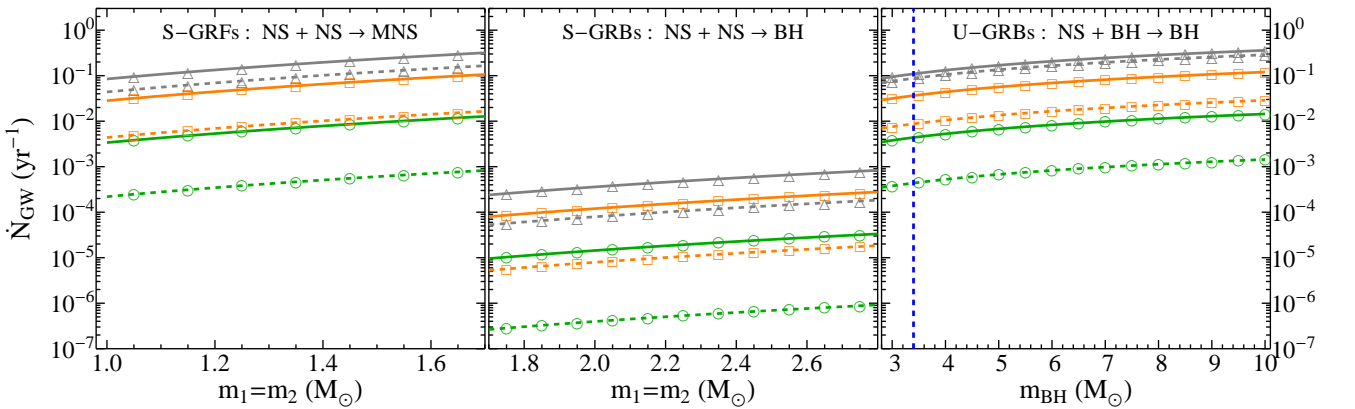


Figure 2. Expected annual GW upper and lower bounds (the solid and the dashed lines, respectively) for the detections expected from S-GRFs (left panel), S-GRBs (middle panel), and U-GRBs (right panel), for three selected observational campaigns: 2015/2016 (O1: green curves with circles), 2017/2018 (O3: orange curve with squares), and 2022+ (gray curve with triangles). The vertical blue dashed line in the plot of U-GRBs separates ν NS-BH binaries produced by BdHN (BH masses equal to the NS critical mass) and BH-SN (BH masses larger than the NS critical mass).

Table 3

Column 1: GRB sub-class. Column 2: inferred number of GRBs per year in the entire Universe, \dot{N}_{GRB} , for each GRB sub-class (see also Fig. 6 in Ruffini et al. 2016). Column 3: number of GRBs observed per year, $\dot{N}_{\text{GRB}}^{\text{obs}}$, obtained from the observations of γ -ray telescopes such as AGILE, BATSE, BeppoSAX, *Fermi*, *HETE-II*, *INTEGRAL*, Konus/WIND and *Swift*, in the indicated years of observations (see also Tables 2–6 in Ruffini et al. 2016). Column 4: expected rate of GW detections by aLIGO of all the GRB sub-classes, computed for three selected observational campaigns: 2015/2016 (O1), 2017/2018 (O3) and the one by the entire network including LIGO-India at design sensitivity, 2022+. The typical masses used here are the same of Table 2.

GRB sub-class	\dot{N}_{GRB} (yr ⁻¹)	$\dot{N}_{\text{GRB}}^{\text{obs}}$ (yr ⁻¹)	\dot{N}_{GW} (yr ⁻¹)
XRFs	144–733	1 (1997–2014)	undetectable
BdHNe	662–1120	14 (1997–2014)	undetectable
BH-SN	\lesssim 662–1120	\lesssim 14 (1997–2014)	undetectable
S-GRFs	58–248	3 (2005–2014)	O1: $(0.4\text{--}8)\times 10^{-3}$ O3: 0.011–0.065 2022+: 0.1–0.2
S-GRBs	2–8	1 (2006–2014)	O1: $(0.4\text{--}8)\times 10^{-6}$ O3: $(0.08\text{--}1.2)\times 10^{-4}$ 2022+: $(0.8\text{--}3.6)\times 10^{-4}$
U-GRBs	662–1120	–	O1: $(0.36\text{--}3.6)\times 10^{-3}$ O3: 0.008–0.032 2022+: 0.076–0.095
U-GRBs (BH-SN)	\lesssim 662–1120	–	O1: 0.0016–0.016 O3: \lesssim 0.029–0.12 2022+: \lesssim 0.3–0.36
GRFs	29–153	1 (2005–2014)	undetectable

maximum possible sensitivity reachable in 2022+ leads to $d_{\text{GW}} \approx 0.2$ Gpc, hence $V_{\text{max}}^{\text{GW}} \approx 0.033$ Gpc³, for such a binary. We can use this information for a (1.4+1.4) M_{\odot} binary and extrapolate it to other binaries with different masses since the d_{GW} scales with the chirp mass as $M_c^{5/6}$ (see Fig. 2).

From the inferred occurrence rates ρ_{GRB} (not to be confused with signal-to-noise ratio ρ) summarized in Table 1, we show in Fig. 2 the expected number of GW detections by aLIGO

$$\dot{N}_{\text{GW}} = \rho_{\text{GRB}} V_{\text{max}}^{\text{GW}}, \quad (15)$$

for S-GRFs, S-GRBs, and U-GRBs.

We compare and contrast in Table 3 for the GRB subclasses: the expected GW detection rate by aLIGO given by Eq. (15), \dot{N}_{GW} , the inferred occurrence rate of GRBs, \dot{N}_{GRB} , and the observed GRB rate from γ -ray telescopes (AGILE, BATSE, BeppoSAX, *Fermi*, *HETE-II*, *INTEGRAL*, Konus/WIND and *Swift*), simply estimated as $\dot{N}_{\text{GRB}}^{\text{obs}} = N_{\text{GRB}}^{\text{obs}}/T_{\text{obs}}$ where $N_{\text{GRB}}^{\text{obs}}$ is the number of GRBs detected in the observing time T_{obs} . The rate \dot{N}_{GRB} is obtained from the GRB specific rate through the reconstruction of the GRB luminosity function and the study of its evolution with the redshift (see Ruffini et al. 2016, for details). This estimate, therefore, is larger than $\dot{N}_{\text{GRB}}^{\text{obs}}$ which is limited to those events beyond the detector sensitivity threshold, falling inside its field of view and within its operational time.

4. CONCLUSIONS

Short and long GRBs have been divided into 7 subclasses according to their binary nature (Ruffini et al. 2016). We summarize in Table 1 their main physical properties characterizing the outcome of X-rays, gamma-rays, high-energy and ultra high-energy detectors, as well as their occurrence rate. Particularly important for the present work is the specification of the *in-states* and *out-states* of the GRB progenitors.

With the knowledge of the nature of the compact object binaries associated with each GRB sub-class, we describe in Sec. 2 the general properties of the GW emission during the inspiral and merger regimes of these binaries. We argue that S-GRFs, S-GRBs and U-GRBs are the GRB sub-classes relevant for the GW analysis. It is manifest that the release of the gravitational energy gain of the system in the merger phase is dominated by the X-rays, gamma-rays and GeV emission (see Table 1). In order to evaluate the GW emission we have made in this work the drastic gedanken assumption that the binary evolution is only driven by GW emission. This assumption is of interest with the only aim of establishing an absolute upper limit and to check the detectability of the GW emission under this most optimistic condition. We compare and contrast in Sec. 2.4 the GW characteristic strain amplitude produced by the inspiral and merger regimes with the strain noise of the broadband detectors eLISA, aLIGO and AdV as well as of the narrow-band resonant bar NAUTILUS. In order to do this we use the cosmological redshift and corresponding luminosity distance of the closest observed source of each sub-class (see Table 2). We show that the inspiral regime is possibly detectable only by aLIGO (see Table 2 and Fig. 1) and

the merger regime is undetectable by any of these instruments.

Therefore, in Sec. 3 we assess quantitatively the GW detectability of the inspiral regime of S-GRFs, S-GRBs and U-GRBs only by aLIGO. We recall that, following (Abbott et al. 2016), we adopt as the threshold for detectability a signal-to-noise ratio equal to 8. We present in Fig. 2 and Table 3 the expected detection rate of the gedanken GW emission. Three observational campaigns of aLIGO are analyzed: O1 (2015/2016), O3 (2017/2018), and 2022+ namely the one by the entire network including LIGO-India at design sensitivity. In Table 3 we compare and contrast this rate with the occurrence rate of the GRB sub-classes and their rate of observations by γ -ray telescopes.

Keeping the above in mind, we conclude for each GRB sub-class:

- I. **XRFs:** their ν NS-NS *out-states* transit, during the inspiral regime which spans the frequency range $f < f_{\text{merger}}/(1+z)$ (see Table 2), first the eLISA frequency band to then enter the aLIGO and AdV ones in the final orbits prior to the merging process (i.e. when $P_{\text{orb}} < 0.2$ s). Resonant bar detectors are not sensitive in this inspiral regime frequency range. The characteristic strain generated by these sources in the inspiral regime is below the sensitivity of eLISA. The merger regime, which expands frequencies from $f_{\text{contact}}/(1+z)$ to $f_{\text{qnm}}/(1+z)$ (see Table 2), is outside the eLISA frequency band but inside the frequency band of aLIGO, AdV and bar detectors. See Fig. 1 for details. These ν NS-NS mergers can lead either to S-GRFs or S-GRBs (see in IV and V below the conclusion about their GW detectability).
- II. **BdHNe:** their ν NS-BH *out-states* transit, during the inspiral regime which spans the frequency range $f < f_{\text{merger}}/(1+z)$ (see Table 2), first the eLISA frequency band to then enter the aLIGO and AdV ones in the final orbits prior to the merging process (i.e. when $P_{\text{orb}} < 0.2$ s). Resonant bar detectors are not sensitive in this inspiral regime frequency range. The characteristic strain generated by these sources in the inspiral regime is below the sensitivity of eLISA. The merger regime, which expands frequencies from $f_{\text{contact}}/(1+z)$ to $f_{\text{qnm}}/(1+z)$ (see Table 2), is outside the eLISA frequency band but inside the frequency band of aLIGO, AdV and bar detectors. See Fig. 1 for details. These ν NS-BH mergers lead to U-GRBs (see in VI below the conclusion about their GW detectability).
- III. **BH-SN:** their ν NS-BH *out-states* transit, during the inspiral regime which spans the frequency range $f < f_{\text{merger}}/(1+z)$ (see Table 2), first the eLISA frequency band to then enter the aLIGO and AdV ones in the final orbits prior to the merging process (i.e. when $P_{\text{orb}} < 0.2$ s). Resonant bar detectors are not sensitive in this inspiral regime frequency range. The characteristic strain generated by these sources in the inspiral regime is below the sensitivity of eLISA. The merger regime, which expands frequencies from $f_{\text{contact}}/(1+z)$ to $f_{\text{qnm}}/(1+z)$ (see Table 2), is outside the eLISA frequency band

but inside the frequency band of aLIGO, AdV and bar detectors. See Fig. 1 for details. These ν NS-BH mergers lead to U-GRBs (see in VI below the conclusion about their GW detectability).

IV. **S-GRFs:** the final orbits of the inspiral regime (when $P_{\text{orb}} < 0.2$ s) fall inside the frequency band of aLIGO, AdV and bar detectors. However, the gedanken GW energy output in the merger regime leads to a characteristic strain which is not sufficient to be detectable either by any of them. See Fig. 1 for details. The inspiral regime is detectable for sources located at distances smaller than 168 Mpc for the O1 aLIGO run and smaller than 476 Mpc for the 2022+ run (see Table 2). The closest S-GRF observed up to now is, however, located at 509 Mpc. See Table 3 for the gedanken GW detection rate.

V. **S-GRBs:** the final orbits of the inspiral regime (when $P_{\text{orb}} < 0.2$ s) fall inside the frequency band of aLIGO, AdV and bar detectors. However, the gedanken GW energy output in the merger regime leads to a characteristic strain which is not sufficient to be detectable either by any of them. See Fig. 1 for details. The inspiral regime is detectable for sources located at distances smaller than 227 Mpc for the O1 aLIGO run and smaller than 640 Mpc for the 2022+ run (see Table 2). The closest S-GRB observed up to now is, however, located at 5842 Mpc. See Table 3 for the gedanken GW detection rate.

VI. **U-GRBs:** the final orbits of the inspiral regime (when $P_{\text{orb}} < 0.2$ s) fall inside the frequency band of aLIGO, AdV and bar detectors. However, the gedanken GW energy output in the merger regime leads to a characteristic strain which is not sufficient to be detectable either by any of them. See Fig. 1 for details. In the case of U-GRBs originating from the BdHN *out-states*, the inspiral regime is detectable for sources located at distances smaller than 235 Mpc for the O1 aLIGO run and smaller than 666 Mpc for the 2022+ run (see Table 2). In the case of U-GRBs originating from the BH-SN *out-states*, the inspiral regime is detectable for sources at distances smaller than 362 Mpc for the O1 aLIGO run and smaller than 1023 Mpc for the 2022+ run (see Table 2). No U-GRB has yet been electromagnetically identified. The closest distance at which is located its possible progenitor, namely a BdHN, is 805 Mpc. See Table 3 for the gedanken GW detection rate.

VII. **GRFs:** The tidal disruption of the WD by the NS produces a not detectable GW emission (see, e.g., Paschalidis et al. 2009).

The most favorable case for the gedanken GW detection by aLIGO, with a rate of $\dot{N}_{\text{GW}} = 0.1\text{--}0.2 \text{ yr}^{-1}$, is that of S-GRFs (see Table 3). In such systems however no BH is formed. The merger of the two NSs will instead lead to a MNS. Among those producing a BH, the most favorable cases are that of U-GRBs from BdHNe with a gedanken rate $\dot{N}_{\text{GW}} = 0.076\text{--}0.095 \text{ yr}^{-1}$ and those from

BH-SN with $\dot{N}_{\text{GW}} = 0.3\text{--}0.36 \text{ yr}^{-1}$ (see Table 3). Realistic \dot{N}_{GW} values will need the assessment of the GW to electromagnetic energy ratio which is necessarily smaller than unity from energy conservation.

ACKNOWLEDGMENTS

J.A.R. acknowledges the support by the International Cooperation Program CAPES-ICRANet financed by CAPES-Brazilian Federal Agency for Support and Evaluation of Graduate Education within the Ministry of Education of Brazil. M.K. and F.G.O. acknowledge the support given by the International Relativistic Astrophysics Erasmus Mundus Joint Doctorate Program under the Grants 2013–1471 and 2012–1710, respectively, from EACEA of the European Commission. M.M. and J.A.R. acknowledge partial support of the project No. 3101/GF4 IPC-11/2015, and the target program of the Ministry of Education and Science of the Republic of Kazakhstan. C.C. and S.F. acknowledge INdAM-GNFM for support.

REFERENCES

- Abbott, B. P., Abbott, R., Abbott, T. D., et al. 2016, *Living Reviews in Relativity*, 19, arXiv:1304.0670
- Allen, B., Anderson, W. G., Brady, P. R., Brown, D. A., & Creighton, J. D. E. 2012, *Phys. Rev. D*, 85, 122006
- Anninos, P., Hobill, D., Seidel, E., Smarr, L., & Suen, W.-M. 1995, *Phys. Rev. D*, 52, 2044
- Astone, P., Ballantini, R., Babusci, D., et al. 2006, *Classical and Quantum Gravity*, 23, S57
- . 2008, *Classical and Quantum Gravity*, 25, 114048
- Becerra, L., Bianco, C. L., Fryer, C. L., Rueda, J. A., & Ruffini, R. 2016, *ArXiv e-prints*, arXiv:1606.02523
- Becerra, L., Cipelletta, F., Fryer, C. L., Rueda, J. A., & Ruffini, R. 2015, *ApJ*, 812, 100
- Belvedere, R., Boshkayev, K., Rueda, J. A., & Ruffini, R. 2014, *Nucl. Phys. A*, 921, 33
- Berger, E. 2014, *ARA&A*, 52, 43
- Bernuzzi, S., Dietrich, T., & Nagar, A. 2015a, *Phys. Rev. Lett.*, 115, 091101
- Bernuzzi, S., Nagar, A., Dietrich, T., & Damour, T. 2015b, *Phys. Rev. Lett.*, 114, 161103
- Bildsten, L., & Cutler, C. 1992, *ApJ*, 400, 175
- Cadelano, M., Pallanca, C., Ferraro, F. R., et al. 2015, *ApJ*, 812, 63
- Camp, J. B., & Cornish, N. J. 2004, *Annual Review of Nuclear and Particle Science*, 54, 525
- Cipelletta, F., Cherubini, C., Filippi, S., Rueda, J. A., & Ruffini, R. 2015, *Phys. Rev. D*, 92, 023007
- Davis, M., Ruffini, R., Press, W. H., & Price, R. H. 1971, *Phys. Rev. Lett.*, 27, 1466
- Davis, M., Ruffini, R., & Tiomno, J. 1972, *Phys. Rev. D*, 5, 2932
- Detweiler, S. 1980, *ApJ*, 239, 292
- Detweiler, S. L., & Szedenits, Jr., E. 1979, *ApJ*, 231, 211
- Eichler, D., Livio, M., Piran, T., & Schramm, D. N. 1989, *Nature*, 340, 126
- Finn, L. S., & Chernoff, D. F. 1993, *Phys. Rev. D*, 47, 2198
- Flanagan, É. É., & Hughes, S. A. 1998, *Phys. Rev. D*, 57, 4535
- Fryer, C. L., Oliveira, F. G., Rueda, J. A., & Ruffini, R. 2015, *Phys. Rev. Lett.*, 115, 231102
- Fryer, C. L., Rueda, J. A., & Ruffini, R. 2014, *ApJ*, 793, L36
- Giacconi, R., & Ruffini, R., eds. 1978, *Physics and astrophysics of neutron stars and black holes*
- Gizzi, D., & Rueda, J. A. 2016, to be submitted
- Goodman, J. 1986, *ApJ*, 308, L47
- Guetta, D., & Della Valle, M. 2007, *ApJ*, 657, L73
- Guetta, D., Pian, E., & Waxman, E. 2011, *A&A*, 525, A53
- Izzo, L., Rueda, J. A., & Ruffini, R. 2012, *A&A*, 548, L5
- Kawaguchi, K., Kyutoku, K., Nakano, H., et al. 2015, *Phys. Rev. D*, 92, 024014
- Klein, A., Barausse, E., Sesana, A., et al. 2016, *Phys. Rev. D*, 93, 024003
- Kobayashi, S., & Mészáros, P. 2003, *ApJ*, 589, 861
- Kovacevic, M., Izzo, L., Wang, Y., et al. 2014, *A&A*, 569, A108
- Landau, L. D., & Lifshitz, E. M. 1975, *The Classical Theory of Fields* (Oxford: Pergamon Press)

- Lazarus, P., Tauris, T. M., Knispel, B., et al. 2014, *MNRAS*, 437, 1485
- Lee, W. H., Ramirez-Ruiz, E., & Page, D. 2004, *ApJ*, 608, L5
- Liang, E., Zhang, B., Virgili, F., & Dai, Z. G. 2007, *ApJ*, 662, 1111
- LIGO Scientific Collaboration, Aasi, J., Abbott, B. P., et al. 2015, *Classical and Quantum Gravity*, 32, 074001
- Maggiore, M. 2007, *Gravitational Waves. Vol. 1: Theory and Experiments* (Oxford University Press)
- Meszaros, P., & Rees, M. J. 1997, *ApJ*, 482, L29
- Mirabel, I. F., & Rodríguez, L. F. 1998, *Nature*, 392, 673
- Nagar, A., Damour, T., & Tartaglia, A. 2007, *Classical Quantum Gravity*, 24, S109
- Narayan, R., Piran, T., & Shemi, A. 1991, *ApJ*, 379, L17
- Paczynski, B. 1986, *ApJ*, 308, L43
- Paschalidis, V., MacLeod, M., Baumgarte, T. W., & Shapiro, S. L. 2009, *Phys. Rev. D*, 80, 024006
- Peters, P. C. 1964, *Phys. Rev.*, 136, 1224
- Peters, P. C., & Mathews, J. 1963, *Phys. Rev.*, 131, 435
- Rangel Lemos, L. J., Bianco, C. L., Mosquera Cuesta, H. J., Rueda, J. A., & Ruffini, R. 2010, in *25th Texas Symposium on Relativistic Astrophysics*, 204
- Rees, M., Ruffini, R., & Wheeler, J. A. 1974, *Black holes, gravitational waves and cosmology* (New York: Gordon and Breach Science Publishers Inc.)
- Rhoades, C. E., & Ruffini, R. 1974, *Physical Review Letters*, 32, 324
- Rigault, M., Aldering, G., Kowalski, M., et al. 2015, *ApJ*, 802, 20
- Rodríguez, J. F., Rueda, J. A., & Ruffini, R. 2016, *ArXiv e-prints*, arXiv:1605.07609
- Rosswog, S., Ramirez-Ruiz, E., & Davies, M. B. 2003, *MNRAS*, 345, 1077
- Rueda, J. A., & Ruffini, R. 2012, *ApJ*, 758, L7
- Ruffini, R., Bernardini, M. G., Bianco, C. L., et al. 2006, in *The Tenth Marcel Grossmann Meeting*, ed. M. Novello, S. Perez Bergliaffa, & R. Ruffini (Singapore: World Scientific), 369
- Ruffini, R., Bernardini, M. G., & Bianco et al., C. L. 2008, in *The Eleventh Marcel Grossmann Meeting*, ed. H. Kleinert, R. T. Jantzen, & R. Ruffini, 368–505
- Ruffini, R., Bianco, C. L., Fraschetti, F., Xue, S.-S., & Chardonnet, P. 2001, *ApJ*, 555, L117
- Ruffini, R., Bernardini, M. G., Bianco, C. L., et al. 2007, in *ESA Special Publication*, Vol. 622, *ESA Special Publication*, 561
- Ruffini, R., Wang, Y., Enderli, M., et al. 2015a, *ApJ*, 798, 10
- Ruffini, R., Muccino, M., Kovacevic, M., et al. 2015b, *ApJ*, 808, 190
- Ruffini, R., Rueda, J. A., Muccino, M., et al. 2016, *ArXiv e-prints*, arXiv:1602.02732
- Shibata, M., & Taniguchi, K. 2011, *Living Rev. Relat.*, 14
- Soderberg, A. M., Kulkarni, S. R., Nakar, E., et al. 2006, *Nature*, 442, 1014
- Sun, H., Zhang, B., & Li, Z. 2015, *ApJ*, 812, 33
- Tauris, T. M., van den Heuvel, E. P. J., & Savonije, G. J. 2000, *ApJ*, 530, L93
- Tauris, T. M., Kaspi, V. M., Breton, R. P., et al. 2015, *Advancing Astrophysics with the Square Kilometre Array (AASKA14)*, 39
- Virgili, F. J., Liang, E.-W., & Zhang, B. 2009, *MNRAS*, 392, 91
- Virgili, F. J., Zhang, B., O'Brien, P., & Troja, E. 2011, *ApJ*, 727, 109
- Wanderman, D., & Piran, T. 2010, *MNRAS*, 406, 1944
- . 2015, *MNRAS*, 448, 3026

What can we really infer from GW 150914?

J. F. Rodriguez,^{1,2} J. A. Rueda,^{1,2,3} R. Ruffini^{1,2,3}

¹*Dipartimento di Fisica and ICRA, Sapienza Università di Roma, P.le Aldo Moro 5, I-00185 Rome, Italy*

²*ICRANet, Piazza della Repubblica 10, I-65122 Pescara, Italy and*

³*ICRANet-Rio, CBPF, Rua Dr. Xavier Sigaud 150, Rio de Janeiro, RJ, 22290-180, Brazil*

(Dated: May 26, 2016)

In a recent letter we have outlined some issues on GW 150914, we hereby give additional details. We analyze the event GW 150914 announced by the Advanced Laser Interferometer Gravitational-Wave Observatory (LIGO) as the gravitational-wave emission of a black-hole binary merger. We show that the parameters of the coalescing system and of the newly formed Kerr black-hole can be extracted from basic results of the gravitational-wave emission during the inspiraling and merger phases without sophisticated numerical simulations. Our strikingly accurate estimates are based on textbook formulas describing two different regimes: 1) the binary inspiraling analysis treated in Landau and Lifshitz textbook, 2) the plunge of a particle into a black-hole, treated in the Rees-Ruffini-Wheeler textbook as well as 3) the transition between these two regimes following Detweiler's treatment of a particle infalling with non-zero angular momentum onto a black-hole. It is stressed that in order to infer any astrophysical information on the masses of the system both regimes have to be independently and observationally constrained by LIGO, which does not appear to be the case.

Keywords: Gravitational-Waves

I. INTRODUCTION

In a recent letter [1], we have pointed out some issues related to GW 150914, the recently announced gravitational-wave signal by the Advanced Laser Interferometer Gravitational-Wave Observatory (LIGO) [2]. We give in this work additional details.

By using numerical relativity templates of the gravitational-wave emission of black-hole binary mergers, the LIGO-Collaboration concluded that the signal, which lasts 0.2 s with increasing gravitational-wave frequency from 35 to ~ 150 Hz, was emitted during the inspiral and merger of a black-hole binary system, followed by the subsequent ringdown of the newly formed black-hole. The binary black-hole parameters obtained from this analysis are: $m_{\text{BH},1} = 36_{-4}^{+5} M_{\odot}$, $m_{\text{BH},2} = 29_{-4}^{+4} M_{\odot}$, and a luminosity distance to the source $d_L = 410_{-180}^{+160}$ Mpc (cosmological redshift $z = 0.09_{-0.04}^{+0.03}$), adopting a flat Λ -cold-dark-matter cosmology with Hubble parameter $H_0 = 67.9 \text{ km s}^{-1} \text{ Mpc}^{-1}$, and matter and dark-energy density parameter $\Omega_m = 0.306$ and $\Omega_{\Lambda} = 0.694$, respectively. The mass and spin parameter of the newly formed black-hole are $m_{\text{BH}} = 62_{-4}^{+4} M_{\odot}$ and $\alpha \equiv cJ_{\text{BH}}/(Gm_{\text{BH}}^2) = 0.67_{-0.07}^{+0.05}$, respectively, being J_{BH} the black-hole angular momentum.

There are two markedly different regimes in the evolution of coalescing binary black-holes: I) the quasi-circular inspiraling phase and II) the final plunge, merger and subsequent ringdown of the newly formed black-hole. We show in this work that the general features of this system can be inferred from a simple analysis of the gravitational-wave signal on the light of the foundations of the gravitational-wave theory and from three classic results: 1) the analysis of the inspiraling phase of a binary system of point-like particles (regime I, see [3]), 2)

the plunge, merger and ringdown analysis based on the approximation of a test-particle falling into a black-hole (regime II, see [4, 5] as well as [6] and appendices therein), and 3) the transition from regime I to regime II based on the approximation of a test-particle falling with non-zero angular momentum into a black-hole [7, 8]. Our treatment evidences that, for the validity of the binary interpretation, it is essential that both regime I and regime II be independently constrained by observations with comparable accuracy.

II. REGIME I: THE INSPIRAL PHASE

The presence of a binary system is the first fundamental assumption to be confirmed by observational data. A binary system, by emitting gravitational-waves, evolves first through what we call here regime I, namely the inspiral phase in which the binary follows quasi-circular orbits. The gravitational-wave energy spectrum in this phase can be estimated from the traditional formula of the quadrupole emission within the classic point-like approximation [3, 6, 9, 10]

$$\frac{dE}{df} = \frac{1}{3}(\pi G)^{2/3} \nu M^{5/3} f^{-1/3}, \quad (1)$$

where $\nu \equiv \mu/M$ is the so-called symmetric mass-ratio parameter, with $\mu = m_1 m_2 / M$ the binary reduced mass, $M = m_1 + m_2$ the total binary mass, and f is the gravitational-wave frequency. We recall that $f = 2f_{\text{orb}}$, where f_{orb} is the orbital frequency, i.e. $f_{\text{orb}} = \omega_{\text{orb}} / (2\pi) = \sqrt{GM/r^3} / (2\pi)$ and r the binary separation distance. We recall that the quantity $M_{\text{chirp}} \equiv \nu^{3/5} M$ is referred to in the literature as the binary chirp mass.

A. Analysis of GW 150914

In order to extract information from the signal related to the regime I it is necessary to make an analysis of the frequency evolution with time since, within this approximation, the binary chirp mass is given by:

$$M_{\text{chirp}} = \frac{c^3}{G} \left(\frac{5}{96\pi^{8/3}} \frac{\dot{f}}{f^{11/3}} \right)^{3/5}. \quad (2)$$

We fit the evolution of the frequency with time in GW 150914 which leads to $M_{\text{chirp}}^{\text{obs}} \approx 30.5 M_{\odot}$, in agreement with the LIGO analysis, $M_{\text{chirp}}^{\text{obs}} = 30.2_{-1.9}^{+2.5} M_{\odot}$, in the detector-frame [11]. We recall that the total mass in the source-frame is $M = M_{\text{obs}}/(1+z)$.

From the definition of chirp mass it follows that the total mass of the system is $M = M_{\text{chirp}}/\nu^{3/5}$. Thus, since $0 < \nu \leq 1/4$, the above value of the chirp mass implies for the total mass a range $70.07 \lesssim M_{\text{obs}}/M_{\odot} < \infty$ in the detector-frame.

When the conservative quasi-circular dynamics following the classic point-like approximation breaks down, the regime II, namely the final plunge, merger and ringdown of the newly formed object, sets in (see section III). We denote the gravitational-wave frequency at which the quasi-circular evolution ends as the plunge starting frequency, f_{plunge} . We adopt here as an estimate that of the last stable orbit (LSO) of a test-particle around a Schwarzschild black-hole:

$$f_{\text{plunge}} \approx f_{\text{LSO}} = \frac{c^3}{G} \frac{1}{6^{3/2}\pi M} \approx 4.4 \frac{M_{\odot}}{M} \text{ kHz}. \quad (3)$$

Thus, the total energy radiated during regime I can be estimated from the binding energy of the LSO which, by extrapolation to the case of a binary of comparable masses, reads

$$\Delta E_{\text{inspiral}} = (1 - \sqrt{8/9})\mu c^2 = (1 - \sqrt{8/9})\nu^{2/5} M_{\text{chirp}} c^2, \quad (4)$$

which for the above value of the chirp mass implies a range $0 < \Delta E_{\text{inspiral}} \lesssim M_{\odot} c^2/(1+z)$.

III. REGIME II: PLUNGE, MERGER AND RINGDOWN

After the regime I of quasi-circular inspiral evolution, it starts the regime II composed by the plunge, merger and ringdown, as first analyzed in Ref. [4, 5] for a test-particle falling radially into a Schwarzschild black-hole. It was shown in Refs. [4, 5] that the gravitational-wave spectrum in this regime II is dominated by the $l = 2$ multipole (quadrupole) emission and that the largest gravitational-wave emission occurs from $r \approx 3GM/c^2$, at the maximum

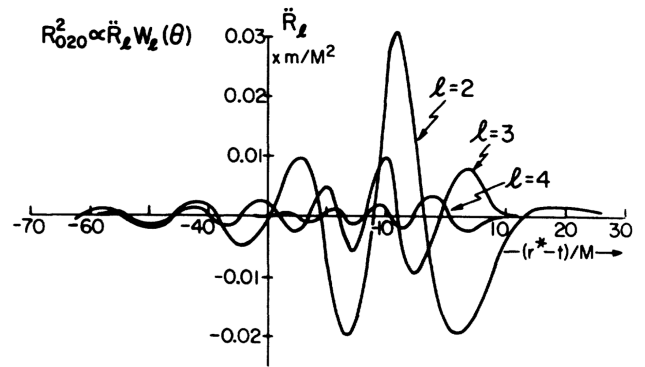


FIG. 1. \ddot{R}_l factors of the Riemann tensor components as a function of the retarded time for $l = 2, 3, 4$. Figure reproduced from Ref. [5] with kind permission of the authors.

of the effective potential

$$V_l(r) = \left(1 - \frac{2m_{\text{BH}}}{r} \right) \times \left[\frac{2\lambda^2(\lambda+1)r^3 + 6\lambda^2 m_{\text{BH}} r^2 + 18\lambda m_{\text{BH}}^2 r + 18m_{\text{BH}}^3}{r^3(\lambda r + 3m_{\text{BH}})^2} \right] \quad (5)$$

where $\lambda = (l-1)(l+2)/2$, and the black-hole horizon. It was there shown that in the limit of large l , the contribution of each multipole to the spectrum peaks at the gravitational-wave frequency

$$f_{\text{peak}}^l = \frac{c^3}{G} \sqrt{(V_l)_{\text{max}}} \approx \frac{c^3}{G} \frac{l}{2\pi\sqrt{27}M}, \quad (6)$$

while the total spectrum obtained by summing over all the multipoles peaks at

$$f_{\text{peak}} \approx \frac{c^3}{G} \frac{0.05}{M} \approx 10.36 \frac{M_{\odot}}{M} \text{ kHz}. \quad (7)$$

The signature of the particle infalling is imprinted in the multipolar structure of the signal. The asymptotic expression of the tide-producing components of the Riemann tensor are [5]: $R_{020}^2(r^*, t) = \sum_l \ddot{R}_l(r^*, t) W_l(\theta) / (\sqrt[2]{2}r)$, where the angular dependence factor is $W_l(\theta) = (\partial^2/\partial\theta^2 - \cot\theta\partial/\partial\theta)Y_{l0}(\theta)$, being Y_{l0} the spherical harmonics and $r^* = r + 2GM/c^2 \ln[c^2 r/(2GM) - 1]$ (see figure 1).

That the multipole spectra obtained in [4] were associated with the 2^l -pole normal-mode vibrations of the black-hole, excited by the gravitational-wave train produced by the in-falling body, was then shown in [12]. Thus, the gravitational-wave spectrum from the peak on is governed by the emission of the vibrational energy of the black-hole driven by gravitational-wave radiation. Such vibrations are known today as black-hole “ringdown” or “ringing tail” [4].

The total gravitational-wave spectrum in the regime II has a peaked form [4, 6] (see figure 2): it first has a raising part that follows a power-law behavior, then

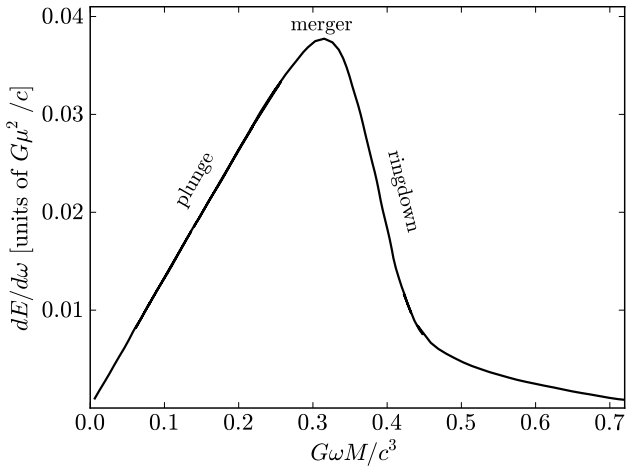


FIG. 2. Spectrum of the gravitational-wave radiation ($l = 2$ multipole) emitted by a test-particle of mass m falling radially into a black-hole of mass M (in geometrical units). This figure has been adapted from the original one in [4].

reaches a maximum to then falling off rapidly. This form of the spectrum was already evident from the first idealized analysis of the radially infalling particle problem in Ref. [13] that considered the motion of the test-particle in the Schwarzschild metric, but the radiation was there estimated in a flat-space linearized theory of gravity.

The spectrum raises during the plunge following approximately a power-law

$$\left(\frac{dE}{df}\right)_{\text{plunge}} \propto \frac{G\mu^2}{c} \left(\frac{4\pi GMf}{c^3}\right)^{4/3}; \quad (8)$$

then it reaches a maximum at the peak frequency (7), the approximate point of the merger, and then it falls off at large frequencies approximately as the exponential

$$\left(\frac{dE}{df}\right)_{\text{ringdown}} \propto \frac{G\mu^2}{c} \exp(-9.9 \times 2\pi GMf/c^3) \quad (9)$$

during the ringing. The spectrum of the $l = 2$ multipole radiation, obtained numerically in [4], is shown in figure 2. We have indicated the location of the plunge, merger and ringdown phases in the frequency-domain. Clearly, one can obtain an approximate formula of the spectrum from the interpolation function

$$\frac{dE}{df} \approx \left[\frac{1}{(dE/df)_{\text{plunge}}} + \frac{1}{(dE/df)_{\text{ringdown}}} \right]^{-1}. \quad (10)$$

The contribution of each multipole to the total energy radiated during the regime II (plunge+merger+ringdown phase) is $E_{2^l\text{-pole}} \approx 0.44(\mu^2/M)c^2 e^{-2l}$, so the total energy radiated to infinity in gravitational-waves is [4]:

$$\Delta E_{\text{merger}} = \sum_{l \geq 2} \int df \left(\frac{dE}{df}\right)_{2^l\text{-pole}} \approx 0.01 \frac{\mu^2}{M} c^2. \quad (11)$$

From all the above we can extract three important theorems:

1. the final gravitational-wave frequency of the inspiral phase, f_{LSO} , is lower than the peak frequency, f_{peak} ;
2. the energy emitted in gravitational-waves during the total inspiral phase is larger than the energy emitted in the final plunge-merger-ringdown phase;
3. the merger point can be set as the point where the gravitational-wave spectrum, dE/df , reaches the maximum value. Then,

$$f_{\text{merger}} \equiv f_{\text{peak}}, \quad (12)$$

where f_{peak} is given by equation (6).

A. Angular momentum in the merger phase

It was shown in Ref. [7, 8] that the energy emitted during the plunge of a test-particle into a black-hole is affected by the initial angular momentum of the particle. The total energy output in form of gravitational-wave radiation was in Ref. [8] computed for selected initial angular momenta of the particle (which correspond to start the plunge of the particle from different orbits). It is worth to notice that in the limit $J = 0$, the total energy emitted approaches the numerical value obtained by [4] [see equation (11)], namely the one of a radially infalling particle, as expected.

The results of the numerical integration of [8] are well-fitted (with a maximum error of $\sim 10\%$) by the phenomenological function

$$\Delta E_{\text{merger}} \approx \Delta E_{\text{merger}}^{J=0} [1 + 0.11 \exp(1.53j)], \quad (13)$$

where $j \equiv cJ/(G\mu M)$ and $\Delta E_{\text{merger}}^{J=0}$ is the energy radiated by a particle falling radially given by equation (11).

Thus, from the knowledge of the angular momentum at the LSO, we can infer the amount of energy emitted during the final merger phase. The energy loss during the regime II is therefore $\Delta E_{\text{merger}} \approx 0.24(\mu^2/M)c^2$, where we have used equations (11), (13), and the fact that $j_{\text{LSO}} = cJ_{\text{LSO}}/(G\mu M) = 2\sqrt{3}$ is the dimensionless angular momentum of a test-particle in the LSO around a Schwarzschild black-hole.

From the amount of energy emitted in this final plunge phase, ΔE_{merger} given by equation (13), we can estimate the angular momentum loss by the gravitational-wave emission in the final plunging, ΔJ_{merger} , as

$$\Delta J_{\text{merger}} \approx \frac{\Delta E_{\text{merger}}}{\pi f_{\text{LSO}}}, \quad (14)$$

which leads to $\Delta J_{\text{merger}} \approx 3.81 G\mu^2/c$.

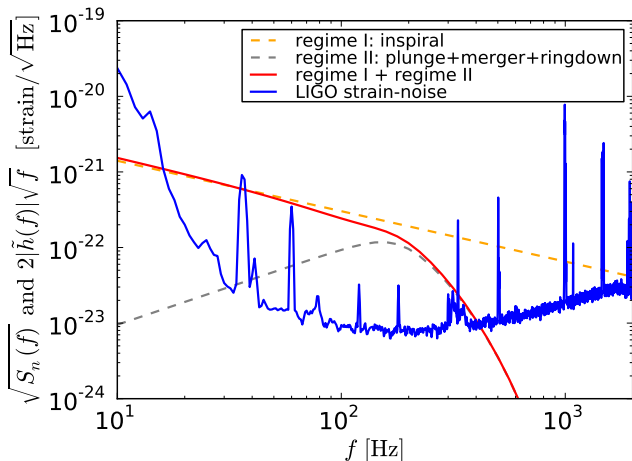


FIG. 3. Comparison of the amplitude spectral density of the signal in the regimes I (dashed orange curve), II (gray dashed curve) and the total signal (I+II, solid red curve) with the one of the LIGO H1 noise (solid blue curve).

B. Analysis of GW 1509014

It is unfortunate that the signal around 150 Hz occurs just at the limit of the sensitivity of LIGO, not allowing a definite observational characterization of regime II (see figures 3–5). Even so, we can proceed with our theoretical analysis by assuming that the evolution of the system follows the above theoretical plunge scenario, originating in a binary system.

We estimate a frequency at maximum strain $f_{\text{peak}}^{\text{obs}} = 144 \pm 4$ Hz where the uncertainties are due to the resolution of the discrete Fourier transform used to obtain the spectrogram. By using the aforementioned theorem 3, we can estimate the total mass of the binary equating the observed peak-frequency to the theoretical prediction (7). We obtain the total mass in the detector frame:

$$M_{\text{obs}} = \frac{10.36 \text{ kHz}}{f_{\text{peak}}^{\text{obs}}} M_{\odot} \approx 72 \pm 2 M_{\odot}, \quad (15)$$

where the quoted errors are associated with the errors in the determination of $f_{\text{peak}}^{\text{obs}}$. This value is to be compared with the total mass in the detector-frame obtained from the analysis based on numerical relativity templates, $M_{\text{obs}} \approx 70.3_{-4.8}^{+5.3} M_{\odot}$ [11], namely, our estimate is off only within a 2.4% of error with respect to the full numerical relativity analysis.

From the knowledge of the chirp mass obtained from regime I, and the total binary mass computed here above, we can extract the mass-ratio of the binary. From the definition of symmetric mass-ratio we have

$$\nu = \frac{\mu}{M} = \left(\frac{M_{\text{chirp}}}{M} \right)^{5/3} \approx 0.24 \pm 0.01, \quad (16)$$

which leads to a mass-ratio

$$q = \frac{m_2}{m_1} = \frac{4\nu}{(1 + \sqrt{1 - 4\nu})^2} \approx 0.67_{-0.11}^{+0.33}, \quad (17)$$

which is within the numerical relativity analysis value $q = 0.79_{-0.19}^{+0.18}$ [11]. Thus, we obtain individual masses

$$m_{\text{BH},1}^{\text{obs}} = \frac{M_{\text{obs}}}{(1 + q)} \approx 43.1_{-7.9}^{+4.3} M_{\odot}, \quad (18)$$

$$m_{\text{BH},2}^{\text{obs}} = \frac{q}{1 + q} M_{\text{obs}} \approx 28.9_{-5.9}^{+6.3} M_{\odot}, \quad (19)$$

which agree with the numerical relativity values $m_{\text{BH},1} = 39.4_{-4.9}^{+5.5} M_{\odot}$, $m_{\text{BH},2} = 30.9_{-4.4}^{+4.8} M_{\odot}$ [2, 11].

With the knowledge of the mass of the binary and the one of the binary components we can now estimate the energy emitted in gravitational-waves using equations (4) and (13) for the regime I and II, respectively. It turns out that for this nearly mass-symmetric binary the two contributions are almost equal with $\Delta E_{\text{inspiral}} \approx \Delta E_{\text{merger}} \approx 1 M_{\odot}$, so a total energy emitted $\Delta E_{\text{tot}} \approx 2 M_{\odot}$.

It is worth to stress that the above will remain mere theoretical speculations, unless the hypothesis of a binary nature of the system is confirmed either by independent astrophysical observations (as, e.g., in the case of binary pulsars whose independent observation in the radio frequencies has allowed tests of the general theory of relativity with unprecedented accuracy [14, 15]), or by direct observations of the ringdown phase (see section V).

IV. MASS AND SPIN OF THE FORMED BLACK-HOLE

In order to give an estimate of the newly formed black-hole parameters, we can use both energy and angular momentum conservation. Energy conservation implies a mass of the newly formed black-hole

$$m_{\text{BH}} \approx M - (1 - 2\sqrt{2}/3)\nu - \Delta E_{\text{merger}}/c^2 \quad (20)$$

$$\approx M\beta(\nu), \quad (21)$$

where $\beta(\nu) \equiv [1 - (1 - 2\sqrt{2}/3)\nu - 0.24\nu^2]$. Angular momentum conservation leads to

$$J_{\text{BH}} = J_{\text{LSO}} - \Delta J_{\text{merger}}, \quad (22)$$

which implies a dimensionless angular momentum of the newly formed black-hole

$$\alpha \equiv \frac{cJ_{\text{BH}}}{Gm_{\text{BH}}^2} \approx \frac{2\sqrt{3}\nu - 3.81\nu^2}{\beta(\nu)^2}. \quad (23)$$

A. Analysis of GW 1509014

Putting together the equations (19), (20), (23), we obtain a straightforward estimate of the parameters of the

final black-hole:

$$m_{\text{BH}} \approx 70_{-2}^{+2} M_{\odot}, \quad \alpha = \frac{cJ_{\text{BH}}}{Gm_{\text{BH}}^2} \approx 0.65_{-0.02}^{+0.02}, \quad (24)$$

to be compared with the numerical relativity analysis $m_{\text{BH}} = 62_{-4}^{+4} M_{\odot}$ and $cJ_{\text{BH}}/(Gm_{\text{BH}}^2) = 0.67_{-0.07}^{+0.05}$ [2, 11].

V. DISCUSSION

There are two markedly different regimes in the evolution of coalescing binary black-holes: I) the inspiraling phase; II) the plunge and merger followed by the ring-down phase of the newly formed black-hole. These two regimes have to be constrained by observations with comparable accuracy. In such a case, our analysis shows that it is possible to extract the parameters of the system, indicated in [2], but from a much simpler analysis of the two regimes in the test-particle approximation without the need of sophisticated numerical simulations. This is quite striking since we would expect that in the real world our test-particle approximation should not be valid in nearly mass-symmetric systems like the one proposed in [2] to explain GW 150914.

The independent observational confirmation of the two regimes and their subsequent matching is indeed essential in order to evaluate:

- 1) the total mass of the system;
- 2) the binary nature of the system and the mass of each binary component;
- 3) the formation of the black-hole horizon including the multipolar structure of the ringing;
- 4) the energy radiated in gravitational-waves.

In absence of these verifications no conclusion can be drawn about the nature of the system. It is therefore unfortunate that the signal around 150 Hz occurs just at the limit of the sensitivity of LIGO, not allowing a definite characterization of regime II (see figures 3–5). Under these conditions, regime I alone is not sufficient to determine the astrophysical nature of GW 150914, nor to assess that it was produced by a binary black-hole merger leading to a newly formed black-hole.

VI. CONCLUSIONS

It is by now clear that the LIGO event GW 150914 represent an epochal event just a few weeks after the first run of the advanced LIGO detector and occurring in the most favorable conditions for detectability. The current situation has manifested striking correspondence between our theoretical prediction and the observations.

The confirmation by observing the late phase of coalescence to a black-hole, the creation of an horizon, the

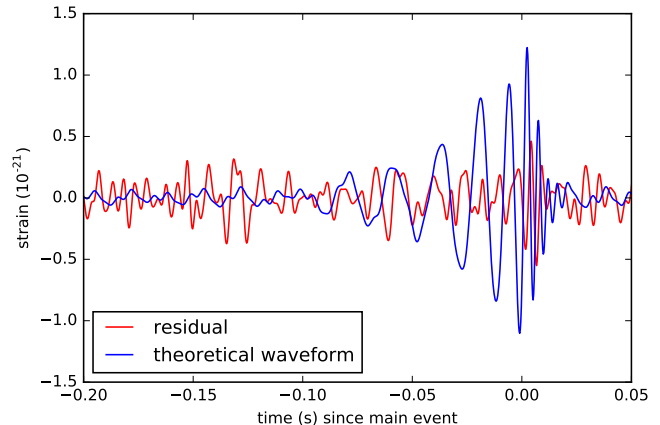


FIG. 4. (Color online) Blue curve: theoretical waveform of the binary black-hole coalescence used in [2] to explain GW 150914. Red curve: residuals from the subtraction of the theoretical waveform to the filtered H1 detector time series. We can see how the theoretical waveform after the first crest after maximum is of the same order as the residuals, impeding the characterization of the ringdown.

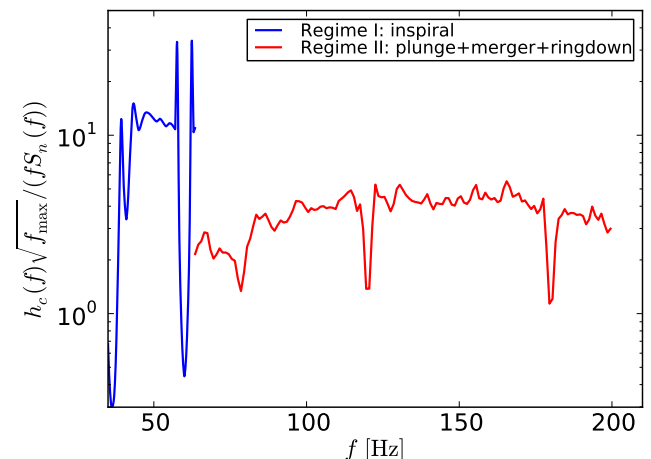


FIG. 5. (Color online) Estimated signal-to-noise ratio of regimes I (blue curve) and II (red curve) as described in this work. We can see how the signal-to-noise ratio decreases at the end of regime II impeding the characterization of the ringdown. The frequency f_{max} is the maximum observed frequency of the signal in each regime.

multipolar structure of the ringing (see figures 3–5) is now open to further inquire in order to uniquely identify and verify the astrophysical nature of the source. A quest for search of previously discarded signals with lower values of signal-to-noise ratio occurring not in the optimal region of sensitivity nor with the optimal localization and directionality should be addressed. Also important is to focus on the observation of merging processes leading either to a more extended or less extended range of frequencies.

We can then conclude:

- A) if these verifications in past or future observations

will materialize, then we are in presence of an outstanding scientific confirmation of the theoretical analysis we here presented on the ground of three fundamental results: 1) the inspiral phase described in [3], 2) the plunging, merger and ringdown phases described in [4, 5] (see also [6] and appendices therein), and 3) the transition from the quasi-circular inspiral phase to the final merger described in [8].

B) On the other hand, if these verifications will not

succeed, the relevance of the present work will be of service for inquiring on alternative sources not originating from a black-hole created in a black-hole binary merger.

C) If this last alternative does not materialize, the relevance of the present work will be more academic and will focus on the perspective that GW 150914 is not of astrophysical nature.

All these three possibilities, at the moment, have to be addressed with equal vigor, each being equally epochal.

-
- [1] J. F. Rodriguez, J. A. Rueda, and R. Ruffini, submitted to MNRASLett.; arXiv:1605.04767 (2016), arXiv:1605.04767 [gr-qc].
- [2] B. P. Abbott, R. Abbott, T. D. Abbott, M. R. Abernathy, F. Acernese, K. Ackley, C. Adams, T. Adams, P. Addesso, R. X. Adhikari, and et al., Phys. Rev. Lett. **116**, 061102 (2016), arXiv:1602.03837 [gr-qc].
- [3] L. D. Landau and E. M. Lifshitz, *Course of theoretical physics - Pergamon International Library of Science, Technology, Engineering and Social Studies, Oxford: Pergamon Press, 1975, 4th rev.engl.ed.* (1975).
- [4] M. Davis, R. Ruffini, W. H. Press, and R. H. Price, Physical Review Letters **27**, 1466 (1971).
- [5] M. Davis, R. Ruffini, and J. Tiomno, Phys. Rev. D **5**, 2932 (1972).
- [6] M. Rees, R. Ruffini, and J. A. Wheeler, *Black holes, gravitational waves and cosmology* (New York: Gordon and Breach Science Publishers Inc., 1974).
- [7] S. L. Detweiler, ApJ **225**, 687 (1978).
- [8] S. L. Detweiler and E. Szedenits, Jr., ApJ **231**, 211 (1979).
- [9] P. C. Peters and J. Mathews, Physical Review **131**, 435 (1963).
- [10] P. C. Peters, Physical Review **136**, 1224 (1964).
- [11] The LIGO Scientific Collaboration and the Virgo Collaboration, ArXiv e-prints (2016), arXiv:1602.03840 [gr-qc].
- [12] W. H. Press, ApJL **170**, L105 (1971).
- [13] R. Ruffini and J. A. Wheeler, in *Proceedings of the Cortona Symposium on Weak Interactions*, edited by L. Radicati (1971).
- [14] R. A. Hulse and J. H. Taylor, ApJL **195**, L51 (1975).
- [15] J. M. Weisberg and J. H. Taylor, in *Binary Radio Pulsars*, Astronomical Society of the Pacific Conference Series, Vol. 328, edited by F. A. Rasio and I. H. Stairs (2005) p. 25, astro-ph/0407149.

What can we really infer from GW 150914?

J. F. Rodriguez,^{1,2} J. A. Rueda,^{1,2,3} R. Ruffini^{1,2,3}

¹*Dipartimento di Fisica and ICRA, Sapienza Università di Roma, P.le Aldo Moro 5, I-00185 Rome, Italy*

²*ICRANet, Piazza della Repubblica 10, I-65122 Pescara, Italy*

³*ICRANet-Rio, CBPF, Rua Dr. Xavier Sigaud 150, Rio de Janeiro, RJ, 22290-180, Brazil*

Accepted XXX. Received YYY; in original form ZZZ

ABSTRACT

We analyze the event GW 150914 announced by the Advanced Laser Interferometer Gravitational-Wave Observatory (LIGO) as the gravitational-wave emission of a black-hole binary merger. We show that the parameters of the coalescing system and of the newly formed Kerr black-hole can be extracted from basic results of the gravitational-wave emission during the inspiraling and merger phases without sophisticated numerical simulations. Our strikingly accurate estimates are based on textbook formulas describing two different regimes: 1) the binary inspiraling analysis treated in Landau and Lifshitz textbook, and 2) the plunge of a particle into a black-hole, treated in the Rees-Ruffini-Wheeler textbook. It is stressed that in order to infer any astrophysical information on the masses of the system both regimes have to be independently and observationally constrained by LIGO, which does not appear to be the case.

Key words: Gravitational Waves

1 INTRODUCTION

It was recently announced by the Advanced Laser Interferometer Gravitational-Wave Observatory (LIGO) the observation, for the first time, of a gravitational wave signal (Abbott et al. 2016). After the data analysis using numerical relativity templates of black-hole binary mergers, they concluded that the signal, which lasts 0.2 s with increasing gravitational-wave frequency from 35 to ~ 150 Hz, was emitted during the inspiral and merger of a binary black-hole, followed by the subsequent ringdown phase of the newly formed black-hole. The binary black-hole parameters obtained from this analysis are: $m_{\text{BH},1} = 36^{+5}_{-4} M_{\odot}$, $m_{\text{BH},2} = 29^{+4}_{-4} M_{\odot}$, and a luminosity distance to the source $d_L = 410^{+160}_{-180}$ Mpc (cosmological redshift $z = 0.09^{+0.03}_{-0.04}$), adopting a flat Λ -cold-dark-matter cosmology with Hubble parameter $H_0 = 67.9 \text{ km s}^{-1} \text{ Mpc}^{-1}$, and matter and dark-energy density parameter $\Omega_m = 0.306$ and $\Omega_{\Lambda} = 0.694$, respectively.

We show in this Letter that the general features of the system that generates GW 150914 can be inferred from a simple analysis of the gravitational-wave signal on the light of the foundations of the gravitational-wave theory and from two classic results: 1) the analysis of the inspiraling phase of a binary system of point-like particles, and 2) the merger analysis based on the approximation of a test-particle falling into a black-hole. It is of course essential for the validity of this approximation that both regimes be independently confirmed by observations.

2 BINARY EVOLUTION

2.1 Inspiral phase

A binary system, by emitting gravitational-waves, evolves through two different phases: the regime I is the “adiabatic” inspiral phase in which the binary follows quasi-circular orbits. The gravitational-wave energy spectrum in this phase can be estimated from the traditional formula of the quadrupole emission within the classic point-like approximation (Peters & Mathews 1963; Peters 1964; Rees et al. 1974)

$$\frac{dE}{df} = \frac{1}{3}(\pi G)^{2/3} \nu M^{5/3} f^{-1/3}, \quad (1)$$

where $\nu \equiv \mu/M$ is the so-called symmetric mass-ratio parameter, with $\mu = m_1 m_2 / M$ the binary reduced mass, $M = m_1 + m_2$ the total binary mass, and f is the gravitational-wave frequency. We recall that $f = 2f_s = 2f_{\text{orb}}$, where f_s the source frequency so the orbital one, i.e. $f_s = f_{\text{orb}} = \omega_{\text{orb}}/(2\pi) = \sqrt{GM/r^3}/(2\pi)$ and r the binary separation distance. We recall that the quantity $M_{\text{chirp}} \equiv \nu^{3/5} M$ is referred in the literature to as the binary chirp mass.

When the conservative quasi-circular dynamics following the classic point-like approximation breaks-down, the regime II, namely the final plunge, merger and ringdown of the newly formed object sets in. We denote the gravitational-wave frequency at which the quasi-circular evolution ends as plunge starting frequency, f_{plunge} . We adopt here as an estimate of the plunge starting frequency, the one of the last

arXiv:1605.04767v2 [gr-qc] 24 May 2016

stable orbit (LSO) of a test-particle around a Schwarzschild black-hole:

$$f_{\text{plunge}} \approx f_{\text{LSO}} = \frac{c^3}{G} \frac{1}{6^{3/2}\pi M} \approx 4.4 \frac{M_{\odot}}{M} \text{ kHz}. \quad (2)$$

Thus, the total energy radiated during the inspiral regime can be estimated from the binding energy of the LSO which, by extrapolation to the case of a binary of comparable masses, reads $\Delta E_{\text{inspiral}} = (1 - \sqrt{8/9})\mu c^2$, where we recall that μ is the binary reduced mass. Thus, for a symmetric binary it gives $\Delta E_{\text{inspiral}} \approx 0.014Mc^2$.

2.2 Plunge, merger and ringdown

After the regime I of quasi-circular inspiral evolution, the regime II composed by the plunge, merger and ringdown, as first analyzed in Davis et al. (1971, 1972) for a test-particle falling radially into a Schwarzschild black-hole, starts. It was shown first by Davis et al. (1971, 1972) that the gravitational-wave spectrum in this regime II is dominated by the $l = 2$ multipole (quadrupole) emission and that the largest gravitational-wave emission occurs from $r \approx 3GM/c^2$, at the maximum of the effective potential

$$V_l(r) = \left(1 - \frac{2m_{\text{BH}}}{r}\right) \times \left[\frac{2\lambda^2(\lambda+1)r^3 + 6\lambda^2 m_{\text{BH}} r^2 + 18\lambda m_{\text{BH}}^2 r + 18m_{\text{BH}}^3}{r^3(\lambda r + 3m_{\text{BH}})^2} \right] \quad (3)$$

where $\lambda = (l-1)(l+2)/2$, and the black-hole horizon. It was there shown that in the limit of large l , the contribution of each multipole to the spectrum peaks at the gravitational-wave frequency

$$f_{\text{peak}}^l = \frac{c^3}{G} \sqrt{(V_l)_{\text{max}}} \approx \frac{c^3}{G} \frac{l}{2\pi\sqrt{27}M}, \quad (4)$$

while, the total spectrum obtained by summing over all the multipoles, peaks at

$$f_{\text{peak}} \approx \frac{c^3}{G} \frac{0.05}{M} \approx 10.36 \frac{M_{\odot}}{M} \text{ kHz}. \quad (5)$$

Then, Press (1971) showed that the multipole spectra obtained in Davis et al. (1971) were associated with the 2^l -pole normal-mode vibrations of the black-hole, excited by the gravitational-wave train produced by the in-falling body. Thus, the gravitational-wave spectrum from the peak on is governed by the emission of the vibrational energy of the black-hole driven by gravitational-wave radiation. Such vibrations are referred today to as black-hole ‘‘ringdown’’ or ‘‘ringing tail’’ (Davis et al. 1971).

As it was shown in Davis et al. (1971), the gravitational-wave spectrum in this phase has a peaked form: it first has a raising part that follows a power-law behavior which can be understood as follows. The solution of the particle radially falling onto the black-hole in linearized theory, i.e. in a flat background, and using Newtonian equations of motion which leads to (Rees et al. 1974)

$$\left(\frac{dE}{df}\right)_{\text{plunge}} \approx 2\pi \times 0.18 \frac{G\mu^2}{c} \left(\frac{4\pi GMf}{c^3}\right)^{4/3}. \quad (6)$$

The spectrum thus raises following approximately (6) until

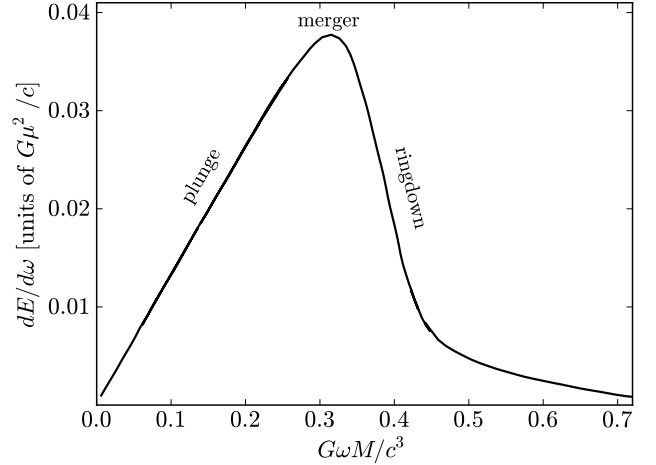


Figure 1. Spectrum of the gravitational-wave radiation ($l = 2$ multipole) emitted by a test-particle of mass m falling radially into a black-hole of mass M (in geometrical units). This figure has been adapted from the original one in Davis et al. (1971).

it reaches a maximum at the peak frequency (5), and then it falls off following an approximate (phenomenological) form

$$\left(\frac{dE}{df}\right)_{\text{ringdown}} \approx 2\pi \frac{G\mu^2}{c} \exp(-9.9 \times 2\pi GMf/c^3). \quad (7)$$

The spectrum of the $l = 2$ multipole radiation as obtained numerically in Davis et al. (1971) is shown in figure 1. We have indicated the location of the plunge, merger and ringdown phases in the frequency-domain. It is clear that an approximate analytic formula of the spectrum can be obtained from the interpolation function

$$\frac{dE}{df} \approx \left[\frac{1}{(dE/df)_{\text{plunge}}} + \frac{1}{(dE/df)_{\text{ringdown}}} \right]^{-1}. \quad (8)$$

The total energy radiated to infinity in gravitational-waves during this plunge+merger+ringdown phase is (Davis et al. 1971):

$$\Delta E_{\text{merger}} = \sum_{l \geq 2} \int df \left(\frac{dE}{df}\right)_{2^l\text{-pole}} \approx 0.01 \frac{\mu^2}{M} c^2. \quad (9)$$

From all the above we can extract three important theorems:

- (i) the final gravitational-wave frequency of the inspiral phase, f_{LSO} , is lower than the peak frequency, f_{peak} ;
- (ii) the energy emitted in gravitational-waves during the total inspiral phase is larger than the energy emitted in the final plunge-merger-ringdown phase;
- (iii) the merger point can be set as the point where the gravitational-wave spectrum, dE/df , reaches the maximum value;
- (iv) from the above, the frequency at merger is

$$f_{\text{merger}} \equiv f_{\text{peak}}, \quad (10)$$

where f_{peak} is given by equation (4).

2.3 Angular momentum in the merger phase

As it was shown in Detweiler & Szedenits (1979), the energy emitted during the plunging of a test-particle into a black-

hole is affected by the initial angular momentum of the particle. The total energy output in form of gravitational-wave radiation was there computed for selected initial angular momenta of the particle (which correspond to start the plunge of the particle from different orbits). It is worth to notice that in the case $J = 0$, the total energy emitted approaches the numerical value obtained in [Davis et al. \(1971\)](#), see equation (9), in the case of radial falling into the black-hole, as expected.

The results of the numerical integration of [Detweiler & Szedenits \(1979\)](#) are well-fitted (with a maximum error of $\sim 10\%$) by the phenomenological function

$$\Delta E_{\text{merger}} \approx \Delta E_{\text{merger}}^{J=0} [1 + 0.11 \exp(1.53j)], \quad (11)$$

where $j \equiv cJ/(G\mu M)$ and $\Delta E_{\text{merger}}^{J=0}$ is the energy radiated by a particle falling radially given by equation (9).

Thus, from the knowledge of the angular momentum at the LSO, we can infer the amount of energy emitted during the final merger phase. The energy loss during the regime II is therefore $\Delta E_{\text{merger}} \approx 0.24(\mu^2/M)c^2$, where we have used equations (9), (11), and the fact that $j_{\text{LSO}} = cJ_{\text{LSO}}/(G\mu M) = 2\sqrt{3}$ is the dimensionless angular momentum of a test-particle in the LSO around a Schwarzschild black-hole.

From the amount of energy emitted in this final plunge phase, ΔE_{merger} given by equation (11), we can estimate the angular momentum loss by the gravitational-wave emission in the final plunging, ΔJ_{merger} , as

$$\Delta J_{\text{merger}} \approx \frac{\Delta E_{\text{merger}}}{\pi f_{\text{LSO}}}, \quad (12)$$

which leads to $\Delta J_{\text{merger}} \approx 3.81G\mu^2/c$.

3 MASS AND SPIN OF THE FORMED BLACK-HOLE

In order to give an estimate of the newly formed black-hole parameters, we can use both energy and angular momentum conservation. Energy conservation implies a mass of the newly formed black-hole

$$m_{\text{BH}} \approx M - (1 - 2\sqrt{2}/3)\nu - \Delta E_{\text{merger}}/c^2 \quad (13)$$

$$\approx M\beta(\nu), \quad (14)$$

where $\beta(\nu) \equiv [1 - (1 - 2\sqrt{2}/3)\nu - 0.24\nu^2]$, while angular momentum conservation leads to

$$J_{\text{BH}} = J_{\text{LSO}} - \Delta J_{\text{merger}}, \quad (15)$$

which implies a dimensionless angular momentum of the newly formed black-hole

$$\alpha \equiv \frac{cJ_{\text{BH}}}{Gm_{\text{BH}}^2} \approx \frac{2\sqrt{3}\nu - 3.81\nu^2}{\beta(\nu)^2}. \quad (16)$$

4 ANALYSIS OF GW 150914

In order to extract more information from the signal it is necessary to make an analysis of the frequency evolution with time. From the binary evolution in the regime I, within

the point-like approximation, it can be inferred the chirp mass of the binary as:

$$M_{\text{chirp}} = \frac{c^3}{G} \left(\frac{5}{96\pi^{8/3}} \frac{\dot{f}}{f^{11/3}} \right)^{3/5}. \quad (17)$$

We fit the evolution of the frequency with time in GW 150914 which leads to $M_{\text{chirp}}^{\text{obs}} \approx 30.5 M_{\odot}$, in agreement with the LIGO analysis, $M_{\text{chirp}}^{\text{obs}} = 30.2_{-1.9}^{+2.5} M_{\odot}$, in the detector-frame ([The LIGO Scientific Collaboration & the Virgo Collaboration 2016](#)).

We estimate a frequency at maximum strain $f_{\text{peak}}^{\text{obs}} = 144 \pm 4$ Hz. The uncertainties are due to the resolution of the discrete Fourier transform used to obtain the spectrogram. By using the aforementioned theorem 3, we can estimate the total mass of the binary equating the observed peak-frequency to the theoretical prediction (5):

$$M_{\text{obs}} = \frac{10.36 \text{ kHz}}{f_{\text{peak}}^{\text{obs}}} M_{\odot} \approx 72 \pm 2 M_{\odot}, \quad (18)$$

where we have computed it in the observer-frame, i.e. in the detector-frame. This value is to be compared with the total mass in the detector-frame obtained from the analysis based on numerical relativity templates, $M_{\text{obs}} \approx 70.3_{-4.8}^{+5.3} M_{\odot}$ ([The LIGO Scientific Collaboration & the Virgo Collaboration 2016](#)), namely, our estimate is off only within a 2.3% of error with respect to the full numerical relativity analysis. Clearly, the total mass in the source-frame is $M = M_{\text{obs}}/(1+z)$.

From the knowledge of the chirp mass and the total binary mass, we can extract the mass-ratio of the binary. From the definition of symmetric mass-ratio we have

$$\nu = \frac{\mu}{M} = \left(\frac{M_{\text{chirp}}}{M} \right)^{5/3} \approx 0.24 \pm 0.01, \quad (19)$$

which leads to a mass-ratio

$$q = \frac{m_2}{m_1} = \frac{4\nu}{(1 + \sqrt{1 - 4\nu})^2} \approx 0.67_{-0.11}^{+0.33}, \quad (20)$$

which is within the numerical relativity analysis value $q = 0.79_{-0.19}^{+0.18}$ ([The LIGO Scientific Collaboration & the Virgo Collaboration 2016](#)). Thus, we obtain individual masses

$$m_{\text{BH},1}^{\text{obs}} = \frac{M_{\text{obs}}}{(1+q)} \approx 43.1_{-7.9}^{+4.3} M_{\odot}, \quad (21)$$

$$m_{\text{BH},2}^{\text{obs}} = \frac{q}{1+q} M_{\text{obs}} \approx 28.9_{-5.9}^{+6.3} M_{\odot}, \quad (22)$$

which agree with the numerical relativity values $m_{\text{BH},1} = 39.4_{-4.9}^{+5.5} M_{\odot}$, $m_{\text{BH},2} = 30.9_{-4.4}^{+4.8} M_{\odot}$ ([Abbott et al. 2016](#); [The LIGO Scientific Collaboration & the Virgo Collaboration 2016](#)).

Therefore, together with the equations (13) and (16), we obtain a straightforward estimate of the parameters of the final black-hole:

$$m_{\text{BH}} \approx 70_{-2}^{+2} M_{\odot}, \quad \frac{cJ_{\text{BH}}}{Gm_{\text{BH}}^2} = 0.65_{-0.02}^{+0.02}, \quad (23)$$

to be compared with the numerical relativity analysis $m_{\text{BH}} = 62_{-4}^{+4} M_{\odot}$ and $cJ_{\text{BH}}/(Gm_{\text{BH}}^2) = 0.67_{-0.07}^{+0.05}$ ([Abbott et al. 2016](#); [The LIGO Scientific Collaboration & the Virgo Collaboration 2016](#)).

5 CONCLUDING REMARKS

There are two markedly different regimes in the evolution of coalescing binary black-holes: I) the inspiraling phase up to merger and II) the final ringdown phase of the newly formed black-hole. The two regimes have to be constrained by observations with comparable accuracy. In that case, our analysis shows that it is possible to extract the parameters of the system, indicated in [Abbott et al. \(2016\)](#), but from a much simpler analysis of the two regimes in the test-particle approximation without the need of sophisticated numerical simulations. This is quite striking since we would expect that in the real world our test-particle approximation should not be valid in nearly mass-symmetric systems like the one proposed in [Abbott et al. \(2016\)](#) to explain GW 150914.

The independent observational confirmation of the two regimes is indeed essential for testing the validity of this approximation, for determining the total mass of the system and the mass of each binary component, as well as the formation of the black-hole horizon.

It is therefore unfortunate that the signal around 150 Hz occurs just at the limit of the sensitivity of LIGO, not allowing a definite characterization of regime II. Under these conditions, regime I alone is not sufficient to determine the astrophysical nature of GW 150914, nor to assess that it was produced by a binary black-hole merger leading to a newly formed black-hole.

REFERENCES

- Abbott B. P., et al., 2016, [Phys. Rev. Lett.](#), **116**, 061102
 Davis M., Ruffini R., Press W. H., Price R. H., 1971, [Physical Review Letters](#), **27**, 1466
 Davis M., Ruffini R., Tiomno J., 1972, [Phys. Rev. D](#), **5**, 2932
 Detweiler S. L., Szedenits Jr. E., 1979, [ApJ](#), **231**, 211
 Peters P. C., 1964, [Physical Review](#), **136**, 1224
 Peters P. C., Mathews J., 1963, [Physical Review](#), **131**, 435
 Press W. H., 1971, [ApJ](#), **170**, L105
 Rees M., Ruffini R., Wheeler J. A., 1974, *Black holes, gravitational waves and cosmology*. New York: Gordon and Breach Science Publishers Inc.
 The LIGO Scientific Collaboration the Virgo Collaboration 2016, preprint, ([arXiv:1602.03840](#))

This paper has been typeset from a $\text{\TeX}/\text{\LaTeX}$ file prepared by the author.

Equilibrium structure of white dwarfs at finite temperaturesK. A. Boshkayev,^{1,2,*} J. A. Rueda,² B. A. Zhami,¹
Zh. A. Kalymova¹ and G. Sh. Balgymbekov¹¹*Department of Physics and Technology, Al-Farabi Kazakh National University,
Al-Farabi avenue 71, Almaty, 050040, Kazakhstan*²*International Center for Relativistic Astrophysics Network,
Piazza della Repubblica 10, Pescara, I-65122, Italy*

*kulantay@mail.ru

Recently, it has been shown by S. M. de Carvalho et al. (2014) that the deviations between the degenerate case and observations were already evident for 0.7-0.8 M_{\odot} white dwarfs. Such deviations were related to the neglected effects of finite temperatures on the structure of a white dwarf. Therefore, in this work by employing the Chandrasekhar equation of state taking into account the effects of temperature we show how the total pressure of the white dwarf matter depends on the mass density at different temperatures. Afterwards we construct equilibrium configurations of white dwarfs at finite temperatures. We obtain the mass-radius relations of white dwarfs for different temperatures by solving the Tolman-Oppenheimer-Volkoff equation, and compare them with the estimated masses and radii inferred from the Sloan Digital Sky Survey Data Release 4.

Keywords: Hot white dwarfs; finite temperatures; general relativity; hydrostatic equilibrium.

PACS numbers: 03.75.Ss; 04.40.Dg; 95.30.Sf; 97.20.Rp

1. Introduction

In astrophysics it is of high importance to construct a realistic physical model of stellar compact objects such as neutron stars and white dwarfs (WDs) which fits with observations. Consequently, all physical phenomena and quantities must be duly taken into account in the equation of state (EoS). Up to now there exist three EoS to describe the degenerate matter of WDs: the Chandrasekhar EoS,¹ the Salpeter EoS^{2,3} and the Relativistic Feynman-Metropolis-Teller (RFMT) EoS.^{4,5,6} The main differences, advantages and drawbacks among these EoS are discussed by Rotondo et al.⁶ in detail. Moreover, according to Shapiro et al.^{6,7} it is necessary to investigate WDs in general relativity (GR) in order to analyze their stability though the corrections of GR can be neglected for low mass WDs.

In this work, we investigate hot white dwarfs by employing the Chandrasekhar EoS¹ including the finite-temperature effects. Similar approach to include the effects

2 *K. B. Boshkayev et al.*

of finite temperatures in case of the RFMT EoS has been used by S. M. de Carvalho et al.⁸

Here we perform similar analyses following S. M. de Carvalho et al.⁸ in order to construct the mass-radius relations of white dwarfs at finite temperatures in GR for the sake of completeness. We compare our results with the estimated masses and radii from the Sloan Digital Sky Survey Data Release 4 (SDSS-E06 catalog).⁹

2. Equation of State

For the sake of clarity we make use of the Chandrasekhar EoS since it is the simplest EoS for WD matter, is well known and widely used in the description of physical properties of WDs.⁶

2.1. Chandrasekhar EoS at finite temperatures

In general, the EoS is determined through the total pressure and the total energy density of matter. Within the Chandrasekhar's approximation, the total pressure is due to the pressure of electrons P_e since the pressure of positive ions P_N (naked nuclei) is insignificant whereas the energy density is due to the energy density of nuclei \mathcal{E}_N as the energy density of the degenerate electrons \mathcal{E}_e is negligibly small. Thus, the Chandrasekhar EoS is given by

$$\mathcal{E}_{Ch} = \mathcal{E}_N + \mathcal{E}_e \approx \mathcal{E}_N = \frac{A}{Z} M_u c^2 n_e, \quad (1)$$

$$P_{Ch} = P_N + P_e \approx P_e, \quad (2)$$

where A is the average atomic weight, Z is the number of protons, $M_u = 1.6604 \times 10^{-24}$ g is the unified atomic mass, c is the speed of light and n_e is the electron number density. In general, the electron number density follows from the Fermi-Dirac statistics and is determined by^{10,11}

$$n_e = \frac{2}{(2\pi\hbar)^3} \int_0^\infty \frac{4\pi p^2 dp}{\exp\left[\frac{\tilde{E}(p) - \tilde{\mu}_e(p)}{k_B T}\right] + 1}, \quad (3)$$

where k_B is the Boltzmann constant, $\tilde{\mu}_e$ is the electron chemical potential without the rest-mass, and $\tilde{E}(p) = \sqrt{c^2 p^2 + m_e^2 c^4} - m_e c^2$, with p and m_e the electron momentum and rest-mass, respectively.

It is possible to show that (3) can be written in an alternative form as

$$n_e = \frac{8\pi\sqrt{2}}{(2\pi\hbar)^3} m^3 c^3 \beta^{3/2} [F_{1/2}(\eta, \beta) + \beta F_{3/2}(\eta, \beta)], \quad (4)$$

where

$$F_k(\eta, \beta) = \int_0^\infty \frac{t^k \sqrt{1 + (\beta/2)t}}{1 + e^{t-\eta}} dt \quad (5)$$

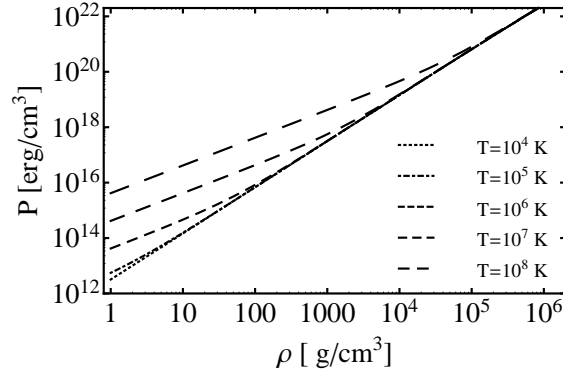


Fig. 1. Total pressure as a function of the mass density in the case of $\mu = A/Z = 2$ white dwarf for selected temperatures in the range $T = (10^4 - 10^8)$ K.

is the relativistic Fermi-Dirac integral, $\eta = \tilde{\mu}_e/(k_B T)$, $t = \tilde{E}(p)/(k_B T)$ and $\beta = k_B T/(m_e c^2)$ are degeneracy parameters.^{8,11}

Consequently, the total electron pressure for $T \neq 0$ K is given by

$$P_e = \frac{2^{3/2}}{3\pi^2 \hbar^3} m_e^4 c^5 \beta^{5/2} \left[F_{3/2}(\eta, \beta) + \frac{\beta}{2} F_{5/2}(\eta, \beta) \right]. \quad (6)$$

In Fig. 1 we plot the total pressure (6) as a function of the total density (1) of the system for selected temperatures $T = [10^4, 10^5, 10^6, 10^7, 10^8]$ K. As one can see the effects of temperature is essential in the range of small densities.

2.2. Chandrasekhar EoS at $T=0$

When $T = 0$ one can write for the number density of the degenerate electron gas the following expression from the Eq. (3)

$$n_e = \int_0^{P_e^F} \frac{2}{(2\pi\hbar)^3} d^3p = \frac{8\pi}{(2\pi\hbar)^3} \int_0^{P_e^F} p^2 dp = \frac{(P_e^F)^3}{3\pi^2 \hbar^3} = \frac{(m_e c)^3}{3\pi^2 \hbar^3} x_e^3 \quad (7)$$

and the total electron pressure

$$\begin{aligned} P_e &= \frac{1}{3} \frac{2}{(2\pi\hbar)^3} \int_0^{P_e^F} \frac{c^2 p^2}{\sqrt{c^2 p^2 + m_e^2 c^4}} 4\pi p^2 dp \\ &= \frac{m_e^4 c^5}{8\pi^2 \hbar^3} [x_e \sqrt{1 + x_e^2} (2x_e^2/3 - 1) + \operatorname{arcsinh}(x_e)], \end{aligned} \quad (8)$$

where $x_e = P_e^F/(m_e c)$ is the dimensionless Fermi momentum.

3. Equations of Stellar Structure and Equilibrium

From spherically symmetric metric

$$ds^2 = e^{\nu(r)} c^2 dt^2 - e^{\lambda(r)} dr^2 - r^2 d\theta^2 - r^2 \sin^2 \theta d\varphi^2, \quad (9)$$

4 *K. B. Boshkayev et al.*

the equations of equilibrium can be written in the Tolman-Oppenheimer-Volkoff (TOV) form,

$$\frac{d\nu(r)}{dr} = \frac{2G}{c^2} \frac{4\pi r^3 P(r)/c^2 + M(r)}{r^2 \left[1 - \frac{2GM(r)}{c^2 r}\right]}, \quad (10)$$

$$\frac{dM(r)}{dr} = 4\pi r^2 \frac{\mathcal{E}(r)}{c^2}, \quad (11)$$

$$\frac{dP(r)}{dr} = -\frac{1}{2} \frac{d\nu(r)}{dr} [\mathcal{E}(r) + P(r)], \quad (12)$$

where the mass enclosed at the distance r is determined through $e^{-\lambda(r)} = 1 - 2GM(r)/(c^2 r)$, $\mathcal{E}(r) = c^2 \rho(r)$ is the total energy density, and $P(r)$ is the total pressure, given by Eqs. (1) and (2).

From the Eqs. (10) and (12) the total pressure can be rewritten in the following form

$$\frac{dP(r)}{dr} = -\frac{GM(r)\rho(r)}{r^2} \left[1 + \frac{P(r)}{\rho(r)c^2}\right] \left[1 + \frac{4\pi r^2 P(r)}{M(r)c^2}\right] \left[1 - \frac{2GM(r)}{rc^2}\right]^{-1}. \quad (13)$$

The TOV equation completely determines the structure of a spherically symmetric body of isotropic material in equilibrium. The first two factors in square brackets represent special relativistic corrections of order $1/c^2$ that arise from the mass-energy relation so that the denominators, \mathcal{E} and Mc^2 , vary relativistically in connection with Einstein's famous equation $E = mc^2$. The last term in brackets is a general relativistic correction due to non-negligible strength of the gravitational potential (in units of c^2) and the meaning of $M(r)$ as the total integrated mass out to a radial distance r . These corrections each act to strengthen the gravitational interaction. If terms of order $1/c^2$ are neglected, the TOV equation becomes the Newtonian hydrostatic equation,

$$\frac{dP(r)}{dr} = -\frac{GM(r)\rho(r)}{r^2}, \quad (14)$$

$$\frac{dM(r)}{dr} = 4\pi r^2 \rho(r) \quad (15)$$

and

$$\frac{d\Phi(r)}{dr} = \frac{GM(r)}{r^2} \quad (16)$$

used to find the equilibrium structure of a spherically symmetric body of isotropic material when general-relativistic corrections are not important. Here $\Phi(r)$ is the Newtonian potential of the gravitational field inside the star.

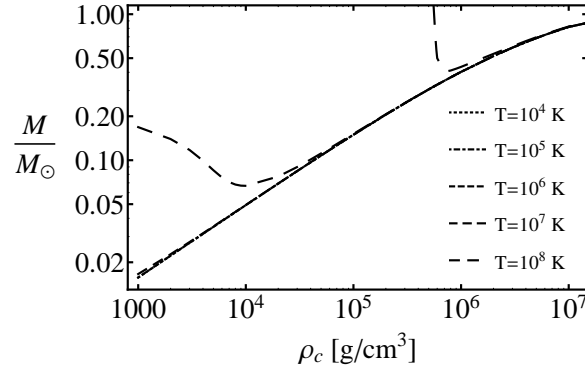


Fig. 2. Total mass versus central density for $\mu = 2$ white dwarfs for selected temperatures from $T = 10^4$ K to $T = 10^8$ K.

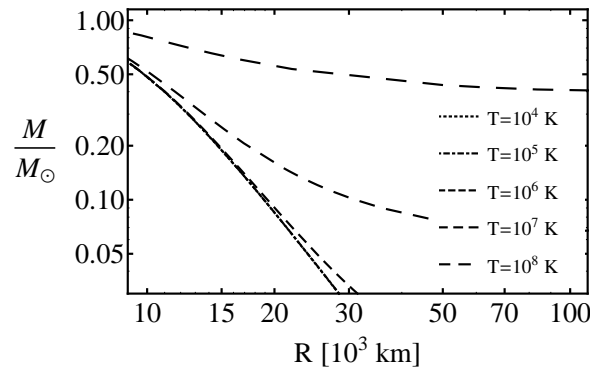


Fig. 3. Mass versus radius for $\mu = 2$ white dwarfs at temperatures $T = [10^4, 10^5, 10^6, 10^7, 10^8]$ K in the range $R = (10^4 - 10^5)$ km.

4. Results

By solving the TOV equations Eqs. (10)-(12) numerically, we obtained mass-central density $M - \rho$, and mass-radius $M - R$ relations for static hot WDs.

In Fig. 2 we plot the mass-central density for $\mu = 2$ white dwarfs using the Chandrasekhar EoS at different temperatures in the range of densities where the finite-temperature effects are more important.

In addition, in Fig. 3 we show the mass-radius relations. One can see that the finite-temperature effects are essential for small mass WDs.

In Fig. 4 we plot $M - R$ relation for hot static white dwarfs with $\mu = 2$ (see Fig. 2) and compare them with the estimated masses and radii of white dwarfs from the Sloan Digital Sky Survey Data Release 4 (see Ref. 9).

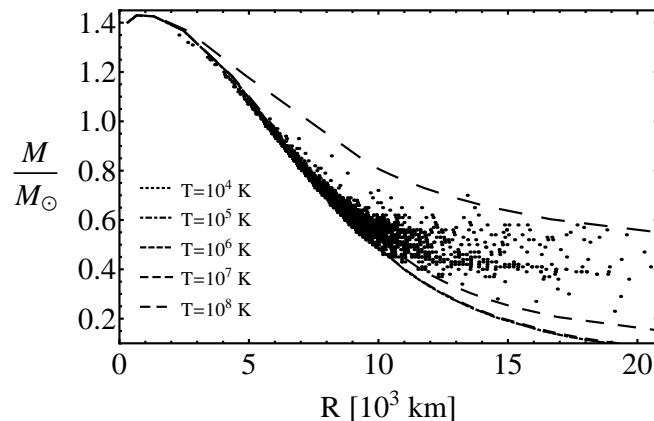


Fig. 4. Mass-radius relations of white dwarfs obtained with the Chandrasekhar EoS (dashed black lines) for selected finite temperatures from $T = 10^4$ K to $T = 10^8$ K and their comparison with the masses and radii of white dwarfs taken from the Sloan Digital Sky Survey Data Release 4 (black dots).

Note, the temperature we use here is the temperature of the WD isothermal core T_c . In order to find the surface effective temperature T_{eff} , one needs to know the temperature gradient (so the heat flux) between the isothermal core and the surface of the star from which photons finally escape, i.e. a T_c - T_{eff} relation. We adopt here the Koester formula $T_{eff}^4/g = 2.05 \times 10^{-10} T_c^{2.56}$, where g is the surface gravity.¹²

5. Conclusion

In this work we studied the properties of static WDs by using the Chandrasekhar EoS at finite-temperatures. To investigate WDs in GR we solved the TOV equation numerically in order to construct $M - \rho$ and $M - R$ relations at finite temperatures. Furthermore we superposed our results with the estimated values of masses and radii obtained by Tremblay et al.⁹ As a result we showed that all observational data, at least in the range of low masses, can be described by the Chandrasekhar EoS at finite-temperatures. In our computations we used the values of temperature of the core of the WD. To compare with the real surface temperature of WDs we exploited the Koester formula which establishes the connection between the effective surface temperature and the temperature of the core of WDs. We found that most of the observed WDs have core temperatures lower than 10^8 K (see Fig. 4). A precise analysis using empirical mass-radius relations obtained from the spectroscopic or photometric measurements of masses and radii is still needed to confirm and extend our results.

Acknowledgments

This work was supported by the Ministry of Education and Science of the Republic of Kazakhstan, Grant No. 3101/GF4 IPC-11/2015.

References

1. S. Chandrasekhar, *Astrophys. J.* **74**, 81 (1931).
2. E. E. Salpeter, *Astrophys. J.* **134**, 669 (1961).
3. E. E. Salpeter and H. M. van Horn, *Astrophys. J.* **155**, 183 (1969).
4. R. P. Feynman, N. Metropolis and E. Teller, *Phys. Rev.* **75**, 1561 (1949).
5. M. Rotondo, J. A. Rueda, R. Ruffini and S.-S. Xue, *Phys. Rev. C* **83**, 045805 (2011).
6. M. Rotondo, J. A. Rueda, R. Ruffini and S.-S. Xue, *Phys. Rev. D* **84**, 084007 (2011).
7. S. L. Shapiro and S. A. Teukolsky, *J. Br. Astronom. Assoc.* **93**, 276 (1983).
8. S. M. de Carvalho, M. Rotondo, J. A. Rueda and R. Ruffini, *Phys. Rev. C* **89**, 015801 (2014).
9. P. E. Tremblay, P. Bergeron and A. Gianninas, *Astrophys. J.* **730**, 128 (2011).
10. L. D. Landau and E. M. Lifshitz, *Statistical Physics. Part 1* (Pergamon Press, Oxford, 1980).
11. F. X. Timmes and D. Arnett, *Astrophys. J. Supl. Ser.* **125**, 277 (1999).
12. D. Koester, *Astronomy and Astrophysics* **52**, 415 (1976).

Rotating Hot White Dwarfs

K. A. Boshkayev,^{1,2} J. A. Rueda^{1,2} and B. A. Zhami^{1,*}

¹*Department of Physics and Technology, Al-Farabi Kazakh National University,
Al-Farabi avenue 71, Almaty, 050040, Kazakhstan*

²*International Center for Relativistic Astrophysics Network,
Piazza della Repubblica 10, Pescara, I-65122, Italy*

**E-mail: zhami.bakytzhan@gmail.com*

We consider the effects of rotation and temperature on the structure of white dwarfs in order to compare them with the estimated data from observations.

Keywords: Rotating White Dwarfs; Hot White Dwarfs; General Relativity.

In this work we construct the mass-radius relation for white dwarfs (WDs) using the Chandrasekhar equation of state (EoS) within general relativity (GR). First we perform computations for zero temperature uniformly rotating WDs at the mass shedding limit within the Hartle formalism¹. Afterwards we superpose our results with the estimated mass-radius relations obtained from the Sloan Digital Sky Survey Data Release 4 (SDSS 4) by Tremblay et al.² As one can see on the left panel of Fig. 1 the difference between theory and observations is quite noticeable.

In order to overcome this problem S. M. de Carvalho et al.³ proposed to include the finite-temperature effects in the EoS. Following this idea we performed similar analysis for static WDs at finite-temperatures by solving the Tolman-Oppenheimer-Volkoff equation (see Ref. 4 for details). The results of Ref. 4 are shown on the right panel of Fig. 1. As one can see the only inclusion of the temperature effects on the EoS and on the structure of the WD leads to a mass-radius relation in better agreement with the observational data with respect to the only inclusion of the rotation effects.

It should be stressed that from the observations usually one infers the effective surface temperature and the surface gravity of WDs. All the rest parameters are estimated by using certain models. However there also exist techniques to measure the masses of WDs in close eclipsing binaries. The data inferred from close binaries are more reliable. Therefore in order to perform more realistic computations one needs to take into account the effects of rotation and temperature together for selected WDs with known

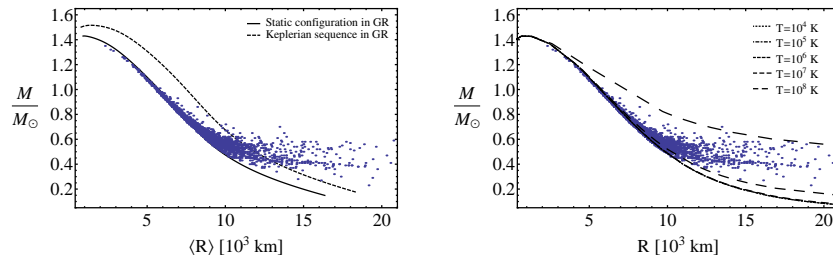


Fig. 1. Mass-radius relation of uniformly rotating WDs (the average radius is defined as $\langle R \rangle = (1/3)(R_p + 2R_e)$, where R_p is the polar radius, R_e is the equatorial radius) obtained with the Chandrasekhar EoS for $T = 0$ K case (left panel) and mass-radius relation of static WDs for selected finite temperatures from $T = 10^4$ K to $T = 10^8$ K (right panel) and their superposition with the estimated masses and radii of WDs taken from the SDSS 4 (blue dots).

parameters. Only after one can make further predictions. This issue is out of the scope of the present work and will be considered elsewhere.

In conclusion, we calculated the masses and radii of cold rotating and hot static WDs in GR i.e. the effects of the rotation and finite-temperature have been considered separately. We compared and contrasted our results with the estimated data from the observations of WDs. Our results cover all the data. For more detailed analysis one needs to consider both effects together and work with more or less model-independent data.

The work was partially supported by Grant No. 3101/GF4 IPC-11/2015 of the MES of the RK.

References

1. K. A. Boshkayev, J. A. Rueda, R. Ruffini and I. Siutsou, On general relativistic uniformly rotating white dwarfs, *Astrophys. J.* **762**, 1 (2013).
2. P.-E. Tremblay, P. Bergeron and A. Gianninas, An improved spectroscopic analysis of DA White Dwarfs from the Sloan Digital Sky Survey Data Release 4, *Astrophys. J.* **730**, 128 (2011).
3. S. M. de Carvalho, M. Rotondo, J. A. Rueda and R. Ruffini, Relativistic Feynman-Metropolis-Teller treatment at finite temperatures, *Astrophys. J.* **730**, 015801 (2014).
4. K. A. Boshkayev, J. A. Rueda, B. A. Zhami, Zh. A. Kalymova and G. Sh. Balgymbekov, Equilibrium structure of white dwarfs at finite temperatures, *Int. J. Mod. Phys.: Conf. Ser.* (in press). arXiv:1510.02024.